

An Investigation into the Rear Melt Ejection of Laser Drilling

Connor Jones, BEng, MSc

Thesis submitted to The University of Nottingham
for the degree of Doctor of Philosophy, March 2018

©British Crown Owned Copyright 2018/AWE

Abstract

This thesis aims to investigate the rear melt ejection of long pulse laser drilling to further the understanding of the melt ejection mechanism and its unpredictable change with various different parameters including, assist gas pressure, laser power, pulse width, beam profile and material type, as well as to provide a clearer understanding of the relationship between these variables and the rear ejecta cloud and its evolution with time.

To do this, modern high-speed filming technology has been combined with advanced image processing and particle tracking programs which have been developed specifically to analyse the rear melt ejection of laser drilling. These techniques have proven successful in analysing large numbers of high-speed videos and outputting large amounts of quantitative data, including particle velocities, diameters and momentums.

Several interesting findings were made, including the observation of three main ejection mechanisms, the central fast jet, the initial jet and radial ejection. The time resolved evolution of the rear ejecta cloud was found to be impacted by numerous exploding particles, across a range of different parameters. Ten frequently occurring archetypal shapes were identified for the rear ejecta cloud, giving an insight into how it changes with respect to different parameters. Also, a strong material dependence was found to impact particle number, velocity, diameter and momentum when comparing mild steel, titanium and aluminium.

The results showed that as well as material type, mean velocity was dependent on assist gas pressure but showed little change with laser power. Across all parameters tested, mean velocity was observed between 4 - 15 ms^{-1}, whilst maximum velocity is expected to be in excess of 90 ms^{-1}.

Mean particle diameter was shown to be dependent on both assist gas pressure and material type, but was also found to have no clear trending relationship to laser power, however variation of up to 50 µm was observed. Across all parameters, mean particle diameter shown to be 200 - 500 µm, with a maximum diameter of up to 1700 µm.

Through all parameters tested, it was apparent that the majority of particles had relatively low momentums for each individual set of results and that the majority of particles were both relatively small and slow through all parameters tested.

Differing trends were observed between a 2kW IPG 2000S fibre laser and a 6kW QCW IPG fibre laser, which were both used in single pulse mode, due to a difference in beam profile and nozzle size. As assist gas pressure was increased, particle number increased for the 2kW laser used but decreased for the 6kW laser used. Also, for the mild steel and aluminium results, when laser power increased, particle number increased for the 2kW laser but decreased for the 6kW laser.

Overall, this work provides a new insight into the long pulse laser drilling melt ejection mechanism and the rear melt ejection process. Future work hopes to further make use of the techniques used in this project to develop on the understanding of the rear particle ejecta cloud and shed further light on newly discovered trends.

Acknowledgements

First and foremost, I would like to thank my supervisors, Katy Voisey and David Hann, for giving me the opportunity to be involved with this project at the very start, and for all of their hard work supporting me through all stages of this process.

I would also like to thank Scott Aitken, Darren Salisbury, Neil Gaspar and Victor Smeeton of AWE for their ongoing support of my work, as well as the rest of the AWE team for making me feel very welcome during my placement. I would also like to thank all of those involved at AWE for making this academic collaboration possible.

I would also like to thank Adam Clare and Sundar Marimuthu for helping me to produce the best work that I could and guiding me through the formal processes.

Finally, I would like to thank all of my friends, family and colleagues that have supported me throughout this journey.

Publications related to this thesis

Peer reviewed journal articles:

[J1] **C. Jones**, D. B. Hann, K.T. Voisey and S. Aitken, 'Application of high speed filming techniques to the study of rearwards melt ejection in laser drilling,'Journal of Laser Applications vol. 29, no. 2, p. 022204, 2017.

Publications in conference proceedings:

[J1] **C. Jones**, D. B. Hann, K.T. Voisey and S. Aitken, 'Application of high speed filming techniques to the study of rearwards melt ejection in laser drilling,'ICALEO Conference 2016, San Diego, USA

[J1] **C. Jones**, D. B. Hann, K.T. Voisey and S. Aitken, 'Application of high speed filming techniques to the study of rearwards melt ejection in laser drilling,'ILAS Conference 2017, Grantham, UK

Contents

Abstract i

Acknowledgements iii
List of Publications iv

List of Abbreviations x

1 Introduction 1

1.1 Introduction . . . 1
1.2 Aims and Objectives . . . 4
1.3 Methodology . . . 5
1.4 Summary . . . 8
References . . . 8

2 Literature Review 15

2.1 Laser Usage . . . 15
2.2 Industrial Usage of Laser Drilling . . . 18
2.3 Recent Studies in Long (Millisecond) Pulse Width Laser Drilling . . . 20
2.3.1 Experimental Parameter Optimisation . . . 22
2.3.2 Drilling Method Comparisons . . . 24
2.3.3 Modelling Techniques . . . 25
2.3.4 Hybrid Approach . . . 26
2.3.5 Novel Applications . . . 28
2.4 Parameter Optimisation Using Statistical Methods . . . 29
2.5 Spatter and Dross . . . 29
2.6 Particle Collection Techniques In Laser Drilling . . . 30
2.7 High-speed Filming . . . 34
2.8 Image Analysis And Processing - Object Tracking . . . 37

References . . . 44

3 Experimental Methodology **79**

3.1 Parameter Selection . . . 80

3.2 High Speed Filming - Particle Tracking . . . 81

3.3 Different Types Of Lasers Used . . . 83

3.4 Streak Tracking . . . 89

3.5 Hole Analysis . . . 90

3.6 Particle Collection and Analysis . . . 93

References . . . 95

4 Image Analysis and Processing Techniques **101**

4.1 MATLAB: Image Analysis and Processing Toolbox . . . 101

4.2 Image Storage . . . 102

4.3 Calibration . . . 104

4.4 Segmentation . . . 106

4.5 Watershed Transform Function . . . 111

4.6 Munkres Assignment Algorithm . . . 115

References . . . 118

5 Image Processing Methodology **120**

5.1 Image Analysis . . . 121

5.1.1 Image Recording Procedure . . . 121

5.1.2 Initial Image Analysis . . . 125

5.1.3 Image Cleaning . . . 125

5.1.4 Particle Identification . . . 127

5.1.5 Particle Tracking . . . 129

5.1.6 Size and Velocity Measurement . . . 133

5.1.7 Data Storage and Graphical Outputs . . . 135

5.2 Experimental Methods . . . 135

5.3 Basic Observations . . . 138

5.4 Development and Application of the Particle Tracking Methods . . . 139

5.5 Particle Tracking Original Method - First Method 139
5.6 Particle Tracking Straight Line Method - Second Method 146
5.7 Particle Tracking Predictive Method - Third Method 150
References 155

6 Rear Ejecta Particle Basic Observations, Particle Number and Tracking Efficiency 156

6.1 High-speed Filming - Basic Observations 156
6.2 Drilling Parameters 160
6.3 Number of Particles 160
6.3.1 2kW Laser 161
6.3.2 6kW Laser 162
6.4 Tracking Efficiency 163
References 164

7 Rear Ejecta Particle Velocity, Size and Momentum 165

7.1 Velocity Results 166
7.1.1 Mean Particle Velocities over 20 frames 166
7.1.2 Particle Velocity Distribution Histogram - Particles combined for all parameters 169
7.2 Diameter Results 170
7.2.1 Mean Particle Diameters over 20 frames 170
7.2.2 Particle Diameter Distribution Histogram - Particles combined for all parameters 173
7.3 Momentum Results 174
7.3.1 Mean Particle Momentum over 20 frames 174
7.3.2 Particle Momentum Distribution Histogram - Particles combined for all parameters 177
References 177

8 Rear Ejecta Particle Cloud Analysis 178

8.1 Particle Cloud 178

8.1.1 Archetype Plots . . . 179
References . . . 189
9 Rear Melt Ejecta Volume **190**
9.1 Relative Total Combined Rear Melt Ejecta Volume . . . 191
9.2 Laser Power Relationship With Rear Melt Ejecta Volume . . . 194
9.3 Gas Pressure With Rear Melt Ejecta Volume . . . 196
9.4 Material Type With Rear Melt Ejecta Volume . . . 199
9.5 Pulse Width With Rear Melt Ejecta Volume . . . 200
9.6 Parameter Significance In Relation To Rear Melt Ejecta Volume . . . 201
References . . . 202
10 Discussion **204**
10.1 Observations . . . 204
10.1.1 Ejection Mechanisms . . . 204
10.1.2 Exploding Particles . . . 211
10.2 Particle Number . . . 215
10.3 Particle Velocity . . . 224
10.4 Particle Size . . . 226
10.5 Particle Momentum . . . 229
10.6 Particle Cloud Distribution . . . 231
References . . . 238
11 Conclusions and Future Work **240**
11.1 Conclusions . . . 240
11.2 Future Work . . . 243
References . . . 247
12 Appendix **248**
12.1 Simple Tracker Copyright . . . 248
12.2 Uncertainty Calculations . . . 248
12.2.1 Particle Velocity . . . 248
12.2.2 Particle Diameters . . . 251

12.2.3 Particle Momentum 253

Glossary of Terms

Nd:YAG	Neodymium-doped Yttrium Aluminium Garnet.
SEM	Scanning Electron Microscope.
Bitmap image	Bitmap is an image file format which is used to show pixels in a pattern which when combined together form an image. The pixels are arranged in a grid of rows and columns, where each pixel is given a value which represents an intensity value.
Vector Image	A vector image is an image file format made up of numerous points connected by lines which are arranged in a specific pattern to make up an image. The shapes made by the points and lines can be combined together to produce shapes, which can be filled with colour. The position of the points, lines and colours are stored within the image data file.
Lumbar Spinal Segment	A lumbar spinal segment is the lower segment of the spine, made up of vertebrae L1 - L5 in human beings.
Bit	A bit is a unit of data used in computing given one of two

	values, 0 or 1 as a binary digit.
Byte	A byte is a unit which generally consists of 8 bits.
8-bit images	8-bit images are a way to store image data for which each pixel represents one 8-bit byte, the maximum number of colour which can be displayed for an 8-bit image is 256.
Over-Saturation	In imaging, over-saturation is the input of colour or light intensity above the maximum value of which can be displayed.
FEA	Finite Element Analysis.
CFD	Computational Fluid Dynamics.
HAZ	Heat Affected Zone.
EDM	Electro-Discharge Machining.
QCW	Quasi Continuous Wave.
SLM	Selective Laser Melting.
Fps	Frames per second.
Cell Array	A cell array is a row or column of cells, as opposed to a matrix which is made up of multiple

	rows or columns of cells.
MATLAB Function	A MATLAB function is a type of MATLAB program that is pre-programmed to produce a certain set of outputs from a certain set of inputs.
Archetype	Archetype is used in this thesis to refer to a particle rear ejecta cloud shape which occurs at a specific moment in time and occurs frequently across a range of parameters.
TBC	Thermal Barrier Coating.
Melt Ejection Fraction	Ratio of material ejected upwards vs. downwards from a laser drilled test piece.

1

Introduction

The introduction chapter familiarises the reader with an overview of the project, the problems that it attempts to solve and why they are of important. This follows on with the aims and objectives and a brief methodology of how the project was carried out alongside some of the important techniques that were used.

* * *

1.1 Introduction

Laser drilling is an advanced manufacturing process which is the preferred process in multiple applications. Its benefit over other methods such as traditional mechanical drilling and EDM drilling techniques it that the non-contact process uses less consumables, can be used to drill angular holes and can drill many holes at high speed. Laser drilling can be conducted with a variety of pulse widths (a measurement of the duration of a laser pulse). The most commonly used pulse widths are banded into groups of what are known as long, short and ultra-short pulse widths. Although short and ultra-short pulse widths are of benefit to many applications due to their high precision performance, they have much slower material removal rates [1.1]. This

project focuses on long-pulse laser drilling and specifically, its unique melt ejection process.

The melt ejection process is a material removal process understood to be driven by the expulsion of molten material within a hole due to the build up of high pressure gradients, caused by vaporisation, which are large enough to overcome the surface tension forces within the material. This results in a very efficient material removal, as the latent heat of vaporisation does not need to be overcome by all of the material in order for it to be removed [1.2]. However, the process is little understood in the terms of outcome prediction, usually optimal drilling conditions are met at least somewhat with the use of trial and error as a multitude of parameters can affect outcomes unpredictably. Ultimately, the aim of this project is to provide academic insight into the melt ejection process, primarily through the observation of rear melt ejection (shown in Figure 1.1), to further its understanding in order to pave the way for future developments of optimisation and technique advancement.

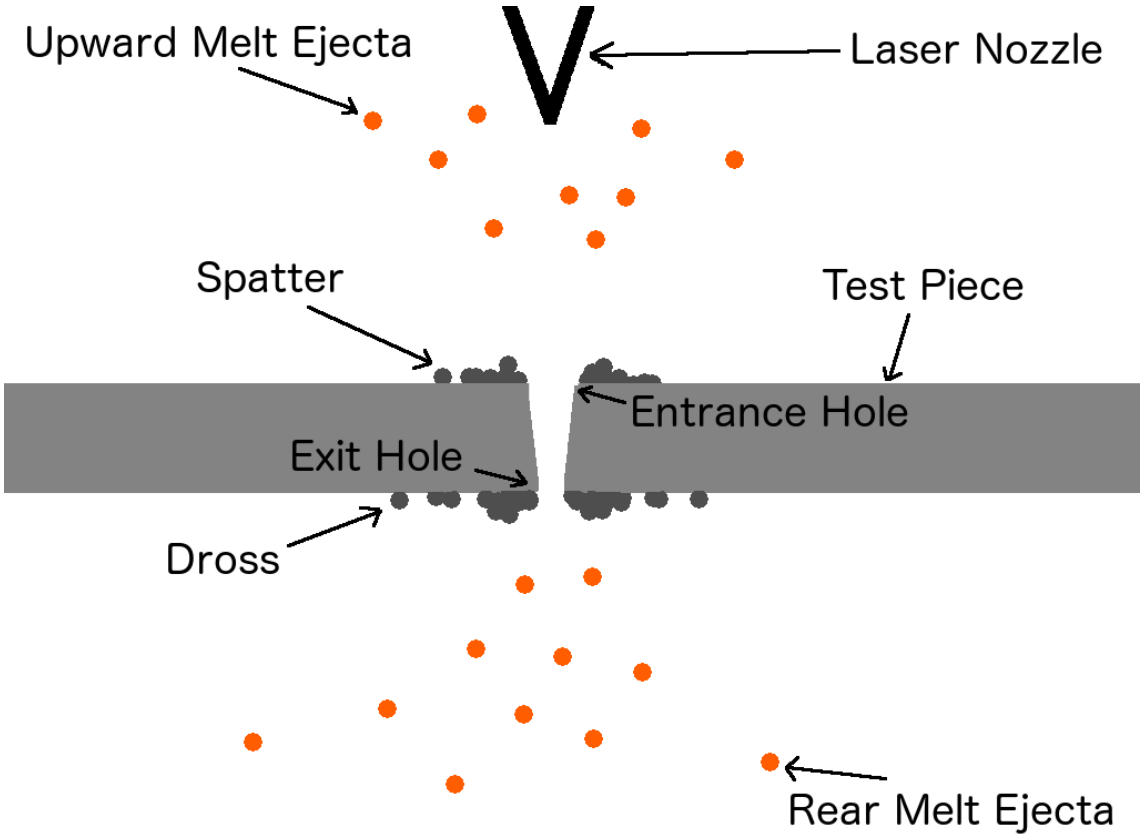


Figure 1.1: Laser Drilling and the build up of ejected material, shown as rear melt ejecta, upward melt ejecta, spatter and dross

Previous research into the underlying mechanisms behind laser drilling has approached the problem in a variety of novel ways. Zhang et al. [1.3] and Low et al. [1.4] used the drilling of transparent media in an attempt to provide an understanding of melt formation within the hole. Voisey et al. [1.2], [1.5] have used various particle collection techniques for analysis and velocity calculation. Sharma et al. [1.6], Ganesh et al. [1.7], Yang et al. [1.8] and Mishra et al. [1.9] have approached laser drilling with a variety of mathematical and computational modelling techniques. Yilbas et al. [1.10] have used streak photography techniques whilst Girardot et al. [1.11] and Voisey et al. [1.2] have used high-speed filming techniques. All of which have provided insight on laser drilling mechanisms and often highlighted the complexity of the melt ejection mechanism.

This project focuses on the use of high-speed imaging and image and analysis particle tracking techniques to observe the behaviour of rear melt ejection and it's change with parameters such as laser power, beam profile, assist gas pressure, material type and pulse width. Rear melt ejection is of particular interest to AWE, industrial collaborators in this project, who require the knowledge of the evolution of the rear ejection particle cloud with time under specific parameters for an internal project. This work has been conducted alongside AWE to provide a solution to their problem, whilst also serving to expand overall insight into the melt ejection process and the behaviour of rear melt ejection under various parameters for the purposes of furthering academic understanding.

1.2 Aims and Objectives

The general aim of this project is to provide a new insight into the long pulse laser drilling melt ejection process. This is done by closely analysing the rear melt ejection process, mostly using high-speed filming, image analysis and processing and particle tracking techniques. Chapter two begins with a literature review of the recent research involving the rear melt ejection process and long pulse width laser drilling. This goes on to provide an introduction and explanation of the essential image analysis and processing techniques which were necessary for the production of the results within this work for the unfamiliar reader. Chapter two concludes with a more specific explanation of how and why these techniques were used within this work. Chapter three presents a methodology of each of the experimental methods used in this work, as well as how and why they were carried out. Chapter four provides a detailed results and a methodology of the exact processes which were carried out for a specific set of results in this work from the experimental set-up and recording of the high speed videos, to the specifics of the particle tracking techniques used and how the results were output in such a way to sum up the evolution of several revisions of the programs, which were produced in order to retain the results seen in

this work. Although a specific set of parameters have been used to demonstrate this, the exact same techniques were applied to all parameters which feature within the results in this work. The results and discussion for this work are given in chapters five and six respectively, whilst the conclusions drawn are summarised in chapter seven, along with future work prospects.

One of the main objectives of this research was to record high-speed videos of the laser drilling process with high definition images to provide a new insight into the rear melt ejection process. After extracting as much qualitative data as possible from the videos, the next main objective was to use image processing techniques to prepare the videos as best as possible to allow for the use of advanced particle tracking techniques. Then, a particle tracking program was created specifically for these videos to provide quantitative results from a large number of videos in order to provide a totally new perception of the rear melt ejection process in terms of the particle cloud evolution with time and the size and speed of ejected particles. For parameters including laser power, assist gas pressure, material type, beam profile and pulse width, analysis of these results were conducted within the project with the objective of identifying any trends which might provide an insight into the process and how different parameters might affect the melt ejection mechanism.

The aim of this work is to use the discussed objectives to provide an in-depth understanding of the real-time evolution of the rear melt ejection particle cloud. This was done to benefit work alongside the industrial partner, AWE, as well as to provide an insight into the laser melt ejection process in terms of the influence of various different parameters and the possible causes behind them.

1.3 Methodology

The project began with a literature review of relevant research. From there, preliminary tests were carried out with the experimental equipment to assess imaging

capabilities and which parameters to investigate. Figure 1.2 reflects the progression of the project with the decided material inputs.

The test materials, material thicknesses and pulse widths were chosen because they were of interest to the industrial collaborator, AWE. The materials mild steel [1.2,1.12–1.21], aluminium [1.9,1.22–1.27,1.29–1.32] and titanium [1.33–1.42] are also found to be prevalent in laser drilling research. The lasers, material thickness and pulse widths were chosen because they were of interest to the industrial collaborator, AWE. The material thicknesses and pulse widths were also ideal because they allowed for single pulse penetration for the majority of parameters tested.

From the experimental results for both lasers, a systematic approach was taken to analyse the data consistently and effectively, as shown in Figure 1.2. The development of the particle tracking program was constantly revised, as illustrated by the feedback loop shown with the dotted line in Figure 1.2.

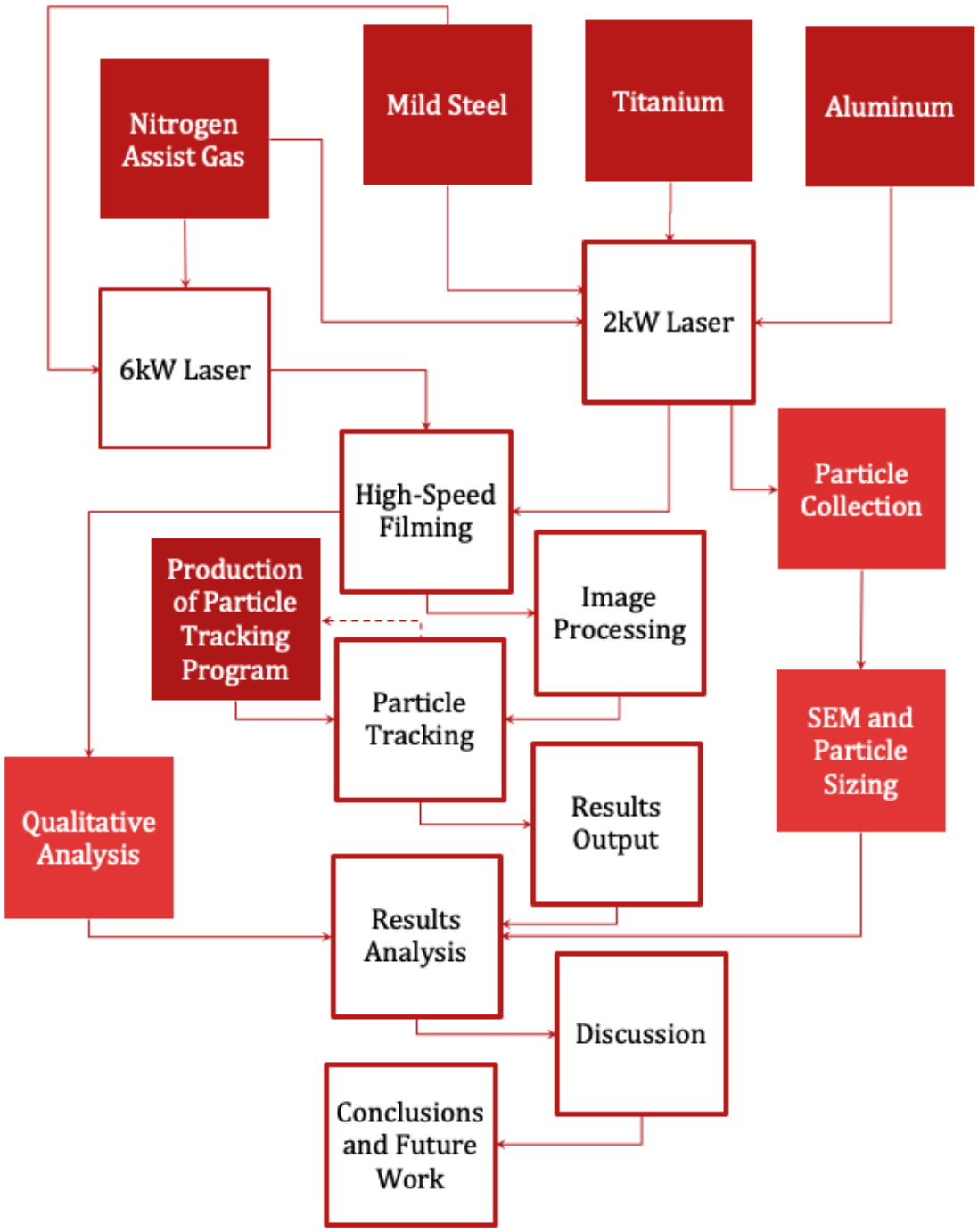


Figure 1.2: Project Methodology Flowchart

1.4 Summary

The main objective of this research is to further understand the relationship between rear melt ejection and different laser drilling parameters to give an insight into the mechanisms occurring within the rear melt ejection process and why they occur. To do this high speed filming was used and a particle tracking algorithm was developed to analyse the speed, size and momentum of ejecta particles. Three rear melt ejection mechanisms were found and different particle cloud development patterns were established for specific laser drilling parameters.

References

[1.1] F. O. Olsen and L. Alting, "Pulsed Laser Materials Processing, ND-YAG versus CO2Lasers," *CIRP Annals - Manufacturing Technology*, vol. 44, no. 1, pp. 141–145, 1995.

[1.2] K. T. Voisey, S. S. Kudesia, W. S. O. Rodden, D. P. Hand, J. D. C. Jones, and T. W. Clyne, "Melt ejection during laser drilling of metals," *Materials Science and Engineering A*, 2003.

[1.3] Y. Zhang, S. Li, G. Chen, and J. Mazumder, "Experimental observation and simulation of keyhole dynamics during laser drilling," *Optics & Laser Technology*, vol. 48, pp. 405–414, jun 2013. [Online]. Available: http://linkinghub.elsevier.com/retrieve/pii/S0030399212005130

[1.4] D. K. Y. Low and L. Li, "An investigation into melt flow dynamics during repetitive pulsed laser drilling of transparent media," *Optics and Laser Technology*, 2001.

[1.5] K. T. Voisey, T. Klocker, and T. W. Clyne, "Measurement of melt ejection velocities during laser drilling of steel, using a novel droplet stream interception

technique," *Acta Materialia*, 2002.

[1.6] S. Sharma, Y. Pachaury, S. N. Akhtar, and J. Ramkumar, "A study on hydrodynamics of melt expulsion in pulsed Nd: YAG laser drilling of titanium," in *COMSOL Conference Pune*, 2015.

[1.7] R. K. Ganesh and A. Faghrit, "A generalized thermal modeling for laser drilling process- I . Mathematical modeling and numerical methodology," vol. 40, no. 14, pp. 3351–3360, 1997.

[1.8] Y. Yang, Z. Chen, and Y. Zhang, "Melt flow and heat transfer in laser drilling," *International Journal of Thermal Sciences*, vol. 107, pp. 141–152, sep 2016. [Online]. Available: http://www.sciencedirect.com/science/article/pii/S1290072915301447

[1.9] S. Mishra and V. Yadava, "Modeling and optimization of laser beam percussion drilling of thin aluminum sheet," *Optics & Laser Technology*, vol. 48, pp. 461–474, jun 2013. [Online]. Available: http://linkinghub.elsevier.com/retrieve/pii/S0030399212005002

[1.10] B. S. Yilbas, "Study of liquid and vapor ejection processes during laser drilling of metals ," *Journal of Laser Applications*, vol. 7, no. 147, 1995.

[1.11] J. Girardot, M. Schneider, L. Berthe, and V. Favier, "Investigation of delamination mechanisms during a laser drilling on a cobalt-base superalloy," *Journal of Materials Processing Technology*, vol. 213, no. 10, pp. 1682–1691, oct 2013. [Online]. Available: http://www.sciencedirect.com/science/article/pii/S0924013613001301

[1.12] M. Ghoreishi, D. K Y Low, and L. Li, "Statistical modelling of laser percussion drilling for hole taper and circularity control," *Proceedings of The Institution of Mechanical Engineers Part B-journal of Engineering Manufacture - PROC*

INST MECH ENG B-J ENG MA, vol. 216, pp. 307–319, 03 2002.

[1.13] M. Ghoreishi, D. K. Y Low, and L. Li, "Comparative statistical analysis of hole taper and circularity in laser percussion drilling," *International Journal of Machine Tools Manufacture - INT J MACH TOOL MANUF*, vol. 42, pp. 985–995, 07 2002.

[1.14] D. K. Y. Low, L. Li, and P. J. Byrd, "Hydrodynamic physical modeling of laser drilling," *Journal of Manufacturing Science and Engineering-transactions of The Asme - J MANUF SCI ENG*, vol. 124, 11 2002.

[1.15] O. B. Nakhjavani and M. Ghoreishi, "Multi criteria optimization of laser percussion drilling process using artificial neural network model combined with genetic algorithm," *Materials and Manufacturing Processes*, vol. 21, pp. 11–18, 01 2006.

[1.16] G. Ng, P. Crouse, and L. Li, "An analytical model for laser drilling incorporating effects of exothermic reaction, pulse width and hole geometry," *International Journal of Heat and Mass Transfer*, vol. 49, pp. 1358–1374, 04 2006.

[1.17] B. Yilbas, A. F. Arif, and A. A. B.J, "Laser cutting of holes in thick sheet metals: Development of stress field," *Optics and Lasers in Engineering - OPT LASER ENG*, vol. 47, pp. 909–916, 09 2009.

[1.18] J. Girardot, P. Lorong, L. Illoul, N. Ranc, M. Schneider, and V. Favier, "Modeling laser drilling in percussion regime using constraint natural element method," *International Journal of Material Forming*, vol. 10, no. 2, pp. 205–219, Apr 2017. [Online]. Available: https://doi.org/10.1007/s12289-015-1269-0

[1.19] G. Ng and L. Li, "The effect of laser peak power and pulse width on the hole geometry repeatability in laser percussion drilling," *Optics Laser Technology*, vol. 33, no. 6, pp. 393 – 402, 2001. [Online]. Available:

http://www.sciencedirect.com/science/article/pii/S0030399201000482

[1.20] R. Sattmann, V. Sturm, and R. Noll, "Laser-induced breakdown spectroscopy of steel samples using multiple q-switch nd:yag laser pulses," *Journal of Physics D: Applied Physics*, vol. 28, no. 10, p. 2181, 1995. [Online]. Available: http://stacks.iop.org/0022-3727/28/i=10/a=030

[1.21] J. Cheng, F.-J. Kahlen, and A. Kar, "Effects of intrapulse structure on hole geometry in laser drilling," *Journal of Laser Applications*, vol. 12, no. 6, pp. 232–238, 2000. [Online]. Available: https://doi.org/10.2351/1.1324714

[1.22] D.-G. AHN and G.-W. JUNG, "Influence of process parameters on drilling characteristics of al 1050 sheet with thickness of 0.2 mm using pulsed nd:yag laser," *Transactions of Nonferrous Metals Society of China*, vol. 19, 09 2009.

[1.23] M. Guillong, I. Horn, and D. Günther, "A comparison of 266 nm, 213 nm and 193 nm produced from a single solid state nd: Yag laser for laser ablation icp-ms," *JOURNAL OF ANALYTICAL ATOMIC SPECTROMETRY*, vol. 18, pp. 1224–1230, 09 2003.

[1.24] C.-C. Ho, J.-J. He, and T.-Y. Liao, "On-line estimation of laser-drilled hole depth using a machine vision method," *Sensors (Basel, Switzerland)*, vol. 12, pp. 10 148–62, 12 2012.

[1.25] C.-C. Ho, G.-R. Tseng, Y.-J. Chang, J.-C. Hsu, and C.-L. Kuo, "Magnetic-field-assisted laser percussion drilling," *The International Journal of Advanced Manufacturing Technology*, vol. 73, no. 1, pp. 329–340, Jul 2014. [Online]. Available: https://doi.org/10.1007/s00170-014-5815-6

[1.26] C.-C. Ho, Y. J. Chang, J.-C. Hsu, C.-M. Chiu, and C.-L. Kuo, "Optical emission monitoring for defocusing laser percussion drilling," *Measurement*, vol. 80, 10 2015.

[1.27] C.-C. Ho, Y. J. Chang, J.-C. Hsu, C.-L. Kuo, and G.-H. Lee, "Characteristics of the thermal strain of gas jet-assisted laser percussion drilling," vol. 28, pp. 1067–1075, 01 2016.

[1.28] C.-C. Ho and J.-J. He, "On-line monitoring of laser-drilling process based on coaxial machine vision," *International Journal of Precision Engineering and Manufacturing*, vol. 15, pp. 671–678, 04 2014.

[1.29] C.-C. Ho, Y.-M. Chen, J.-C. Hsu, Y. J. Chang, and C.-L. Kuo, "Characteristics of the effect of swirling gas jet assisted laser percussion drilling based on machine vision," *Journal of Laser Applications*, vol. 27, 10 2015.

[1.30] H. Singh, S. Kwan, D. Tam, N. Mamalis, K. Maclean, and I. Ahmed, "Fracture and dislocation of a glass intraocular lens optic as a complication of neodymium:yag laser posterior capsulotomy: Case report and literature review," *Journal of Cataract and Refractive Surgery*, vol. 41, no. 10, pp. 2323–2328, 2015, cited By 1. [Online]. Available: https://www.scopus.com/inward/record.uri?eid=2-s2.0-84952332605&doi=10.1016%2fj.jcrs.2015.09.013&partnerID=40&md5=5055f48b565192dd481e3921f2ca7dae

[1.31] L. Tunna, W. O'Neill, A. Khan, and C. Sutcliffe, "Analysis of laser micro drilled holes through aluminium for micro-manufacturing applications," *Optics and Lasers in Engineering - OPT LASER ENG*, vol. 43, pp. 937–950, 09 2005.

[1.32] Y. Zang, X. Ni, and B. Han, "The ejection angle of molten aluminum induced by millisecond pulsed laser," *Journal of Applied Physics*, vol. 116, pp. 013 104–013 104, 07 2014.

[1.33] S. Bandyopadhyay, J. S. Sundar, G. Sundararajan, and S. Joshi, "Geometrical features and metallurgical characteristics of nd:yag laser drilled holes in thick in718 and ti–6al–4v sheets," *Journal of Materials Processing*

Technology, vol. 127, no. 1, pp. 83 – 95, 2002. [Online]. Available: http://www.sciencedirect.com/science/article/pii/S0924013602002704

[1.34] S. Bandyopadhyay, H. Gokhale, J. S. Sundar, G. Sundararajan, and S. Joshi, "A statistical approach to determine process parameter impact in nd:yag laser drilling of in718 and ti-6al-4v sheets," *Optics and Lasers in Engineering*, vol. 43, no. 2, pp. 163 – 182, 2005. [Online]. Available: http://www.sciencedirect.com/science/article/pii/S0143816604001435

[1.35] R. Goyal and A. Dubey, "Modeling and optimization of geometrical characteristics in laser trepan drilling of titanium alloy," *Journal of Mechanical Science and Technology*, vol. 30, pp. 1281–1293, 03 2016.

[1.36] R. Goyal and A. K. Dubey, "Hybrid approach for modeling and optimization of hole taper during laser trepan drilling of ti-6al-4v alloy sheet," *Procedia Materials Science*, vol. 5, pp. 1781 – 1790, 2014, international Conference on Advances in Manufacturing and Materials Engineering, ICAMME 2014. [Online]. Available: http://www.sciencedirect.com/science/article/pii/S221181281400738X

[1.37] W. S. O. Rodden, S. S. Kudesia, D. Hand, and J. Jones, "Use of "assist" gas in the laser drilling of titanium," *Journal of Laser Applications*, vol. 13, 10 2001.

[1.38] B. Yilbas, "Investigation into drilling speed during laser drilling of metals," *Optics Laser Technology*, vol. 20, no. 1, pp. 29 – 32, 1988. [Online]. Available: http://www.sciencedirect.com/science/article/pii/0030399288900096

[1.39] B. S. Yilbas, "A study of affecting parameters in the laser hole-drilling of sheet metals," *Journal of Mechanical Working Technology*, vol. 13, no. 3, pp. 303 – 315, 1986. [Online]. Available: http:

//www.sciencedirect.com/science/article/pii/0378380486900227

[1.40] B. Yilbas, "Parametric study to improve laser hole drilling process," *Journal of Materials Processing Technology*, vol. 70, no. 1, pp. 264 – 273, 1997. [Online]. Available: http://www.sciencedirect.com/science/article/pii/S0924013697000769

[1.41] B. S. Yilbaş, A. Z. Şahin, and R. Davies, "Laser heating mechanism including evaporation process initiating laser drilling," *International Journal of Machine Tools and Manufacture*, vol. 35, no. 7, pp. 1047 – 1062, 1995. [Online]. Available: http://www.sciencedirect.com/science/article/pii/089069559400062O

[1.42] B. Yilbas, S. Akhtar, and C. Karatas, "Laser trepanning of a small diameter hole in titanium alloy: Temperature and stress fields," *Journal of Materials Processing Technology*, vol. 211, no. 7, pp. 1296 – 1304, 2011. [Online]. Available: http://www.sciencedirect.com/science/article/pii/S0924013611000586

2

Literature Review

This chapter summarises a literature review of work in the area of millisecond pulse, melt based laser drilling.

* * *

2.1 Laser Usage

Lasers have become a part of everyday life in the developed world. They are heavily used across a wide range of industries, with a vast range of applications such as: optical disk drives [2.1], laser printers [2.2], barcode scanners [2.3], fibre optics [2.4]. laser eye surgery [2.5], autonomous driving [2.6], laser directed energy weapons [2.7], space junk removal [2.8], speed guns [2.9], rangefinders [2.10] and many more.

In modern times, lasers have become very useful in industrial manufacturing. Here some of the main processes are: laser cutting [2.11–2.17], laser welding [2.18–2.20], additive manufacturing [2.21–2.26], laser marking [2.27–2.31], laser milling [2.32], laser surface treatment [2.33–2.36] and of course laser drilling. Each of these processes can be carried out with a wide range of laser types and parameters.

Branching off further, the laser drilling process can be broken down into four main

types: single pulse drilling [2.37–2.40], percussion drilling [2.41–2.46], trepanning [2.47–2.52] and helical drilling [2.53–2.55].

Single pulse laser drilling is the same as percussion drilling but with a single pulse. During this process the workpiece is irradiated with a single laser pulse, the laser beam does not move relative to the workpiece. It is the most effective of the laser drilling processes [2.37] as it is the quickest of the four laser drilling processes [2.55] and is usually paired with the melt ejection mechanism that is prevalent with a millisecond pulse width for maximum material removal [2.37–2.40].

However, the major downside to single pulse drilling is that it lacks precision [2.55]. Because of this, it is best used for applications where many holes need to be drilled quickly, where quality is less important. Industry generally prefers the improved hole quality of the other three processes over single pulse drilling, however it does have applications in industry, such as, scribing and the manufacture of filters in the automotive industry [2.56]. One area in which single pulse drilling is very useful is in academic studies [2.37–2.40]. This is because it simplifies a complicated process, and is particularly beneficial when trying to understand the melt ejection mechanism.

A laser beam that is stationary relative to the workpiece is also used for percussion drilling, where multiple pulses are used. Using multiple pulses opens up the possibility of pulse train shaping. Percussion drilling is a time dependent process, since once a material is irradiated by a pulse, heat remains in the hole for a period of time, as does ejecta. Often the remaining thermal energy and ejecta from the previous pulse can interfere with the next irradiation process. Markcoons et al. [2.57] demonstrated how pulse train shaping, the temporal aspect of each pulse, can impact drilling efficiency and various hole quality measures.

After single pulse drilling, percussion drilling has the next quickest drilling duration [2.55] compared to the trepanning and helical drilling. Although it provides

better precision in terms of hole quality, it still cannot compete with trepanning or helical drilling [2.55]. Percussion drilling is widely used in the aerospace industry for drilling effusion cooling holes aero-engine components [2.58], it is especially useful here because the process can be used to drill difficult materials such as superalloys and ceramics at acute angles [2.59].

Trepanning is a drilling process in which a piercing hole is made using single pulse / percussion drilling followed by a laser cutting procedure in which a hole, circular or otherwise, is cut out from this point. Often the original piercing hole is removed entirely, therefore, any defects caused by this initial hole are fully or partially removed. Trepanning is particularly useful for providing consistency and creating large holes of any shape [2.56].

Compared to percussion drilling, trepanning produces more rear melt ejection than upward melt ejection [2.59]. This benefits the hole quality because common defects, spatter and thickness of the recast layer are reduced [2.60]. However, its main downside is that it slower than percussion drilling by a factor of 4-10 [2.59].

Helical drilling is another type of laser drilling process. Similar to trepanning, the laser beam moves relative to the workpiece. However, the beam rotates, twists and turns during the drilling process to provide an improved hole quality and allow for more complex shapes.

Helical drilling has the highest level of precision but has the slowest drilling time [2.55]. It is mostly used with short and ultrashort pulses [2.61].

Pulse width is a very important factor in laser drilling, this is the length of each individual laser pulse. They can be divided up into long, short and ultrashort pulse widths. Each pulse width is generally dominated by each of three specific mechanisms, melt ejection, hot ablation and cold ablation respectively [2.62].

Shorter pulse lasers are advantageous in terms of hole quality due to their potential to create non-thermal ablation [2.45]. This allows the laser to evaporate material quickly before much heat conduction can occur around the hole, minimising melt and preventing thermal related defects [2.63]. The downside of this is that ultra-short pulse lasers are expensive and their material removal rate is very slow, due to low repetition rates [2.63].

On the other hand, long (millisecond) pulse widths, which remove material primarily by melt expulsion rather than vaporisation, are much more efficient. They have a much higher material removal rate, although are prone to more thermal defects and lesser hole quality. Despite this, long pulse laser drilling has become an important manufacturing process in a range of applications, most notably in the aerospace industry in the drilling of aero-engine components.

This work focuses on the melt ejection process and therefore single pulse drilling with a millisecond pulse width has been used. This allows for a simplified analysis of the melt ejection process in relation to rear melt ejecta.

2.2 Industrial Usage of Laser Drilling

Lasers has been extensively used for drilling applications since the inception of the application in the early 1960s [2.43]. These applications have included a wide range of materials from baby bottle nipples to the piercing of diamonds [2.64].

Today, laser drilling is still used extensively in modern manufacturing processes to create a wide range of components [2.61]. Specific applications and industries tend to favour specific types of drilling and pulse widths depending on their requirements for material removal speed and hole quality.

Ultrashort and short pulse widths tend to be used when high quality holes are required with a low amount of material removal. One such application is the drilling

of inkjet nozzles to 28 µm in diameter using excimer lasers [2.65]. Another application is the drilling of diamond, although transparent in a wide range of wavelengths, diamond turns to graphite under the high power densities, which can be provided by nanosecond pulse excimer lasers and ultrashort femtosecond lasers [2.66].

Many short and ultrashort pulse width applications use trepanning and helical drilling due to their increased precision. For example, in the laser drilling of fuel injector holes, ultrashort pulse widths can be used with helical drilling [2.67]. In the production of microvia holes in Printed Circuit Boards (PCBs), trepanning is part of a two step laser drilling process [2.68].

Single pulse drilling in the millisecond regime is more favoured by applications that require a large amount of material removal at high-speed. One of these applications is the drilling of stainless steel fuel filters in the automotive industry to drill up to 600 holes per second [2.69,2.70]. Single pulse drilling is also used for the drilling of suture holes in surgical needles [2.71]. Another application is to produce aerostatic bearings, around 100 - 1000 holes are drilled per bearing in materials such as aluminium, stainless steel, brass or plastic - usually 0.8mm thick [2.71]. Single pulse drilling is also used in the aerospace industry to minimise aerodynamic drag and reduce fuel consumption. This is done by drilling holes at the wings and fin of an aeroplane to encourage a laminar flow [2.72].

The majority of long pulse drilling applications are found in the aerospace industry, using percussion drilling and trepanning, where many thousands of holes are required in a short cycle times [2.56]. Cooling holes of small diameter are produced in aero-engine components such as, combustion rings, turbine blades, nozzle guide vanes and after-burners [2.58]. These components are generally made of nickel superalloys, which are generally difficult to machine with conventional processes [2.73].

These holes are generally produced by Electro-Discharge Machining (EDM) and Electro-Chemical Machining (ECM) methods [2.74]. However, laser drilling has its

advantages. As well as its material removal efficiency, long pulse drilling is valued in the aerospace industry because of its potential to drill at acute angles and to drill through thermal barrier coatings (TBCs) - these are non-conducting materials which prevent the use of EDM and ECM methods [2.73]. It's main disadvantages, for both single pulse and percussion drilling, relate to hole quality, some of these defects relate to thermal effects such as recast layer, heat affected zone and micro-cracks [2.75] but also include defects such as spatter formation [2.75] and back wall strike for hollow components (due to rear melt ejection) [2.76].

2.3 Recent Studies in Long (Millisecond) Pulse Width Laser Drilling

Laser drilling is widely used in a range of industry applications. The majority of these are focused on similar issues, even though each application has specific requirements. These issues are summarised in the performance parameters in Figure 2.1. Laser drilling performance parameters are generally based around hole quality, with the exception of the concern of back wall strike for the drilling of hollow components [2.76].

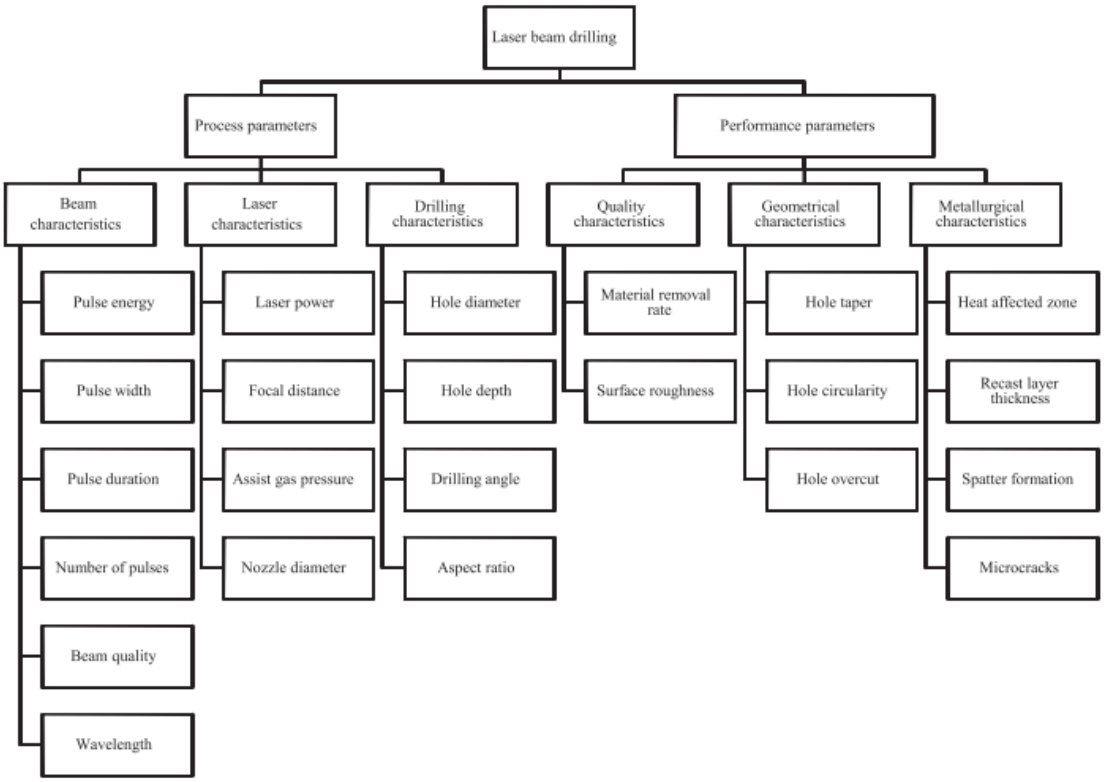


Figure 2.1: Important process and performance parameters in laser drilling [2.75]

Most of the research available for long pulse laser drilling is therefore focused on controlling hole quality issues. The majority of this research centres on a combination of experimental and statistical modelling optimisation of the process parameters shown in Figure 2.1 to control hole quality as well as the use of hybrid approaches such as using multiple lasers or drilling methods. The majority of other research uses numerical modelling and FEA techniques to try to simulate the relationships between process parameters and performance parameters in order to predict hole quality under certain process parameters and to understand the underlying processes.

In terms of materials, many laser drilling studies are focused on nickel superalloy [2.39,2.49,2.77–2.79], which is widely used within the aerospace, marine, chemical and automobile industries [2.75]. Other heavily investigated metals of include: steel [2.43,2.80–2.89], which is one of the most commonly used materials in the world

and is used frequently for construction and architectural fabrications [2.75], aluminium [2.90–2.101], which is commonly drilled in PCBs [2.75] as well as widely used in the space, marine, chemical, construction and automotive industries [2.102]and titanium [2.40,2.41,2.47–2.49,2.103–2.107] which is used in some aircraft turbine engine components [2.108–2.111], as well as heavily used throughout the aerospace, automotive and medical industries [2.75]. Research concerning non-metallic materials for laser drilling focuses mainly on ceramics [2.75], one reason for this is the advantage of laser drilling to operate as a non-contactless process at high working temperatures without tool wear [2.112,2.113]. Other non-metallic materials include glass, polymers and composites [2.75].

The remainder of this section will focus on a summary of the most recent academic studies which consider long pulse drilling to give the reader an understanding of the current interest in this field. This is a small section of the overall laser drilling research, of which much is focused on short and ultrashort laser drilling. As mentioned, the long pulse regime is dominated by the melt ejection mechanism, which is the focus of the this thesis. The work is broken down into sections of experimental parameter optimisation, drilling method comparisons, modelling techniques, hybrid approaches and novel applications.

2.3.1 Experimental Parameter Optimisation

Marimuthu et al. [2.114] investigated the fundamental aspects of millisecond pulsed Quasi-Continuous Wave (QCW) fibre trepanning of 5mm thick nickel superalloy. The study investigated the relationship between QCW process parameters on the hole quality parameters recast layer, oxide layer, hole surface characteristic and fatigue performance. It was shown that the QCW high average power (2000W) increased trepanning speed up to 500mm/min without a loss of hole quality. It was also shown that a low peak power and high pulse frequency was preferential to a high peak power and a low pulse frequency for increased hole quality.

Bahar et al. [2.115] conducted a process parameter optimisation study on the long pulse laser drilling of 1-3mm thick titanium alloy using a 550W Nd:YAG solid state laser to improve hole quality. Design of Experiment (DOE) techniques were used and the key measured performance parameters were characterised as a minimisation of taper, HAZ and spatter. It was observed that a nitrogen assist gas produced the least hole taper and that nozzle focus position influenced hole size and volume of spatter. Laser power was shown to be a significant driver in hole quality, where an increase in laser power was found to correlate to a larger hole size and more spatter.

Markcoons et al. [2.57] investigated the effects of pulse train shaping on the millisecond pulse drilling of 0.8 - 2mm thick mild steel using a 2kW ytterbium fibre laser. Three methods were compared, single pulse drilling, multi-pulse drilling and Linear Ramping-Up Pulse (LRUP). The methods were compared by experimentally evaluating the minimum number of pulses / pulse width that was required to achieve breakthrough in the test piece. Markcoons et al. [2.57] found that both multiple pulse tests typically increased drilling efficiency by 35% with linear multi-pulse drilling being the most efficient. It was also observed that pulse train shaping does not increase the hole quality, as single pulses produced the smallest entrance variation and recast layer thickness of the three methods.

Stephen et al. [2.116] conducted a study on the laser drilling of titanium sheet with single pulse and percussion drilling using long pulses with a QCW fibre laser for the application of aerospace leading edges. It was shown that both single pulse and percussion drilling with long pulses is suitable for achieving industrial level through holes for Hybrid Laminar Flow Control (HLFC) applications for which structures require more than 300 50 µm diameter holes are required with deviations of less that 3 µm.

2.3.2 Drilling Method Comparisons

Ebrahimzade et al. [2.117] examined the optimal drilling parameters for laser drilling, comparing long pulse, ultrashort pulse trepanning and percussion drilling of nickel based superalloy with an APS deposited TBC coating for multiple drilling angles. Hole microstructure aspects where analysed as well as cyclic oxidation experiments and FEA to investigate the effects of delamination. It was found that percussion drilling caused more cracking and increased recast layer than trepanning. Fibre laser drilling produced poorer hole defects than flash lamp laser drilling due to the higher pulse frequency of the fibre laser. Overall, percussion and inclined drilling were shown to have a reduced hole quality and increased oxidation compared to trepanning and vertical drilling.

Antar et al. [2.118] conducted a comparison of modern high speed EDM and the QCW 20kW fibre laser drilling 0.8mm holes in nickel based aerospace alloy of 5 - 10mm thickness. Drill speed, recast layer and hole taper were the key variables investigated. Laser drilling was shown to be significantly faster (¡3ms compared to 48ms), which EDM was shown to produce a better hole quality.

Rihakova et al. [2.119] compared the hole quality produced by millisecond pulse percussion drilling 2mm thick alumina using a 2Bar compressed air assist gas for two lasers. The two lasers compared were an Nd:YAG LASAG KLS 246-102 laser and a QCW ytterbium fibre laser YLR-150/1500 QCW IPG. Rihakova et al. [2.119] found that the QCW fibre laser produced narrower holes due to its smaller spot size and higher beam quality. The Nd:YAG laser showed that entrance and exit holes increased proportionally with pulse length and pulse energy. Higher numbers of pulses were also shown to improve hole circularity.

A study was carried out by Imran et al. [2.78] to compare the differences in surface integrity between three drilling techniques for nickel-based superalloy. EDM, micro-mechanical drilling and long pulse laser drilling were the techniques com-

pared. Backscatter Electron (BSE), Electron Backscatter Diffraction (EBSD) and nano-indentation techniques were used to assess surface hardness, grain disorientation, plastic deformation and HAZ in order to characterise surface integrity. The results showed that micro-mechanical drilling is superior to both EDM and long pulse laser drilling in these aspects.

2.3.3 Modelling Techniques

In 2015, Sharma et al. [2.120] produced a multi-phase axisymmetric model using COMSOL Multiphysics to study the effects of different laser beams in the long pulse drilling of titanium. An ideal gaussian beam was compared with a top hat beam in terms of temperature distribution, melt velocity and shape of the keyhole. It was found that an ideal gaussian beam produced increased taper and leaves a poor finish within the hole due to the increased adherence of molten material. The top hat beam was found to produce less taper, however resulted in a build up of molten material near the edge of the hole as irradiation increased.

In 2018, Sharma et al. [2.121] investigated the upward melt ejection of long pulse percussion drilling using a 2D free surface numerical model for the QCW laser drilling of blind holes. The model was validated through comparison with experimental tests based on measured hole geometries. It was found that during initial pulses, recoil pressure was the dominant factor in expulsion of melt. Further pulses where shown to cause shadowing, where surface tension drags melt up, constricting the hole near the entrance. The shadowing effect was shown to cause a significant amount of melt to remain in the hole. The study by Sharma et al. [2.121], breaks down long pulse percussion drilling into a non-uniform process of several regimes, keyhole digging, melt shadowing and melt reclosure.

Yang et al. [2.122] created a numerical model of long pulse drilling which explicitly includes the melt flow effect through the equation of momentum conservation. The model demonstrates that the effect of melt flow on material removal can be ignored

in some cases.

Zhang et al. [2.39] investigated the melt ejection mechanism with a numerical simulation and validating experimental investigation based on the long pulse laser drilling of 304 stainless steel and aluminium. The study showed that aluminium was found to have a develop a thick liquid zone for the process parameters relative to stainless steel and therefore is expected to produce a larger quantity of melt ejecta because of this. The experimental methods used an Nd:YAG laser for millisecond drilling of stainless steel and aluminium. The melt ejection simulations were validated using a shadow-graphic technique, weighing of collected melt and test piece, microscope imaging as well as observations of surface methodology and cross-sections of the keyhole.

In 2018, Wang et al. [2.123] investigated the effects of the thermal stress and hole formation from millisecond laser percussion drilling on TBC coated super nickel alloy using an FEA model with thermo-mechanical coupled analysis. The model was validated with an experimental study. The delamination phenomenon was addressed in particular, and it was found that the solidification rate and sequence between different materials can play a prominent role in crack formation. It was also found that a stagnation phenomenon can occur at low laser peak power compared to high laser peak power.

2.3.4 Hybrid Approach

Qin et al. [2.124] investigated the use of combined millisecond and nanosecond pulses for the drilling of aluminium with a 5kW disk laser and a Q-switched Nd:YLF laser. Improved drilling efficiency was achieved using the combined method and a numerical model was created to understand the physical processes. The nanosecond pulses were perceived to create shock waves which assisted the ejection of the melt created by the initial millisecond pulses. For deeper holes, the method failed when the nanosecond laser beam moved out of focus.

Wang et al. [2.125] investigated the use of magnetic assistance and / or assist gas for melt ejection during millisecond laser drilling. High speed photography was used to assess the melt ejection performance. Co-axial assist gas was shown to be the most effective method for promoting plume dispersion and enhancing the drilling efficiency of both blind and through hole drilling - however, a hybrid approach was shown to be most effective. Standard hole quality measures were also used for hole entrance and exit diameters, hole depth and recast layer thickness.

Wang et al. [2.126] also investigated the use of magnetic assistance with ultrasonic assistance for the long pulse laser drilling process, in an attempt to improve hole quality. It was demonstrated that the process could be used to increase hole quality based on the assessment of various drilling performance parameters for both blind and through holes.

Wang et al. [2.4] followed up the previous study with an investigation to improving hole quality in the drilling of TBCs by using a two step laser drilling approach. To do this, a millisecond percussion drilling was used, directly followed by a femtosecond (ultrashort) trepanning. This was shown to produce high quality holes.

Sun et al. [2.127] carried out a study on the use of long pulse laser drilling alongside ECM. The laser was first used to drill the hole in 304 stainless steel, whilst ECM was used to remove the recast layer as a post machining process. A numerical model was produced to simulate the process, which was validated experimentally. The method proved effective in improving hole quality.

Duan et al. [2.128] also used ECC as a post processing technique to remove the recast layer formed during long pulse laser drilling. The material drilled was 1.1mm thick Inconel 718 sheet. Oxidative assist gas was shown to be incompatible with the process, whereas, non-oxidative assist gas allowed for the successful removal of the recast layer. The optimised process was shown to be four times more efficient than conventional ECC.

2.3.5 Novel Applications

Geng et al. [2.129] used a sieve plate with a 300W lamp-pumped Nd:YAG laser for the percussion drilling of 2mm stainless steel with millisecond pulse widths with a 0.24mm spot size. The sieve plate was used in order to create holes of a smaller diameter.Pulse frequency, focal plane position, sieve diameter and distance to the target were chosen as variables, whilst entrance and exit diameter as well as hole taper were assessed as output variables. Focal plane and distance was found to have a large effect whilst pulse frequency had a minimal effect on hole diameter and taper. The sieve plate was shown to effectively produce smaller holes with less taper. Holes produced were shown to be 10% smaller than the focused spot diameter and 20% smaller than would be produced in normal drilling.

Maclean et al. [2.130] studied the single pulse laser drilling of through holes in semiconductor wafers using millisecond pulses with a 2kW ytterbium fibre laser. The process was demonstrated to create holes of 70 µm and 600 µm in diameter in crystal silicon. Holes were also produced of 200 - 400 µm in diameter in indium phosphide and 100 - 600 µm in indium antimonide for the first time.

Saini et al. [2.52] investigated the long pulse trepanning of Zirconia Toughened Alumina (ZTA) using an Nd:YAG laser. The effects of process parameters on recast layer thickness, microcrack width and hardness was investigated. It was concluded that pulsed Nd:YAG lasers may be suitable for the trepanning / machining of ZTA plate (an extremely difficulty to machine material by conventional methods).

Shin et al. [2.131] conducted a study to investigate the use of a copper reflector for the long pulse drilling of glass using a ytterbium fibre laser. The reflector was situated below the glass so that the beam was reflected back through. It was found that the drilling was more effective with the reflector across various pulse widths and glass thicknesses. However, concerns are presented regarding the inclusion of contaminants from the copper laser plume.

2.4 Parameter Optimisation Using Statistical Methods

Advanced optimisation artificial intelligence algorithms have been used to study parameters in laser drilling. Nakhjavani [2.83] used a genetic algorithm and artificial neural network techniques to optimise input parameters (peak power, pulse width, pulse frequency, number of pulses, assist gas pressure, and focal plane position) to predict the optimum desired output parameters (hole entrance diameter, circularity of hole entrance and hole exit and hole taper).

Dhara et al. [2.132] used artificial neural networks to attempt to develop a strategy to predict optimum parameters settings for the generation of a maximum depth of groove with a minimum height of recast layer.

Priyadarshini et al. [2.133] used a hybrid of Fuzzy TOPSIS and Taguchi artificial intelligence optimisation techniques for the optimisation of multiple response characteristics in the millisecond laser drilling process, such as minimising the HAZ and maximising hole circularity and material removal rate. For the drilling of high carbon steel with an Nd:YAG laser and oxygen assist gas, the optimal variables were found to be a pulse width of 1.7 ms, a pulse rate of 5 Hz and an assist gas flow rate of 4 l/min for a pressure of approximately 3Bar.

All in all, these techniques follow a popular trend in recent long pulse laser drilling research to better understand the effects of different parameters on hole quality.

2.5 Spatter and Dross

In laser drilling, melt ejecta is ejected upwards out of the hole entrance and often lands back on the workpiece, resolidifying and adhering around the periphery of the hole. The adhered droplets are known as spatter [2.75]. Dross is essentially

the same as spatter, however, it is caused by rear melt ejection and adheres to the rear of the hole. Spatter and dross constitute to two of the inherent defects in laser drilling [2.134].

In laser drilling studies, the issue of spatter adherence is addressed much more frequently than dross, however dross is still recognised as an unwanted defect in the process. This is likely because during the percussion drilling of through holes, melt ejection is only directed upwards, until the breakthrough pulse. Also, spatter is assisted by gravity, whereas gravity acts against dross formation.

Removal of spatter can require extra pre or post machining or finishing processes, increasing process complexity, production time and cost [2.135,2.136]. A number of spatter techniques exist to either reduce or prevent spatter generation [2.137].

There are a multitude of methods that have been demonstrated to reduce the adherence of spatter as pre-processing methods. For example, coating materials can be applied to the workpiece to reduce spatter adherence [2.138]. Coating the workpiece with paraffin wax or silicon grease [2.139] or the use of a surfactant fluid [2.140,2.141] have also been shown to reduce spatter adherence .

Physical approaches can also be used during the process, such as vibration techniques to improve the fluidity of molten material [2.142], use of a shielding gas nozzle to create a suction effect on melt ejecta [2.143], chemically spraying specific solutions onto the workpiece that are combined with the assist gas [2.144] or simple parameter optimisation to reduce spatter generation [2.136]. Post-processing techniques have also be used effectively, such as chemical etching [2.145,2.146].

2.6 Particle Collection Techniques In Laser Drilling

Particle collection has the potential to be a useful tool within laser drilling in order to further understand the process. As well as allowing for the opportunity to

investigate the particles themselves that are formed during laser drilling in terms of size, presence of oxide layers, etc. high efficiency particle collection allows for a calculation of volume removal, and a determination of the melt ejection fraction - the ratio of volume ejected upwards to rearwards.

Solana et al. [2.147], used particle collection to calculate the mass removal during laser drilling as a ratio of liquid to solid - at the time of ejection. In 2001, Solana assumed that the majority of the material ejected out of the top of aluminium and titanium samples during millisecond laser drilling, would be in a liquid state, whilst the majority of the material ejected out of the bottom would be solid state. To test this, an Nd:YAG laser with millisecond pulses was used to collect the upward ejection produced by 6-12 shots on a glass slide which was placed between the laser and the material, in the assumption that the molten material would adhere to the slide. The slide was then weighed and compared with its original weight in order to calculate the mass of the material that had adhered.

The diameters of the entrance and exit holes were then measured and used to calculate the hole volume. Knowing the density of the test material, the volume was then compared with the mass measurements and the percentage of mass which adhered to the glass slide as upward ejection was calculated. Combining the measurements of the captured upward ejecta with the recast which had adhered to the laser side of the test-piece allowed for a calculation of the total material lost through upward ejection. The rear ejection volume was then calculated by taking the upward ejection volume away from the calculated volume of the hole. Under the assumption that the rear ejected material was solid, Solana [2.147] calculated a value for the ratio of solid to liquid ejection. A melt ejection fraction of forty percent - the material lost from the hole that was calculated to be upwardly ejected, compared to 70% for titanium (taking into account oxide layers formed).

Voisey, Klocker et al. [2.148] used an innovative rotating, slotted-plate device as a

part of a particle collection method for upward ejection during laser drilling with an Nd:YAG laser at millisecond pulse-widths during the drilling of 2.85mm thick mild steel. By setting the angular velocity of the rotating plate, it was possible to specify the collection of particles, onto a glass slide, that where moving at a certain speed - assuming that all particles were ejected at the same time. Particle velocities were calculated to be approximately 1m/s for both 0.8J and 1.4J pulses.

Further work by Voisey, Kudesia et al. [2.89] again investigated particle collection of certain speeds using the same rotating, slotted plate as well as collecting particles in a closed container for size distribution analysis using a Malvern Mastersizer. In order to collect the particles into the container, it was made sure that the walls of the container were far enough away so that particles would have re-solidified by the time that they had collided. Average particle diameters were calculated as 24 µm for 1.4 J, 0.4 ms pulses, 10 µm for 2.5 J, 0.5 ms pulses and 45 µm for 2.5 J, 0.9 ms pulses

Glass slide collection, similar to that used by Solana [2.147], was also used. However, in order to determine the melt ejection fraction the mass of the test piece itself was measured to see how much was lost, as well as the mass gain on the glass slide - this of course included the ejection that had re-solidified onto the material as the recast layer. A range of materials were studied, and it was discovered that a melt ejection fraction of the order of around fifty percent was discovered for all materials except tungsten, which was much lower.

Wen et al. [2.149] carried out particle collection when drilling through a copper test-piece using an Nd:YAG laser with a nanosecond pulse width. The particles first passed through a DMA (Differential Mobility Analyser), for size calculation, before being passed through a NAS (Nanometer Aerosol Sampler) so that they could be collected on a silicon nitride film (commonly used for chemical vapour deposition). Once collected on the film, the particles were then analysed using scanning electron

and transmission electron microscopy for particle sizing and comparison with the DMA results, as well as analysis of their geometry and aggregation. The study examined the trends that occurred between particle size and particle number in comparison to drilling with helium and argon. Particles differed between helium and argon, with particle diameters less than 10 nm and 30 nm respectively.

Low et al. [2.150] conducted tests using oxygen assisted percussion drilling of Nimonic 263 alloy using an Nd:YAG laser. A glass tube device was glued to the sample with a rubber O-ring. Thermal insulating bulk fibre and cotton gauze was placed at the end of the tube for collection of rear ejected particles. The tube was bent at 30 degrees, presumably to allow for the use of the device with the laser set-up available.This resulted in many of the particles sticking to the glass bend of the tube rather than being collected in the cotton gauze. As with Solana [2.147] and Voisey, Kudesia [2.89], a microbalance was used. The weight of the collection device and work piece were weighed before and after an average of nine holes were ablated. The melt ejection fraction was calculated for the chosen parameters, with an upward ejection fraction of 60-80% for different pulse shapes and 20-40% for downward ejection.

Ideally, it would be most informative to measure the particles collected through rear and upward ejection as well as the test piece itself before and after drilling. This would allow a useful assessment of the ejection fraction for how much material was lost through upward ejection in comparison with rear ejection as well as the material lost through vaporisation. High-speed imaging in this work has demonstrated the possibility for melt ejection particles to be ejected across a full 180 degree range, therefore the collection method used by Low et al. [2.150] for rear melt ejection was perhaps the most effective in terms of capturing the rear ejected particles, as well as the use of a closed container by Voisey, Kudesia et al. [2.89]. However a device to prevent any upwardly ejected particles from escaping at extreme angles has not been demonstrated in any of the discussed work. It is also important to note that the ma-

jority of these collection methods risk changes to the size and shape of the particles due to collisions with solid objects, although Wen et al. [2.149] appears to have been successful in using a silicon nitride film to collect the nanoparticles ejected through nanosecond drilling. Potential for a liquid medium within a closed particle collection device would be a preferable solution for preserving particle geometries.

2.7 High-speed Filming

High-speed filming is frequently used within the literature on laser drilling, however much of the work that is related to melt ejection has been conducted using relatively low resolution images that are not suitable for particle tracking. For particle tracking to be made possible, images must be filmed using a fast enough frame rate and suitable exposure time to allow for individual particles to be made out, rather than streaks.

A technique that can be found in the older literature that is still of use today is streak photography. In 1995, Yilbas et al. [2.153] used a high-speed drum camera to rotate a 1.5m length of film at approximately 3000rpm to record streak photographs to analyse the upward melt ejection of 1.2mm thick titanium, tantalum, nickel and stainless steel test pieces with 1.48 millisecond pulses. The resulting images were used to calculate particle velocities, as well as analysing the different phases of the rear ejection process. Values of 105 - 115 m/s were observed for Tantalum, 110 - 150 m/s for Nickel, 150 - 170 m/s for stainless steel and 150 - 180 m/s for titanium. Although this is method is useful for obtaining some velocities, it is not useful for the application of particle tracking.

In 2001, Solana et al. [2.147] used a high-speed camera set-up to view the rear melt ejection process at 40,500fps. This was for an Nd:YAG laser in the millisecond range, for the drilling of aluminium and titanium test-pieces. The images were used to calculate the ejection velocities of the particles, as well as to confirm that

a solid particle is ejected from the exit hole of the material in the secondary stage of the ejection. Ejection velocity was deemed to be 5-20m/s, although the method of obtaining these results was not indicated. However, the images are of very low quality compared to those taken using modern equipment and they are not suitable for particle tracking.

In 2001 Low and Li [2.154] used high-speed filming at 1000 / 2000 frames per second with a Kodak Ektapro EM camera to observe the laser drilling of a 18.5mm transparent sugar based material, using a carbon dioxide laser in pulsed mode with a millisecond pulse width. The camera was used to view the cross section of the hole through a transparent test piece in an attempt to further understand the melt ejection mechanism of millisecond pulse drilling. Upward and downward ejection was also recorded and particle velocities were measured as 0.8 - 4.1 m/s from streaks. The images were enhanced using image processing techniques to invert the grayscale colour-map and adjust the tone.

The transparent media does allow for an improved understanding of the melt pool dynamics within the hole, however, the majority of the ejection process within the material was obscured from view due to vaporisation and bubbling. These tests and those similar in nature present the potential to provide an insight into the melt ejection process that occurs within metals although, it is important to note that the mechanical properties of the sugar based material are very different to that of commonly laser drilled metals.

Zhang et al. [2.155] followed up this study with the laser drilling of transparent GG17 glass using a carbon dioxide laser in a continuous mode with an argon assist gas. A high-speed camera, capable of 4500 frames per second, was used with a dimmer glass in order to attenuate intense light. Zhang's [2.155] tests were conducted alongside the production of a Finite Element Model (FEM), which was used to simulate the laser drilling process. As with work by Low and Li [2.154], the GG17 glass used in

these tests, although relatively strong, differs significantly in mechanical properties from commonly laser drilled metals.

As well as looking at particle sizes, Voisey, Kudesia et al. [2.89] used high-speed filming to as part of an investigation into the melt ejection process in aluminium, titanium and tungsten. A Kodak Ektapro high-speed camera was used to film ejection at 27,000 frames per second with an interference filter to block out excess light. The average velocity for a laser power density of 0.079MW mm^{-2} was recorded as 12 m s^{-1}, 10^{-1} and 5 m s^{-1} for titanium, aluminium and nickel respectively. For a power density of 0.087 $MWmm^{-2}$, the average velocities recorded were 15ms^{-1}, 15ms^{-1} and 8ms^{-1} for titanium, aluminium and nickel respectively. Although a high frame rate was used during this testing, the images produced are relatively low quality compared to modern capabilities and individual particles can not be identified from the presented images.

More recently, Marimuthu et al. [2.61] used high-speed filming methods to visualise the upward melt ejection process. A Photron high speed camera was used at 24096fps to film the percussion drilling of 2mm thick Nimonic 263 nickel super alloy using a 20kW QCW IPG fibre laser using millisecond pulse widths. The videos were used to observe two regimes in the melt ejection process: primarily, melt ejection exiting the drilling key-hole and secondarily the melt ejection flying away from the laser drilling zone. The videos were also used to observe the time of drilling. It was found that upward ejection starts around 80 µs after the the laser is turned on, regardless of drilling parameters. The time duration of the ejection was found to depend on the laser parameters, lasting for approximately 200 - 300 µs.

High-speed filming has also been used effectively to observe melt ejection in other laser processing methods, such as selective laser melting and laser welding.

In 2017, Repossini et al. [2.151] used an Olympus I-speed 3 high-speed camera to record ejecta during the selective laser melting (SLM) process at a rate of 1000

frames per second. Using image segmentation, Repossini [2.151] was able to identify and plot the locations of the ejecta particles with respect to time, relative to the laser melt point. As well as the spread, the number and average size of the particles were also recorded.

Also in 2017, Andani et al. [2.152] used a FASTCAM 1024 PCl to investigate the ejecta produced during SLM, at up to 6000 fps. Andani et al. [2.152] also used an image segmentation technique, Otsu's method for thresholding, to segment particles, outputting particle number and particle size. Andani et al. [2.152] identified that a higher number of laser beams used in the SLM process lead to increased spatter and that particle size is higher for pre-alloyed powders and that the particles produced by spatter were spherical.

Luo et al. [2.156] used high-speed filming to investigate the ejection plume produced during the laser welding of 20mm thick Q345 low alloy steel with a 10kW IPG fiber laser within a vacuum. A FASTCAM-Super 10KC was used with a frame rate of 1000fps and an exposure time of 1.5ms. The camera was useful at identifying a consistent change in ejection direction throughout the welding process, and a decrease in this phenomenon at a lower ambient pressure. It was also found that the swaying of the ejection cloud decreased melt pool stability, hence affecting the weld quality.

2.8 Image Analysis And Processing - Object Tracking

Visual object tracking is applied in a large range of applications, such as: autonomous vehicles [2.157,2.158], traffic flow monitoring [2.159], surveillance and security [2.160], robotics [2.161], human machine interaction [2.162], medical diagnostic systems and activity recognition [2.163] to name a few. Challenges faced

by the different applications can be very different and require very different outputs in terms of accuracy, fidelity or data types. Therefore, there are countless algorithms and approaches to each individual problem, many of them which are irrelevant to this work.

Chenouard et al. [2.164] conducted a study on the objective comparison of fourteen particle tracking methods for a bio-imaging application. The study found that no universally best method of particle tracking exists and suggests that just because a particle tracking method works well for a specific application, does not mean that it will work well or be optimal for another. This suggests that currently, customised tracking algorithms may be the best approach for dealing with specific applications. Because of this, rather than discussing the countless different approaches, this literature review will focus on explaining the generalised basics that are shared across all particle tracking programs. It will also introduce some studies where object tracking has been applied to very similar applications to give an insight into its use and what methodology was used.

Grinberg [2.165] defines object tracking as the continuous location of objects in an environment through the processing of data from sensors such as sonars, radars, lidars or video cameras. Grinberg [2.165] divides this task into four sub-groups: object detection, measurement generation, data association and dynamic state estimation.

Object detection is the first crucial process in object tracking, it is the processing of raw sensor data (images for a camera) and filtering out background noise to provide individual detections of each individual object. This can be done using thresholding techniques, for example, picking out regions of intensity above a certain threshold in an image. Further to this, segmentation techniques can then be applied to separate out connected images. For example, the watershed transform function is a very useful segmentation method that can be applied to microscopic images of cells,

which are often very close together.

Measurement generation is simply the generation of measurements for each object from the detected data. These measurements, such as object size, can be calculated using standard methods. For example, $A = \pi r^2$ can be used to calculate the area of a circle. However, for this information to be of use to a user it must be calibrated using known measurements.

Data association is the conversion of the detected object data into known tracks in the temporal domain. There are many known techniques that can be used for this, each with their own advantages and disadvantages. One very simple technique is known as the nearest neighbour algorithm [2.166], this is an intuitive approach that assumes that the object nearest to the objects last known position is its new position. Many more advanced techniques use a probability based approach. There are generally two approaches to data association, these are recognised as online or offline. Online is a recursive method using live data input, whilst offline makes use of globally available data recorded as a batch or throughout the complete time period [2.167].

Dynamic state estimation is a commonly used approach for the filtering of noisy sensors in object tracking. It is defined as the estimation of state of an object based on raw sensor position data. One commonly used approach is Kalman Filtering [2.168]. Dynamic state estimation is recognised as a probability based approach, it is very useful in radar tracking applications.

Luo et al. [2.167] categorised multiple object tracking using three different criteria: initialisation method, processing mode and type of output. The initialisation mode is broken down into two types, detection-based tracking and detection-free tracking. Detection-based tracking is defined by Luo et al. [2.167] as a strategy in which objects are first detected using an object detector and then linked into a trajectory. The number of objects may change as objects appear and disappear between frames,

based on detection. Detection-free tracking [2.169–2.171] requires manual initialisation of a fixed number of objects in the first frames, which are then localised in subsequent frames [2.167].

Processing mode is the second criteria used for categorisation by Luo et al. [2.167]. It can be broken down into either online or offline tracking. They differ in whether or not observations from future frames are utilised to handle the current frame. During online tracking [2.169–2.172], images are handled sequentially, and tracks are appended additively. This approach is necessary for real-time applications such as radar. Offline tracking [2.173–2.175,2.175–2.181] uses observation data as a whole or in batches to link together trajectories, theoretically, this can result in a better solution, however cannot be done in real time [2.167].

The third criteria for categorising multiple object tracking according to Luo et al. [2.167] is the type of output. These can be broken into two types, either deterministic or probabilistic. Deterministic methods result in outputs that do not change upon multiple runs, whereas probabilistic methods do [2.167]. Some examples of deterministic methods include [2.174,2.175,2.182–2.191]. Probabilistic examples include [2.172,2.192–2.198].

Currently, the image analysis and object tracking methods that have been carried out in this work appear to be unique in their application to the laser drilling field. However, the use of image analysis and object tracking is wide spread across many other fields. This section will focus on reviewing the image analysis work that has been conducted on similar problems that pose many of the same challenges.

Work by Williams et al. [2.21] used image analysis and processing techniques to record ejected particles that were ejected by the selective laser melting process during additive manufacturing of stainless steel. An FLIR A35 IR camera was mounted coaxially to the laser beam inside the build chamber of a Renishaw AM250 LPBF machine. The camera was used to record the powder bed at a rate of 50,000fps for

128x128 pixel images. In order to assess the number of particles for each frame, segmentation was carried out using Otsu's method [2.199] combined with a Watershed Transform Function to distinguish particles from the raw intensity images (object detection). A median filter was applied to these images to remove the laser heated zone (LHZ). A threshold criterion of 1400°C was also applied to the calibrated infra-red images to assess the size and morphology of the melt pool (within the LHZ). The number of ejected particles was used to differentiate and compare between different inter-layer cooling times in the process.

Repossini et al. [2.200] also used particle analysis and processing methods for object detection when assessing ejected particles in the selective laser melting process of 18Ni (300) maraging steel powder for in situ monitoring. A Olympus I-speed 3 camera was used in the visible range and placed outside of the build chamber in an off-axial set-up. Images were recorded at 1000fps. The recorded videos were thresholded using Otsu's method [2.199]. The LHZ was labelled separately to the ejecta within the images using size and position discriminators, since the LHZ is larger than the ejected particles and positioned in a similar location in each frame. The detected particles in the images were used to obtain particle number, average size and spatial spread, which were captured within statistical descriptors. This was then compared with selective laser melting using different energy densities and patterns were observed between under, normal and over-melting. Repossini et al. [2.200] propose that this could be useful for in-situ defect recognition.

The same approach was repeated for in situ monitoring of the selective laser melting of zinc powder by Grasso et al. [2.201], co-authors of the first paper, for a new study using an infra-red camera. This was used to discern a specific defect that is found for zinc powder due to excessive heat accumulation. It was found that the object detection methods used were more effective at detecting the defect than monitoring of infra-red images alone.

Unrelated to laser processing, Guildenbecher et al. [2.202] used digital in-line holography for the object tracking of fragments of water formed from the impact of a single water drop onto a thin film of water. Guildenbecher et al. [2.202] also applied the same method to burning aluminium particles that arise from the combustion of solid rocket propellant, this being a similar problem to that presented by rear melt ejection. Following intensity thresholding for object detection, which is described in [2.203], a Hungarian linker algorithm was used for data association to assess the number, velocity and size of the particles. The use of digital inline holography allowed for the particles to be analysed in 3D, meaning that the velocity in the Z direction was calculated as well as the X and Y. However, a relatively large uncertainty in the Z positions of the particles (9.4 multiplied by the mean measured diameter) invalidated these results. To overcome this, a regression based system was used within MATLAB to reduce the uncertainty of the Z positions to 0.3 multiplied by the mean measured diameter.

Wood et al. [2.204] used image processing techniques object tracking methods to characterise unmanned aerial vehicle (UAV) images of a volcanic plume. A semi-automatic segmentation technique using the MATLAB 'Image Segmenter' program was used to detect the plume. A 3D volume estimation space carving framework algorithm was then used to assess the data of the plume in batches to piece together an overall plume representation. Plume shape and quantitative properties: top height, drift direction and volume were calculated temporally. Wood et al. [2.204] propose that the adopted method could be useful within the field of volcano monitoring as it allows for plume evolution and dynamic behaviour to be studied.

Watson et al. [2.205] explored fragmentation due to hypervelocity impacts (HVI) using object tracking methods in 3D. For HVI, the velocity distribution of fragments is not fully understood and the study of such fragments has numerous applications, such as orbital debris or planetary impact [2.205]. The study by Watson et al. [2.205] used two Shimadzu high-speed cameras, capable of 10 million frames per second.

Both cameras were split into two dual views using mirrors, providing four separate views of rear ejecta. The cameras were used to film the impact of a 3mm aluminium sphere onto a 5mm thick CFRP plate at 7.2km/s. For object detection, a top-hat filter was applied to preserve intensity peaks and eliminate other features, thresholding was carried out to remove background pixels, a gaussian blur was applied to remove small variations in intensity and a gaussian fit was applied for subpixel accuracy. Objects were detected as local maxima in the images. Object tracking was carried out with the assumption that fragments travel in straight lines at constant velocities. A random sample consensus algorithm (RANSAC) was then used to identify fragments moving in straight lines at constant velocities. False trajectories were then filtered out based on whether or not they converged on the initial start point within a certain tolerance level. Using these methods, Watson et al. [2.205] were successful in achieving their aim of applying object tracking methods in 3D to measure the velocities of fragments from HVI.

Object tracking within HVI is an expanding field and several other studies have been conducted using similar methods effectively. Traditionally, HVI studies use high-speed cameras and radiographs to study the morphological aspects of the debris cloud [2.206,2.207]. However, recent advances in high-speed camera technology has opening up methods to track the individual fragmentation particles [2.205]. Other HVI studies that make use of object tracking include the study of crater formation in sand [2.208–2.210]. Other HVI studies have investigated the size and velocity of fragments from geological materials [2.211,2.212] as well as satellite shields [2.213].

Rear melt ejecta particle tracking deals with issues such as numerous high-speed particles and high-occlusion rates, whilst having specific characteristics that can be advantageous, such as relatively straight trajectories and high particle to background contrast. The reviewed studies are relatively novel applications of object tracking methods that relate to closely to rear melt ejecta because they share many of the same characteristics. This is conflicting with many of the recent high-interest appli-

cations such as autonomous driving [2.157,2.158] and robotics [2.161], which are very different problems to those that are faced in the tracking of rear melt ejecta in laser drilling. Perhaps the closest relating high-interest application of object tracking to rear melt ejecta is particle tracking velocimetry (PTV).

PTV is a similar method to particle image velocimetry (PIV), in which fluids are seeded with particles and tracked using camera / laser sensors. Both methods are used to track fluid flows for scientific applications, however, PTV is a Lagrangian approach [2.214], focused on tracking the flow of individual particles, whereas, PIV is a Eulerian approach that focuses on the observation of process dynamics at prescribed locations [2.215]. PTV presents similar challenges to the tracking of rear melt ejecta due to the large number of small particles and their high occlusion rates. High contrast rates can also be a a shared characteristic, depending on the PTV illumination method. However, one key difference is the directionality of the particles, as the fluid flows are less likely to travel on straight paths. PTV has been widely applied across fluid research, from small-scale air flows [2.216–2.221] to large-scale [2.222–2.225], water stream flows [2.226] to the study of flow statistics in heat exchangers [2.227].

References

[2.1] R. A. Potyrailo, W. G. Morris, R. Wroczynski, L. Hassib, P. Miller, B. Dworken, A. M. Leach, S. Boyette, and C. Xiao, "Multi-wavelength operation of optical disk drives for chemical and biological analysis," *Sensors and Actuators, B: Chemical*, vol. 136, no. 1, pp. 203–208, 2009.

[2.2] I. Kubiak, "The influence of the structure of useful signal on the efficacy of sensitive emission of laser printers," *Measurement: Journal of the International Measurement Confederation*, vol. 119, no. September 2016, pp. 63–76, 2018.

[2.3] S. Mor Cases, K. Jianwattananukul, K. Saenyot, S. Lekchaum, and K. Locharoenrat, "Portable laser 1-D barcode scanner for material identification," *Materials Today: Proceedings*, vol. 5, no. 7, pp. 15 143–15 148, 2018. [Online]. Available: https://doi.org/10.1016/j.matpr.2018.04.072

[2.4] H. Wang, L. Li, S. Zhu, Y. Xu, and N. Ren, "Effect of water-based ultrasonic vibration on the quality of laser trepanned microholes in nickel super-alloy workpieces," *Journal of Materials Processing Technology*, vol. 272, no. June 2018, pp. 170–183, 2019.

[2.5] T. Sakimoto, M. I. Rosenblatt, and D. T. Azar, "Laser eye surgery for refractive errors," *Lancet*, vol. 367, no. 9520, pp. 1432–1447, 2006.

[2.6] Y. Cui, J. Wu, H. Xu, and A. Wang, "Lane change identification and prediction with roadside LiDAR data," *Optics and Laser Technology*, vol. 123, no. July 2019, p. 105934, 2020. [Online]. Available: https://doi.org/10.1016/j.optlastec.2019.105934

[2.7] Y. Kalisky and O. Kalisky, "Applications and performance of high power lasers and in the battlefield," *Optical Materials*, vol. 34, no. 2, pp. 457–460, 2011. [Online]. Available: http://dx.doi.org/10.1016/j.optmat.2011.04.005

[2.8] B. Dobos and J. Prazak, "To Clear or to Eliminate? Active Debris Removal Systems as Antisatellite Weapons," *Space Policy*, vol. 47, pp. 217–223, 2019.

[2.9] N. Teed and A. K. Lund, "The effect of laser speed-measuring devices on speed limit law enforcement in Charleston, South Carolina," *Accident Analysis and Prevention*, vol. 25, no. 4, pp. 459–463, 1993.

[2.10] C. Kownacki, "Design of an adaptive Kalman filter to eliminate measurement faults of a laser rangefinder used in the UAV system," *Aerospace Science and Technology*, vol. 41, pp. 81–89, 2015. [Online]. Available:

http://dx.doi.org/10.1016/j.ast.2014.12.008

[2.11] L. Shanjin and W. Yang, "An investigation of pulsed laser cutting of titanium alloy sheet," *Optics and Lasers in Engineering*, vol. 44, no. 10, pp. 1067–1077, 2006.

[2.12] K. A. Ghany and M. Newishy, "Cutting of 1.2 mm thick austenitic stainless steel sheet using pulsed and CW Nd:YAG laser," *Journal of Materials Processing Technology*, vol. 168, no. 3, pp. 438–447, 2005.

[2.13] R. Rao and V. Yadava, "Multi-objective optimization of Nd:YAG laser cutting of thin superalloy sheet using grey relational analysis with entropy measurement," *Optics and Laser Technology*, vol. 41, no. 8, pp. 922–930, 2009.

[2.14] A. Sharma, V. Yadava, and R. Rao, "Optimization of kerf quality characteristics during Nd: YAG laser cutting of nickel based superalloy sheet for straight and curved cut profiles," *Optics and Lasers in Engineering*, vol. 48, no. 9, pp. 915–925, 2010. [Online]. Available: http://dx.doi.org/10.1016/j.optlaseng.2010.03.005

[2.15] A. K. Dubey and V. Yadava, "Multi-objective optimization of Nd:YAG laser cutting of nickel-based superalloy sheet using orthogonal array with principal component analysis," *Optics and Lasers in Engineering*, vol. 46, no. 2, pp. 124–132, 2008.

[2.16] W. S. Lau, T. M. Yue, T. C. Lee, and W. B. Lee, "Materials Processing Technology Un-conventional machining of composite materials," *Journal of Materials Processing Technology*, vol. 48, pp. 199–205, 1995.

[2.17] K. Huehnlein, K. Tschirpke, and R. Hellmann, "Optimization of laser cutting processes using design of experiments," *Physics Procedia*, vol. 5, no. PART 2, pp. 243–252, 2010. [Online]. Available: http:

//dx.doi.org/10.1016/j.phpro.2010.08.050

[2.18] F. A. Fernandes, D. F. Oliveira, and A. B. Pereira, "Optimal parameters for laser welding of advanced high-strength steels used in the automotive industry," *Procedia Manufacturing*, vol. 13, pp. 219–226, 2017. [Online]. Available: https://doi.org/10.1016/j.promfg.2017.09.052

[2.19] M. Morawiec, M. Różański, A. Grajcar, and S. Stano, "Effect of dual beam laser welding on microstructure–property relationships of hot-rolled complex phase steel sheets," *Archives of Civil and Mechanical Engineering*, vol. 17, no. 1, pp. 145–153, 2017.

[2.20] W. Guo, L. Li, S. Dong, D. Crowther, and A. Thompson, "Comparison of microstructure and mechanical properties of ultra-narrow gap laser and gas-metal-arc welded S960 high strength steel," *Optics and Lasers in Engineering*, vol. 91, no. November 2016, pp. 1–15, 2017. [Online]. Available: http://dx.doi.org/10.1016/j.optlaseng.2016.11.011

[2.21] R. J. Williams, A. Piglione, T. Rønneberg, C. Jones, M. S. Pham, C. M. Davies, and P. A. Hooper, "In situ thermography for laser powder bed fusion: Effects of layer temperature on porosity, microstructure and mechanical properties," *Additive Manufacturing*, vol. 30, no. March, p. 100880, 2019. [Online]. Available: https://doi.org/10.1016/j.addma.2019.100880

[2.22] P. A. Hooper, "Melt pool temperature and cooling rates in laser powder bed fusion," *Additive Manufacturing*, vol. 22, no. May, pp. 548–559, 2018. [Online]. Available: https://doi.org/10.1016/j.addma.2018.05.032

[2.23] S. K. Panda, S. Padhee, A. K. Sood, and S. S. Mahapatra, "Optimization of Fused Deposition Modelling (FDM) Process Parameters Using Bacterial Foraging Technique," *Intelligent Information Management*, vol. 01, no. 02,

pp. 89–97, 2009.

[2.24] K. A. Ibrahim, B. Wu, and N. P. Brandon, "Electrical conductivity and porosity in stainless steel 316L scaffolds for electrochemical devices fabricated using selective laser sintering," *Materials and Design*, vol. 106, pp. 51–59, 2016. [Online]. Available: http://dx.doi.org/10.1016/j.matdes.2016.05.096

[2.25] F. Xie, X. He, S. Cao, and X. Qu, "Structural and mechanical characteristics of porous 316L stainless steel fabricated by indirect selective laser sintering," *Journal of Materials Processing Technology*, vol. 213, no. 6, pp. 838–843, 2013. [Online]. Available: http://dx.doi.org/10.1016/j.jmatprotec.2012.12.014

[2.26] S. Pal, H. R. Tiyyagura, I. Drstvenšek, and C. S. Kumar, "The effect of post-processing and machining process parameters on properties of stainless steel PH1 product produced by direct metal laser sintering," *Procedia Engineering*, vol. 149, no. June, pp. 359–365, 2016. [Online]. Available: http://dx.doi.org/10.1016/j.proeng.2016.06.679

[2.27] I. Shivakoti, G. Kibria, and B. B. Pradhan, "Predictive model and parametric analysis of laser marking process on gallium nitride material using diode pumped Nd:YAG laser," *Optics and Laser Technology*, vol. 115, no. January, pp. 58–70, 2019. [Online]. Available: https://doi.org/10.1016/j.optlastec.2019.01.035

[2.28] G. Odintsova, Y. Andreeva, A. Salminen, H. Roozbahani, L. Van Cuong, R. Yatsuk, V. Golubeva, V. Romanov, and V. Veiko, "Investigation of production related impact on the optical properties of color laser marking," *Journal of Materials Processing Technology*, vol. 274, no. August 2018, p. 116263, 2019. [Online]. Available: https://doi.org/10.1016/j.jmatprotec.2019.116263

[2.29] M. Naumova, I. Morozova, and P. Borisov, "Investigating the features of color laser marking process of galvanic chrome plating in order to create a controlled color image formation at given marking," *Materials Today: Proceedings*, no. xxxx, pp. 10–13, 2019. [Online]. Available: https://doi.org/10.1016/j.matpr.2019.08.044

[2.30] C. Leone, E. Bassoli, S. Genna, and A. Gatto, "Experimental investigation and optimisation of laser direct part marking of Inconel 718," *Optics and Lasers in Engineering*, vol. 111, no. May, pp. 154–166, 2018.

[2.31] J. Cheng, J. Zhou, C. Zhang, Z. Cao, D. Wu, C. Liu, and H. Zou, "Enhanced laser marking of polypropylene induced by "core-shell" ATO@PI laser-sensitive composite," *Polymer Degradation and Stability*, vol. 167, pp. 77–85, 2019. [Online]. Available: https://doi.org/10.1016/j.polymdegradstab.2019.06.022

[2.32] D. T. Pham, S. S. Dimov, and P. V. Petkov, "Laser milling of ceramic components," *International Journal of Machine Tools and Manufacture*, vol. 47, no. 3-4, pp. 618–626, 2007.

[2.33] L. A. Dobrzański, T. Tański, A. D. Dobrzańska-Danikiewicz, E. Jonda, M. Bonek, and A. Drygała, "Structures, properties and development trends of laser-surface-treated hot-work steels, light metal alloys and polycrystalline silicon," in *Laser Surface Engineering*, ser. Woodhead Publishing Series in Electronic and Optical Materials, J. Lawrence and D. G. Waugh, Eds. Woodhead Publishing, 2015, pp. 3–32. [Online]. Available: http://www.sciencedirect.com/science/article/pii/B9781782420743000015

[2.34] P. Shukla and J. Lawrence, "Characterization and modification of technical ceramics through laser surface engineering," in *Laser Surface Engineering*, ser. Woodhead Publishing Series in Electronic and Optical Materials,

J. Lawrence and D. G. Waugh, Eds. Woodhead Publishing, 2015, pp. 107–134. [Online]. Available: http://www.sciencedirect.com/science/article/pii/B9781782420743000052

[2.35] G. Sun and R. Zhou, "Mechanical properties improvement of metallic rolls by laser surface alloying," in *Laser Surface Engineering*, ser. Woodhead Publishing Series in Electronic and Optical Materials, J. Lawrence and D. G. Waugh, Eds. Woodhead Publishing, 2015, pp. 59–96. [Online]. Available: http://www.sciencedirect.com/science/article/pii/B9781782420743000039

[2.36] B. S. Yilbas, F. Patel, and C. Karatas, "Laser surface treatment of aisi 304 steel with the presence of b4c particles at the surface," in *Laser Surface Engineering*, ser. Woodhead Publishing Series in Electronic and Optical Materials, J. Lawrence and D. G. Waugh, Eds. Woodhead Publishing, 2015, pp. 97–105. [Online]. Available: http://www.sciencedirect.com/science/article/pii/B9781782420743000040

[2.37] K. Xia, N. Ren, H. Wang, and C. Shi, "Analysis for effects of ultrasonic power on ultrasonic vibration-assisted single-pulse laser drilling," *Optics and Lasers in Engineering*, vol. 110, no. July, pp. 279–287, 2018. [Online]. Available: https://doi.org/10.1016/j.optlaseng.2018.04.022

[2.38] K. T. Voisey, S. S. Kudesia, W. S. O. Rodden, D. P. Hand, J. D. C. Jones, and T. W. Clyne, "Melt ejection during laser drilling of metals," *Materials Science and Engineering A*, 2003.

[2.39] T. Z. Zhang, Z. C. Jia, H. C. Cui, D. H. Zhu, X. W. Ni, and J. Lu, "Analysis of melt ejection during long pulsed laser drilling," *Chinese Physics B*, vol. 25, no. 5, 2016.

[2.40] W. S. O. Rodden, S. S. Kudesia, D. P. Hand, and J. D. C. Jones, "Use of

"assist" gas in the laser drilling of titanium," *Journal of Laser Applications*, vol. 13, no. 5, pp. 204–208, 2001.

[2.41] B. S. Yilbas, "Parametric study to improve laser hole drilling process," *Journal of Materials Processing Technology*, vol. 70, no. 1-3, pp. 264–273, 1997.

[2.42] A. Stournaras, K. Salonitis, and G. Chryssolouris, "Optical emissions for monitoring of the percussion laser drilling process," *International Journal of Advanced Manufacturing Technology*, vol. 46, no. 5-8, pp. 589–603, 2010.

[2.43] J. Cheng, F.-J. Kahlen, and A. Kar, "Effects of intrapulse structure on hole geometry in laser drilling," *Journal of Laser Applications*, vol. 12, no. 6, pp. 232–238, 2000.

[2.44] G. Ng and L. Li, "The effect of laser peak power and pulse width on the hole geometry repeatability in laser percussion drilling," *Optics & Laser Technology*, vol. 33, no. 6, pp. 393–402, sep 2001. [Online]. Available: http://www.sciencedirect.com/science/article/pii/S0030399201000482

[2.45] I. Arrizubieta, a. Lamikiz, S. Martínez, E. Ukar, I. Tabernero, and F. Girot, "Internal characterization and hole formation mechanism in the laser percussion drilling process," *International Journal of Machine Tools and Manufacture*, vol. 75, pp. 55–62, dec 2013. [Online]. Available: http://linkinghub.elsevier.com/retrieve/pii/S0890695513001375

[2.46] S. Sato, H. Hidai, S. Matsusaka, A. Chiba, and N. Morita, "Drilling, bonding, and forming conductive path in the hole by laser percussion drilling," *Precision Engineering*, vol. 61, no. September 2019, pp. 147–151, 2020. [Online]. Available: https://doi.org/10.1016/j.precisioneng.2019.10.007

[2.47] B. S. Yilbas, S. S. Akhtar, and C. Karatas, "Laser trepanning of a small diameter hole in titanium alloy: Temperature and stress fields," *Journal*

of Materials Processing Technology, vol. 211, no. 7, pp. 1296–1304, 2011. [Online]. Available: http://dx.doi.org/10.1016/j.jmatprotec.2011.02.012

[2.48] R. Goyal and A. K. Dubey, "Modeling and optimization of geometrical characteristics in laser trepan drilling of titanium alloy," *Journal of Mechanical Science and Technology*, vol. 30, no. 3, pp. 1281–1293, 2016.

[2.49] ——, "Hybrid Approach for Modeling and Optimization of Hole Taper During Laser Trepan Drilling of Ti-6Al-4V Alloy Sheet," *Procedia Materials Science*, vol. 5, pp. 1781–1790, 2014.

[2.50] W. T. Chien and S. C. Hou, "Investigating the recast layer formed during the laser trepan drilling of Inconel 718 using the Taguchi method," *International Journal of Advanced Manufacturing Technology*, vol. 33, no. 3-4, pp. 308–316, 2007.

[2.51] S. Kumar, A. K. Dubey, and A. K. Pandey, "Computer-aided genetic algorithm based multi-objective optimization of laser trepan drilling," *International Journal of Precision Engineering and Manufacturing*, vol. 14, no. 7, pp. 1119–1125, 2013.

[2.52] S. K. Saini and A. K. Dubey, "Study of material characteristics in laser trepan drilling of ZTA," *Journal of Manufacturing Processes*, vol. 44, no. June 2018, pp. 349–358, 2019. [Online]. Available: https://doi.org/10.1016/j.jmapro.2019.06.017

[2.53] H. Zhang, J. Di, M. Zhou, Y. Yan, and R. Wang, "An investigation on the hole quality during picosecond laser helical drilling of stainless steel 304," *Applied Physics A: Materials Science and Processing*, vol. 119, no. 2, pp. 745–752, 2015.

[2.54] C. He, J. Bühring, and A. Gillner, "Helical drilling of three-dimensional

conical converging-diverging nozzle in steel using ultrashort laser pulses," *Procedia CIRP*, vol. 74, pp. 305–309, 2018. [Online]. Available: https://doi.org/10.1016/j.procir.2018.08.120

[2.55] C. Fornaroli, J. Holtkamp, and A. Gillner, "Laser-beam helical drilling of high quality micro holes," *Physics Procedia*, vol. 41, pp. 661–669, 2013. [Online]. Available: http://dx.doi.org/10.1016/j.phpro.2013.03.130

[2.56] S. Dhar, N. Saini, and R. Purohit, "A review on laser drilling and its Techniques," *International Conference on Advances in Mechanical Engineering*, vol. 2006, no. Ame, 2006.

[2.57] D. Markcoons and K. Voisey, "An Investigation to Determine if the Laser Drilling Capabilities of a 2 kW Fibre Laser can be Enhanced Using Pulse Train Shaping," vol. 39, no. 1/2, pp. 17–33, 2017.

[2.58] H. K. Sezer and L. Li, "Mechanisms of acute angle laser drilling induced thermal barrier coating delamination," *Journal of Manufacturing Science and Engineering, Transactions of the ASME*, vol. 131, no. 5, pp. 0 510 141–0 510 146, 2009.

[2.59] H. Sezer, L. Li, M. Schmidt, A. Pinkerton, B. Anderson, and P. Williams, "Effect of beam angle on HAZ, recast and oxide layer characteristics in laser drilling of TBC nickel superalloys," *International Journal of Machine Tools and Manufacture*, vol. 46, no. 15, pp. 1972–1982, dec 2006. [Online]. Available: http://www.sciencedirect.com/science/article/pii/S0890695506000101

[2.60] A. Horn, R. Weichenhain, S. Albrecht, E.-W. Kreutz, J. Michel, M. Niessen, V. Kostrykin, W. Schulz, A. Etzkorn, K. Bobzin, E. Lugscheider, and R. Poprawe, "Microholes in zirconia-coated Ni-superalloys for transpiration cooling of turbine blades," in *High-Power Laser Ablation III*, C. R. Phipps,

Ed., vol. 4065, International Society for Optics and Photonics. SPIE, 2000, pp. 218–226. [Online]. Available: https://doi.org/10.1117/12.407331

[2.61] S. Marimuthu, M. Antar, and J. Dunleavey, "Characteristics of micro-hole formation during fibre laser drilling of aerospace superalloy," *Precision Engineering*, vol. 55, no. August 2018, pp. 339–348, 2019. [Online]. Available: https://doi.org/10.1016/j.precisioneng.2018.10.002

[2.62] W. Schulz, U. Eppelt, and R. Poprawe, "Review on laser drilling I. Fundamentals, modeling, and simulation," *Journal of Laser Applications*, vol. 25, no. 1, p. 012006, 2013.

[2.63] W. R. Harp, J. R. Dilwith, and J. F. Tu, "Laser ablation using a long-pulsed, high-fluence, CW single-mode fiber laser," *Journal of Materials Processing Technology*, vol. 198, no. 1-3, pp. 22–30, 2008.

[2.64] S. R. Bolin, "Nd:YAG Laser Applications Survey," in *Materials Processing - Theory and Practices*, ser. Materials Processing: Theory and Practices, M. BASS, Ed. Elsevier, 1983, vol. 3, pp. 407–438. [Online]. Available: http://www.sciencedirect.com/science/article/pii/B9780444863966500143

[2.65] N. B. Dahotre, *Laser fabrication and machining of materials / Narendra B. Dahotre, Sandip P. Harimkar.*, S. P. Harimkar, Ed. New York: New York : Springer, 2008.

[2.66] J. Meijer, "Laser beam machining (LBM), state of the art and new opportunities," *Journal of Materials Processing Technology*, vol. 149, no. 1-3, pp. 2–17, 2004.

[2.67] J. A. Clarke and J. Profeta, "Laser Micro-Drilling Applications," in *PROCEEDINGS OF THE 2004 ADVANCED LASER APPLICATIONS CONFERENCE & EXPOSITION*, vol. 2. Advanced Laser Applications Confer-

ence & Exposition, 2004, pp. 94–100.

[2.68] M. C. Gower, "Industrial applications of pulsed laser micromachining," *Conference on Lasers and Electro-Optics Europe - Technical Digest*, vol. 7, no. 2, p. 247, 1998.

[2.69] R. Holtz and M. Jokiel, "Optimized laser applications with lamp-pumped pulsed Nd:YAG lasers," *ICALEO 2002 - 21st International Congress on Applications of Laser and Electro-Optics, Congress Proceedings*, vol. 170024, 2002.

[2.70] J. Rapp, *Laser with Bosch: a flexible tool in serial production of an automotive supplier*, ser. Society of Photo-Optical Instrumentation Engineers (SPIE) Conference Series, 2003, vol. 4831, pp. 390–396.

[2.71] R. Poprawe, *Tailored Light 2*, 1st ed. Springer-Verlag Berlin Heidelberg, 2011.

[2.72] J. Bahnmüller, T. Herzinger, F. Dausinger, M. Beck, and A. Giering, "Characterization of pulsed Nd:YAG-laser beams as an optimization tool in laser drilling applications," vol. 82, pp. 82–91, 2000.

[2.73] A. K. Nath, *Laser Drilling of Metallic and Nonmetallic Substrates*. Elsevier, 2014, vol. 9. [Online]. Available: http://dx.doi.org/10.1016/B978-0-08-096532-1.00904-3

[2.74] W. M. Steen, K. G. Watkins, and J. Mazumder, *Laser Material Processing*. Springer London, 2010. [Online]. Available: https://books.google.co.uk/books?id=gPsq0HHAU4UC

[2.75] G. D. Gautam and A. K. Pandey, "Pulsed Nd:YAG laser beam drilling: A review," *Optics and Laser Technology*, vol. 100, pp. 183–215, 2018. [Online]. Available: https://doi.org/10.1016/j.optlastec.2017.09.054

[2.76] H. K. Sezer, L. Li, S. Leigh, and Z. Liu, "Continous wave fiber laser keyhole drilling for the production of zero tapered, low recast holes in ni-alloys," *29th International Congress on Applications of Lasers and Electro-Optics, ICALEO 2010 - Congress Proceedings*, vol. 103, no. 2010, pp. 101–110, 2010.

[2.77] W. Duan, X. Dong, K. Wang, Z. Fan, X. Mei, W. Wang, and J. Lv, "Effect of temporally modulated pulse on reducing recast layer in laser drilling," *International Journal of Advanced Manufacturing Technology*, vol. 87, no. 5-8, pp. 1641–1652, 2016. [Online]. Available: http://dx.doi.org/10.1007/s00170-016-8362-5

[2.78] M. Imran, P. T. Mativenga, A. Gholinia, and P. J. Withers, "Assessment of surface integrity of Ni superalloy after electrical-discharge, laser and mechanical micro-drilling processes," *The International Journal of Advanced Manufacturing Technology*, vol. 79, no. 5, pp. 1303–1311, jul 2015. [Online]. Available: https://doi.org/10.1007/s00170-015-6909-5

[2.79] Z. Fan, X. Dong, K. Wang, W. Duan, R. Wang, X. Mei, W. Wang, J. Cui, X. Yuan, and C. Xu, "Effect of drilling allowance on TBC delamination, spatter and re-melted cracks characteristics in laser drilling of TBC coated superalloys," *International Journal of Machine Tools and Manufacture*, vol. 106, pp. 1–10, 2016. [Online]. Available: http://dx.doi.org/10.1016/j.ijmachtools.2016.03.008

[2.80] M. Ghoreishi, D. K Y Low, and L. Li, "Statistical modelling of laser percussion drilling for hole taper and circularity control," *Proceedings of The Institution of Mechanical Engineers Part B-journal of Engineering Manufacture - PROC INST MECH ENG B-J ENG MA*, vol. 216, pp. 307–319, 03 2002.

[2.81] M. Ghoreishi, D. K. Y Low, and L. Li, "Comparative statistical analysis of hole taper and circularity in laser percussion drilling," *International Journal*

of Machine Tools Manufacture - INT J MACH TOOL MANUF, vol. 42, pp. 985–995, 07 2002.

[2.82] D. K. Y. Low, L. Li, and P. J. Byrd, "Hydrodynamic physical modeling of laser drilling," *Journal of Manufacturing Science and Engineering-transactions of The Asme - J MANUF SCI ENG*, vol. 124, 11 2002.

[2.83] O. B. Nakhjavani and M. Ghoreishi, "Multi criteria optimization of laser percussion drilling process using artificial neural network model combined with genetic algorithm," *Materials and Manufacturing Processes*, vol. 21, pp. 11–18, 01 2006.

[2.84] G. Ng, P. Crouse, and L. Li, "An analytical model for laser drilling incorporating effects of exothermic reaction, pulse width and hole geometry," *International Journal of Heat and Mass Transfer*, vol. 49, pp. 1358–1374, 04 2006.

[2.85] B. Yilbas, A. F. Arif, and A. A. B.J, "Laser cutting of holes in thick sheet metals: Development of stress field," *Optics and Lasers in Engineering - OPT LASER ENG*, vol. 47, pp. 909–916, 09 2009.

[2.86] J. Girardot, P. Lorong, L. Illoul, N. Ranc, M. Schneider, and V. Favier, "Modeling laser drilling in percussion regime using constraint natural element method," *International Journal of Material Forming*, vol. 10, no. 2, pp. 205–219, 2017.

[2.87] G. Ng and L. Li, "The effect of laser peak power and pulse width on the hole geometry repeatability in laser percussion drilling," *Optics Laser Technology*, vol. 33, no. 6, pp. 393 – 402, 2001. [Online]. Available: http://www.sciencedirect.com/science/article/pii/S0030399201000482

[2.88] R. Sattmann, V. Sturm, and R. Noll, "Laser-induced breakdown spectroscopy

of steel samples using multiple q-switch nd:yag laser pulses," *Journal of Physics D: Applied Physics*, vol. 28, no. 10, p. 2181, 1995. [Online]. Available: http://stacks.iop.org/0022-3727/28/i=10/a=030

[2.89] K. T. Voisey, S. S. Kudesia, W. S. O. Rodden, D. P. Hand, J. D. C. Jones, and T. W. Clyne, "Melt ejection during laser drilling of metals," *Materials Science and Engineering A*, 2003.

[2.90] D.-G. AHN and G.-W. JUNG, "Influence of process parameters on drilling characteristics of al 1050 sheet with thickness of 0.2 mm using pulsed nd:yag laser," *Transactions of Nonferrous Metals Society of China*, vol. 19, 09 2009.

[2.91] M. Guillong, I. Horn, and D. Günther, "A comparison of 266 nm, 213 nm and 193 nm produced from a single solid state nd: Yag laser for laser ablation icp-ms," *JOURNAL OF ANALYTICAL ATOMIC SPECTROMETRY*, vol. 18, pp. 1224–1230, 09 2003.

[2.92] C.-C. Ho, J.-J. He, and T.-Y. Liao, "On-line estimation of laser-drilled hole depth using a machine vision method," *Sensors (Basel, Switzerland)*, vol. 12, pp. 10 148–62, 12 2012.

[2.93] C.-C. Ho, G.-R. Tseng, Y.-J. Chang, J.-C. Hsu, and C.-L. Kuo, "Magnetic-field-assisted laser percussion drilling," *The International Journal of Advanced Manufacturing Technology*, vol. 73, no. 1, pp. 329–340, Jul 2014. [Online]. Available: https://doi.org/10.1007/s00170-014-5815-6

[2.94] C.-C. Ho, Y.-M. Chen, J.-C. Hsu, Y.-J. Chang, and C.-L. Kuo, "Characteristics of the effect of swirling gas jet assisted laser percussion drilling based on machine vision," *Journal of Laser Applications*, vol. 27, no. 4, p. 042001, 2015. [Online]. Available: http://dx.doi.org/10.2351/1.4923019

[2.95] C.-C. Ho, Y. J. Chang, J.-C. Hsu, C.-L. Kuo, and G.-H. Lee, "Characteristics

of the thermal strain of gas jet-assisted laser percussion drilling," vol. 28, pp. 1067–1075, 01 2016.

[2.96] C.-C. Ho and J.-J. He, "On-line monitoring of laser-drilling process based on coaxial machine vision," *International Journal of Precision Engineering and Manufacturing*, vol. 15, pp. 671–678, 04 2014.

[2.97] C.-C. Ho, Y.-M. Chen, J.-C. Hsu, Y. J. Chang, and C.-L. Kuo, "Characteristics of the effect of swirling gas jet assisted laser percussion drilling based on machine vision," *Journal of Laser Applications*, vol. 27, 10 2015.

[2.98] S. Mishra and V. Yadava, "Modeling and optimization of laser beam percussion drilling of nickel-based superalloy sheet using Nd: YAG laser," *Optics and Lasers in Engineering*, vol. 51, no. 6, pp. 681–695, 2013. [Online]. Available: http://dx.doi.org/10.1016/j.optlaseng.2013.01.006

[2.99] H. Singh, S. Kwan, D. Tam, N. Mamalis, K. Maclean, and I. Ahmed, "Fracture and dislocation of a glass intraocular lens optic as a complication of neodymium:yag laser posterior capsulotomy: Case report and literature review," *Journal of Cataract and Refractive Surgery*, vol. 41, no. 10, pp. 2323–2328, 2015, cited By 1. [Online]. Available: https://www.scopus.com/inward/record.uri?eid=2-s2.0-84952332605&doi=10.1016%2fj.jcrs.2015.09.013&partnerID=40&md5=5055f48b565192dd481e3921f2ca7dae

[2.100] L. Tunna, W. O'Neill, A. Khan, and C. Sutcliffe, "Analysis of laser micro drilled holes through aluminium for micro-manufacturing applications," *Optics and Lasers in Engineering - OPT LASER ENG*, vol. 43, pp. 937–950, 09 2005.

[2.101] Y. Zang, X. Ni, and B. Han, "The ejection angle of molten aluminum induced by millisecond pulsed laser," *Journal of Applied Physics*, vol. 116, pp. 013 104–013 104, 07 2014.

[2.102] G. Norkey, A. K. Dubey, and S. Agrawal, "Artificial Intelligence Based Modeling and Optimization of Heat Affected Zone in Nd: YAG Laser Cutting of Duralumin Sheet," *J. Intell. Fuzzy Syst.*, vol. 27, no. 3, pp. 1545–1555, may 2014. [Online]. Available: http://dl.acm.org/citation.cfm?id=3184235.3184277

[2.103] S. Bandyopadhyay, J. S. Sundar, G. Sundararajan, and S. Joshi, "Geometrical features and metallurgical characteristics of nd:yag laser drilled holes in thick in718 and ti–6al–4v sheets," *Journal of Materials Processing Technology*, vol. 127, no. 1, pp. 83 – 95, 2002. [Online]. Available: http://www.sciencedirect.com/science/article/pii/S0924013602002704

[2.104] S. Bandyopadhyay, H. Gokhale, J. S. Sundar, G. Sundararajan, and S. Joshi, "A statistical approach to determine process parameter impact in nd:yag laser drilling of in718 and ti-6al-4v sheets," *Optics and Lasers in Engineering*, vol. 43, no. 2, pp. 163 – 182, 2005. [Online]. Available: http://www.sciencedirect.com/science/article/pii/S0143816604001435

[2.105] B. Yilbas, "Investigation into drilling speed during laser drilling of metals," *Optics Laser Technology*, vol. 20, no. 1, pp. 29 – 32, 1988. [Online]. Available: http://www.sciencedirect.com/science/article/pii/0030399288900096

[2.106] B. S. Yilbas, "A study of affecting parameters in the laser hole-drilling of sheet metals," *Journal of Mechanical Working Technology*, vol. 13, no. 3, pp. 303 – 315, 1986. [Online]. Available: http://www.sciencedirect.com/science/article/pii/0378380486900227

[2.107] B. S. Yilbaş, A. Z. Şahin, and R. Davies, "Laser heating mechanism including evaporation process initiating laser drilling," *International Journal of Machine Tools and Manufacture*, vol. 35, no. 7, pp. 1047 – 1062, 1995. [Online]. Available: http://www.sciencedirect.com/science/article/pii/

0890695594000062O

[2.108] A. K. Pandey and A. K. Dubey, "Multiple quality optimization in laser cutting of difficult-to-laser-cut material using grey–fuzzy methodology," *The International Journal of Advanced Manufacturing Technology*, vol. 65, no. 1, pp. 421–431, mar 2013. [Online]. Available: https://doi.org/10.1007/s00170-012-4181-5

[2.109] ——, "Modeling and optimization of kerf taper and surface roughness in laser cutting of titanium alloy sheet," *Journal of Mechanical Science and Technology*, vol. 27, no. 7, pp. 2115–2124, jul 2013. [Online]. Available: https://doi.org/10.1007/s12206-013-0527-7

[2.110] ——, "Fuzzy expert system for prediction of kerf qualities in pulsed laser cutting of titanium alloy sheet," *Machining Science and Technology*, vol. 17, no. 4, pp. 545–574, 2013. [Online]. Available: https://doi.org/10.1080/10910344.2013.806182

[2.111] R. R. Boyer, "An overview on the use of titanium in the aerospace industry," *Materials Science and Engineering: A*, vol. 213, no. 1, pp. 103–114, 1996. [Online]. Available: http://www.sciencedirect.com/science/article/pii/0921509396102331

[2.112] P. R. Soni and T. V. Rajan, "Laser Beam Machining of High Temperature Ceramic Products," *Transactions of the Indian Ceramic Society*, vol. 44, no. 2, pp. 42–47, 1985. [Online]. Available: https://doi.org/10.1080/0371750X.1985.10822731

[2.113] Y. Liang and S. P. Dutta, "Application trend in advanced ceramic technologies," *Technovation*, vol. 21, no. 1, pp. 61–65, 2001. [Online]. Available: http://www.sciencedirect.com/science/article/pii/S0166497200000195

[2.114] S. Marimuthu, M. Antar, J. Dunleavey, D. Chantzis, W. Darlington, and P. Hayward, "An experimental study on quasi-CW fibre laser drilling of nickel superalloy," *Optics and Laser Technology*, vol. 94, pp. 119–127, 2017. [Online]. Available: http://dx.doi.org/10.1016/j.optlastec.2017.03.021

[2.115] N. D. Bahar, S. Marimuthu, and W. J. Yahya, "Pulsed Nd: YAG laser drilling of aerospace materials (Ti-6Al-4V)," *IOP Conference Series: Materials Science and Engineering*, vol. 152, no. 1, 2016.

[2.116] A. Stephen, R. Ocana, J. Esmoris, C. Thomy, C. Soriano, F. Vollertsen, and R. Sanchez, "Laser micro drilling methods for perforation of aircraft suction surfaces," *Procedia CIRP*, vol. 74, pp. 403–406, 2018. [Online]. Available: https://doi.org/10.1016/j.procir.2018.08.157

[2.117] V. Ebrahimzade, H. Uchtmann, L. Singheiser, M. Krüger, and J. Malzbender, "Microstructure and cyclic oxidation behavior of APS TBC systems drilled with various laser methods," *Surface and Coatings Technology*, vol. 378, no. September, p. 125018, 2019. [Online]. Available: https://doi.org/10.1016/j.surfcoat.2019.125018

[2.118] M. Antar, D. Chantzis, S. Marimuthu, and P. Hayward, "High Speed EDM and Laser Drilling of Aerospace Alloys," *Procedia CIRP*, vol. 42, no. Isem Xviii, pp. 526–531, 2016. [Online]. Available: http://dx.doi.org/10.1016/j.procir.2016.02.245

[2.119] L. Rihakova and H. Chmelickova, "Laser drilling of alumina ceramics using solid state Nd:YAG laser and QCW fiber laser: Effect of process parameters on the hole geometry," *Advances in Production Engineering And Management*, vol. 12, no. 4, pp. 412–420, 2017.

[2.120] S. Sharma, Y. Pachaury, S. N. Akhtar, and J. Ramkumar, "A study on hy-

drodynamics of melt expulsion in pulsed Nd: YAG laser drilling of titanium," in *COMSOL Conference Pune*, 2015.

[2.121] A. Sharma and V. Yadava, "Experimental analysis of Nd-YAG laser cutting of sheet materials – A review," *Optics and Laser Technology*, vol. 98, pp. 264–280, 2018. [Online]. Available: http://dx.doi.org/10.1016/j.optlastec.2017.08.002

[2.122] Y. Yang, Z. Chen, and Y. Zhang, "Melt flow and heat transfer in laser drilling," *International Journal of Thermal Sciences*, vol. 107, pp. 141–152, 2016. [Online]. Available: http://dx.doi.org/10.1016/j.ijthermalsci.2016.04.006

[2.123] R. Wang, W. Duan, K. Wang, X. Dong, Z. Fan, X. Mei, W. Wang, and S. Zhang, "Computational and experimental study on hole evolution and delamination in laser drilling of thermal barrier coated nickel superalloy," *Optics and Lasers in Engineering*, vol. 107, no. March, pp. 161–175, 2018. [Online]. Available: https://doi.org/10.1016/j.optlaseng.2018.03.019

[2.124] Y. Qin, D. J. Förster, R. Weber, T. Graf, and S. Yang, "Numerical study of the dynamics of the hole formation during drilling with combined ms and ns laser pulses," *Optics and Laser Technology*, vol. 112, no. September 2018, pp. 8–19, 2019. [Online]. Available: https://doi.org/10.1016/j.optlastec.2018.10.057

[2.125] W. C. Wang, B. Zhou, S. H. Xu, Z. M. Yang, and Q. Y. Zhang, "Recent advances in soft optical glass fiber and fiber lasers," *Progress in Materials Science*, vol. 101, no. June 2018, pp. 90–171, 2019.

[2.126] H. Wang, Y. Xu, H. Zheng, W. Zhou, N. Ren, X. Ren, and T. Li, "Monitoring and analysis of millisecond laser drilling process and performance

with and without longitudinal magnetic assistance and/or assist gas," *Journal of Manufacturing Processes*, vol. 48, no. October, pp. 297–312, 2019. [Online]. Available: https://linkinghub.elsevier.com/retrieve/pii/S1526612519303597

[2.127] A. Sun, Y. Chang, and H. Liu, "Numerical simulation of laser drilling and electrochemical machining of metal micro-hole," *Optik*, vol. 181, no. November 2018, pp. 92–98, 2019. [Online]. Available: https://doi.org/10.1016/j.ijleo.2018.11.156

[2.128] W. Duan, X. Mei, Z. Fan, J. Li, K. Wang, and Y. Zhang, "Electrochemical corrosion assisted laser drilling of micro-hole without recast layer," *Optik*, vol. 202, no. July 2019, p. 163577, 2020. [Online]. Available: https://doi.org/10.1016/j.ijleo.2019.163577

[2.129] Y. Geng, K. Wang, X. Dong, W. Duan, X. Mei, and W. Wang, "Laser drilling of micro-holes with small diameter beyond the limits of focused spot by using a sieve plate or a cover plate," *International Journal of Advanced Manufacturing Technology*, vol. 87, no. 9-12, pp. 2471–2484, 2016.

[2.130] J. O. Maclean, C. Tangkijcharoenchai, S. Coomber, and K. T. Voisey, "Laser drilling of micro-holes in single crystal silicon, indium phosphide and indium antimonide using a continuous wave (CW) 1070 nm fibre laser with millisecond pulse widths," *Procedia CIRP*, vol. 74, pp. 407–412, 2018. [Online]. Available: https://doi.org/10.1016/j.procir.2018.08.158

[2.131] J. Shin, S. G. Kang, C. Park, and J. O. Kim, "A study on the effect of Cu reflector in glass drilling using a pulsed NIR laser," *Optics and Laser Technology*, vol. 116, no. March, pp. 328–337, 2019.

[2.132] S. K. Dhara, A. S. Kuar, and S. Mitra, "An artificial neural network approach on parametric optimization of laser micro-machining

of die-steel," *The International Journal of Advanced Manufacturing Technology*, vol. 39, no. 1, pp. 39–46, Oct 2008. [Online]. Available: https://doi.org/10.1007/s00170-007-1199-1

[2.133] M. Priyadarshini, P. P. Tripathy, D. Mishra, and S. Panda, "Multi Characteristics Optimization of Laser Drilling Process Parameter Using Fuzzy-TOPSIS Method," *Materials Today: Proceedings*, vol. 4, no. 8, pp. 8538–8547, 2017. [Online]. Available: https://doi.org/10.1016/j.matpr.2017.07.200

[2.134] M. M. Okasha, P. T. Mativenga, L. Li, and H. K. Sezer, "Laser drilling of nickel alloy : Effect of process gases on drilling time and hole quality LASER DRILLING OF NICKEL ALLOY : EFFECT OF PROCESS GASES ON DRILLING TIME," vol. 127, no. 2010, 2013.

[2.135] D. Guo, K. Cai, Y. Huang, and L. T. Li, "A novel anti-spatter and anti-crack laser drilling technique: Application to ceramics," *Applied Physics A: Materials Science and Processing*, vol. 76, no. 7, pp. 1121–1124, 2003.

[2.136] A. G. Demir, B. Previtali, and M. Bestetti, "Removal of spatter by chemical etching after microdrilling with high productivity fiber laser," *Physics Procedia*, vol. 5, no. PART 1, pp. 317–326, 2010. [Online]. Available: http://dx.doi.org/10.1016/j.phpro.2010.08.152

[2.137] M. Hasan, J. Zhao, and Z. Jiang, "A review of modern advancements in micro drilling techniques," *Journal of Manufacturing Processes*, vol. 29, pp. 343–375, 2017. [Online]. Available: http://dx.doi.org/10.1016/j.jmapro.2017.08.006

[2.138] C. A. Biffi and B. Previtali, "Spatter reduction during titanium microdrilling using pulsed fiber laser," *ICALEO 2008 - 27th International Congress on Applications of Lasers and Electro-Optics, Congress Proceedings*, vol. 106, pp.

27–36, 2008.

[2.139] D. K. Low, L. Li, A. G. Corfe, and P. J. Byrd, "Spatter-free laser percussion drilling of closely spaced array holes," *International Journal of Machine Tools and Manufacture*, vol. 41, no. 3, pp. 361–377, 2001.

[2.140] C. M. Sharp, R. E. Mueller, J. Murthy, M. H. McCay, and J. Cutcher, "Novel anti-spatter technique for laser drilling: Applications to surface texturing," *Laser Institute of America, Proceedings*, vol. 83, no. Pt 1, 1997.

[2.141] J. Kamalu and P. Byrd, "Laser drilling of mild steel using an anti-spatter coating," *ICALEO'97 proceedings, San Diego*, pp. 156–164, 1997.

[2.142] M. Mori and H. Kumehara, "Application of ultrasonic laser machining to laser deep-drilling technique," *Bull Jpn Soc Precis Eng*, vol. 10, no. 4, pp. 177–178, 1976. [Online]. Available: https://www.scopus.com/inward/record.uri?eid=2-s2.0-0017243606{&}partnerID=40{&}md5=fcec3060aa8493ddbfa119f4b6c704b2

[2.143] C. A. Biffi and B. Previtali, "Spatter reduction in nanosecond fibre laser drilling using an innovative nozzle," *International Journal of Advanced Manufacturing Technology*, vol. 66, no. 9-12, pp. 1231–1245, 2013.

[2.144] N. Orita, "Laser cutting method for high chromium steel and a device to carry out that method," 1988.

[2.145] R. M. Hudson, *Pickling and Descaling*, C. Cotell, J. Sprague, and F. J. Smidt, Eds. ASM International, 1994.

[2.146] A. Bloyce, P. Morton, and T. Bell, *Surface Engineering of Titanium and Titanium Alloys*, C. Cotell, J. Sprague, and F. J. Smidt, Eds. ASM International, 1994.

[2.147] P. Solana, P. Kapadia, J. Dowden, W. S. O. Rodden, S. S. Kudesia, D. P. Hand, and J. D. C. Jones, "Time dependent ablation and liquid ejection processes during the laser drilling of metals," *Optics Communications*, 2001.

[2.148] K. T. Voisey, T. Klocker, and T. W. Clyne, "Measurement of melt ejection velocities during laser drilling of steel, using a novel droplet stream interception technique," *Acta Materialia*, 2002.

[2.149] S.-b. Wen, X. Mao, R. Greif, and R. Russo, "Experimental and theoretical studies of particle generation after laser ablation of copper with a background gas at atmospheric pressure ," 2007.

[2.150] D. Low, L. Li, and P. Byrd, "The influence of temporal pulse train modulation during laser percussion drilling," *Optics and Lasers in Engineering*, vol. 35, no. 3, pp. 149–164, 2001. [Online]. Available: http://www.sciencedirect.com/science/article/pii/S0143816601000082

[2.151] G. Repossini, V. Laguzza, M. Grasso, and B. M. Colosimo, "On the use of spatter signature for in-situ Monitoring of Laser Power Bed Fusion," *Additive Manufacturing*, vol. 16, pp. 35–48, 2017. [Online]. Available: http://www.sciencedirect.com/science/article/pii/S2214860416303402

[2.152] M. Taheri Andani, R. Dehghani, M. R. Karamooz-Ravari, R. Mirzaeifar, and J. Ni, "Spatter formation in selective laser melting process using multi-laser technology," *Materials and Design*, vol. 131, pp. 460–469, 2017. [Online]. Available: http://dx.doi.org/10.1016/j.matdes.2017.06.040

[2.153] B. S. Yilbas, "Study of liquid and vapor ejection processes during laser drilling of metals ," *Journal of Laser Applications*, vol. 7, no. 147, 1995.

[2.154] D. K. Y. Low and L. Li, "An investigation into melt flow dynamics during repetitive pulsed laser drilling of transparent media," *Optics and Laser*

Technology, 2001.

[2.155] Y. Zhang, S. Li, G. Chen, and J. Mazumder, "Experimental observation and simulation of keyhole dynamics during laser drilling," *Optics & Laser Technology*, vol. 48, pp. 405–414, jun 2013. [Online]. Available: http://linkinghub.elsevier.com/retrieve/pii/S0030399212005130

[2.156] Y. Luo, X. Tang, S. Deng, F. Lu, Q. Chen, and H. Cui, "Dynamic coupling between molten pool and metallic vapor ejection for fiber laser welding under subatmospheric pressure," *Journal of Materials Processing Technology*, vol. 229, pp. 431–438, 2016. [Online]. Available: http://dx.doi.org/10.1016/j.jmatprotec.2015.09.048

[2.157] M. Brown, J. Funke, S. Erlien, and J. C. Gerdes, "Safe driving envelopes for path tracking in autonomous vehicles," *Control Engineering Practice*, vol. 61, pp. 307–316, 2017. [Online]. Available: http://dx.doi.org/10.1016/j.conengprac.2016.04.013

[2.158] V. A. Laurense, J. Y. Goh, and J. C. Gerdes, "Path-tracking for autonomous vehicles at the limit of friction," *Proceedings of the American Control Conference*, pp. 5586–5591, 2017.

[2.159] B. Tian, Q. Yao, Y. Gu, K. Wang, and Y. Li, "Video processing techniques for traffic flow monitoring: A survey," *IEEE Conference on Intelligent Transportation Systems, Proceedings, ITSC*, pp. 1103–1108, 2011.

[2.160] S. Sivanantham, N. N. Paul, and R. S. Iyer, "Object tracking algorithm implementation for security applications," *Far East Journal of Electronics and Communications*, vol. 16, no. 1, pp. 1–13, 2016.

[2.161] S. Heinrich, P. Springstübe, T. Knöppler, M. Kerzel, and S. Wermter, "Continuous convolutional object tracking in developmental robot scenarios,"

Neurocomputing, vol. 342, pp. 137–144, 2019. [Online]. Available: https://doi.org/10.1016/j.neucom.2018.10.086

[2.162] J. Severson, "Human-Digital Media Interaction Tracking," 2010.

[2.163] J. K. Aggarwal and L. Xia, "Human activity recognition from 3D data: A review," *Pattern Recognition Letters*, vol. 48, pp. 70–80, 2014. [Online]. Available: http://dx.doi.org/10.1016/j.patrec.2014.04.011

[2.164] N. Chenouard, I. Smal, F. De Chaumont, M. Maška, I. F. Sbalzarini, Y. Gong, J. Cardinale, C. Carthel, S. Coraluppi, M. Winter, A. R. Cohen, W. J. Godinez, K. Rohr, Y. Kalaidzidis, L. Liang, J. Duncan, H. Shen, Y. Xu, K. E. Magnusson, J. Jaldén, H. M. Blau, P. Paul-Gilloteaux, P. Roudot, C. Kervrann, F. Waharte, J. Y. Tinevez, S. L. Shorte, J. Willemse, K. Celler, G. P. Van Wezel, H. W. Dan, Y. S. Tsai, C. O. De Solórzano, J. C. Olivo-Marin, and E. Meijering, "Objective comparison of particle tracking methods," *Nature Methods*, vol. 11, no. 3, pp. 281–289, 2014.

[2.165] M. Grinberg, *Feature-Based Probabilistic Data Association for Video-Based Multi-Object Tracking*, 2018.

[2.166] B. W. Silverman and M. C. Jones, "E. Fix and J.L. Hodges (1951): An Important Contribution to Nonparametric Discriminant Analysis and Density Estimation: Commentary on Fix and Hodges (1951)," *International Statistical Review / Revue Internationale de Statistique*, vol. 57, no. 3, pp. 233–238, 1989. [Online]. Available: http://www.jstor.org/stable/1403796

[2.167] W. Luo, J. Xing, A. Milan, X. Zhang, W. Liu, X. Zhao, and T.-K. Kim, "Multiple Object Tracking: A Literature Review," *arXiv preprint arXiv:1409.7618v4*, pp. 1–18, 2014. [Online]. Available: http://arxiv.org/abs/1409.7618

[2.168] R. E. Kalman, "A New Approach to Linear Filtering and Prediction Problems," *Journal of Basic Engineering*, vol. 82, no. 1, pp. 35–45, 1960. [Online]. Available: https://doi.org/10.1115/1.3662552

[2.169] W. Hu, X. Li, W. Luo, X. Zhang, S. Maybank, and Z. Zhang, "Single and multiple object tracking using log-euclidean riemannian subspace and block-division appearance model," *IEEE Transactions on Pattern Analysis and Machine Intelligence*, vol. 34, no. 12, pp. 2420–2440, 2012.

[2.170] L. Zhang and L. Van Der Maaten, "Structure preserving object tracking," *Proceedings of the IEEE Computer Society Conference on Computer Vision and Pattern Recognition*, no. 3, pp. 1838–1845, 2013.

[2.171] ——, "Preserving structure in model-free tracking," *IEEE Transactions on Pattern Analysis and Machine Intelligence*, vol. 36, no. 4, pp. 756–769, 2014.

[2.172] J. Zhang, L. Lo Presti, and S. Sclaroff, "Online multi-person tracking by tracker hierarchy," *Proceedings - 2012 IEEE 9th International Conference on Advanced Video and Signal-Based Surveillance, AVSS 2012*, pp. 379–385, 2012.

[2.173] B. Yang, C. Huang, and R. Nevatia, "Learning affinities and dependencies for multi-target tracking using a CRF model," *Proceedings of the IEEE Computer Society Conference on Computer Vision and Pattern Recognition*, vol. 2, pp. 1233–1240, 2011.

[2.174] W. Brendel, M. Amer, and S. Todorovic, "Multiobject tracking as maximum weight independent set," *Proceedings of the IEEE Computer Society Conference on Computer Vision and Pattern Recognition*, pp. 1273–1280, 2011.

[2.175] B. Yang and R. Nevatia, "Multi-target tracking by online learning of non-linear motion patterns and robust appearance models," *Proceedings of the IEEE Computer Society Conference on Computer Vision and Pattern Recog-*

nition, vol. 1, pp. 1918–1925, 2012.

[2.176] B. Song, T.-Y. Jeng, E. Staudt, and A. K. Roy-Chowdhury, "A Stochastic Graph Evolution Framework for Robust Multi-target Tracking," in *Proceedings of the 11th European Conference on Computer Vision: Part I*, ser. ECCV'10. Berlin, Heidelberg: Springer-Verlag, 2010, pp. 605–619. [Online]. Available: http://dl.acm.org/citation.cfm?id=1886063.1886109

[2.177] Z. Qin and C. R. Shelton, "Improving multi-target tracking via social grouping," *Proceedings of the IEEE Computer Society Conference on Computer Vision and Pattern Recognition*, pp. 1972–1978, 2012.

[2.178] C. H. Kuo, C. Huang, and R. Nevatia, "Multi-target tracking by on-line learned discriminative appearance models," *Proceedings of the IEEE Computer Society Conference on Computer Vision and Pattern Recognition*, pp. 685–692, 2010.

[2.179] J. F. Henriques, R. Caseiro, and J. Batista, "Globally optimal solution to multi-object tracking with merged measurements," *Proceedings of the IEEE International Conference on Computer Vision*, pp. 2470–2477, 2011.

[2.180] D. Sugimura, K. M. Kitani, T. Okabe, Y. Sato, and A. Sugimoto, "Using individuality to track individuals: Clustering individual trajectories in crowds using local appearance and frequency trait," *Proceedings of the IEEE International Conference on Computer Vision*, no. Iccv, pp. 1467–1474, 2009.

[2.181] W. Choi and S. Savarese, "Multiple target tracking in world coordinate with single, minimally calibrated camera," *Lecture Notes in Computer Science (including subseries Lecture Notes in Artificial Intelligence and Lecture Notes in Bioinformatics)*, pp. 553–567, 2010.

[2.182] G. Duan, H. Ai, S. Cao, and S. Lao, "Group Tracking: Exploring Mutual

Relations for Multiple Object Tracking," in *Computer Vision – ECCV 2012*, A. Fitzgibbon, S. Lazebnik, P. Perona, Y. Sato, and C. Schmid, Eds. Berlin, Heidelberg: Springer Berlin Heidelberg, 2012, pp. 129–143.

[2.183] L. Zhang, Y. Li, and R. Nevatia, "Global data association for multi-object tracking using network flows," *26th IEEE Conference on Computer Vision and Pattern Recognition, CVPR*, 2008.

[2.184] C. Huang, B. Wu, and R. Nevatia, "Robust Object Tracking by Hierarchical Association of Detection Responses," in *Computer Vision – ECCV 2008*, D. Forsyth, P. Torr, and A. Zisserman, Eds. Berlin, Heidelberg: Springer Berlin Heidelberg, 2008, pp. 788–801.

[2.185] Y. Li, C. Huang, and R. Nevatia, "Learning to associate: HybridBoosted multi-target tracker for crowded scene," *2009 IEEE Conference on Computer Vision and Pattern Recognition*, pp. 2953–2960, 2010.

[2.186] H. Pirsiavash, D. Ramanan, and C. C. Fowlkes, "Globally-optimal greedy algorithms for tracking a variable number of objects," *Proceedings of the IEEE Computer Society Conference on Computer Vision and Pattern Recognition*, pp. 1201–1208, 2011.

[2.187] J. Berclaz, F. Fleuret, E. Türetken, and P. Fua, "Multiple object tracking using k-shortest paths optimization," *IEEE Transactions on Pattern Analysis and Machine Intelligence*, vol. 33, no. 9, pp. 1806–1819, 2011.

[2.188] A. A. Butt and R. T. Collins, "Multi-target tracking by lagrangian relaxation to min-cost network flow," *Proceedings of the IEEE Computer Society Conference on Computer Vision and Pattern Recognition*, pp. 1846–1853, 2013.

[2.189] X. Shi, H. Ling, J. Xing, and W. Hu, "Multi-target tracking by RANK-1 tensor approximation," *Proceedings of the IEEE Computer Society Conference*

on Computer Vision and Pattern Recognition, pp. 2387–2394, 2013.

[2.190] A. Milan, S. Roth, and K. Schindler, "Continuous energy minimization for multitarget tracking," *IEEE Transactions on Pattern Analysis and Machine Intelligence*, vol. 36, no. 1, pp. 58–72, 2014.

[2.191] A. Andriyenko, K. Schindler, and S. Roth, "Discrete-continuous optimization for multi-target tracking," *Proceedings of the IEEE Computer Society Conference on Computer Vision and Pattern Recognition*, pp. 1926–1933, 2012.

[2.192] J. Xing, H. Ai, L. Liu, and S. Lao, "Multiple player tracking in sports video: A dual-mode two-way Bayesian inference approach with progressive observation modeling," *IEEE Transactions on Image Processing*, vol. 20, no. 6, pp. 1652–1667, 2011.

[2.193] Junliang Xing, H. Ai, and S. Lao, "Multi-object tracking through occlusions by local tracklets filtering and global tracklets association with detection responses," *2009 IEEE Conference on Computer Vision and Pattern Recognition*, pp. 1200–1207, 2010.

[2.194] M. D. Breitenstein, F. Reichlin, B. Leibe, E. Koller-Meier, and L. Van Gool, "Robust tracking-by-detection using a detector confidence particle filter," *Proceedings of the IEEE International Conference on Computer Vision*, pp. 1515–1522, 2009.

[2.195] M. Yang, Fengjun Lv, Wei Xu, and Yihong Gong, "Detection driven adaptive multi-cue integration for multiple human tracking," *2009 IEEE 12th International Conference on Computer Vision*, pp. 1554–1561, 2010.

[2.196] D. Mitzel and B. Leibe, "Real-time multi-person tracking with detector assisted structure propagation," *Proceedings of the IEEE International Confer-*

ence on Computer Vision, pp. 974–981, 2011.

[2.197] M. Rodriguez, J. Sivic, I. Laptev, J.-Y. Audibert, Ecole, and N. Supérieure, "Data-driven Crowd Analysis in Videos," *IEEE International Conference on Computer Vision*, 2011. [Online]. Available: https://www.di.ens.fr/willow/pdfscurrent/rodriguez11a.pdf

[2.198] D. B. Reid, "An algorithm for tracking multiple targets," *IEEE Transactions On Automatic Control*, vol. 24, no. 6, pp. 843–854, 1979.

[2.199] N. Otsu, "A threshold selection method from gray-level histograms," *IEEE Transactions on Systems, Man, and Cybernetics*, vol. 9, no. 1, pp. 62–66, Jan 1979.

[2.200] G. Repossini, V. Laguzza, M. Grasso, and B. M. Colosimo, "On the use of spatter signature for in-situ Monitoring of Laser Power Bed Fusion," *Additive Manufacturing*, vol. 16, pp. 35–48, 2017. [Online]. Available: http://www.sciencedirect.com/science/article/pii/S2214860416303402

[2.201] M. Grasso, A. G. Demir, B. Previtali, and B. M. Colosimo, "In situ monitoring of selective laser melting of zinc powder via infrared imaging of the process plume," *Robotics and Computer-Integrated Manufacturing*, 2018.

[2.202] D. R. Guildenbecher, M. A. Cooper, and P. E. Sojka, "High-speed (20kHz) digital in-line holography for transient particle tracking and sizing in multiphase flows," *Applied Optics*, 2016.

[2.203] D. R. Guildenbecher, L. Engvall, J. Gao, T. W. Grasser, P. L. Reu, and J. Chen, "Digital in-line holography to quantify secondary droplets from the impact of a single drop on a thin film," *Experiments in Fluids*, vol. 55, no. 3, 2014.

[2.204] K. Wood, A. Albadra, L. Berthoud, A. Calway, M. Watson, H. Thomas, T. Richardson, E. Liu, and G. Chigna, "Determining the three-dimensional structure of a volcanic plume using Unoccupied Aerial System (UAS) imagery," *Journal of Volcanology and Geothermal Research*, 2019. [Online]. Available: https://doi.org/10.1016/j.jvolgeores.2019.106731

[2.205] E. Watson, N. Kunert, R. Putzar, H. G. Maas, and S. Hiermaier, "Four-view split-image fragment tracking in hypervelocity impact experiments," *International Journal of Impact Engineering*, vol. 135, no. October 2019, p. 103405, 2020. [Online]. Available: https://doi.org/10.1016/j.ijimpeng.2019.103405

[2.206] A. J. Piekutowski, "Characteristics of debris clouds produced by hypervelocity impact of aluminum spheres with thin aluminum plates," *International Journal of Impact Engineering*, vol. 14, no. 1, pp. 573–586, 1993. [Online]. Available: http://www.sciencedirect.com/science/article/pii/0734743X9390053A

[2.207] Q. Zhang, Y. Chen, F. Huang, and R. Long, "Experimental study on expansion characteristics of debris clouds produced by oblique hypervelocity impact of LY12 aluminum projectiles with thin LY12 aluminum plates," *International Journal of Impact Engineering*, vol. 35, no. 12, pp. 1884–1891, 2008. [Online]. Available: http://dx.doi.org/10.1016/j.ijimpeng.2008.07.026

[2.208] J. T. Heineck, P. H. Schultz, and J. L. B. Anderson, "Application of three-component PIV to the measurement of hypervelocity impact ejecta," *Journal of Visualization*, vol. 5, no. 3, pp. 233–241, 2002. [Online]. Available: https://www.scopus.com/inward/record.uri?eid=2-s2.0-23044532337{&}doi=10.1007{%}2FBF03182331{&}partnerID=40{&}md5=f5bf7c41b1767c0f560465273277d213

[2.209] B. Hermalyn and P. H. Schultz, "Time-resolved studies of hypervelocity vertical impacts into porous particulate targets: Effects of projectile density on early-time coupling and crater growth," *Icarus*, vol. 216, no. 1, pp. 269–279, 2011. [Online]. Available: http://dx.doi.org/10.1016/j.icarus.2011.09.008

[2.210] B. Hermalyn, J. T. Heineck, E. T. Schairer, and H. Peter, "Measurement of Ejecta from Hypervelocity Impacts with a Generalized High-Speed Two-Frame 3D Hybrid Particle Tracking Velocimetry Method," *17th International Symposium on Applications of Laser Techniques to Fluid Mechanics*, pp. 7–10, 2014.

[2.211] M. Gulde, L. Kortmann, M. Ebert, E. Watson, J. Wilk, and F. Schäfer, "Robust optical tracking of individual ejecta particles in hypervelocity impact experiments," *Meteorit. Planet. Sci.*, vol. 9, pp. 1–9, 2017.

[2.212] M. Schimmerohn, E. Watson, M. Gulde, L. Kortmann, and F. Schäfer, "Measuring ejecta characteristics and momentum transfer in experimental simulation of kinetic impact," *Acta Astronautica*, vol. 156, no. March 2018, pp. 297–300, 2019.

[2.213] E. Watson, M. Gulde, L. Kortmann, M. Higashide, F. Schaefer, and S. Hiermaier, "Optical fragment tracking in hypervelocity impact experiments," *Acta Astronautica*, vol. 155, no. February 2018, pp. 111–117, 2019. [Online]. Available: https://doi.org/10.1016/j.actaastro.2018.11.036

[2.214] S. Fu, P. H. Biwole, and C. Mathis, "Particle tracking velocimetry for indoor airflow field: A review," *Building and Environment*, vol. 87, pp. 34–44, 2015.

[2.215] F. Ballio, D. Pokrajac, A. Radice, and S. A. Hosseini Sadabadi, "Lagrangian and Eulerian Description of Bed Load Transport," *Journal of Geophysical Research: Earth Surface*, vol. 123, no. 2, pp. 384–408, 2018.

[2.216] Y. Suzuki and N. Kasagi, "Turbulent air flow measurement with the aid of three-dimensional particle tracking velocimetry in a curved square duct," *Nihon Kikai Gakkai Ronbunshu, B Hen/Transactions of the Japan Society of Mechanical Engineers, Part B*, vol. 65, no. 632, pp. 1291–1298, 1999.

[2.217] S. J. Lee and S. Kim, "Simultaneous measurement of size and velocity of microbubbles moving in an opaque tube using an X-ray particle tracking velocimetry technique," *Experiments in Fluids*, vol. 39, no. 3, pp. 490–495, 2005.

[2.218] M. Virant and T. Dracos, "3D PTV and its application on Lagrangian motion," *Measurement Science and Technology*, vol. 8, no. 12, pp. 1539–1552, 1997. [Online]. Available: https://www.scopus.com/inward/record.uri?eid=2-s2.0-0031366202{&}doi=10.1088{%}2F0957-0233{%}2F8{%}2F12{%}2F017{&}partnerID=40{&}md5=d3b19ece7cdd7937027aa8e9f332d846

[2.219] M. Holzner, A. Liberzon, N. Nikitin, B. Luthi, W. Kinzelbach, and A. Tsinober, "A Lagrangian investigation of the small-scale features of turbulent entrainment through particle tracking and direct numerical simulation," *Journal of Fluid Mechanics*, vol. 598, pp. 465–475, 2008.

[2.220] S. Kim and S. J. Lee, "Measurement of Dean flow in a curved micro-tube using micro digital holographic particle tracking velocimetry," *Experiments in Fluids*, vol. 46, no. 2, pp. 255–264, 2009.

[2.221] S.-i. Satake, T. Kunugi, K. Sato, T. Ito, H. Kanamori, and J. Taniguchi, "Measurements of 3D flow in a micro-pipe via micro digital holographic particle tracking velocimetry," *Measurement Science and Technology*, vol. 17, no. 7, pp. 1647–1651, jun 2006. [Online]. Available: https://doi.org/10.1088{%}2F0957-0233{%}2F17{%}2F7{%}2F002

[2.222] C. Resagk, E. Lobutova, R. Rank, D. Müller, T. Putze, and H.-g. Maas,

"Measurement of large-scale flow structures in air using a novel 3D particle tracking velocimetry technique," *Physical Review*, no. January, pp. 26–29, 2006.

[2.223] E. Lobutova, C. Resagk, R. Rank, and T. Putze, "Visualisation of Large-Scale Flow Structures in Air Using a Novel 3D Particle," pp. 1–6, 2006.

[2.224] E. Lobutova, C. Resagk, R. Rank, and D. Müller, "Extended Three Dimensional Particle Tracking Velocimetry for Large Enclosures," 2009.

[2.225] E. Lobutova, C. Resagk, and T. Putze, "Investigation of large-scale circulations in room air flows using three-dimensional particle tracking velocimetry," *Building and Environment*, vol. 45, no. 7, pp. 1653–1662, 2010. [Online]. Available: http://dx.doi.org/10.1016/j.buildenv.2010.01.016

[2.226] F. Tauro, R. Piscopia, and S. Grimaldi, "PTV-Stream: A simplified particle tracking velocimetry framework for stream surface flow monitoring," *Catena*, vol. 172, no. September 2018, pp. 378–386, 2019.

[2.227] L. Beckedorff, R. Nieuwenhuizen, T. M. Bolwerk, A. S. Monteiro, K. V. de Paiva, J. G. Kuerten, C. W. van der Geld, and J. L. Oliveira, "Flow statistics in plate and shell heat exchangers measured with PTV," *International Journal of Heat and Fluid Flow*, vol. 79, no. August, p. 108461, 2019. [Online]. Available: https://doi.org/10.1016/j.ijheatfluidflow.2019.108461

3

Experimental Methodology

Throughout this work many different experimental methods were used to investigate the rear melt ejection of laser drilling. Primarily, two lasers were used for drilling, a 2kW fibre laser and a 6kW QCW fibre laser. A range of parameters were conducted on each of these laser systems for means of comparison.

Mostly an automated particle tracking method was used throughout the testing using a Phantom V12.1 high speed camera. Also an IDT full colour camera was also used for streak tracking tests.

Some particle collection tests were carried out using glycol as a catchment medium.

* * *

3.1 Parameter Selection

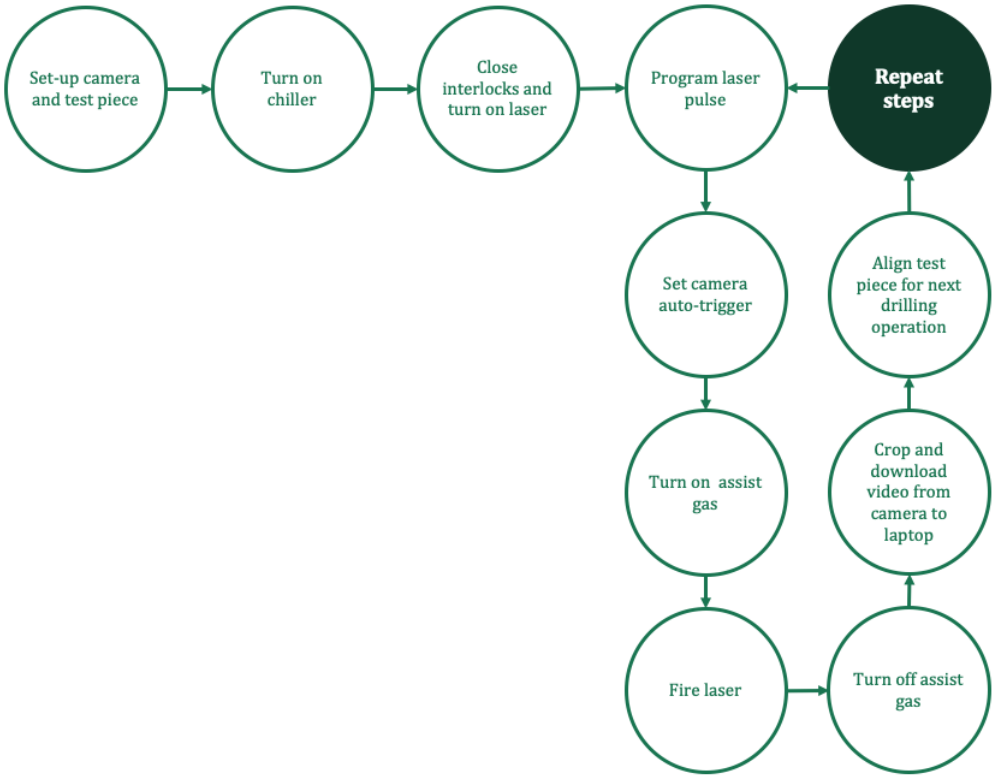


Figure 3.1: Laser drilling and high speed filming methodology

Figure 3.1 shows the laser drilling and high speed filming methodology which was used to obtain all of the high speed videos used within this work.

Throughout the laser drilling tests a multitude of parameters were investigated. These include various types of material, including, mild steel, aluminium and titanium. These were chosen because they were of interest to the industrial partner, AWE, and also because steel [3.1–3.11], aluminium [3.12–3.23] and titanium [3.24–3.33] are commonly used for laser drilling research.

A 1mm thickness was chosen for the majority of testing as preliminary experiments suggested that this was an ideal choice for single pulse drilling, as full penetration was reliably achieved with the chosen standard parameters using the lowest chosen power of 500W. However, a 2mm thickness was chosen for aluminium as this was of

interest to the industrial partner.

10ms was chosen as the standard pulse width, as in preliminary testing this proved suitable for penetration under the majority of tested conditions. Pulse widths of 2 ms and 5 ms were also investigated for some parameters.

Nitrogen was consistently used as an assist gas throughout the tests because it is an inert gas that would minimise oxidation, however its pressure was varied. The pressures used ranged from no assist gas at all to 2Bar, 5Bar, 8Bar and 12Bar. Using oxygen or air would have caused oxidation. This could add further complications into the process which are not necessary when trying to understand the process of rear melt ejection, added brightness caused by oxidation could also lead to over-saturated images in high speed filming tests. This is because oxidation is an exothermic process which produces heat and light.

3.2 High Speed Filming - Particle Tracking

For all particle tracking tests a Phantom V12.1 high speed camera was used, capable of recording HD 1280 x 1280 pixel greyscale images at 6200 frames per second (fps). A 105mm lens was used for the majority of filming, protected from the ejecta by a transparent IPG fused silica laser lens cover. The camera was chosen as it provided the required picture quality and frame rate, colour images were also deemed to be of little benefit for tracking purposes. The lens was chosen as it provided the best balance of zoom, frame size and picture quality for particle tracking when compared to others in preliminary tests. The protective lens cover was chosen because it provided tested protection against the ejecta and provided the clear transparency necessary to prevent degradation of the image quality.

The lens was set to the smallest aperture possible (f/45), reducing the depth of focus. This allowed for the smallest amount of light possible, which helped to prevent

over-saturation within the images, due to the large amount of light produced on breakthrough. It also helped to reduce the focal length as much as possible. External lighting was tested but was not sufficient for achieving adequate brightness of the particles for tracking.

After doing this, the depth of the focal plane was tested with a calibration plate and measured to be less than 20mm. This means that all particles further or closer than 20mm from the camera in the Z plane were out of focus, and therefore would be cancelled out by the particle tracking program. When measuring in 2D, it is ideal to eliminate the particles moving towards or away from the camera in the Z plane as their exact velocities are difficult to calculate. However, by measuring the particles across a single plane, we can assume that the dispersion is symmetrical (across multiple videos) and calculate the particle dispersion through 360 degrees.

The camera was mounted on a Manfrotto tripod and aligned perpendicular to the laser beam and focused very slightly upwards at the hole breakthrough point from beneath the test piece. Ideally the camera would be positioned perfectly perpendicular to the test piece, however, due to its size and weight, it is difficult to achieve this position consistently. Focusing on the rear side of the test piece allows for increased reliability that initial breakthrough is captured.

To focus the camera, a calibration plate is aligned directly under the laser in the same plane as the field of view of the camera. The camera is then positioned as close to the laser as possible whilst still being focused on the calibration image, 230mm away. This allows for a view which is as zoomed in as possible without a loss of image quality using the given equipment. Zooming in close is useful as it means that the particles appear larger on the screen, making them easier to track. Early work using a less zoomed in view proved to make particle tracking less effective. This is because a less zoomed in image increases calibration uncertainty, whereas using a more zoomed in view decreases calibration uncertainty and therefore increases the

precision of measurements.

The camera was connected by ethernet port to a laptop running Phantom software. The camera constantly runs on a loop until triggered. The software allows for frames to be recorded either side of the trigger point. The software was set to record frames either side of an image based auto trigger. The image based auto trigger was set up to activate due to an increase in intensity at the point of breakthrough within the image. Due to the large number of high quality images, file sizes were very large. To keep this to a minimum, for each video recorded the exact frame of breakthrough was manually identified and the prior hundred frames and latter 300 frames were saved to the laptop hard drive in the raw (.cine) file format.

As well as decreasing the lens aperture to decrease the image intensity, the exposure time of the camera was limited through the Phantom software. 1 µs was used as the chosen exposure time, as in preliminary testing this proved to limit the image intensity as much as possible whilst not losing any particles. The frame rate was kept at 6200fps for 1024 x 1024 images, this is because it is the fastest possible frame rate for the Phantom V12.1 camera without reducing the image quality.

During testing it was noticed that some slight movement occurred to the camera between runs. The main problem with this is that the particle tracking method relies on an exact pixel value for the point of ejection. In order to minimise this deviation, the camera was recalibrated after every 50 videos.

3.3 Different Types Of Lasers Used

2kW Laser An IPG YLR-2000 multimode Ytterbium 2kW fibre laser was one of the lasers used for the drilling tests. The laser specifications are shown the table below.

Laser	Ytterbium Fibre Laser
Collimation Length	125 mm
Focal Length	120 mm
Wavelength	1070 nm
Spot size	192 µm
Mode of Operation	Pulsed
Max. pulse power	2000 W
Pulse duration	0.2 - 100 ms
Nozzle diameter	1 mm
Cooling	Water cooled
Power Tunability	10 - 100 %

Table 3.1: Specifications of the 2kW laser

A beam profile analysis was run on the 2kW laser using a PRIMES FM120 focus monitor, a digital representation of the beam profile was created with PRIMES Laser Diagnostic Software and is shown in Figure 3.2. The information provided is useful for comparing the beam profile with the 6kW laser which was also used within this work.

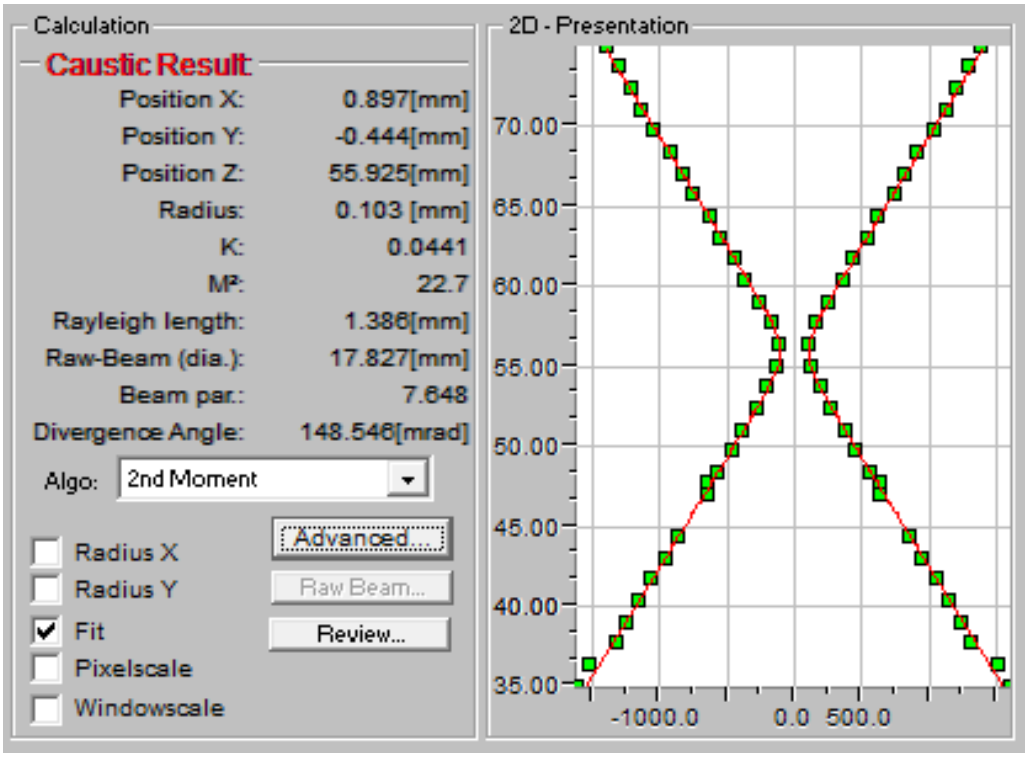


Figure 3.2: 2kW Laser Beam Profile Analysis

The laser nozzle is aligned vertically aiming towards a traversing XY stage which is situated directly below it. The XY stage is controlled by a separate unit which allows for a test piece to be moved accurately by a precise measurement, as little as 0.01mm at a time. The same unit controls the movement of the laser nozzle which is capable of moving in the Z direction, towards and away from the test piece with the same accuracy. When setting up a drill test, the XY stage is traversed to align the test piece directly under the nozzle. A small piece of steel of exactly 1mm in thickness is then placed on top of the test piece beneath the nozzle. The nozzle is then traversed in the Z direction carefully until it just makes contact with the steel, before the steel is removed. This allows for a consistent calibration of the laser beam so that its focus point is situated directly at the surface of the test material - this is because the focal length of the laser beam is the length of the drilling head plus 1mm, hence why the 1mm steel is used as a way to measure.

A specially made rig, shown in Figure 3.3. was securely attached to the XY stage using screws. The rig is 700mm long, 100mm tall and 250mm wide with a Z shaped cross section, it is made out of mild steel sections of 5mm in thickness, to provide maximal stability and minimal bending. The rig is used to provide a stable base, so that a test piece can be suspended above the XY stage, allowing the camera to film the rear melt ejection that occurs through the exit hole. For the drilling experiments a 60x60mm test piece was used with a thickness ranging between 1-2mm. This size was chosen as in preliminary testing it proved to provide a minimal amount of deflection, whilst being large enough for several holes to be drilled without having to replace the test piece, this is necessary to drill as many holes as possible in less time.



Figure 3.3: Rig used to secure test piece during laser drilling

In order to prevent upward melt ejection from interfering with the camera images, a flexible plastic shield was attached to the test piece and attached to the laser drill head. This was done in such a way to prevent any upward melt ejection from being recorded in the images whilst allowing all rearward melt ejection to be fully visible.

IPG LaserNet software was used on a laptop to control the laser and create programs to tailor the laser pulses. The programs were used to control pulse power and pulse width. For this investigation, a new program was created for each set of fifty shots. For each of these a single laser pulse was used, whilst pulse width and laser power

were used as variables.

Once the camera had been set to auto-trigger, the test piece was in position and the laser program had been set, the nitrogen assist gas was set to the chosen pressure. The laser was then turned on.

Once a shot had been completed and the gas had been turned off, the recorded video was analysed and cropped to 400 frames (64.5 ms), before being saved to the laptop, this process took approximately three minutes. The set-up was then reset and repeated.

Fifty videos were taken per parameter because preliminary results showed that this was an achievable number to aim for which would allow a significant number of repeats which would highly increase the accuracy of the analysis, whilst still allowing for a large number of parameters to be investigated. This is demonstrated in Section 12.2, where the 95th percentile is largely influenced by the number of particles, which is more than sufficiently large due to the use of fifty videos.

6kW Laser An IPG YLS-600-6000-MM-AC-QCW Ytterbium fibre laser was also used to conduct laser drilling tests. The specifications are shown in the table below.

Laser	Ytterbium Fibre Laser
Collimation Length	50 mm
Focal Length	200 mm
Wavelength	1070 nm
Spot size	200 µm
Mode of Operation	CW or Pulsed
Max. CW power	600 W
Max. pulse power	6300 W
Pulse duration	0.2 - 50 ms
Nozzle diameter	3 mm
Cooling	Air cooled
Power Tunability	10 - 100 %

Table 3.2: Specifications of the 6kW laser

A beam profile analysis was run on the 6kW laser using a PRIMES FM120 focus monitor, A digital representation of the beam profile was created with PRIMES Laser Diagnostic Software and is shown in Figure 3.4.

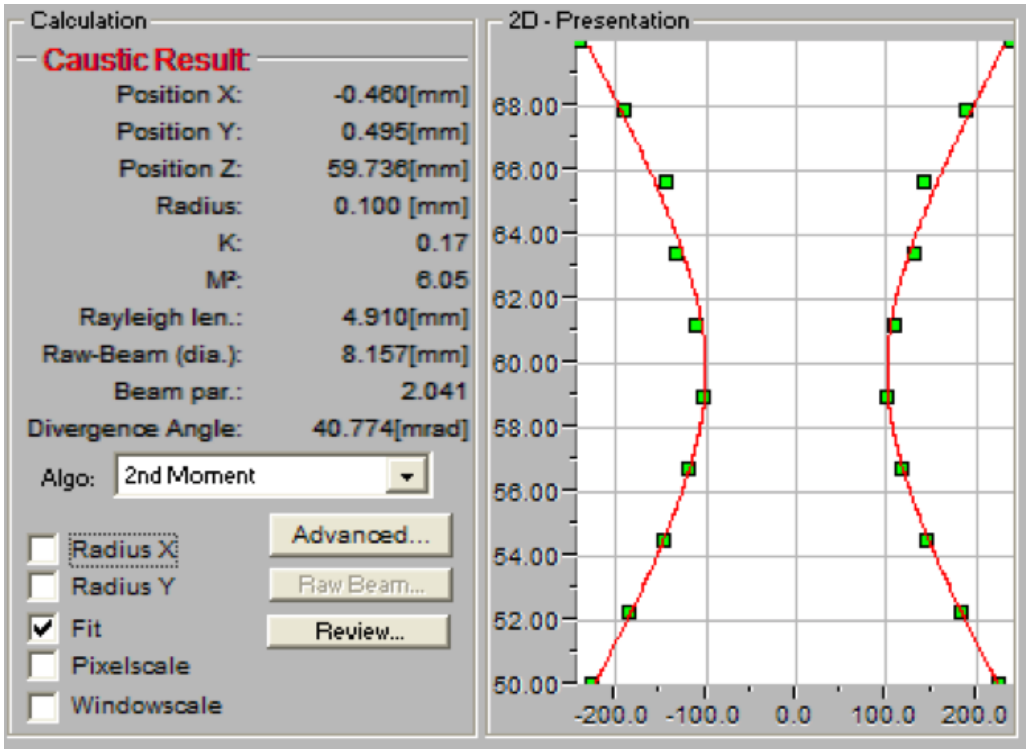


Figure 3.4: 6kW Laser Beam Profile Analysis

For the 6kW laser, a near identical process was used. The laser was set up with the same system and the same XY stage etc. The only difference was that the chiller did not need to be turned on as the laser was self cooled and some of the experiments were conducted without any assist gas.

3.4 Streak Tracking

An IDT full colour camera capable of recording full colour 1280 by 800 pixel images at 500 frames per second was used for the streak tracking tests. An exposure time of 1 µs was used.

Preliminary testing showed that 500fps produced an ideal streak size, that allowed for all of the visible particles to produce streaks, without the streaks being too long so that their end points were situated out of image.

The IDT camera was mounted on a tripod in the same position as the Phantom camera, perpendicular to the ground, angled very slightly upwards at the exit hole and set up with an image based auto trigger using IDT Motion Studio software. The camera was also calibrated in the same way as the Phantom camera.

As with the Phantom camera, the IDT camera was connected to a laptop directly by ethernet by which the camera was digitally controlled and the videos were downloaded to its hard drive.

3.5 Hole Analysis

The first step of hole analysis was using an optical microscope. A Nikon Digital Sight DSR 11 microscope was used to view both the hole entrance and exit. These holes were then measured in diameter using the Nikon software. The diameter was recorded along with the images with a scale bar for future reference, as shown in Figure 3.5.

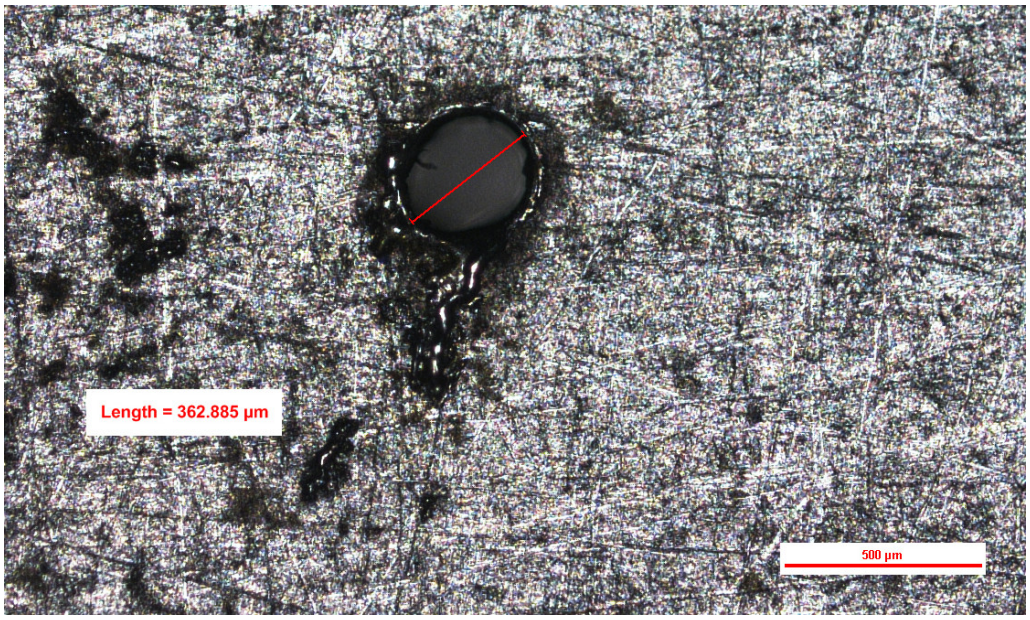


Figure 3.5: Optical Microscope Image of Entrance Hole for 2kW Laser, 2000W Laser Power, 5Bar Assist Gas

The cross sections were then analysed. To look at the cross sections the samples must be cut. At first a guillotine was used to cut the samples down into more manageable sizes. A Brilliant 220 machine was then used to accurately cut the samples just short of the hole centres. A sample was lined up in the machine with the help of a built in laser alignment tool and a cutting disc was installed. The basic cut program was then set to run with a cutting speed of a maximum of 0.05mm/s to ensure that the cut was accurate and did not damage the cutting wheel. It took approximately ninety minutes to cut each sample. The samples contained multiple holes which were spaced apart in a straight line. The sample was cut along a slight angle of the alignment of these holes. This made it easier to find the centre of the hole when removing the material in the grinding process.

Next the samples were mounted in resin. To do this, mounting clips were used to allow the samples to be stood vertically, with the holes facing down. They could then be individually placed in a METASERV mounting machine and surrounded with solid particles of polyfast conductive resin. The METASERV machine was then used to apply heat and pressure to melt the resin particles which can then surround the sample before solidifying to create a secure mount.

Next the samples were cleaned using cotton with distilled water, followed by industrial methylated spirit, then dried. They could then be ground using a Qualipol grinder/polishing machine. The samples were grinded with an assisting flow of distilled water in order to smooth the the sample surface as a prior step to polishing as well as to remove enough material so that the chosen hole cross sections could be analysed through their centres. A range of carbide abrasive papers were used with the Qualipol machine to achieve this, ranging in grit size from the largest, P240, which was used for the bulk of material removal, before gradually scaling down to P1200 to achieve the desired finish without removing too much material.

When the sample was sufficiently smooth and the correct amount of material had

been removed, they were finely polished using diamond wheels with grit sizes of 6 µm and then, 1 µm. This was necessary in order to provide the required finish.

After thoroughly cleaning the samples with distilled water and industrial methylated spirit and drying them completely, they could be etched. Chemical etching selectively corrodes micro-structural features, for these samples it was carried out to allow for differences in the material to be viewed by microscope. These included the recast layers and heat affected zones and any other regions that had undergone phase change or structural transformation during the laser drilling process. Without etching it would be very difficult to view these samples by microscope as the finely polished finish would reflect large amounts of light.

2% Nital was used as the chemical etchant and applied for 20 seconds. The samples would then be cleaned using distilled water and industrial methylated spirt and dried before being viewed under an optical microscope. Once appropriately etched, all of the samples were analysed using a Nikon Digital Sight DSR 11 optical microscope. Quantitive measures were obtained by measuring the size of heat affected zones and recast layers, and the images were stored for future analysis.

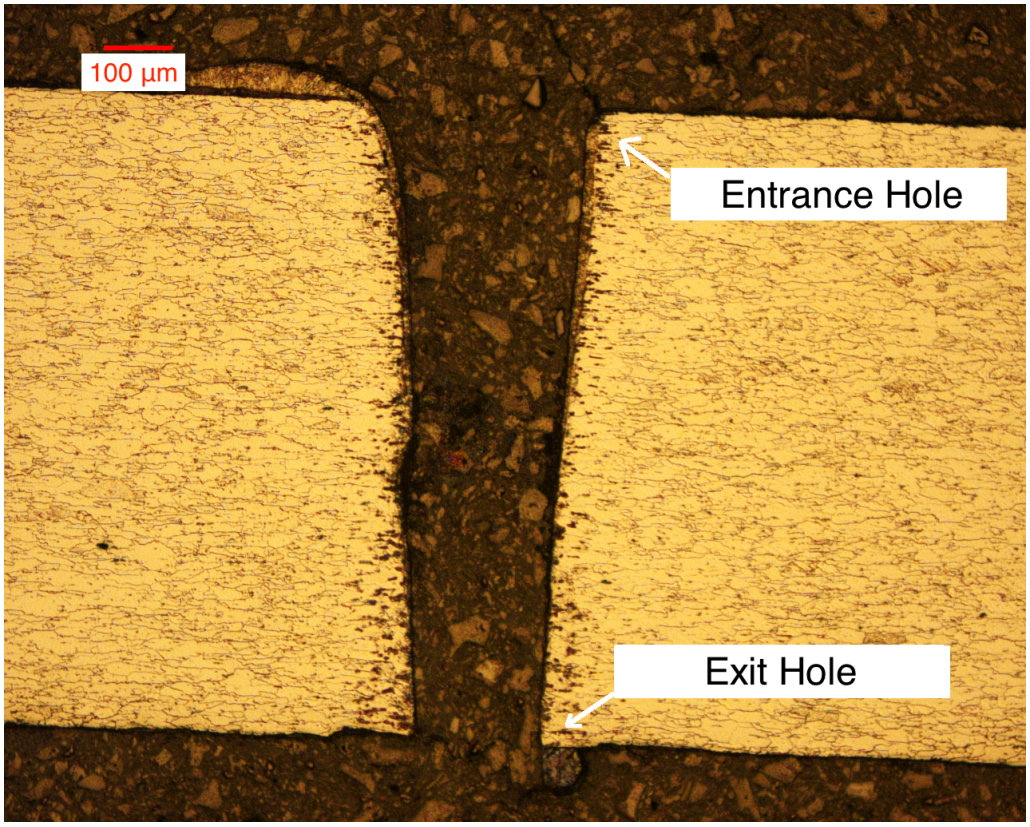


Figure 3.6: Etched Cross-Section - 2kW Laser, 500W Laser Power, 5Bar Assist Gas, Mild Steel, 10ms Pulse Width

3.6 Particle Collection and Analysis

Particle collection experiments were set up with the 2kW laser and subsequent set-up. Additional to the usual set-up, an aluminium tray, 291 x 242 x 51mm was filled with 300ml of glycol and placed on the XY stage directly under the predicted exit hole. The collection basin was positioned at a point as close as possible to the breakthrough point without being so close as to allow for the high pressure gas flow to force the glycol out of the basin. Although the ejecta was dispersed across a wide angle, the set-up was able to capture the majority of particles, which are ejected directly below the laser. Glycol was selected as the appropriate capture medium as its high viscosity was useful in slowing down the velocity of the ejected particles

so that they would not adhere to the bottom of the basin, it was also useful as it prevented oxidation of the particles over time, as would have been expected with water. A large number of particles were required for particle analysis, therefore 1000 holes were drilled to ensure that a large amount accrued within the glycol.

Particle sizing analysis was to be carried out using a Malvern Mastersizer 3000. This device is able to accurately measure the sizes of suspended particles within a fluid from 0.01 µm - 3500 µm using laser light scattering techniques. However, isopropyll was the preferred fluid of choice for the system therefore the particles were first removed from the glycol by filter paper and added to 600ml of isopropyl. The Malvern Mastersizer is also able to measure the sizes of dry particles, however the wet method was chosen as this required a much smaller number of particles.

The Malvern Mastersizer software was used to output the raw data of the particle sizing results, as well as average and percentile results. These were then directly compared to the particle sizing results from the particle tracking investigations.

As well as particle sizing using a Malvern Mastersizer 3000, the particles were examined with a scanning electron microscope. To do this, the captured particles, removed from glycol, were mounted on an appropriate metal stub using double-stick, electrically conductive carbon tape. The specimen was then sputter coated with a thin layer of electrically conducive platinum in a plasma chamber, before being viewed using a JEOL 6400 SEM (Scanning Electron Microscope), producing images such as shown in Figure 3.7.

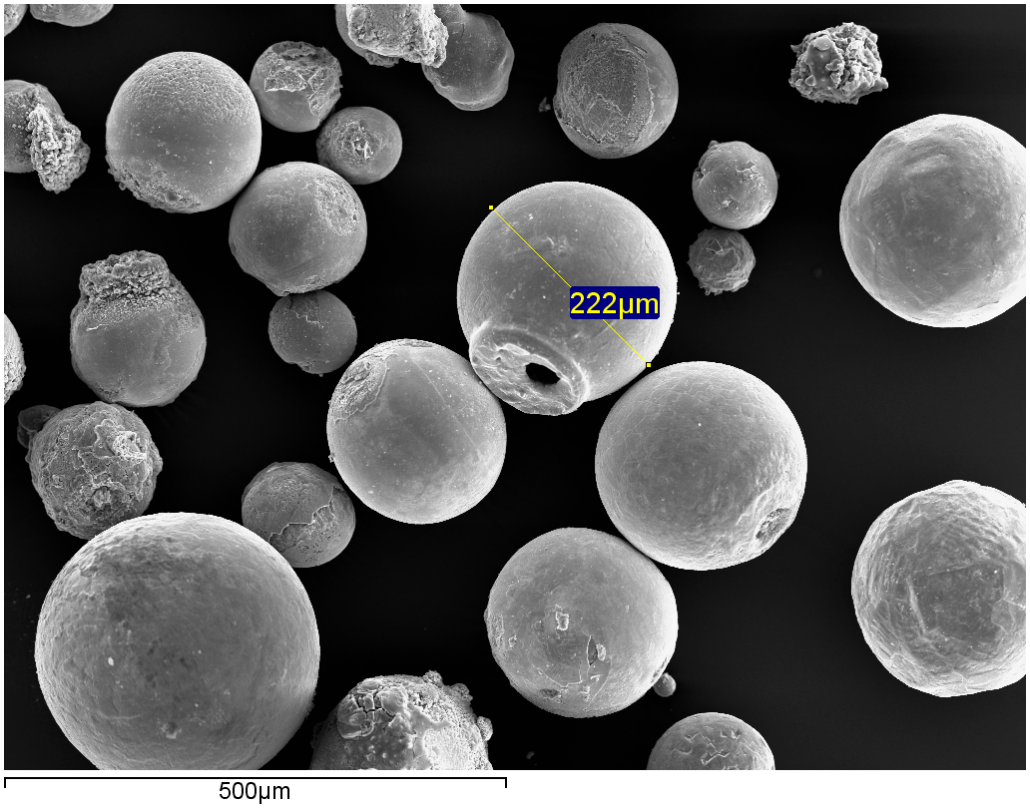


Figure 3.7: Scanning Electron Microscopy (SEM) image of mild steel particles captured from 2kW laser, 1000W laser power, 2Bar Nitrogen assist gas experiments

References

[3.1] M. Ghoreishi, D. K Y Low, and L. Li, "Statistical modelling of laser percussion drilling for hole taper and circularity control," *Proceedings of The Institution of Mechanical Engineers Part B-journal of Engineering Manufacture - PROC INST MECH ENG B-J ENG MA*, vol. 216, pp. 307–319, 03 2002.

[3.2] M. Ghoreishi, D. K. Y Low, and L. Li, "Comparative statistical analysis of hole taper and circularity in laser percussion drilling," *International Journal of Machine Tools Manufacture - INT J MACH TOOL MANUF*, vol. 42, pp. 985–995, 07 2002.

[3.3] D. K. Y. Low, L. Li, and P. J. Byrd, "Hydrodynamic physical modeling of laser drilling," *Journal of Manufacturing Science and Engineering-transactions of The Asme - J MANUF SCI ENG*, vol. 124, 11 2002.

[3.4] O. B. Nakhjavani and M. Ghoreishi, "Multi criteria optimization of laser percussion drilling process using artificial neural network model combined with genetic algorithm," *Materials and Manufacturing Processes*, vol. 21, pp. 11–18, 01 2006.

[3.5] G. Ng, P. Crouse, and L. Li, "An analytical model for laser drilling incorporating effects of exothermic reaction, pulse width and hole geometry," *International Journal of Heat and Mass Transfer*, vol. 49, pp. 1358–1374, 04 2006.

[3.6] B. Yilbas, A. F. Arif, and A. A. B.J, "Laser cutting of holes in thick sheet metals: Development of stress field," *Optics and Lasers in Engineering - OPT LASER ENG*, vol. 47, pp. 909–916, 09 2009.

[3.7] J. Girardot, P. Lorong, L. Illoul, N. Ranc, M. Schneider, and V. Favier, "Modeling laser drilling in percussion regime using constraint natural element method," *International Journal of Material Forming*, vol. 10, no. 2, pp. 205–219, Apr 2017. [Online]. Available: https://doi.org/10.1007/s12289-015-1269-0

[3.8] G. Ng and L. Li, "The effect of laser peak power and pulse width on the hole geometry repeatability in laser percussion drilling," *Optics Laser Technology*, vol. 33, no. 6, pp. 393 – 402, 2001. [Online]. Available: http://www.sciencedirect.com/science/article/pii/S0030399201000482

[3.9] R. Sattmann, V. Sturm, and R. Noll, "Laser-induced breakdown spectroscopy of steel samples using multiple q-switch nd:yag laser pulses," *Journal of Physics D: Applied Physics*, vol. 28, no. 10, p. 2181, 1995. [Online]. Available: http://stacks.iop.org/0022-3727/28/i=10/a=030

[3.10] J. Cheng, F.-J. Kahlen, and A. Kar, "Effects of intrapulse structure on hole geometry in laser drilling," *Journal of Laser Applications*, vol. 12, no. 6, pp. 232–238, 2000. [Online]. Available: https://doi.org/10.2351/1.1324714

[3.11] K. T. Voisey, S. S. Kudesia, W. S. O. Rodden, D. P. Hand, J. D. C. Jones, and T. W. Clyne, "Melt ejection during laser drilling of metals," *Materials Science and Engineering A*, 2003.

[3.12] D.-G. AHN and G.-W. JUNG, "Influence of process parameters on drilling characteristics of al 1050 sheet with thickness of 0.2 mm using pulsed nd:yag laser," *Transactions of Nonferrous Metals Society of China*, vol. 19, 09 2009.

[3.13] M. Guillong, I. Horn, and D. Günther, "A comparison of 266 nm, 213 nm and 193 nm produced from a single solid state nd: Yag laser for laser ablation icp-ms," *JOURNAL OF ANALYTICAL ATOMIC SPECTROMETRY*, vol. 18, pp. 1224–1230, 09 2003.

[3.14] C.-C. Ho, J.-J. He, and T.-Y. Liao, "On-line estimation of laser-drilled hole depth using a machine vision method," *Sensors (Basel, Switzerland)*, vol. 12, pp. 10 148–62, 12 2012.

[3.15] C.-C. Ho, G.-R. Tseng, Y.-J. Chang, J.-C. Hsu, and C.-L. Kuo, "Magnetic-field-assisted laser percussion drilling," *The International Journal of Advanced Manufacturing Technology*, vol. 73, no. 1, pp. 329–340, Jul 2014. [Online]. Available: https://doi.org/10.1007/s00170-014-5815-6

[3.16] C.-C. Ho, Y. J. Chang, J.-C. Hsu, C.-M. Chiu, and C.-L. Kuo, "Optical emission monitoring for defocusing laser percussion drilling," *Measurement*, vol. 80, 10 2015.

[3.17] C.-C. Ho, Y. J. Chang, J.-C. Hsu, C.-L. Kuo, and G.-H. Lee, "Characteristics of the thermal strain of gas jet-assisted laser percussion drilling," vol. 28, pp.

1067–1075, 01 2016.

[3.18] C.-C. Ho and J.-J. He, "On-line monitoring of laser-drilling process based on coaxial machine vision," *International Journal of Precision Engineering and Manufacturing*, vol. 15, pp. 671–678, 04 2014.

[3.19] C.-C. Ho, Y.-M. Chen, J.-C. Hsu, Y. J. Chang, and C.-L. Kuo, "Characteristics of the effect of swirling gas jet assisted laser percussion drilling based on machine vision," *Journal of Laser Applications*, vol. 27, 10 2015.

[3.20] S. Mishra and V. Yadava, "Modeling and optimization of laser beam percussion drilling of thin aluminum sheet," *Optics & Laser Technology*, vol. 48, pp. 461–474, jun 2013. [Online]. Available: http://linkinghub.elsevier.com/retrieve/pii/S0030399212005002

[3.21] H. Singh, S. Kwan, D. Tam, N. Mamalis, K. Maclean, and I. Ahmed, "Fracture and dislocation of a glass intraocular lens optic as a complication of neodymium:yag laser posterior capsulotomy: Case report and literature review," *Journal of Cataract and Refractive Surgery*, vol. 41, no. 10, pp. 2323–2328, 2015, cited By 1. [Online]. Available: https://www.scopus.com/inward/record.uri?eid=2-s2.0-84952332605&doi=10.1016%2fj.jcrs.2015.09.013&partnerID=40&md5=5055f48b565192dd481e3921f2ca7dae

[3.22] L. Tunna, W. O'Neill, A. Khan, and C. Sutcliffe, "Analysis of laser micro drilled holes through aluminium for micro-manufacturing applications," *Optics and Lasers in Engineering - OPT LASER ENG*, vol. 43, pp. 937–950, 09 2005.

[3.23] Y. Zang, X. Ni, and B. Han, "The ejection angle of molten aluminum induced by millisecond pulsed laser," *Journal of Applied Physics*, vol. 116, pp. 013 104–013 104, 07 2014.

[3.24] S. Bandyopadhyay, J. S. Sundar, G. Sundararajan, and S. Joshi,

"Geometrical features and metallurgical characteristics of nd:yag laser drilled holes in thick in718 and ti–6al–4v sheets," *Journal of Materials Processing Technology*, vol. 127, no. 1, pp. 83 – 95, 2002. [Online]. Available: http://www.sciencedirect.com/science/article/pii/S0924013602002704

[3.25] S. Bandyopadhyay, H. Gokhale, J. S. Sundar, G. Sundararajan, and S. Joshi, "A statistical approach to determine process parameter impact in nd:yag laser drilling of in718 and ti-6al-4v sheets," *Optics and Lasers in Engineering*, vol. 43, no. 2, pp. 163 – 182, 2005. [Online]. Available: http://www.sciencedirect.com/science/article/pii/S0143816604001435

[3.26] R. Goyal and A. Dubey, "Modeling and optimization of geometrical characteristics in laser trepan drilling of titanium alloy," *Journal of Mechanical Science and Technology*, vol. 30, pp. 1281–1293, 03 2016.

[3.27] R. Goyal and A. K. Dubey, "Hybrid approach for modeling and optimization of hole taper during laser trepan drilling of ti-6al-4v alloy sheet," *Procedia Materials Science*, vol. 5, pp. 1781 – 1790, 2014, international Conference on Advances in Manufacturing and Materials Engineering, ICAMME 2014. [Online]. Available: http://www.sciencedirect.com/science/article/pii/S221181281400738X

[3.28] W. S. O. Rodden, S. S. Kudesia, D. Hand, and J. Jones, "Use of "assist" gas in the laser drilling of titanium," *Journal of Laser Applications*, vol. 13, 10 2001.

[3.29] B. Yilbas, "Investigation into drilling speed during laser drilling of metals," *Optics Laser Technology*, vol. 20, no. 1, pp. 29 – 32, 1988. [Online]. Available: http://www.sciencedirect.com/science/article/pii/0030399288900096

[3.30] B. S. Yilbas, "A study of affecting parameters in the laser hole-

drilling of sheet metals," *Journal of Mechanical Working Technology*, vol. 13, no. 3, pp. 303 – 315, 1986. [Online]. Available: http://www.sciencedirect.com/science/article/pii/0378380486900227

[3.31] B. Yilbas, "Parametric study to improve laser hole drilling process," *Journal of Materials Processing Technology*, vol. 70, no. 1, pp. 264 – 273, 1997. [Online]. Available: http://www.sciencedirect.com/science/article/pii/S0924013697000769

[3.32] B. S. Yilbaş, A. Z. Şahin, and R. Davies, "Laser heating mechanism including evaporation process initiating laser drilling," *International Journal of Machine Tools and Manufacture*, vol. 35, no. 7, pp. 1047 – 1062, 1995. [Online]. Available: http://www.sciencedirect.com/science/article/pii/089069559400062O

[3.33] B. Yilbas, S. Akhtar, and C. Karatas, "Laser trepanning of a small diameter hole in titanium alloy: Temperature and stress fields," *Journal of Materials Processing Technology*, vol. 211, no. 7, pp. 1296 – 1304, 2011. [Online]. Available: http://www.sciencedirect.com/science/article/pii/S0924013611000586

4

Image Analysis and Processing Techniques

Any different image analysis and processing application can make use of various techniques and methods. For those not familiar with the chosen techniques and methods used in this work, this chapter has been produced to act as an introduction and explanation to the components which are used within this work.

This should help the unfamiliar reader to more easily understand why and how these components have been used in subsequent sections which are directly relevant to rear melt ejection.

* * *

4.1 MATLAB: Image Analysis and Processing Toolbox

MATLAB is a programming language and a numerical computing environment which has been proven to be particularly effective in the fields of science, economics

and engineering. MATLAB has many built in preconfigured commands to help users with common complex functions.

Many of MATLABs preconfigured commands are accessible through specific toolboxes - add ons to the MATLAB environment. One such toolbox is the Image and Processing Toolbox. This toolbox is extremely useful for image and processing applications and is the reason why MATLAB was selected as the programming language of choice for this work. Many of the commands identified throughout this chapter are part of the Image and Processing Toolbox.

4.2 Image Storage

In image analysis and processing applications, the original image itself is the raw data file, along with the metadata, containing all of the original information such as the camera settings etc. Because of this, storing of the image is very important.

In this work raw images are downloaded directly from a high speed camera, and they are stored and processed in their raw form.

Often storing large or detailed raw images can be a problem as they require a lot of storage space, particularly images from high speed imaging devices due to the large number of frames. Compression is a way of countering this by making each image file smaller. However, it must be taken into account that compressing an image can cause loss of necessary image detail. Ideally, the images should be kept in their raw format, as even conversion to lossless image formats can cause a loss of image data.

In their most basic form, digital images are made up of a spatial arrangement of pixels. A pixel is a picture element; pixels make up small, usually uniformly sized, square elements of a picture. Numerous pixels can be placed together to produce a whole image that is recognisable by the human eye.

Pixels are often represented as numerical values. In a binary image, each pixel is represented as either a 0 or a 1 (white or black). Binary images can be very important in image analysis and processing due to their simplicity. This is because they allow for simplified computational tasks such as object recognition as shown in Figure 4.1 and Figure 4.2.



Figure 4.1: Original image containing coins

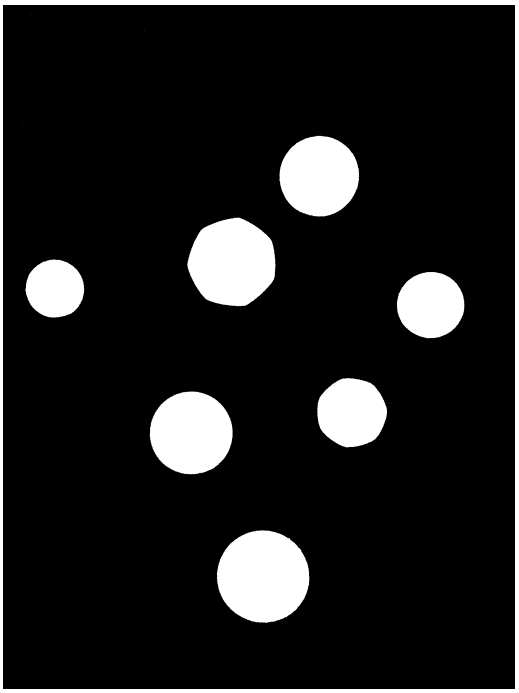


Figure 4.2: Image converted to a binary image

The brightness value of a pixel can be stored as a numerical component. For example, if a binary image is converted to a grayscale image, then the values of 0 or 1 will be given numerical values between 0 and 1 to reflect their intensity between white and black so that a grayscale image can be formed.

Most modern digital systems store and display 8-bit images, these are images in which each pixel is stored as one byte (8 bits). This allows a grayscale image to store one of 256 intensity values for each pixel (2^8) ranging between white and black with many variations of grey in between. This is usually more than sufficient for

viewing a colourless image with the human eye. However the Phantom V12.1 camera used in this work goes up to 12-bit (2^{12}). This means that more complete image data is stored, which can be useful when editing the image in post processing.

Colour images are digitally stored with the use of colour channels. For example, in an RGB image there are three colour channels, red, green and blue. Each colour channel is assigned its own grayscale image. Each grayscale image is designated either red, green or blue, and its intensities are allocated variations of that colour. When all three grayscale images are combined with respect to their colour channel, they can be displayed as a full colour image.

It should be noted that there are many other ways to store images, for example CMYK (Cyan, Magenta, Yellow and Black) colour channels are also commonly used to display colour images. Image pixels can also be stored in many other clever ways, using processes such as vectorisation to compress image size or alter image quality etc. Some of these methods are lossless, meaning that none of the raw data is lost during compression, others are not and potentially important data can be lost.

4.3 Calibration

Calibration is the means of comparing something of unknown value with something of known value in order to calculate the unknown value. There are many different types of image calibration, each with different purposes, these include, camera re-sectioning, colour mapping and radiometric calibration. A basic form of spatial calibration was chosen for this application because it allows for the measurement of lengths within the images.

Length can be measured in pixels directly from an image calculating the Euclidean distance between two co-ordinates. Area can also be measured in pixels by counting

the number of square pixels within a specific object or space.

However, measurements of lengths within images are limited. Any length measurement is limited by the number of pixels in a bitmap image, with one pixel being the smallest possible measurement and the largest measurement being the width or height of the image. This is also true of area measurements, where the smallest area is one pixel squared and the largest area is the width x height in pixels.

Images measurements are further limited by image quality. The more blurred an image is, the more difficult it becomes to depict where an object within the image becomes. For this reason, increasing the number of pixels within an already digitally stored image will not increase the measurement accuracy. Instead, a new higher resolution image must be captured in which more pixels are contained or the objects are better defined.

When measuring objects in images, image perspective must be taken into account. Forced perspective is a technique often used in movies to depict characters as much smaller or larger than their respective actor/actresses. This is accomplished by having the actor/actress stand much closer or further away than the rest of the set/cast in order to make them appear as relatively larger or smaller. Because of this, to use an object of known size to calibrate an image, it must either be equidistant from the camera as the object being measured or the distances between each object and the camera must be known so that they can be taken into account. Equation (4.1) can be used to calculate the length of an object in metres closer or nearer to the camera than a calibration image, as long as the distance between the two objects is known.

$$b = \frac{a}{1 - \frac{d}{D}} \tag{4.1}$$

Where D is distance between the camera and the image in metres, d is the distance between the calibration image and the object, a is the length of the calibration image in pixels b is the length of the new image in pixels.

For the calibration image, it is a good idea to use an object with clear, known size markings such as a ruler. Graph paper was used in this project.

A calibration factor must be calculated. This is done by measuring a known quantity from an image in pixels. The known size measurement can then be divided by the number of pixels to give the calibration factor in units size per pixel.

$$C_F = \frac{L}{n_p} \tag{4.2}$$

Where C_F is the calibration factor measured in metre per pixel, L is the length in metres and n_p is the number of pixels.

All subsequent image measurements can then be recorded in pixel value and converted to known measurement units later. This is done by simply multiplying the length in pixels l by the calibration factor.

$$L = C_F \times l \tag{4.3}$$

Calibration factors are particularly useful when a calibration object of known size cannot be easily included within the image that requires object measurement. In this case, a separate image can be recorded either prior or post image acquisition with the calibration object, as long as the camera remains in the same place. This way a calibration factor can be calculated from a separate calibration image, which can then be used to measure the size of objects within the intended image.

4.4 Segmentation

In image processing, segmentation is the act of dividing up an image into multiple components which can then be labelled. It is useful for defining specific objects and/or a group of objects within an image. In particle tracking, any object that is tracked must first be segmented and identified in all frames over which the tracking is carried out.

Manual segmentation is the simplest form of segmentation. To manually segment an image, each section of interest must be highlighted and labelled as a separate component of an image. Different labels can be given to every part of the image or just one to a small segment. Many different segments can also be labelled if necessary.

Figure 4.3 gives an example of a photograph from a group of medical photographs where manual segmentation was carried out to label multiple different parts of the image.

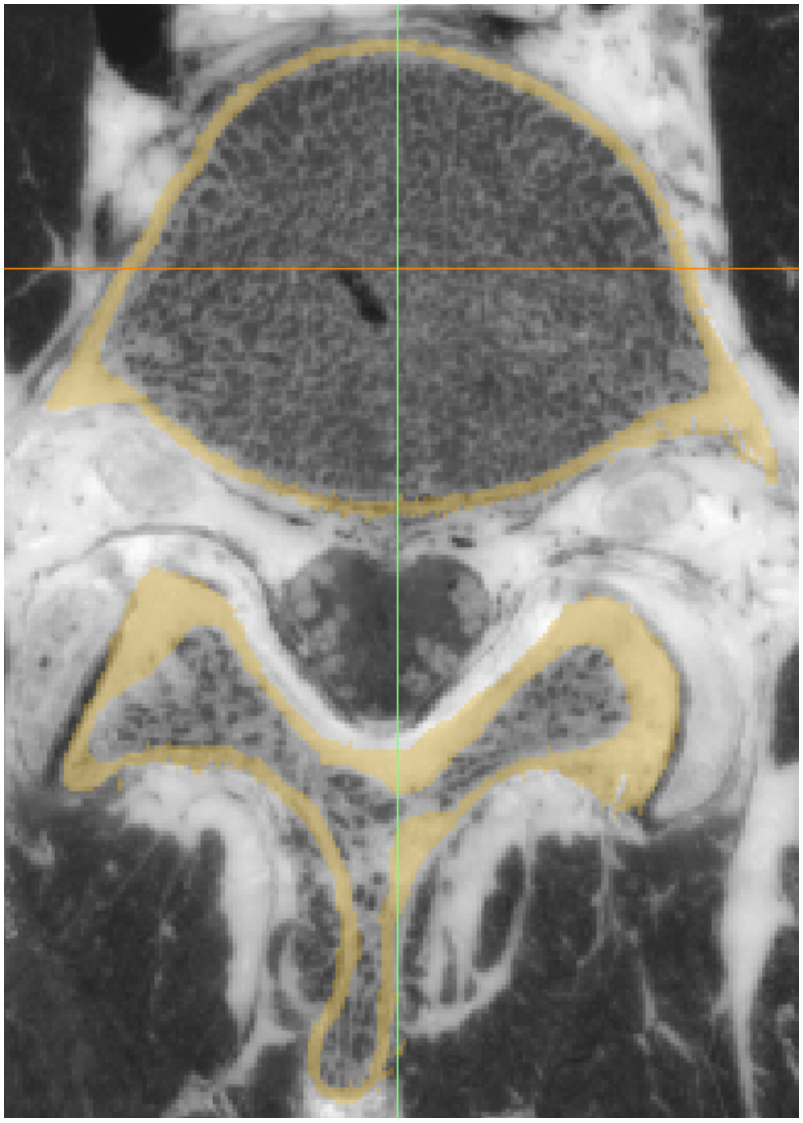


Figure 4.3: Photograph of a lumbar spinal vertebra with cortical bone segmentation represented by yellow colouring [4.1]

The advantage of segmenting an image is that it allows the user to focus on different segments of the image separately. This allows the user to remove certain segments from the image or focus on sole components separately.

Segmenting an image breaks it up into different regions which can be viewed separately. This also allows these different regions to be analysed separately in regards to intensity, shape, size or colour. Or, they can be edited separately in a number of

different ways.

In the following example, the manual segmentation of numerous 2D pictures, one of which is shown in Figure 4.3, were combined together to form a 3D model of a lumbar spinal segment - shown in Figure 4.4. This allowed for a 3D model to be produced that could be used for FEA modelling applications whilst depicting accurate material properties, such as tensile strength, for each separate tissue within the model due to prior segmentation.

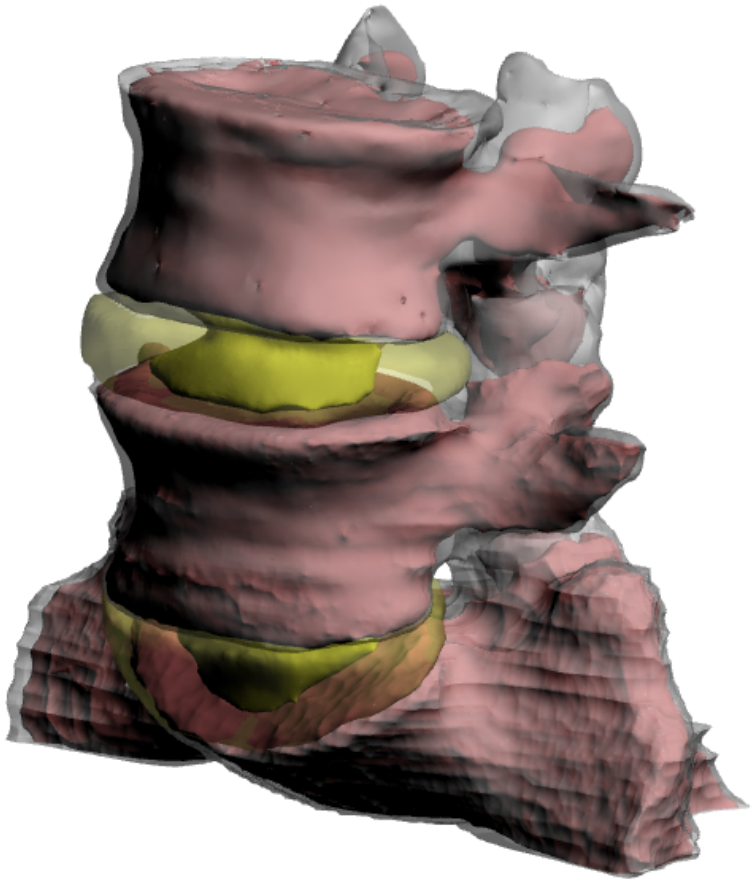


Figure 4.4: 3D lumbar spinal segment model, made of multiple, separately segmented tissues [4.1]

As well as manual segmentation, there are numerous automated methods and algorithms that assist with segmentation. Shape, size and intensity can all be used to

help segment separate objects within images.

A simple example of automated image segmentation is that of a CT scans. CT scans are useful non-invasive procedures that allow for medical practitioners to view human tissues within the body with respect to density. Because of this, bone, one of the densest tissues within the body, is displayed with a very high intensity on CT scans. Because medical practitioners know the range of expected intensity thresholds of bone in a CT scan they are able to automatically segment out the skeletal components of image by removing all other intensities that lie outside of that range. This allows for a much clearer image of bone, and only bone, to be created much more quickly than if it was manually segmented.

Many more algorithms can also be implemented to automatically segment even very complex images. For example, satellite photographs can often be quickly segmented to define the locations of roads and rivers etc. This allows for large-scale satellite photographs to be used to help build up digital maps much more quickly than they otherwise could. Algorithms such as this can take into account many variables and discriminate on a combination of object size, colour, intensity and shape.

Thresholding is a semi-automated form of segmentation. It is often used to convert a grayscale image into a binary image. A grayscale image is made up of a range intensities between 0 - 256. During thresholding, a set point intensity is chosen. All intensities below this threshold are then converted to white whilst all intensities above this threshold are converted to black. This leaves only a binary image - see previous Figure 4.1 and Figure 4.2. Thresholding is featured heavily within this work to segment bright particles from a dark background.

4.5 Watershed Transform Function

The Watershed Transform Function is an image segmentation tool which is built into the MATLAB Image Analysis and Processing Toolbox and is based on the Fernand Meyer algorithm [4.2].

The Watershed Transform Function is particularly effective at segmenting numerous objects within complex images such as microscopic medical images containing biological tissue and telescopic images containing numerous stars and other astrological objects. The function uses a euclidean distance map of the original image, which is a map that represents the distance of each pixel to each non-zero pixel in an image. An example of a binary image is shown in Figure 4.5 and a subsequent euclidean distance map of the image is shown in Figure 4.6.

Figure 4.5: Sample Binary Image - Each square represents a pixel, containing a 1 or a 0 binary value

0	0	0	0	0
0	0	1	1	0
0	0	1	1	0
1	0	0	0	0
1	1	0	0	0

Figure 4.6: Euclidean Distance Map - Each value represents the distance in pixels of a pixel from the nearest 1 value in the original binary image shown in Figure 4.5

2.24	1.41	1	1	1.41
2	1	0	0	1
1	1	0	0	1
0	1	1	1	1.41
0	0	1	2	2.24

The origin of the name watershed, as described by Russ [4.3], comes from the idea of viewing euclidean distance maps as mountains, where the mountain peaks are the centre of the objects and the lowest points, where the water would run down from a mountain, are the watersheds. Therefore the watershed line is the ideal place to draw a boundary to separate touching objects.

The Watershed Transform Function works by identifying each mountain peak, also known as catchment basins, within the image to clearly define the watershed line between them.

The first step in the process of applying the Watershed Transform Function is to obtain a binary image clearly outlining the objects of interest, in this case particles, as shown in Figure 4.7.

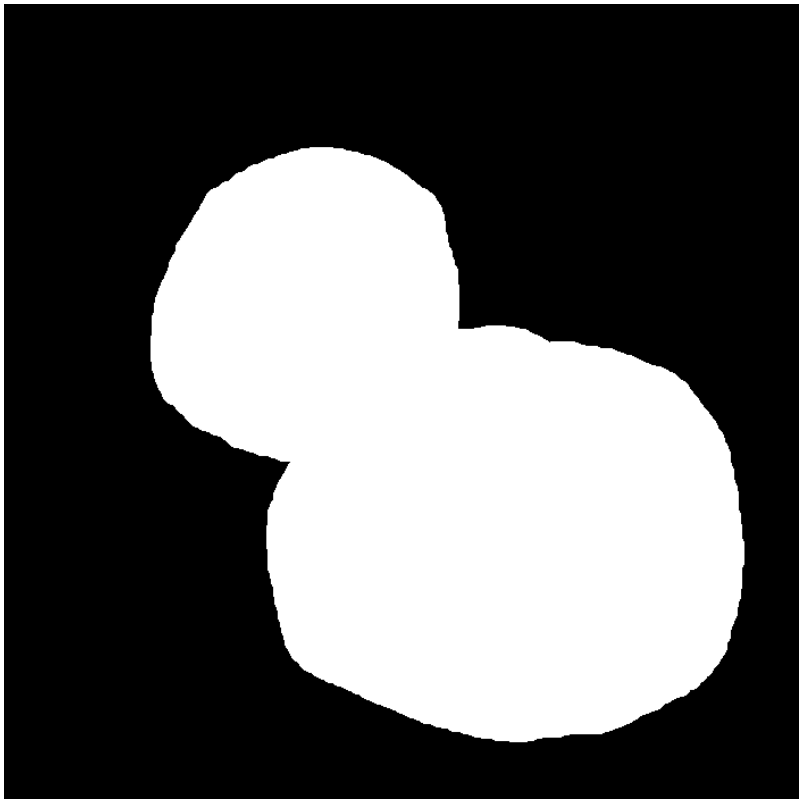


Figure 4.7: Binary image of two touching particles

The next step is to calculate the euclidean distance map of the image, also known as the distance transform. The euclidean distance map is a matrix in which every pixel from the original image is replaced with a new value. The new value is a measurement in pixels of the distance from that point to the nearest non-zero pixel in the original image - these values are not always integers. The euclidean distance map can be computed in MATLAB using the bwdist command.

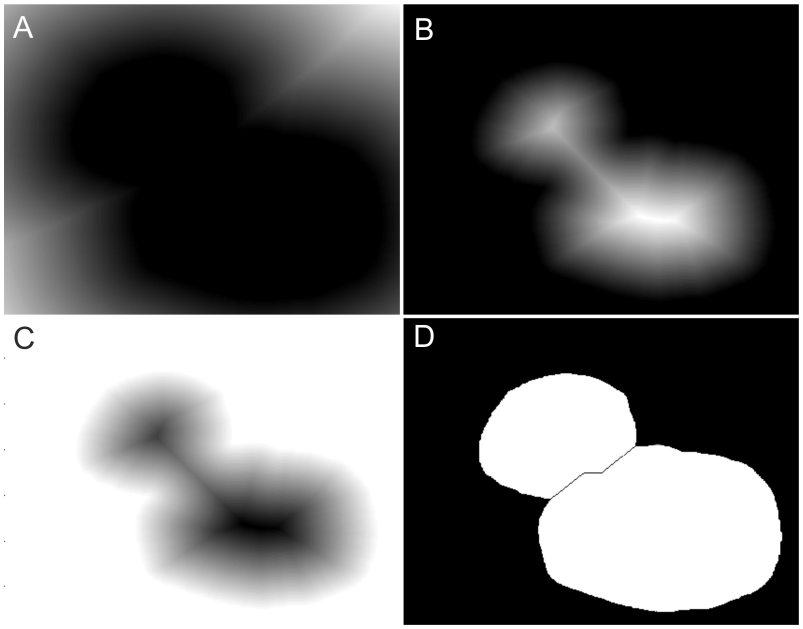


Figure 4.8: A - Distance Transform Image, B - Complement of Distance Transform, C - Negated Complement of Distance Transform, D - Negated Complement of Distance Transform Image with Watershed Function Applied

The distance transform of the binary image can be displayed as its own image, this is shown in Figure 4.8A. By calculating the mathematical complement of each value within the distance transform matrix, image Figure 4.8B is created. The image shown in image Figure 4.8C is then created simply by negating all of the values within the complement matrix. This simply flips the dark and light areas around in the image, as this is the preferred format for the MATLAB Watershed Function.

Ultimately, this process creates an image from the original where the two original particles appear where the higher points - centre of the particles - are darkest, whilst the watershed lines are lighter.

Using MATLAB, the watershed command can then be applied to this image, outputting the image shown in image Figure 4.8D. As seen, image Figure 4.8D shows an image similar to the original, however, with the presence of a clear watershed

line defining the two particles.

The presence of this watershed line is necessary to allow for automated segmentation and labelling processes to be carried out with increased accuracy. If there is no separation of two particles by a watershed line, as in Figure 4.7, then an automated segmentation and labelling algorithm will identify both objects as a single object. If a watershed line does physically separate the two objects as in Figure 4.8D then an automatic segmentation and labelling algorithm will label the two particles as two separate objects.

The Watershed Transform Function is fully explained by Russ [4.3], whilst MATLAB's online guide clearly defines how the process can be carried out using MATLAB [4.4].

4.6 Munkres Assignment Algorithm

In particle tracking, the Munkres assignment algorithm can be used to calculate the shortest distances between particles. To best inform the reader, an explanation of the Munkres assignment algorithm will be explained here, for use within many fields and applications. Section 5.1.5 will later detail how such an algorithm can be used effectively in a particle tracking environment.

The Munkres Assignment Algorithm [4.5], also known as the Hungarian Algorithm is used to calculate the optimal assignment from a n x n cost matrix. There are numerous applications where cost matrices arise, and therefore many for which the Munkres Assignment Algorithm is useful.

A cost matrix is made up of cost values between different workers and different jobs. When each worker has a different cost for a different job, it is often useful to calculate the cheapest way to carry out all of the jobs, assuming that no two jobs can be assigned to the same worker and vice versa.

Assuming a cost matrix is a 3 x 3 matrix (with three workers and three jobs), calculating the cheapest cost can be quite simple. To do this, each combination of each job can be calculated - for which there are six, and then the combination giving the lowest overall cost can be chosen as the cheapest. However, this can prove problematic for large cost matrices with much larger n values, due to the large number of combinations that increase exponentially with the value of n.

The Munkres Assignment Algorithm allows for the calculation of the cheapest possible solution without calculating every single combination, hence making calculation much quicker and more feasible for large values of n. To do this, the algorithm consists of up to five steps.

Munkres Assignment Algorithm:

$$A = \begin{bmatrix} 30 & 35 & 10 \\ 20 & 15 & 25 \\ 35 & 45 & 20 \end{bmatrix}$$

Matrix A shows a 3 x 3 cost matrix where each column represents a job and each row represents a worker. For an assignment to be correct, each job must be assigned a worker without assigning more than one job per worker or more than one worker per job. The goal is to find the correct assignment that sums to the lowest overall cost.

Step 1: Row Reduction

The smallest value in each row must be identified and then subtracted from every value in that row (including itself) - when applied to matrix A, this will produce matrix B as shown:

$$B = \begin{bmatrix} 20 & 25 & 0 \\ 5 & 0 & 10 \\ 15 & 25 & 0 \end{bmatrix}$$

Step 2: Column Reduction

The smallest value in each column must then be identified and subtracted from every value in that column (including itself)- when applied to matrix B, this will produce matrix C as shown:

$$C = \begin{bmatrix} 15 & 25 & 0 \\ 0 & 0 & 10 \\ 10 & 25 & 0 \end{bmatrix}$$

Step 3: Test for Optimal Assignment

In the next step a test must be carried out by drawing a minimal number of straight lines through any of the rows or columns containing zero so that every zero in the matrix has a straight line passing through it, such that matrix C becomes:

$$C = \begin{bmatrix} 15 & 25 & 0 \\ \cancel{0} & \cancel{0} & \cancel{10} \\ 10 & 25 & 0 \end{bmatrix}$$

If the number of lines drawn are equal to n (n = 3 for matrix C), then step 4 can be skipped. However, for matrix C this is not the case as there are only two lines drawn.

Step 4: Shift Zeroes

Step 4 is used to ensure that the number of strikethrough lines equal n. To do this, the smallest value within the matrix (excluding zero), in this case 10, is subtracted from all other values within the matrix that are not covered by a line. The same

value is then added on to any values that intersect two lines, producing matrix D from matrix C.

$$D = \begin{bmatrix} 5 & 15 & 0 \\ 0 & 0 & 20 \\ 0 & 15 & 0 \end{bmatrix}$$

Step 5: Final Assignment

Now that the number of lines are equal to n, a final assignment can be computed. This is done by selecting n zeroes within the matrix D. However, any of the zeroes chosen cannot be within the same row or column as another chosen zero.

The chosen zeroes for matrix D are highlighted below, they represent the positions of the lowest cost solution to the original cost matrix A - it should be noted that there is often more than one variation of the lowest cost solution, however they will all sum to the same value.

$$\begin{pmatrix} 5 & 15 & 0 \\ 0 & 0 & 20 \\ 0 & 15 & 0 \end{pmatrix} \qquad \begin{pmatrix} 30 & 35 & 10 \\ 20 & 15 & 25 \\ 35 & 45 & 20 \end{pmatrix}$$

The lowest cost solution to the problem is therefore the sum of these three values, 35, 15 and 10, which gives a low cost of 60.

References

[4.1] C. Jones, "The segmentation and development of a lumbar spinal model for the development and finite element analysis of a spinal implant," Master's thesis, University of Nottingham, 2014.

[4.2] F. Meyer, "Topographic distance and watershed lines," *Signal Processing*,

vol. 38, no. 1, pp. 113 – 125, 1994, mathematical Morphology and its Applications to Signal Processing. [Online]. Available: http://www.sciencedirect.com/science/article/pii/0165168494900604

[4.3] J. C. Russ, *The Image Processing Handbook, Sixth Edition*, 6th ed. Boca Raton, FL, USA: CRC Press, Inc., 2011.

[4.4] (2002). [Online]. Available: https://uk.mathworks.com/company/newsletters/articles/the-watershed-transform-strategies-for-image-segmentation.html

[4.5] J. Munkres, "Algorithms for the assignment and transportation problems," *Journal of the Society for Industrial and Applied Mathematics*, vol. 5, no. 1, pp. 32–38, 1957. [Online]. Available: https://doi.org/10.1137/0105003

5

Image Processing Methodology

This section contains detailed results and methodology for the 1000W laser power, 10ms pulse results with a 5Bar Nitrogen assist gas using 1mm thick mild steel. The specifics of the MATLAB process are included, as well as its progression through all stages of development.

By looking at a single set of results, the acquisition and importance of individual values can be demonstrated. The same process was carried out to acquire all of the particle analysis results within this work, with the exception of the early, less effective, particle tracking methods. Therefore, this chapter provides specific details on how the results within this work were obtained through particle tracking methods.

* * *

5.1 Image Analysis

5.1.1 Image Recording Procedure

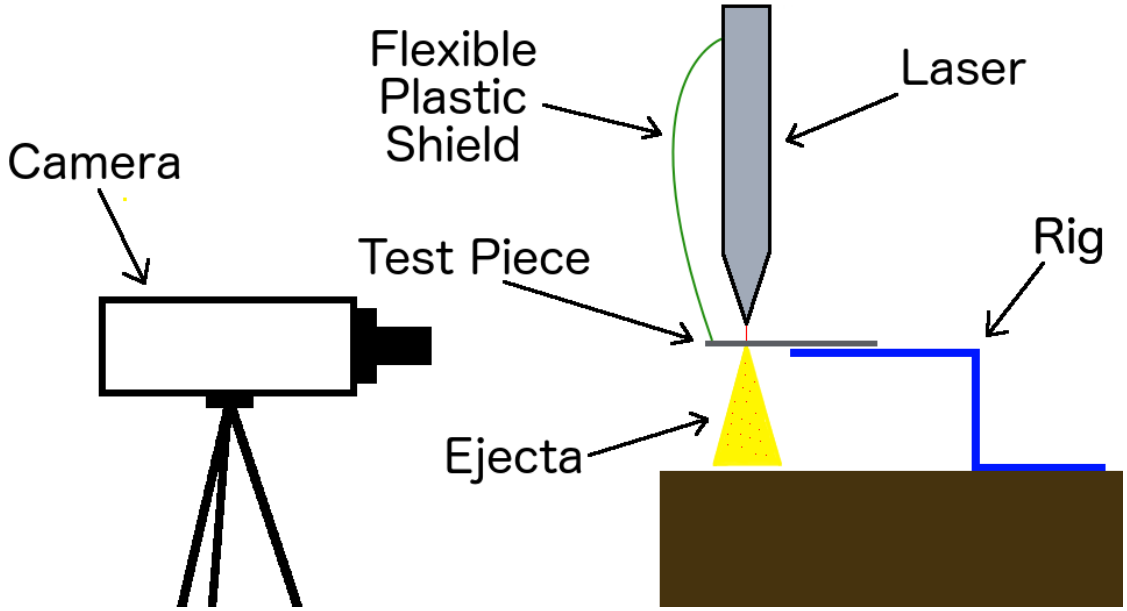


Figure 5.1: Laser Drilling Set-Up

A vertically incident laser set-up was used to drill through 60x60mm test pieces of 1mm thickness for the majority of data collection experiments. The laser was focused on the top surface of the sample. Nitrogen was used as the assist gas, coaxially with the laser beam. Full details of the experimental set-up can be found in Chapter 3.

A Vision Research Phantom V12.1 camera, capable of recording 1280 x 800 pixel images at 6200fps was aligned perpendicular to the laser beam and directed at the bottom of the anticipated exit hole, directly below the focus point of the laser beam. This allowed for total view of rear melt ejection without interference from upward ejection. A flexible polymer sheet was also attached to the test piece to prevent any upward melt ejection from interfering with the rear ejection videos.

Primarily, a Sigma 105mm F2.8 Ex DG Macro OS lens was used for the particle tracking experiments, as this allowed for the majority of ejected particles to appear large enough so that they could be tracked effectively whilst still allowing for an encompassing field of view, effective for displaying particle dispersion. The lens was covered by an IPG lens protection cover glass to protect it from the ejecta.

Prior to the laser tests, a calibration image was taken, as shown in Figure 5.15. To do this, graph paper was stuck on to a solid metal block, with clear markings of specific size. This was then set so that the graph paper was directly underneath the anticipated breakthrough point, parallel to the camera. The camera was then focussed onto the markings on the paper to ensure that any particles inline with the exit hole would be in focus. An image was then recorded of the paper, using a relatively high exposure time for future calibration, before being removed.

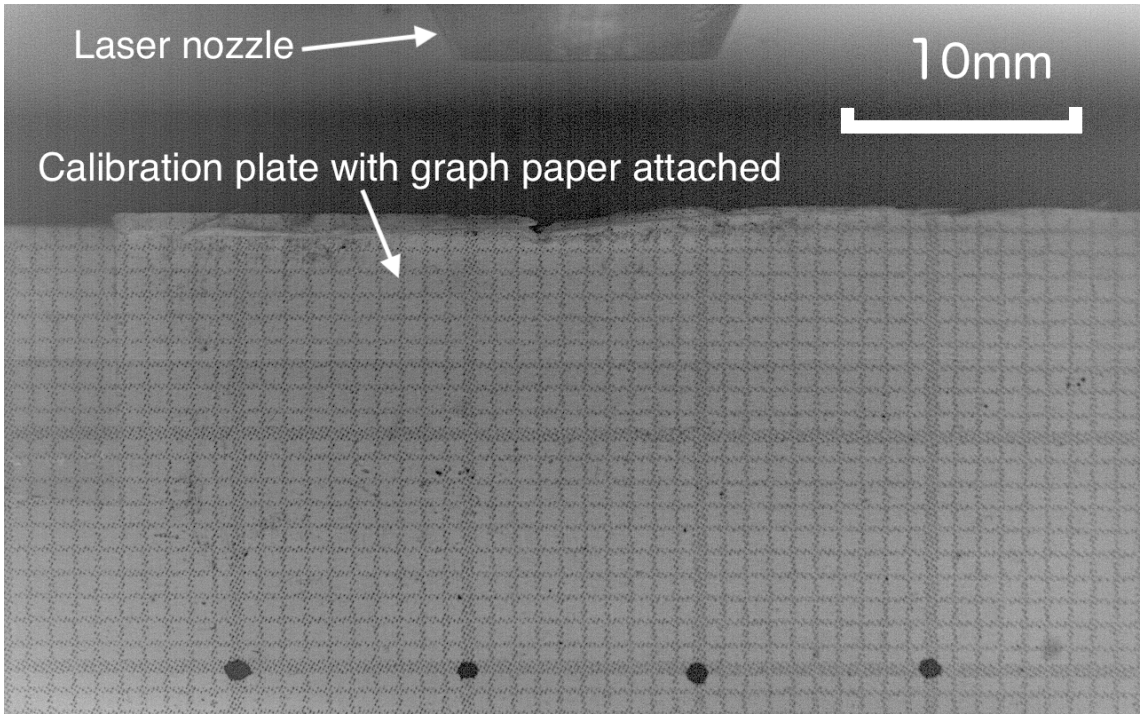


Figure 5.2: Calibration Image

Exposure time is the period of time for which the digital sensor in the camera is exposed to a light source. This can be altered physically by changing the length of

time that the shutter remains open. If the shutter remains open for a long period of time, a lot of light will be absorbed by the digital sensor. When looking at bright objects this can become a problem because it can produce an over-saturated image see Figure 5.3.

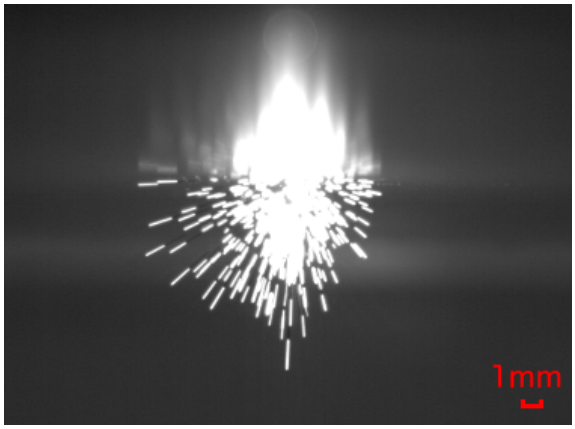


Figure 5.3: Oversaturated Image taken with Phantom V12.1: 160 µs Exposure Time, 1000W Laser Power, 10ms pulse width, 5Bar Nitrogen Assist gas, Mild Steel

An over-saturated image is one which has been taken with a set-up that is too sensitive to light, overexposing the image. This can cause problems as large amounts of light can overpower the image, replacing much of the image detail with whiteness. For this work, this is a problem as it makes it more dificult to pick out individual particles and measure sizes. In Figure 5.3, it is also clear that streaking occurs due to overexposure, where a single round particle appears as a line rather than a circle. This makes it very difficult to measure particle size.

An exposure time was selected using the Phantom camera software, as such to reduce the light in the image as much a possible, whilst still being able to see the majority of the clearly defined particles. For the 105mm camera lens, an exposure time of 1.55 µs was found to produce the best images.

Minimising the exposure time decreases the likelihood of over-saturation in images, which is important, when analysing such an intense light source in order to produce

an image with clearly defined particles. However, increasing the exposure time can also be useful for creating streaked images, useful for streak tracking, but problematic for particle tracking. To create streaks an image must be over-exposed so that light is absorbed from a bright particle continually whilst it passes through different points in space. This is shown in Figure 5.4.

Figure 5.4: Streak Images taken with IDT camera: 500 µs Exposure Time, 1000W Laser Power, 10ms pulse width, 5Bar Nitrogen Assist gas, Mild Steel

The Phantom V12.1 camera records using a cyclic buffer. It can be triggered at an any point and set to record a chosen number of frames before or after the trigger point. For these tests, an image based auto trigger was used. This was done by manually highlighting an area around the point of breakthrough on the camera image and choosing a minimal intensity for which it would trigger. This means that as soon as breakthrough occurs, the increased brightness at that point of the image would cause the camera to trigger, enabling the camera to record frames either side of breakthrough and hence capturing the entire period of melt ejection.

However, the image based auto trigger is not exact at pinpointing the frame in which breakthrough occurs in each video, therefore a manual selection of frames was then carried out, storing exactly 100 frames before breakthrough and 300 frames after breakthrough, using the trigger frame as a reference point.

100 frames (16.1 ms) prior to breakthrough were chosen for use in background removal, whilst 300 frames afterwards (48.4ms) were deemed adequate to assess the full rear ejection process in all cases of the parameters observed.

The image files were stored in their raw .cine file format, ensuring that no image data or metadata was lost through image compression or optimisation. In their raw format, each 400 frame video takes up 647MB of storage space.

5.1.2 Initial Image Analysis

The initial stages of image analysis were conducted manually. A number of videos from each parameter were observed and analysed for the presence of patterns, similarities and anonymities.

Although simple, this method of analysis can be crucial when analysing complex images, this is because as advanced and as effective as image analysis and processing methods can be in extracting numerical data, they can fall vastly behind the complex ability of the human eye and the human mind in certain areas.

The results from manual observations are shown in Section 6.1.

5.1.3 Image Cleaning

Background removal can be a very complex process in image processing and analysis. There are a multitude of advanced techniques available to deal with complex images, many of which fall into the group of aforementioned threshold and segmentation techniques as well as noise filtering methods such as Gaussian filtering, box filtering, median filtering and Laplacian filtering etc.

However, for the images discussed, background removal is a minor issue. This is because due to the intense brightness of the laser melt ejection, the exposure time is very low, around 1 µm. This means that very little light is let into the camera lens, essentially blacking out the majority of the surroundings around the ejected particles.

Therefore, a basic background removal method, known as gaussian filtering is enough to eliminate the interference of any potential background noise.

To do this, the initial 100 frames taken before the trigger point are selected as the background removal frames. The pixel values in each of these images are then

combined together and divided by the total number of images. This new image, shown in Figure 5.5, made up of median pixel values, is subtracted away from all images, which are to be used for tracking, eliminating any potential background noise interference.

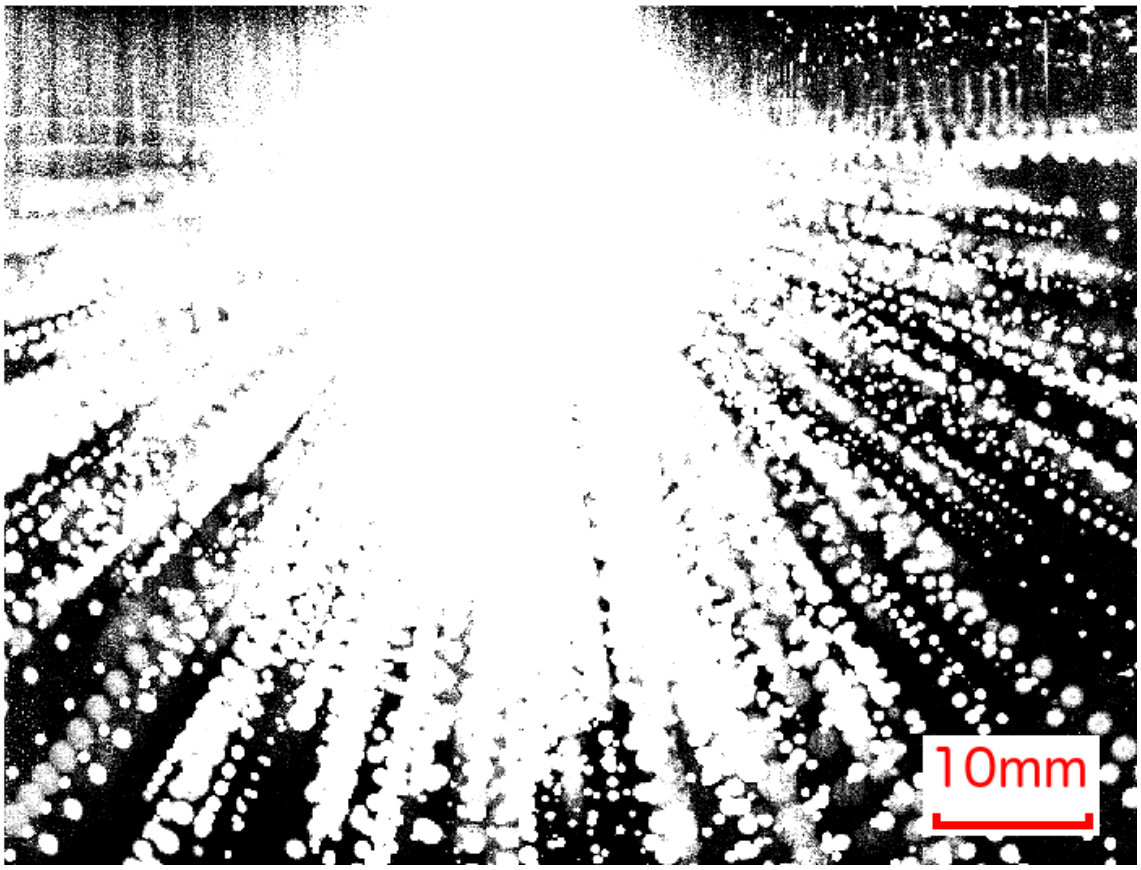


Figure 5.5: Median Image Taken Over Multiple Frames: 1000W Laser Power, 10ms pulse width, 5Bar Nitrogen Assist gas, Mild Steel

Other potential background interference problems arise from the possibility of reflections being created by the bright light emitted from the ejected particles. To minimise this, reflective objects were kept out of the frames as best as possible, and the rig was painted with matte finish.

Despite this, reflections can occasionally appear as very large particles within the images. To prevent this the imopen tool was used within Matlab with a relatively large

disk structural element of seven pixels in radius. This tool dilates and erodes objects within an image around the chosen structural element. This can be used effectively for multiple reasons within image processing environments, such as smoothing, however here it was used to remove all particles larger than seven pixels in diameter (approximately 300 µm).

As well as reflections, this process removes excessively large particles. This is necessary, as particles which are out of focus and travelling towards the camera can sometimes appear as very large. Removing these particles is required as they can distort the results. Through trial and error runs, it was found that 7 pixels is the optimum size to eliminate the majority of out of focus pixels without eliminating large pixels which are in focus. Figure 5.6.



Figure 5.6: Binary image of ejected particles including large reflection

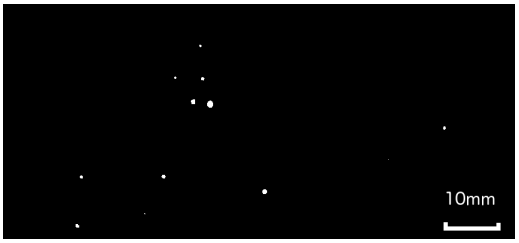


Figure 5.7: Binary image of ejected particles with large reflection removed

5.1.4 Particle Identification

Thresholding is used to separate the particles from the remaining background. The Phantom V12.1 camera, used within this work, is capable of producing up to 12-bit pixel depth. This means that pixel intensity values can range from 0 for pure black and 4096 for pure white (2^{12}).

By observing the colormap, and testing with trial and error, it has become clear that the pixel intensity value of 500 is a consistently useful cut off point that allows

the relatively black background to be removed from the relatively white particles within all of the obtained images. Therefore, the threshold level is set to 500. This leaves a binary image where all pixels below an intensity of 500 are converted to 0 and all pixels above are converted to 1.

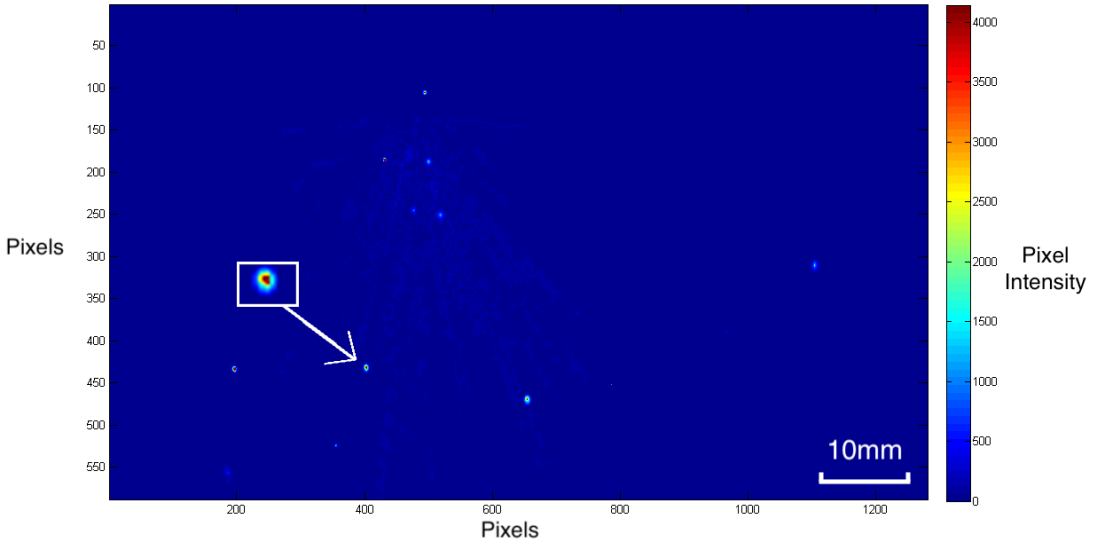


Figure 5.8: Colormap used for thresholding

A potential problem that presents itself in the images is those particles that are passing off of the screen, leaving only a section of a particle in view. Although very few of these particles occur in frames - less than 1%, these particles can potentially hurt the accuracy of velocity measurements and provide totally false results for particle size.

To remedy this problem, the MATLAB command - imclearborder - was used to remove any particles that are touching the edge of the image. This way, they will then be treated as if they have already left the image and will therefore not be analysed, which is preferable to providing false results.

Once a clear image has been produced showing only the particles of interest, it is important that they are properly segmented and labelled. This allows each individ-

ual particle to be tracked one by one, and aims to limit false results arising from more than one particle being tracked as a single cohesion, which can happen if two particles are overlapping each other on the screen.

The Watershed Transform function method was chosen because it was found to be highly effective when segmenting the particles for these images.

To carry this out, the MATLAB bwdist command was first used to create a distance transform of the binary image. The complement of this image was then taken and made negative, before a threshold was applied to suppress shallow minima below the height of 0.5, as this value was proven to be effective through trial and error for the segmentation outputs required for all images tested. The Watershed Transform Function was then applied using the inbuilt MATLAB algorithm.

The Watershed Transform output was then used as a mask to label the location of each individual particle on the original grayscale image. This was done using the built in MATLAB function regionprops. As well as labelling the position of each individual particle on the original grayscale image, regionprops was used to store the centroid location, the equivalent diameter and the maximum intensity of each of the identified particles.

5.1.5 Particle Tracking

Once all of the particle centroids have been identified, the particles can then be matched up between two consecutive frames and tracked. This will allow for particle velocity calculations.

To do this, a modified version of Jean-Yves Tinevez's Simple Tracker [5.1] MATLAB function is used. Looking at only two adjacent frames, the modified tracker function labels the centroids from the first frame as sources and those from the second frame as targets, with the input point of ejection being labelled as the sourcepoint.

Using their cartesian co-ordinates, the track function then calculates the magnitude of a vector between each target centroid and the sourcepoint using the pythagorean theorem, in the same way that the velocities are calculated from the resulting tracks, as shown in Figure 5.12. The sourcepoint, as shown in Figure 5.12, is the point at which the particles first exit the hole, this is the first place in which all of the particles originate from on camera.

The angle between each of the vectors and the vertical is then calculated using trigonometric functions, giving the angle α, as shown in Figure 5.9.

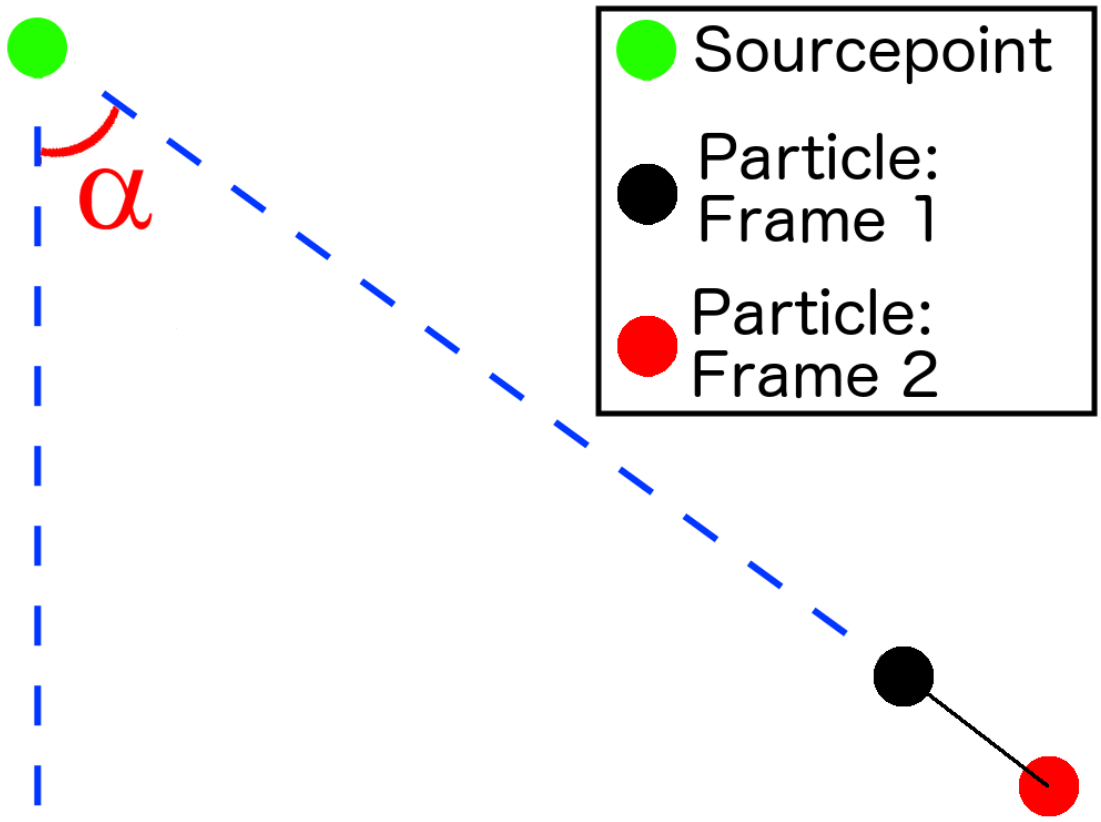


Figure 5.9: The angle α must be calculated for each track in order to predict a particles position in frame 2

The magnitude of the vector in pixels, multiplied by 0.03, plus 10, is then used along the same angle as the vector, away from the sourcepoint, to identify a location for

a predicted particle position. The dynamic length of the magnitude multiplied by 0.03, plus 10 was chosen as it proved to identify the most tracks correctly through trial and error when compared to various other lengths.

The Munkres Assignment Algorithm, as originally included in the Simple Tracker [5.1] function, is used to identify the centroid in the latter frame which is most likely to correspond to the predicted particle, by linking the centroid with the predicted particle of the lowest cost in terms of distance from the centroid. The process of finding the lowest cost is described in Section 4.6.

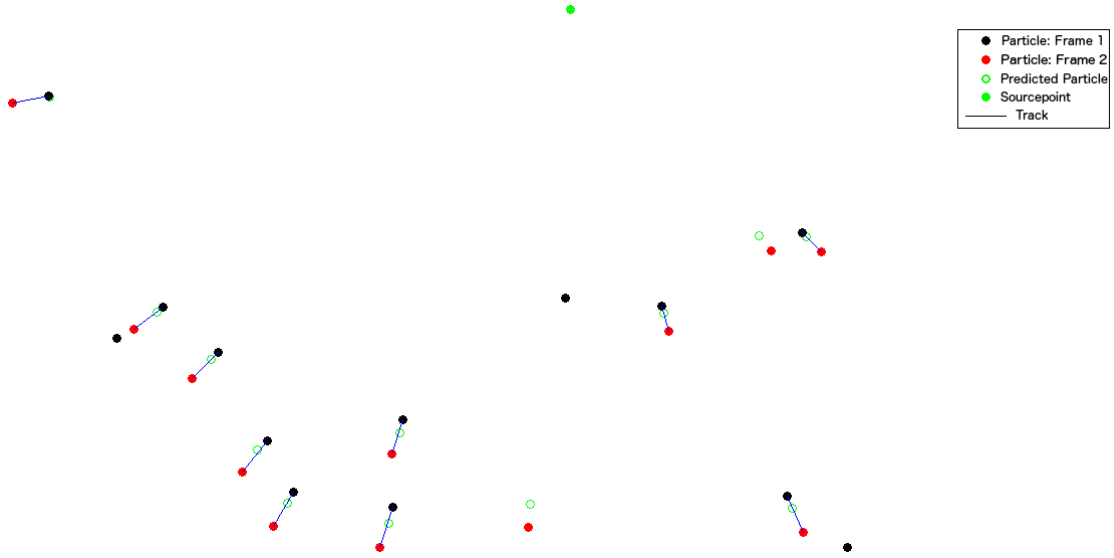


Figure 5.10: Tracks created between centroids of subsequent frames using predicted particle locations - 500W Laser Power, 8Bar Nitrogen Assist Gas, Mild Steel

To further increase the likelihood of matching the correct centroids to the correct predicted particles, bounding boxes were used as shown in Figure 5.11. These boxes were used to limit the number of centroids which could be linked to a specific predicted particle by direction as well as distance. This is done by creating boxes which run along the direction of the vector created between the predicted particle and the sourcepoint - the anticipated track direction. The boxes were made 4 pixels in width as this observed as optimal when running trial and error tests for numerous

videos in terms of producing the highest number of correctly linked particles. The length of the box, with the predicted particle placed in the centre, is variable and can be adjusted within the program with the "max linking distance" variable depending on the parameters.

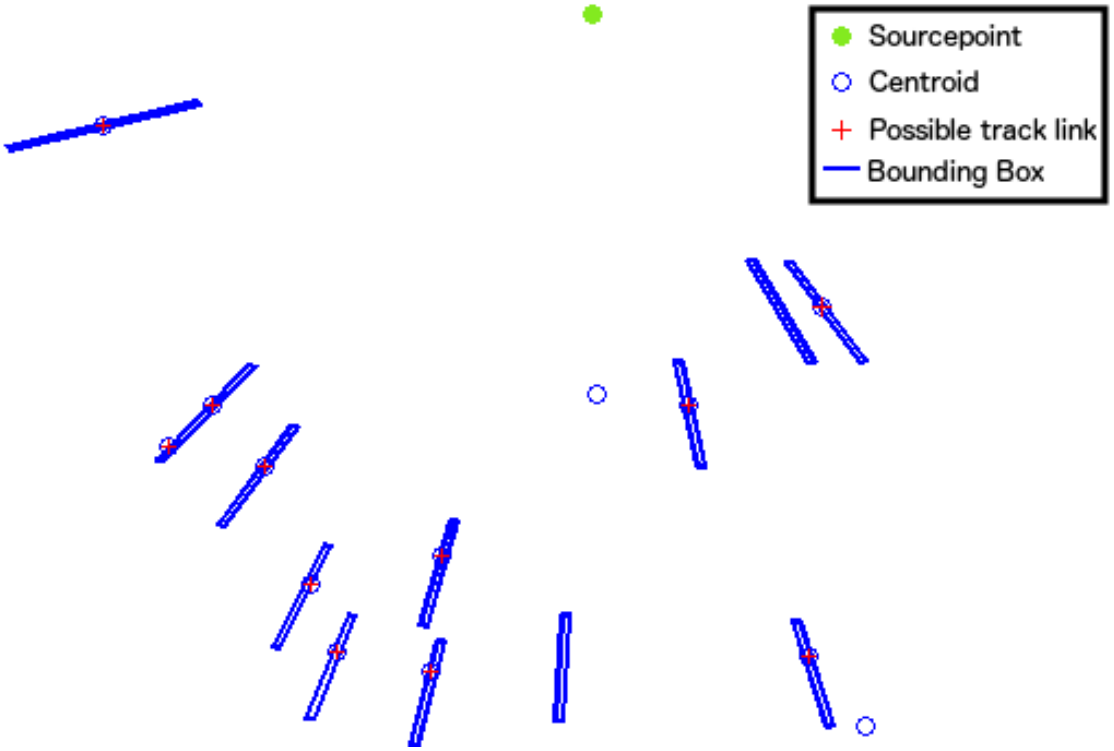


Figure 5.11: Shows bounding boxes with a length of 50 pixels, used to limit particles which can be potentially linked to a predicted particle location - 500W Laser Power, 8Bar Nitrogen Assist Gas, Mild Steel

Therefore, the Munkres Assignment Algorithm will only assign a predicted particle location to a centroid that falls within the confines of its corresponding boundary box. The second frame centroid will then be linked to the first frame centroid which corresponds to the same predicted particle location producing a track. This track can then be used for velocity calculation.

5.1.6 Size and Velocity Measurement

Once each track has been successfully established, it can then be used for the calculation of velocity of each tracked particle.

To do this, one by one, each track is separated into its individual points and frames by centroid, centroid 1 and centroid 2. Each centroid is then broken down into its Cartesian components, X and Y. The difference between each X component and each Y component is then calculated in pixels.

Geometrically, this then provides the lengths, in pixels, of the opposite and adjacent sides of a right-angled triangle as shown in Figure 5.12. The Pythagorean Theorem can then be used to calculate the hypotenuse.

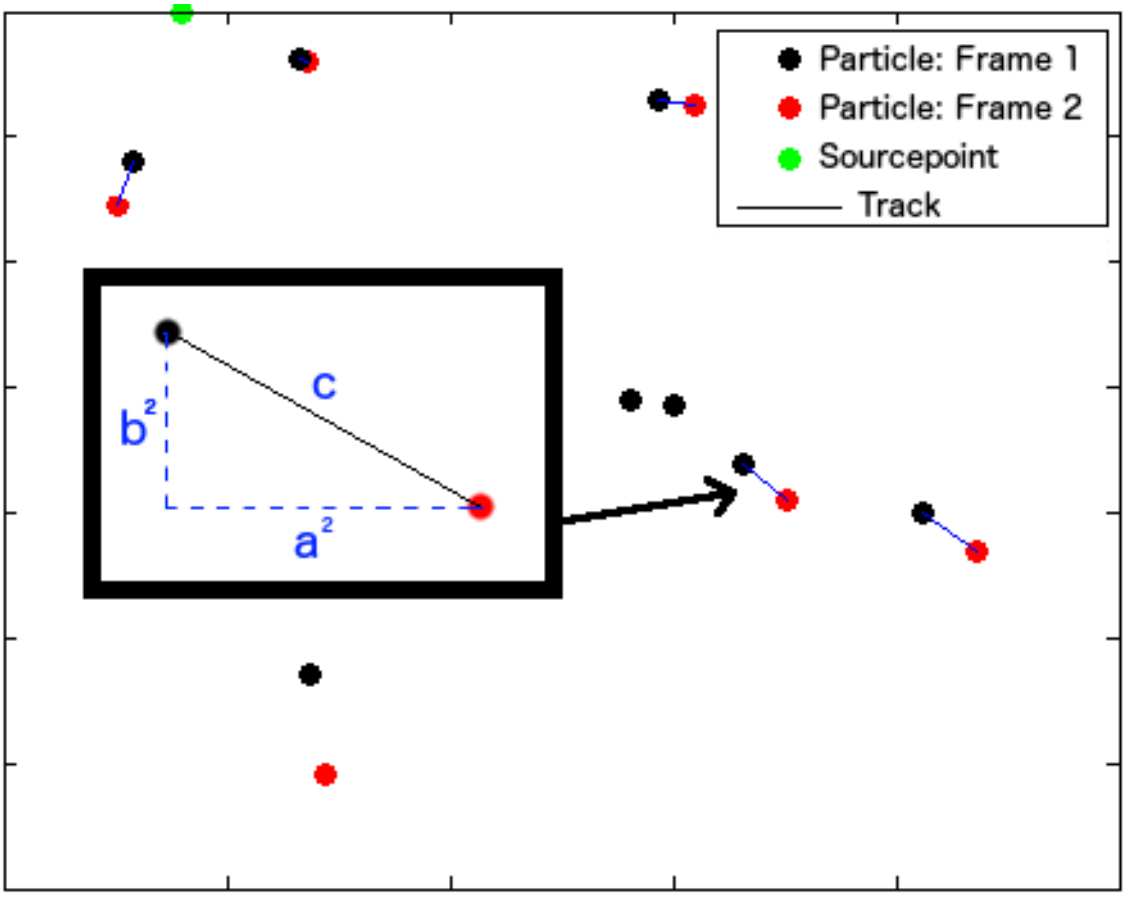


Figure 5.12: Distance between two particles in subsequent frames can be calculated using Pythagorean Theorem for velocity calculation

Once the length between the two points within a track has been calculated, it is important that we convert the length to a true length as to calculate a true speed. This is done by multiplying the length by the previously calculated calibration factor, given in metres per pixel, as shown in Equation (4.3). This of course gives the length between points 1 and 2 in metres.

The speed is then calculated by dividing the calculated distance in metres by the time taken between two frames in an image.

$$S = \frac{D}{t} \tag{5.1}$$

For these images taken with the Phantom V12.1 camera, the frame rate used is 6200fps. Therefore, the time between frames in seconds (t) is calculated by dividing the number of frames by the frame rate in frames per second.

$$t = \frac{1}{6200} \tag{5.2}$$

The speed is then stored in metres per second for each track separately, as well as used to calculate an average of all of the tracks within a certain video or group of videos.

The particle size data is stored as the diameter. This is automatically calculated in pixels using the MATLAB "regionprops" tool, which outputs the equivalent diameter. As the particles are not always perfectly round, the equivalent diameter becomes a useful calculation. This is an approximation that is calculated by measuring the true area of the particle, as it appears in the image, from which the diameter is calculated in pixels, using:

$$EquivalentDiameter = \sqrt{\frac{4A}{\pi}} \tag{5.3}$$

As with the velocity measurements, these must be converted to metres using the previously calculated calibration factor using Equation (4.3).

5.1.7 Data Storage and Graphical Outputs

For each video analysed, a MATLAB .dat file is created to store the essential processed data. Within this file the calculated centroid co-ordinates, velocities and equivalent diameters are stored, as well as the co-ordinates of the source point (point of rear particle breakthrough).

A separate matrix of velocities in relation to particle size is also stored. This matrix contains fewer values than the particle size matrix as fewer velocities are recorded than particle sizes. This is due mostly to the difficulty in tracking particles that disappear off of the screen on consecutive frames.

The usefulness of a matrix which tracks particle velocity in correspondence to particle size allows for this data to be plotted against each other in order to help identify any existing trends.

Once the data is stored it can quickly and easily be loaded into a new MATLAB program, to be output in a multitude of ways using various different plotting techniques.

5.2 Experimental Methods

A flexible plastic shield was attached to a 1mm thick, 60x60mm mild steel test piece. The test piece was then installed on the rig using large metal clips, in such a way that half of the test piece was overhanging the rig and the clips were not obscuring the cameras view point or the laser path. The flexible plastic shield was then suspended from the upper components of the laser set-up so that upward ejection would be contained without obscuring the cameras view of the rear ejection, as shown in Figure 5.13.

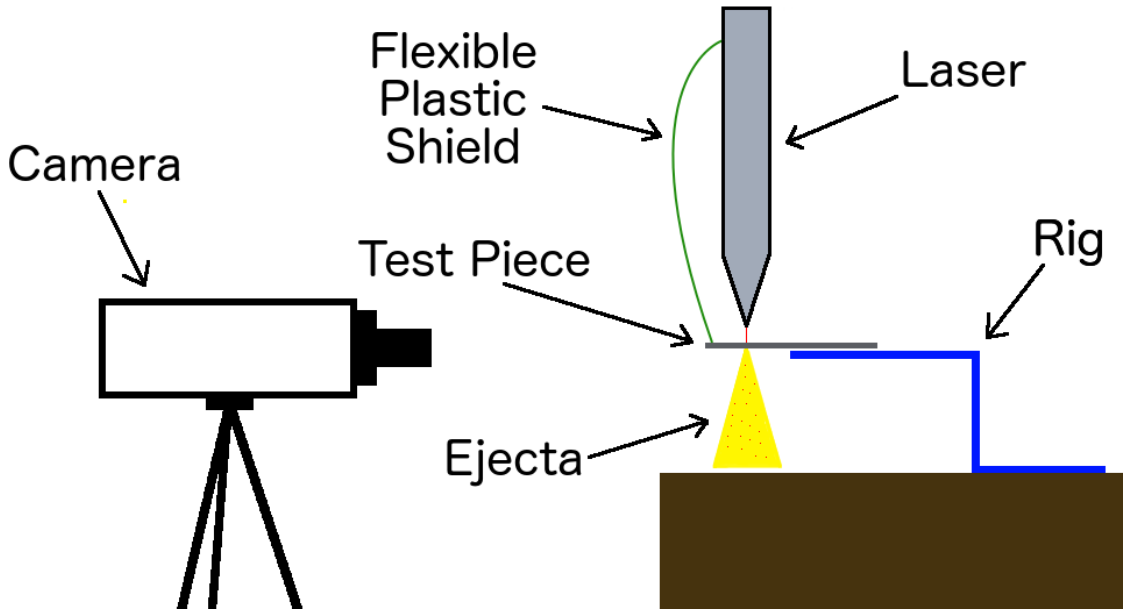


Figure 5.13: Laser Drilling Set-Up

The calibration plate was then aligned directly below the test piece, inline with the laser nozzle, facing the camera. Using the camera software, the exposure was set to 2000 µs so that the calibration plate could be viewed under normal lighting conditions. The tripod and the camera were then positioned so that the camera was pointing up at the rear surface of the test piece by approximately 5 degrees, with the centre of the calibration plate aligned in the centre of the image, with the expected ejection point aligned just below the top of the image. This positioning allowed for the maximal viewing of the rear ejection particles as well as the exact point of breakthrough.

A single frame was then recorded and stored on the laptop hard drive of the calibration plate in the .cine file format, to be used as a calibration image later. A back up .png file was also taken and stored.

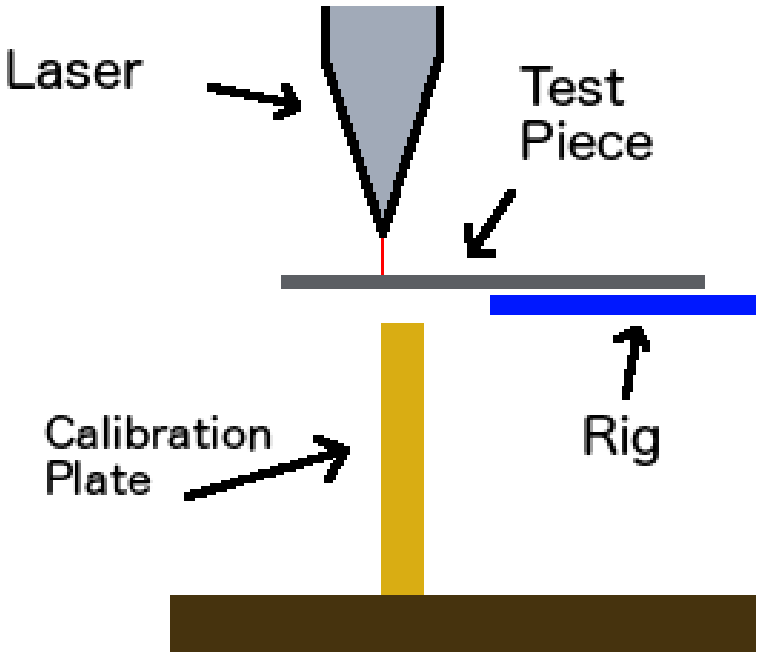


Figure 5.14: Position of calibration plate in set-up during calibration

An image-based auto-trigger margin was then set-up. Using the calibration plate for alignment, the margin was set up just below the point of ejection, centrally, approximately 250 x 250 pixels in size.

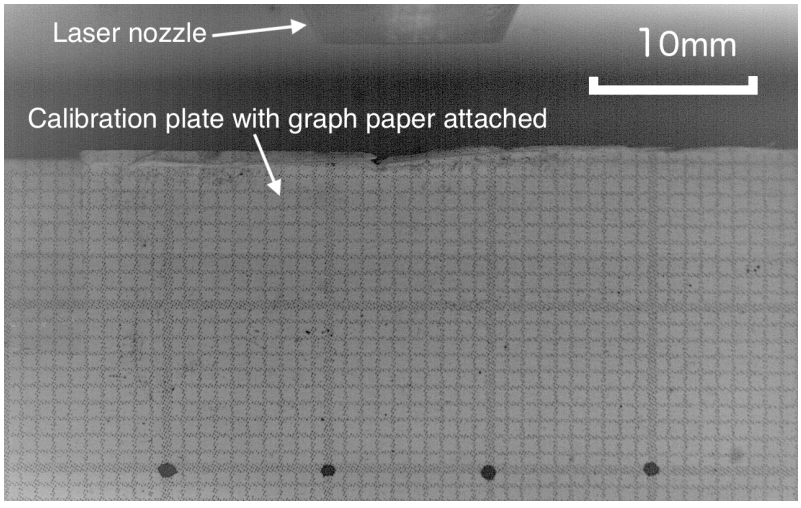


Figure 5.15: View of calibration plate from camera

The calibration plate was then removed. The camera exposure was set to 4 µs, the

frame rate to 6200fps and the image auto-trigger, consisting of both threshold and area, were both set to 2 - the lowest possible settings without triggering due to the normal light within the room. The drilling process was then carried out.

5.3 Basic Observations

The first stage of the analysis was conducted manually. Video numbers 1, 10, 20, 30, 40 and 50 were observed and compared both between the same parameter videos and those recorded for other parameters, so that any important commonalities or differences could be identified.

Commonalities observed for single parameter included:

- Thousands of rear particles were ejected over the course of each video
- Ejecta dispersion appearing through full 180 degrees relative to melt hole
- Approximately 6 µs until breakthrough
- Presence of exploding particles
- Presence of a central fast jet
- Fast, narrow stream of relatively small particles travelling downwards directly below the ejection point
- Larger, slower moving cloud of well dispersed particles moving through 180 degrees away from the ejection point

Differences observed included:

- Varying symmetry, left or right side of the screen may have more particles, or they may appear fairly balanced, between same parameter videos

- Relatively, many more particles were apparent in 500W and 1000W videos than were seen in higher power 1500W and 2000W videos for the same parameters
- The central fast jet is apparent in these videos, but not for those carried out with no assist gas for the same parameters.

5.4 Development and Application of the Particle Tracking Methods

The particle tracking method used within this work evolved throughout the project. To simplify the development of the program that was used to produce this work, three iterations will be referred to, the differences of which reflect the key changes that were made throughout the process. The first will be referred to as the original method, the second, the straight line method and the third as the predictive method (the most efficient method which was used to obtain the results presented in this thesis).

Each of the methods will be detailed as applied to the single set of 1000W results that are the basis of this chapter.

5.5 Particle Tracking Original Method - First Method

Only the first 50 videos will be used, the 51st is kept as a spare should any of the files become corrupted or lost. Once complete, the program can be run.

Each of the methods consists of three main input functions, the first of these is used for segmentation of the particles, the second for particle tracking and the third to produce graphical outputs.

The segmentation function requires multiple inputs for each set of videos, the first

of which are the start and finish frames. Six frames were tracked in total as this produced more correct tracks than five or seven when compared visually.

The particles are very close together and collectively produce a large amount of light through the earliest instances of breakthrough, a shown in Figure 5.16. This makes particle tracking very difficult. Therefore, the five frames chosen were taken 15 frames (2.42 ms) after breakthrough of the test piece. This allowed for a time soon after ejection, for all of the videos, before many particles had moved out of the image, but long enough afterwards so that the majority of particles were not so clustered together that they could not be individually distinguished.

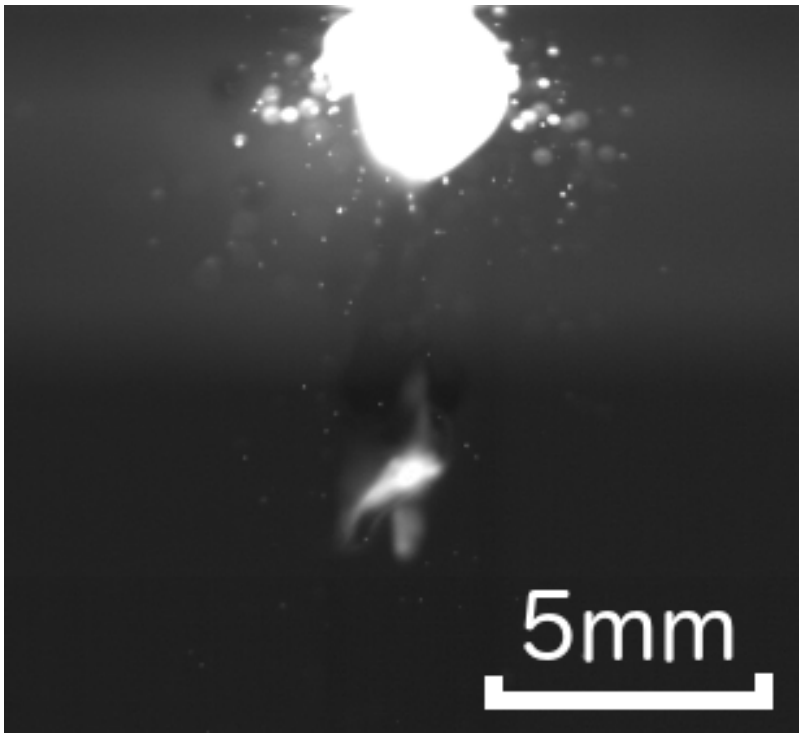


Figure 5.16: Early Ejection, 484 µs after breakthrough for the 6kW laser, 6300W laser power, 1Bar nitrogen assist gas, 10ms laser pulse, mild steel

As well as the tracking frames, the total frames used for background removal must be chosen. The first 50 frames were chosen for this set of results as they were proven to provide a sufficient amount of background removal whilst a higher number would

have slowed down the program.

The number of videos must also be input. For these results 50 were chosen as this was an achievable number to record for many different parameters during the duration of these tests, given the resources available. Comparisons of the particle dispersions of 50 videos are generally symmetric and uniform in shape between different parameters, unlike individual videos. This would suggest that 50 is a useful number of videos for providing accurate results. This is demonstrated in Figure 5.17.

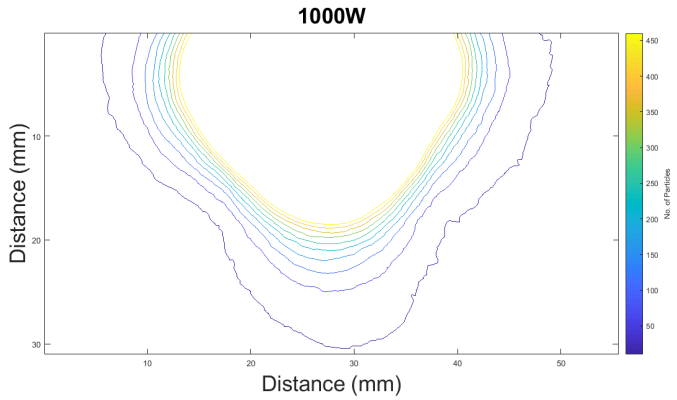


Figure 5.17: Contour plot showing a symmetrical particle cloud 968 µs after breakthrough for the 2kW Laser, 5Bar assist gas, 10ms pulse width, mild steel, 1000W laser power results

The laser power input is required as well as a skeleton filename for the file importation within this function in the form of " 'Steel_5Bar_1000W_10ms' num2str(NU, '%03d') '.cine"'. It is important that the skeleton filename matches the naming convention of the videos themselves except for the video number which is replaced by 'num2str(NU, '%03d')'. This allows the function to segment each of the videos in numerical order. Of course, it is also important to input the number of videos, as this will work alongside the naming convention.

The images used within this work were cropped along the horizontal at the point

of breakthrough in order to prevent any upward ejection or particle reflections from distorting the results. To do this the required image size and crop axis must be identified. In MATLAB this is done using the imcrop command, which requires four inputs in the form [xmin ymin width height], with the xmin and ymin being the upper-left-most value of the desired crop and the width and height being the size of the desired cropped image in pixels. For this set of results, [0 137 1285 800] was used to crop out all of the pixels above the y pixel values of 137.

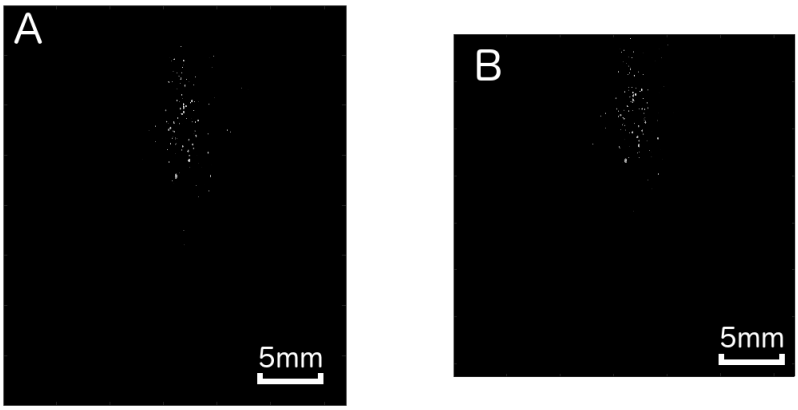


Figure 5.18: Comparison of non-cropped (A) and cropped image (B) for a 2kW Laser, 8Bar nitrogen assist gas, mild steel, 10ms pulse width, 500W laser power video

The final input requirements are dependent on the image set and must be checked. An image threshold must be established to segment the image. This value can be automatically calculated using the MATLAB 'graythresh' function, however, it does not always produce the optimal value, therefore it must either be edited or manually replaced by a number. For this set of results the 'graythresh' value is divided by three, because this produced an optimal result when testing using trial and error. This value can be checked by running a single video through the function for comparison with the original video. If the threshold is too high phantom particles will appear where they are not present in the original video, a level just below this is ideal to minimise particle loss due to thresholding.

Similarly, the background removal process must be checked and can be done so

quickly by running a single video to see if particle losses occur. If they do, these can be limited by scaling down the intensity of the median image, which is taken across all of the images in the data set and removed from each of the analysed frames. If the median image intensity is scaled down too much, background objects such as reflections may begin to appear as particles within the segmented results, therefore scaling down to a point just higher than this is optimal. For this set of results the intensity of the median image was scaled down to values between 0 and 30.

Once the inputs are completed the function can be run on all 50 videos. This will output 50 MATLAB data files, which are kilobytes in size, containing three variables named 'allCentroids', 'allDiameters' and 'n_frames'.

The first variable, 'allCentroids', is a cell array containing six cells. Each cell represents one of the analysed frames. Within each cell are two columns with a row for representing each particles. The first column contains the x-coordinates of each of the particles, whilst the second row contains the corresponding y-coordinates.

The second variable, 'allDiameters', similarly is a cell array containing 6 cells to represent each frame analysed. However, each cell contains only one column. Again each row represents a particle. The value contains a pixel measurement of the particle equivalent diameter. Equivalent diameter is an output of the MATLAB command 'regionprops', this calculates the equivalent diameter of a circle from its area using the formula sqrt(4*Area/pi). For this application this equivalent diameter allows for a more accurate measurement of diameter as it allows for values which do not have to be rounded to a whole pixel.

The final variable, 'n_frames', simply contains a single value, the number of frames.

Storing these relatively small data files allows for the tracking function to access the required information quickly and efficiently without having to access the large video files constantly. This is a particularly advantageous when tweaking the tracking

function to achieve the required results.

The original tracking function is the base for the other two methods. It makes use of the pre-assembled Simple Tracker [5.1] program created by Jean-Yves Tinevez, which is freely available on the MATLAB File Exchange [5.1]. The Simple Tracker [5.1] makes use of four functions, three of which are based on commonly used algorithms, the Hungarian Linker, Munkres and Nearest Neighbour algorithms. However, the Nearest Neighbour function is not used in this work.

Again inputs are required, such as the number of videos, the starting frame and the laser power. These inputs help the function to access the correct set of data files.

Critical inputs include the time between frames, 1/6200 seconds for this set of results and the calibration factor. The calibration must be calculated previously in metres per pixel. The Phantom Cine Viewer software was used to do this. The longest horizontal point distance between two, centimetre, graph squares in the image were identified and the number of squares between them summed, in this case eight, meaning a distance of 80mm, which was used for calibration.

The behaviour of the simple tracker program [5.1] has 'max_linking_distance', 'max_gap_closing' and 'debug' inputs. These can be tweaked to achieve the desired tracking from a specific set of results.

The input 'max_linking_distance' introduces a distance limit for which particles can be linked together in a track. For this set of results a value of 50 pixels was used. This means that any particles further than 50 pixels from another particle in the adjacent frame cannot be linked together. However a track can span a distance of more than 50 pixels across multiple frames. The value of 50 was chosen as it was large enough to allow majority of particles to be linked whilst eliminating erroneous results that were clearly not linked. In this data set it is possible that some of the

particles within the central fast jet may have travelled more than 50 pixels within a single frame, however, due to the large number of particles within the image it is near impossible for a particle to be correctly tracked over this distance and it is more likely that the high velocity particle will be linked with a different particle than itself in the adjacent frame, causing a false track.

The Simple Tracker program [5.1] has a gap closing function which can link tracks in which the particle is missing in one of the frames. The 'max_gap_closing' input allows the user to select a value for the number of frames up to which the same particle can be identified. The value of 0 was chosen for this set of results as it did not appear to cause an increase in erroneous results.

The 'debug' input simply provides some live printed feedback of the tracking process when turned on. For these results it was set to 'true'.

Once the inputs have been addressed, the function can be run. Three outputs are produced and stored as MATLAB data files, these are named 'Size_Diameters' and 'Track_Velocities'. 'Track_Velocities' contains a single row of velocity values measured in metres per second. Each velocity represents an individual track and is an average of the velocities calculated between each particle using speed = distance / time, where time is the time between frames, calculated from the frame rate as 1/6200 seconds.

'Size_Diameters' are simply the equivalent diameters which were recorded in the segmentation program, but for the first frame only. They are stored as a single row, with each column representing a different particle.

The final function which requires input is the graphical function. The graphical function is used as a means of creating useful graphical outputs for data analysis purposes, although it is of course possible to simply output the data from the stored files and analyse it using another program or method.

As with previous functions the graphical function requires the number of videos and the start frame value as inputs. It is then able to identify and access the required data files that were created with the tracking function.

The graphical function outputs two histogram types for comparison, one for velocity and one from size, it does this by processing the data from the 'Track_Velocities' variable and the 'Size_Diameters' variable.

Inputs are required to modify the axis values, graph sizes, bin sizes, axis and graph titles. It is important to note that the bin size of the particle diameter histogram is limited by the pixel size of the images as this will produce incomprehensible graphs.

5.6 Particle Tracking Straight Line Method - Second Method

The Straight Line Method represents an improved iteration of the Original Method and addresses some of its key issues. Mainly, the high number of erroneous tracks.

When compared to the live videos by eye, it is clear to see that many of the tracks are wrong, as shown in Figure 5.19A. The incorrect tracks are noticeably wrong because they tend to jump around in all directions, rather than following a straight line, as the majority of particles do in the videos. Because the Simple Tracker Program [5.1] was designed for simple tracking problems, it does not do well when tracking complex problems with numerous particles moving at various different velocities, such as those in the images provided.

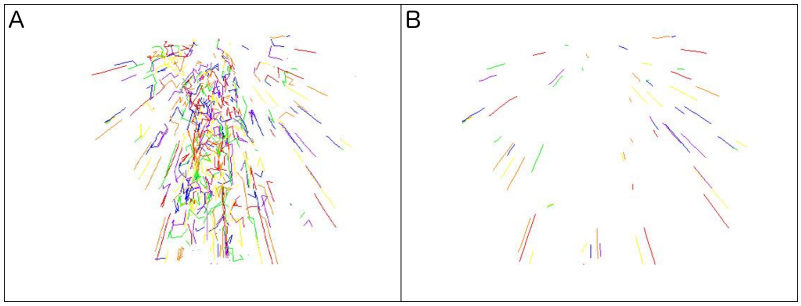


Figure 5.19: Comparison of original tracks (A) and same tracks after straight line method is applied (B) for a 2kW Laser, 2Bar nitrogen assist gas, mild steel, 10ms pulse width, 500W laser power video

However, it was found that when the obviously incorrect tracks were removed manually, one by one, that the results appeared to be useful in that most of the correct tracks appeared to match the particle behaviour in the videos exactly. It also seemed reasonable that the large number of videos, 50, would be adequate to allow for the lack of efficiency with this method. The tracking efficiency for this set of results is around 54%, however this varies with each set of results, as shown in Figure 6.6.

Manually removing large numbers of incorrect tracks proved to be very time consuming, greatly limiting the number of videos which could be analysed during this project and hence parameters. To resolve this issue, the straight line method was developed to automatically remove the incorrect tracks by taking advantage of their lack of uniform directionality, the results of which are shown in Figure 5.19B.

Data validation methods were included in this iteration of the program. Input prompts were used to ensure that the user had to manually input the number of videos, frame start, frame end and laser power, in order to sure that they were set each time the program was run.

Loops were also introduced for the laser power variable, enabling the MATLAB program to run more efficiently for multiple laser powers, meaning that multiple

videos for many different laser powers could be processed without the need for user intervention in between.

It was noticed that the centroids identified when using the Original Program weren't always accurate, with two or more particles that appeared to be touching each other in the binary images being assigned to a single centroid. In order to prevent this issue from occurring, the watershed algorithm was introduced. This allowed for the touching particles within any image to be separated by a very small line. This allowed the 'regionprops' command to correctly identify the centroid of each individual particle.

The implementation of this feature meant that a new input must be accounted for before running the function, the 'imhmin' value. If during test runs there were any problems due to the watershed function, regarding multiple particles being identified as single centroids or single particles being identified as multiple particles (oversegmentation), then the 'imhmin' value must be changed. The 'imhmin' value is the chosen threshold value, below which shallow minima are suppressed. 0.5 was chosen as the optimal value for this set of results.

The same outputs were given from the updated segmentation function as 'allCentroids', 'allDiameters' and 'n_frames'.

Prompts were also introduced to the tracking function for laser power, number of videos and frame start. As well as all of the inputs required for the Original Program, a gradient 'L' value input was introduced.

The tracking function of the straight line method eliminates incorrect, non-straight lines. To do this it measures the distance of the entire track and compares it to the distance between the first and final point of the track. As even correct tracks are not perfectly straight, the length between these distances are unlikely to be exactly the same. Therefore, some leeway must be allowed in the distance, enough that correct

tracks are not removed but the majority of incorrect tracks are. The difference in between lengths has been given as a multiple of the original track length as a product of the input value 'L', therefore an 'L' value of 0.1 means that the length of all tracks will be eliminated of which do not fall within the range of the length between their first and last point plus or minus ten percent.

The value of 'L' is very important in producing reliable results. To ensure an optimum value multiple tests were run. The highest value of 'L' possible with no clearly incorrect tracks was chosen as it is preferable to eliminate all incorrect tracks whilst sacrificing some correct tracks because although loss of correct tracks sacrifice efficiency, the presence of a high number of incorrect tracks invalidates the results. For this set of results, 0.015 was chosen as the 'L' value, meaning that tracks with lengths that varied by more than 1.5% the distance between their end to end length were eliminated. The number of particles successfully tracked using the straight line method is shown in Figure 5.20

Power (W)	Shots	Total number of particles analyzed	Particles analyzed per shot
Particle tracking 2 bar			
500	50	1418(11.4%)	28
1000	50	1416(18.7%)	28
1250	50	1104(21.2%)	22
1500	50	276(29.2%)	6
Particle tracking 5 bar			
500	50	1854(14.8%)	37
1000	50	1701(14.7%)	34
1250	50	1404(16.2%)	28
1500	50	596(25.9%)	12

Figure 5.20: Straight Line Tracking Results

Originally, the straight line method was developed to use gradient as a comparison within tracks rather than length, however, 'L' was eventually chosen as it provided

simpler, more efficient programming.

Additional to the Original Method, which produced the outputs, 'Track_Velocities' and 'Size_Diameters', the Straight Line Method produced the outputs 'L' and 'Size_Velocities'. 'L' of course referenced the length value previously discussed. Unlike 'Track_Velocities' which includes all of the velocities for each track identified, 'Size_Velocities' includes only the tracks for the first frame (as 'Size_Diameters' does for the diameter values), also, these velocities are stored as a single row, in which each column represents a particle. Each numbered column corresponds directly to the numbered column within the 'Size_Diameters' variable. This is important as it allows for velocity and size data to be paired together for further analysis.

As with the other functions, the graphical function was updated to include prompts for the frame start value, the number of videos as well as the 'L' value.

The 'Size_Velocities' data presented an opportunity to present the combined size and velocity data together. To do this momentum plots were produced.

The Straight Line Method graphical function also included other graphical inputs so that the data could be visualised in a variety of ways. These included scatter graphs, momentum and kinetic energy

5.7 Particle Tracking Predictive Method - Third Method

Although the Straight Line Method proved useful for producing reliable useful results, it was very inefficient. This meant that many more videos had to be recorded than were necessary and particles in the most clustered areas of the images, towards the middle, were repeatedly not being tracked. This meant that the data results provided did not fairly reflect the properties of all of the rear ejected particles.

To resolve this, the Predictive Method was produced. The Simple Tracker [5.1] program tracks particles by looking for those closest to it in subsequent frames. With the Predictive Method, the Simple Tracker [5.1] was updated to predict the position of the particle in subsequent frames and then to search for the particles nearest to that point, as shown in Figure 5.21.

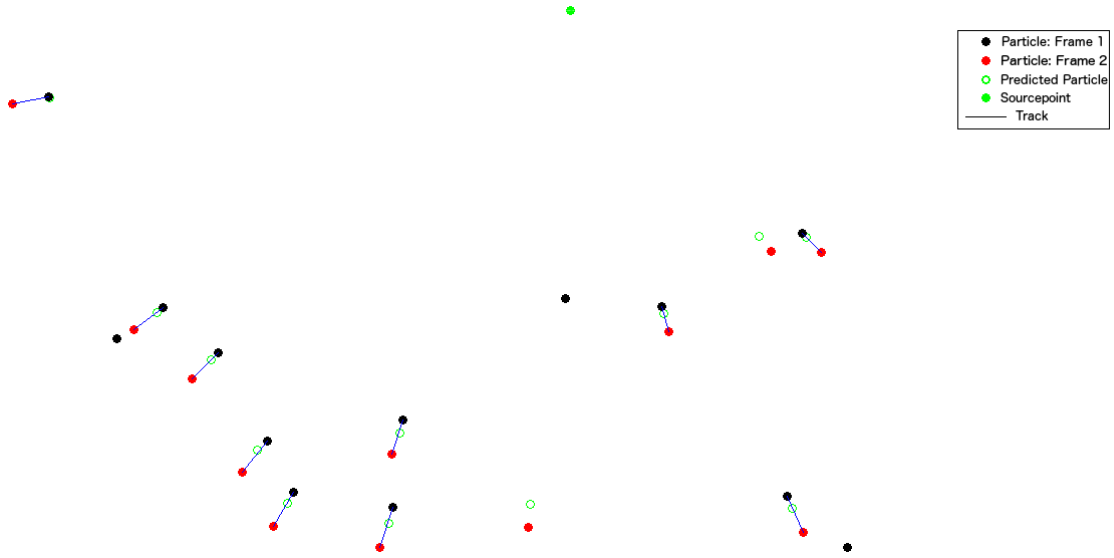


Figure 5.21: Tracks created between centroids of subsequent frames using predicted particle locations - 500W Laser Power, 8Bar Nitrogen Assist Gas, Mild Steel

To predict the particle, the program calculates the vector between the source point (point of breakthrough) and uses the length and angle of this vector to predict the location of the particle in subsequent frames. Originally, this method was then combined with the Simple Tracker [5.1] method of identifying the particle, most likely to be the same by using the Hungarian Algorithm with reference to the predicted point.

Although this method vastly improved the results, it was further improved with the use of a bounding box. Using geometric calculations, the Predictive Method program creates a rectangular box around each predicted particle, along the direction of the line formed between the predicted particle and source point as shown in

Figure 5.22.

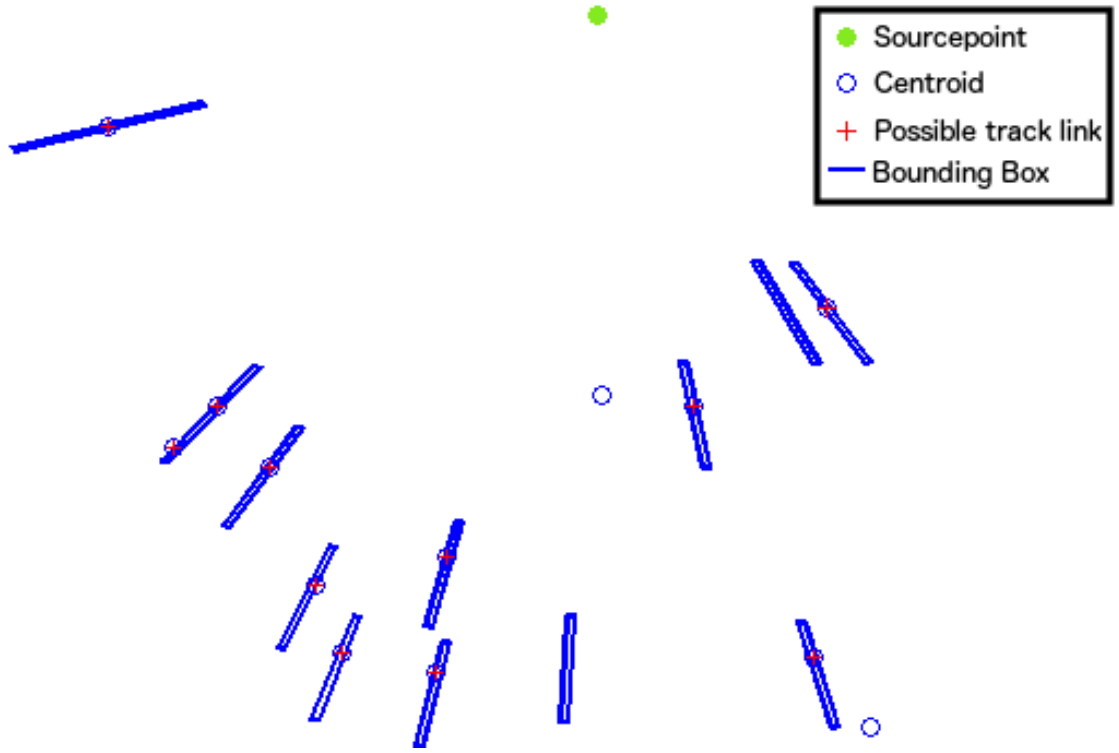


Figure 5.22: Shows bounding boxes with a length of 50 pixels, used to limit particles which can be potentially linked to a predicted particle location - 500W Laser Power, 8Bar Nitrogen Assist Gas, Mild Steel

The size of this box is predetermined by the user such that all correct particles fall within it, whilst the majority of incorrect particles fall outside of it. The Hungarian Linker function is then only able to search for particles which fall within the specific box. Due to this, the box technique not only dramatically decreases the likelihood of an incorrect track, but it also vastly improves the efficiency of the program and hence the time taken for it to run.

To increase the accuracy of the Predictive Method, it is possible to analyse only two frames at a time. This greatly improves the speed at which the program can run and decreases the likelihood for error to occur within a track.

The program layout of the Predictive Method differs in that it combines both the segmentation and the tracking functions together. The prompting inputs are removed in favour of a 'uigetfile' MATLAB function which allows the user to select the appropriate videos manually by selecting them within a pop up window. This makes the program more user-friendly as the user does not have to respond to prompts with an exact answer.

As well as file selection, the inputs required are frame rate in seconds, start frame, background removal frame and the crop area. The 'max_linking_distance', 'max_gap_closing' and 'debug' are no longer important but are set to 50, 3 and true as default.

New inputs require a six digit tag which is included in the output filenames, making different sets of results easy to identify. For this set of results the date of the videos is used in six digit format in the order of day-month-year.

For the Predictive Method, a calibration file is required, rather than a single calibration factor. This is a standardised MATLAB file which must contain four columns, the first column containing the filename of each video in chronological order. The second column must contain the calibration factor in mm/pixel (as this is the form given in the Phantom Cine Viewer software), the value can be the same for all videos if the camera has not been removed. However, this allows for the opportunity for the calibration factor to change easily through a single set of results should the camera be moved and need to be recalibrated during a set of experiments. The third and fourth columns display the source point X and Y coordinates respectively. The source point is the exact point of breakthrough and can be identified when viewing the videos in the Phantom Cine Viewer software. This value is very important to the Predictive Method, therefore the source point should ideally be checked and recorded for each video, as the camera in the chosen set-up has a tendency to move very slightly throughout long experiments due to gravity etc.

The calibration file must be named with the six digit tag in the format '000000_CALFILE'

and stored in the same folder as the MATLAB function files.

Once all of the inputs are ready, the function can be run in order to process the appropriate images, segment the particles, identify the centroids and diameters, track the particles through the updated Simple Tracker [5.1] function, calculate the velocities of each track through a new velocity calculator function and produce the required output data files.

As well as 'Size_Diameters', 'Size_Velocities' and 'Track_Velocities', the source point data is stored as well as the X-Y-coordinates for each particle centroid for both frames. As the centroids are the most important output of raw data, this means that other methods of analysis or tracking can be carried out without having to segment the data again.

The updated graphical output function again makes use of user prompts and requires the inputs of, the six digit tag, the calibration file - which must be present within the folder containing the MATLAB file, the density of the material in $kg.m^3$ for volume calculations, the gas pressure used in Bar, the frame start number, the pulse width, the number of videos which the user would like to include and the material used.

Once the inputs have been entered, the function processes the data from the pre-created MATLAB file. With the use of a new 'VelocitySizeReader' function, it is easy for the user to select for which laser powers they would like to compare, by running only the sections that they require - previous iterations required that all powers were run even if the data was non-existent for certain powers.

In the same way, a new function has been created for each output graph. This means that the user can pick and choose which graphs to output by running the required sections.

As well as the previously included graphs, velocity histograms, size histograms, 3D histograms between size, velocity and particle number, scatter graphs, kinetic energy and momentum histograms, others are included. These include a track/particle counter which makes it easier for the user to identify the number or particles and tracks identified, as well as the percentage difference between the two - useful for highlighting the tracking efficiency. This data is also available on a graph between track and particle numbers.

A stats calculator program was also developed, which outputs an excel sheet containing the mean, median, standard deviation, 25th and 75th percentile values for both particle velocity and particle diameter for each set of videos.

A contour plot option is also included, using the recorded X-Y-coordinate values. The contour plot is useful for identifying the areas of particle dispersion at certain time points after breakthrough, when used in combination with multiple videos. This can provide data on the outer ranges of particle dispersion, as well as the most dense regions, proving useful for analysis of the particle dispersion cloud with time.

References

[5.1] J.-Y. Tinevez, "Simple Tracker - copyright see Appendix Section 12.1," 2018. [Online]. Available: https://www.mathworks.com/matlabcentral/fileexchange/34040-simple-tracker

6

Rear Ejecta Particle Basic Observations, Particle Number and Tracking Efficiency

This section presents the analysis and results for the basic observations, particle number and tracking efficiency which are taken from the recorded videos.

* * *

6.1 High-speed Filming - Basic Observations

A vast quantity of information can be stored within an image. The high-speed filming processes used within this work allow for 6200 images to be created during every second of filming time. Many of the image analysis and processing techniques used within this work are aimed towards obtaining quantised numerical data so that it can be analysed using graphical and statistical techniques. However, although these techniques are very useful, because they are so specific they can often miss out on very important data within the images. For this reason, the images were first analysed manually, one by one, to see what trends and comparisons could be drawn

by eye between the different parameters.

The following general observations were made across all of the different laser set ups for different parameters:

- Exploding particles:

  In these images, the presence of a number of exploding particles were observed through all parameters, this is a previously undocumented phenomenon in rear melt ejection. This is important, not only because it provides an insight into the melt ejection process, but also because it can complicate particle tracking.

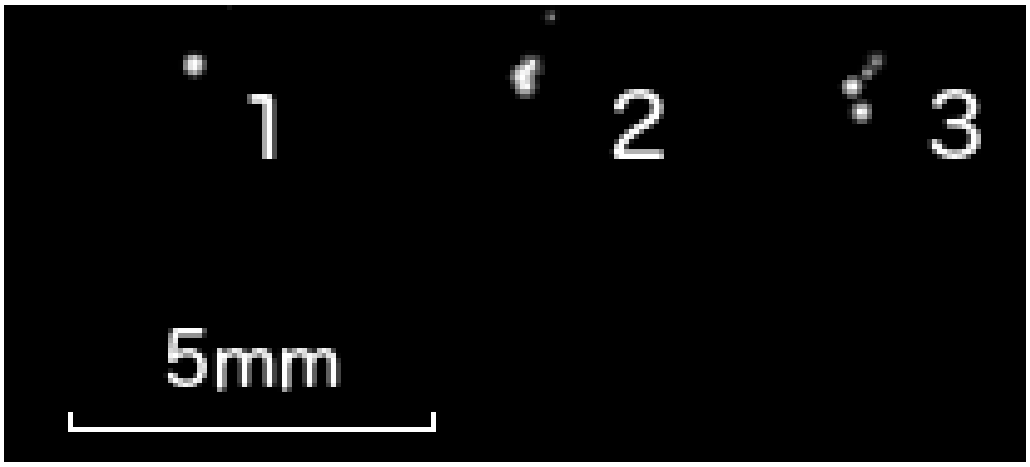


Figure 6.1: An Exploding Particle shown through 3 frames (483 µs - 2kW Laser, 1000W Laser Power, 2Bar Nitrogen Assist Gas

- Central Fast Jet:

  A central fast jet was observed in experiments with assist gas, but not those without. This is a phenomenon in which some of the ejected particles are ejected at a much higher velocity than those around them, directly beneath the exit hole, as opposed to the majority of those which are more widely dispersed and travelling much slower.

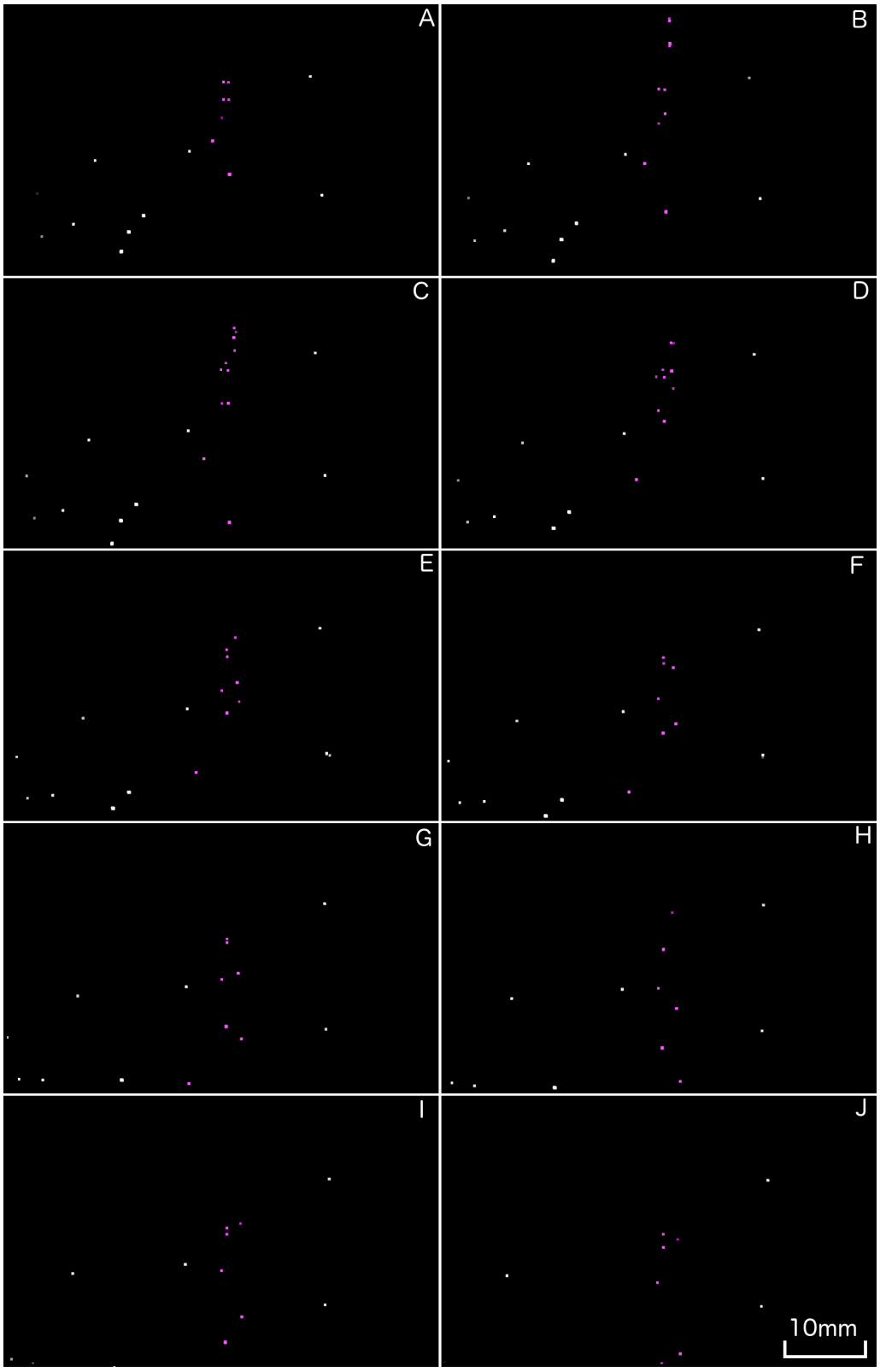


Figure 6.2: Presence of a Central Fast Jet, Highlighted in Red - 6kW Laser, 6300W, 5Bar Nitrogen Assist Gas, 10ms Pulse Width

- Number of Particles:

  Other clear findings from observation of the images include trends of particle numbers in relation to laser power. Although exact particle numbers were not determined by clear observation, there was a clear difference in particle numbers for certain parameters. Trends like this are important because as well as providing a quick understanding of the importance of different variables, they help to validate the tracking findings.

- Velocity Measurements:

  For these videos, some velocity measurements were taken. To do this the inbuilt Phantom measurement software tools were used. The software allows the user to click on a beginning and end point of a particle track, therefore a start point is selected in one frame, then an end point is selected at a later frame. The software then provides a distance in metres, which can be used along with the time, which is calculated from the number of frames, by the user to determine the velocity of a particle. The velocity of random particles from the widely dispersed particle cloud were manually calculated and averaged for comparison with random particle velocities from the central fast jet, which were also averaged for a range of parameters.

  The approximate velocity of particles in the particle cloud were around 5m/s, whilst the approximate velocity of particles in the central fast jet were in excess of 30m/s. This data provides a useful comparison between the velocities of the two particle types and numbers that can be used to validate results from the particle tracking method.

6.2 Drilling Parameters

2kW Laser, 10ms Pulse Width

Laser Power	Assist Gas Pressure and Material								
	1mm Material Thickness						2mm Material Thickness		
	2Bar - MS	5Bar - MS	8Bar - MS	12Bar - MS	8Bar - Ti	12Bar - Ti	8Bar - Al	12Bar - Al	2Bar - MS
500W	X	X	X	X	O	X	O	O	N\A
1000W	X	X	X	X	X	X	O	O	X
1250W	X	X	X	X	X	X	O	O	N\A
1500W	X	X	X	X	X	X	O	O	N\A
2000W	N\A	X	X	X	X	X	X	X	N\A

X - Successful Breakthrough O - No Breakthrough N/A - Test not attempted

6kW Laser, Mild Steel

Laser Power	Assist Gas Pressure and Pulse Width					
	1mm Material Thickness					
	0Bar - 10ms	0Bar - 5ms	0Bar - 2ms	1Bar - 10ms	2Bar - 10ms	5Bar - 10ms
500W	O	O	O	O	O	O
1000W	X	O	O	O	O	O
1250W	X	O	O	O	O	O
1500W	X	O	O	X	O	O
2000W	X	O	O	X	X	O
3000W	X	O	O	X	X	O
4000W	X	X	O	X	X	O
5000W	X	X	O	X	X	X
6000W	X	X	O	X	X	X
6300W	N\A	X	O	X	X	X

X - Successful Breakthrough O - No Breakthrough N/A - Test not attempted

Figure 6.3: Laser Drilling Parameters

Figure 6.3 shows all of the laser parameters tested. For all of the tests where breakthrough was successful, fifty high-speed videos were recorded and particle tracking methods were carried out for each parameter.

6.3 Number of Particles

This section shows the results for the particle numbers, as measured from the particle tracking method. The data represents the cumulative number of particles through 20 frames of ejection and how this number varies with a change of process parameters.

6.3.1 2kW Laser

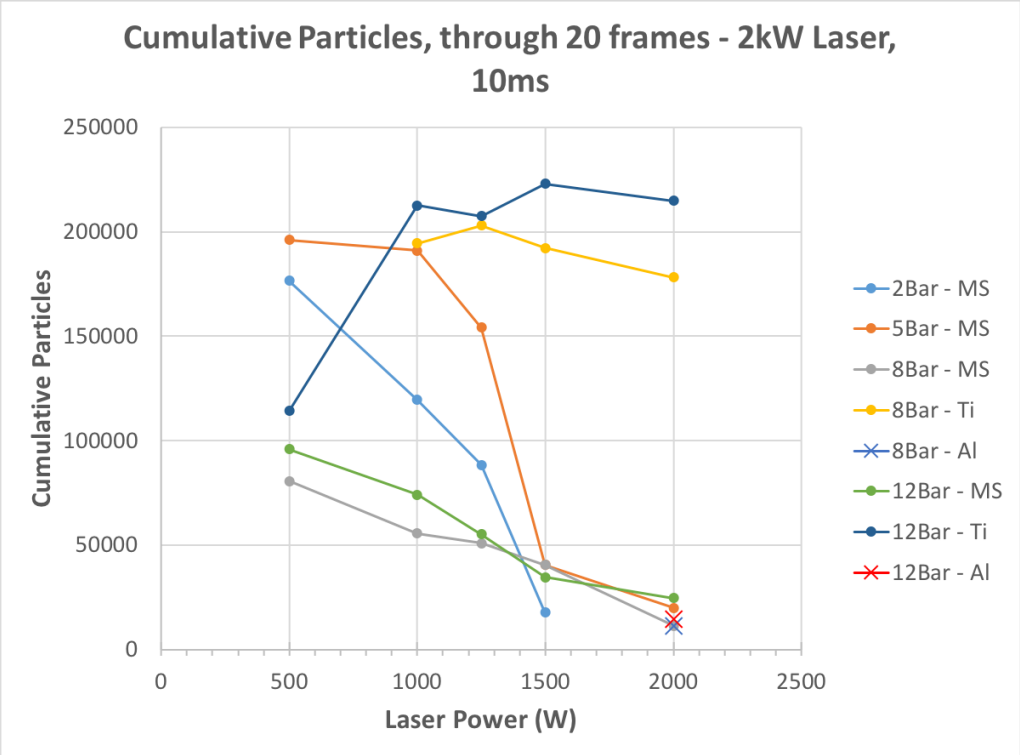


Figure 6.4: Cumulative Particle Numbers over 50 videos - 2kW Laser, 10ms

Figure 6.4 shows a general decrease in cumulative particle number as laser power increases for the mild steel results. This pattern is not observed for the titanium results, where there is little change in cumulative particle number with power except for between 500W and 1000W for the 12Bar tests.

6.3.2 6kW Laser

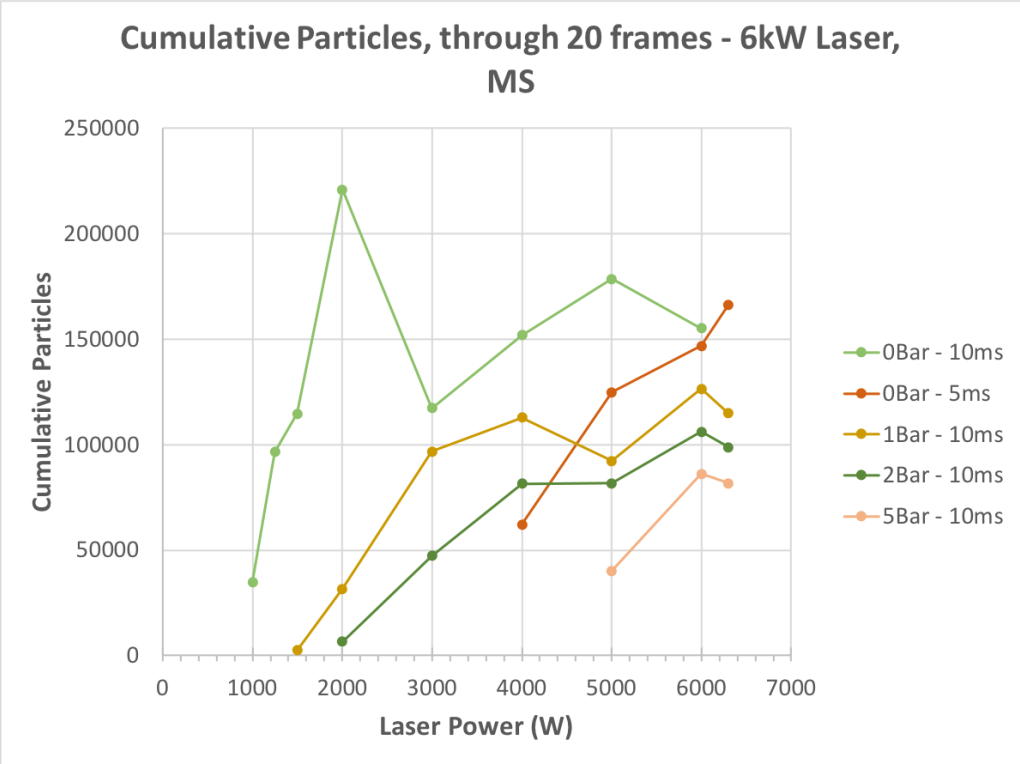


Figure 6.5: Cumulative Particle Numbers over 50 videos - 6kW Laser, Mild Steel, 10ms

Figure 6.4 shows that for the 2kW laser results, cumulative number of particles generally increases with laser power increase. In general, the rate of particle number is shown to decrease as laser power increases further. However, particle number does slightly decrease between 6000 - 6300W laser power for all of the tests, except for the 5ms pulse width test. An anomaly is shown at 2000W for the no assist gas test with a 10ms pulse width, where particle number dramatically increases by around 100%.

It is shown that the cumulative particle number and its relation to power differs greatly between the 2kW and the 6kW laser. The 2kW laser shows a general decrease in cumulative particle number whereas the 6kW laser shows a general increase.

6.4 Tracking Efficiency

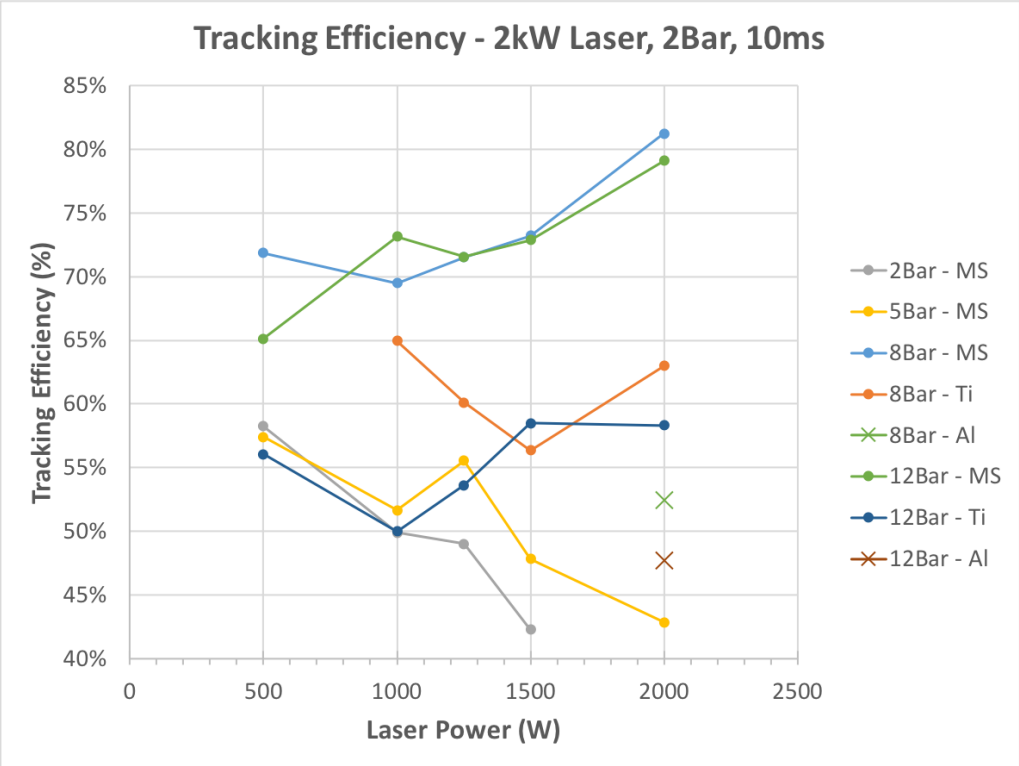


Figure 6.6: Tracking Efficiency over 50 videos - 2kW Laser, 10ms Pulse Width

Figure 6.6 shows that tracking efficiency varies between 40 - 82.5% for the 2kW laser results. The 8Bar and 12Bar mild steel results are shown to have the highest tracking efficiency, and this efficiency tends to increase as laser power increases. The opposite is shown for the 2Bar and 5Bar mild steel results. No clear pattern is shown for the titanium results, which vary between 50 - 65% efficiency.

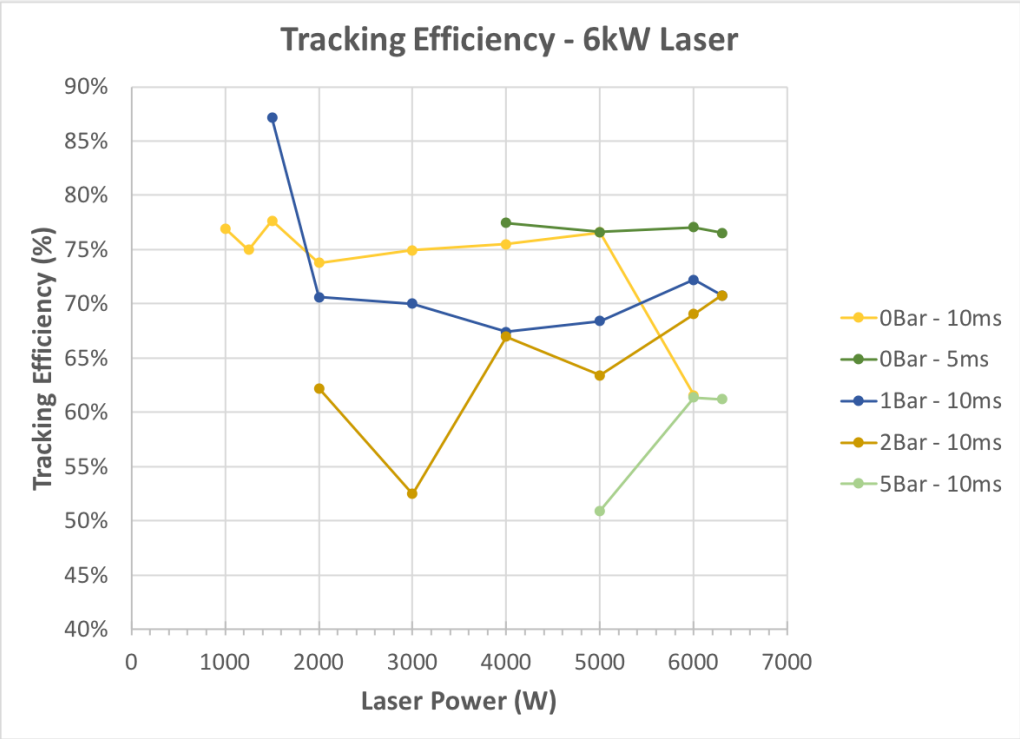


Figure 6.7: Tracking Efficiency over 50 videos - 6kW Laser, Mild Steel, 10ms Pulse Width

Figure 6.7 shows that tracking efficiency is between 50 - 87.5% for the 6kW laser tests. The no assist gas tests are shown to have higher tracking efficiencies than the assist gas tests in general.

References

7

Rear Ejecta Particle Velocity, Size and Momentum

This section provides the results and analysis of the particle velocity, size and momentum results from the high speed filming tests.

* * *

7.1 Velocity Results

7.1.1 Mean Particle Velocities over 20 frames

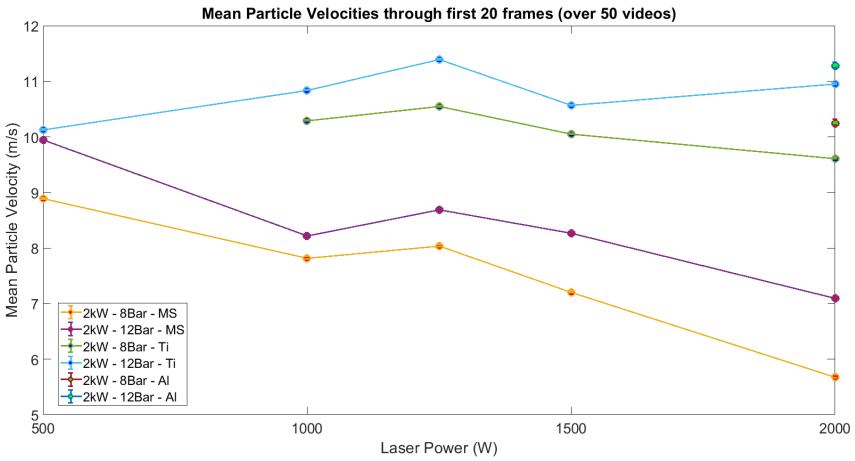


Figure 7.1: Mean Particle Velocities over 20 frames (for 50 videos each) - 2kW Laser, 10ms Pulse Width - 105mm Camera Lens

- Figure 7.1 shows that for mild steel mean particle velocity generally decreases with laser power, with a small increase in mean particle velocity between 1000W and 1250W.

- The same increase in mean particle velocity is seen between 1000W and 1250W for titanium, however no general decrease with laser power or other clear trend is observed.

- For mild steel, a difference of up to $3ms^{-1}$ in mean particle velocity is observed for different powers for the same assist gas pressure. For titanium however, a maximum difference of only $1.5ms^{-1}$ is observed.

- A clear relationship between assist gas pressure and mean particle velocity is shown in fig. 7.1. For all materials and powers shown, a 12Bar assist gas pressure produces a higher mean particle velocity than an 8Bar assist gas pressure. This difference ranges from 0.5 - $1.25ms^{-1}$.

- Error bars are presented in fig. 7.1, however, they are very small and difficult to see as the error is so low for all results.

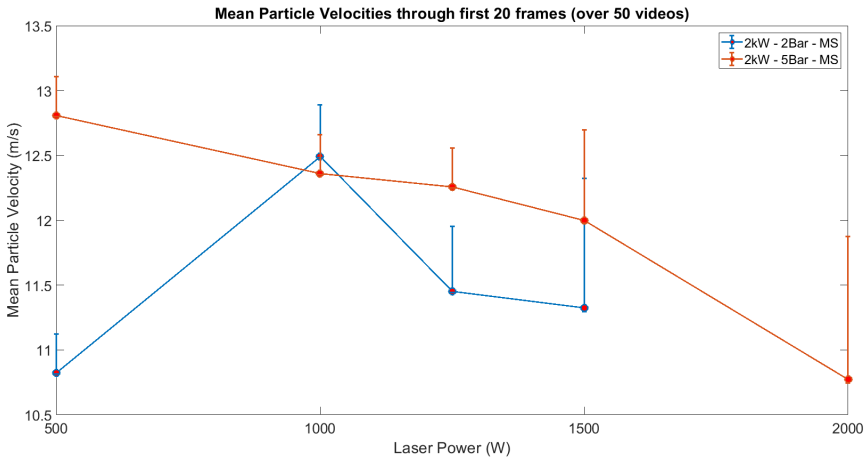


Figure 7.2: Mean Particle Velocities over 20 frames (for 50 videos each) - 2kW Laser, 10ms Pulse Width - 60mm Camera Lens

- In fig. 7.2 a consistent decrease of mean particle velocity with laser power is shown as power increases for a 5Bar assist gas pressure. A clear pattern is not observed for a 2Bar assist gas.

- For the parameters shown in fig. 7.2, a 5Bar assist gas is generally shown to produce a higher mean particle velocity than a 2Bar assist gas for like parameters. Although, this is not true at 1000W laser power, at which a 2Bar assist gas produces a mean particle velocity around 0.1ms^{-1} higher than a 5Bar assist gas. However, it must be noted that these values fall within the error bars shown and therefore and as such the result can be disregarded as an anomaly.

- A maximum difference of 3ms^{-1} is shown between like assist gas pressures for differences in laser power.

- A difference of between 0.1 - 2ms^{-1} is observed between like powers for different assist gas pressures in fig. 7.2.

- The error bars shown for fig. 7.2 are one sided due to the effect of the focal depth on the high speed filming set-up which could result in particles having a higher velocity than that measured, but not lower. The relatively large difference in comparison to the other results is due to the difference in filming set-up and hence these results have been presented separately.

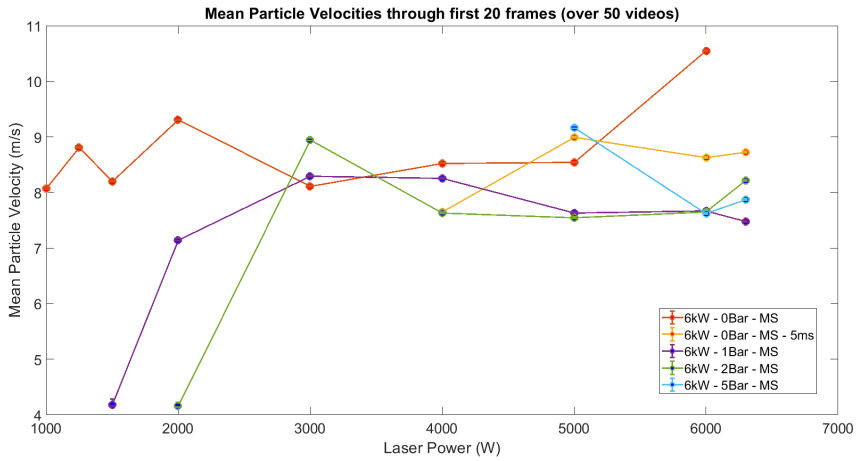


Figure 7.3: Mean Particle Velocities over 20 frames (for 50 videos each) - 6kW Laser, 10ms Pulse Width (5ms pulse width where specified) - 105mm Camera Lens

- Figure 7.3 shows a relatively large increase in mean particle velocity by up to 5ms^{-1} in results for 1Bar and 2Bar assist gas pressures between breakthrough and 3000W laser power. This rapid increase is followed by a general slight decrease in mean particle velocity.

- For the other assist gas pressures shown in fig. 7.3, no clear pattern with laser power is shown, with a maximum difference of 2.5ms^{-1} between like assist gas pressure mean particle velocities.

- Generally, fig. 7.3 shows that mean particle velocity shows little variation across all assist gas pressures and powers with most falling between 7.5 - 9.5ms^{-1}.

- For the results shown, no loss in mean particle velocity is shown, as might be

expected, when no assist gas is present.

- Error bars are presented in fig. 7.3, however, they are very small and difficult to see as the error is so low for all results.

7.1.2 Particle Velocity Distribution Histogram - Particles combined for all parameters

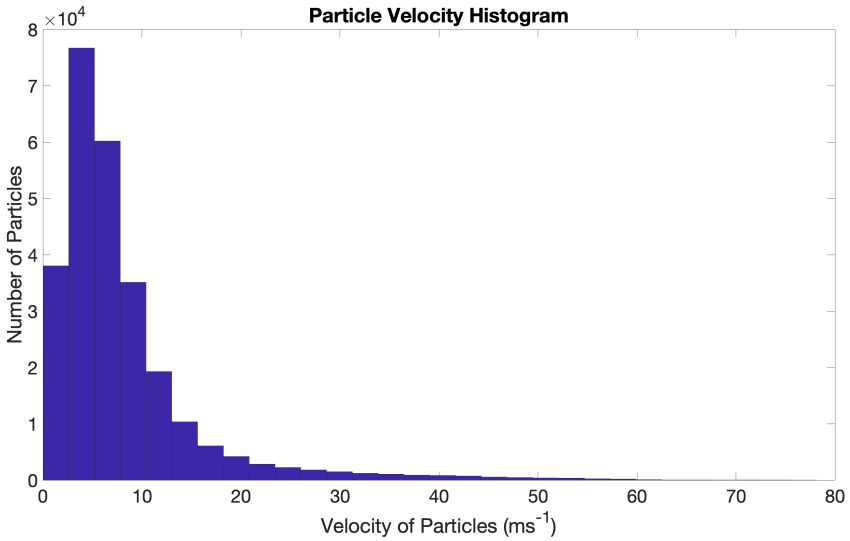


Figure 7.4: Particle Velocities over 50 videos - combined results for all parameters

- The histogram shown in fig. 7.4 shows the particle velocity distribution combined for all parameters tested. When compared separately, a similar distribution is shown across all parameters.

- Figure 7.4 shows a doubling in particle number from around 2 - 4ms^{-1} particle velocity

- An exponential decay is shown in particle velocity from around 4 - 60ms^{-1}

- The largest particle velocities are shown to be just under 80ms^{-1}

7.2 Diameter Results

7.2.1 Mean Particle Diameters over 20 frames

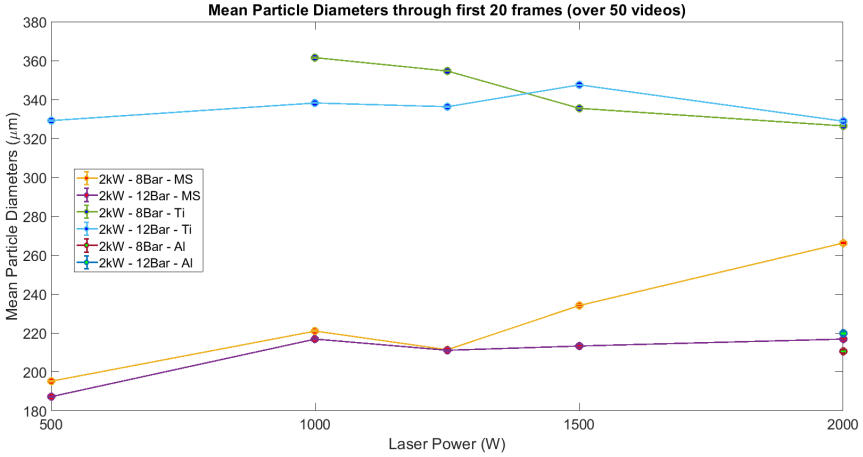


Figure 7.5: Mean Particle Diameters over 20 frames (for 50 videos each) - 2kW Laser, 10ms Pulse Width, Mild Steel - 105mm Camera Lens

- In Figure 7.5, no clear trend is apparent for laser power in relation to particle size, however a maximum difference of 60 µm in mean particle diameter is shown between different powers for the same assist gas pressures.

- In Figure 7.5 most mean particle diameters are shown to be within 50 µm of each other for titanium at 8Bar and 12Bar assist gas pressures, the same is true for mild steel. However, mean particle diameter is shown to be 50 - 150 µm higher for titanium than mild steel and aluminium for the same laser power. This suggests that for the parameters shown that material type is strongly related to particle size, whilst assist gas pressure is of less significance.

- For the results shown for mild steel with the 2kW laser, it is clear that a lower assist gas pressure produces a higher particle diameter. However, no clear trend is observed for the titanium results in this regard. Also, for the single aluminium parameter shown, the opposite to mild steel is apparent, as

a higher pressure produces a larger particle diameter.

- Diameters are shown to be within 10 µm for 8Bar and 12Bar aluminium.
- Error bars are presented in Figure 7.1, however, they are very small and difficult to see as the error is so low for all results.

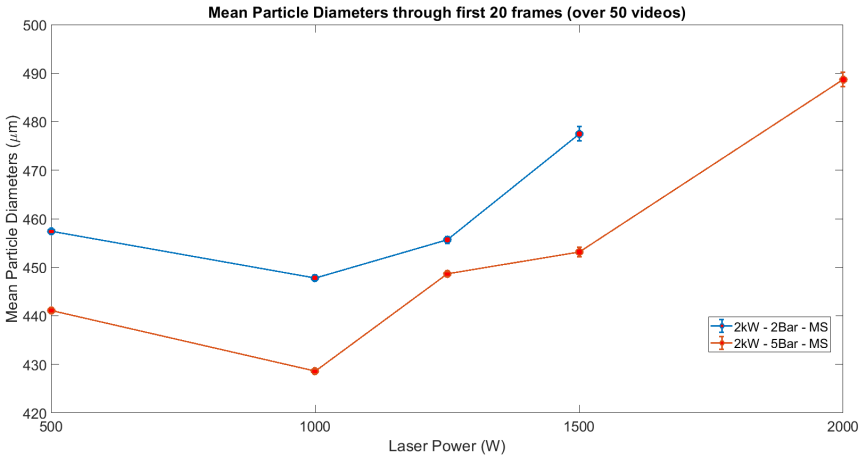


Figure 7.6: Mean Particle Diameters over 20 frames (for 50 videos each) - 2kW Laser, 10ms Pulse Width, Mild Steel - 60mm Camera Lens

- Figure 7.6 shows that mean particle diameter decreases from 500W to 1000W before continually increasing up to 2000W for both 5Bar and 1500W for 2Bar assist gas pressures.
- A relatively small difference of 10 - 20 µm is seen for the results given between 2Bar and 5Bar assist gas pressures.
- A maximum difference of 60 µm is apparent across all parameters shown in Figure 7.6 .
- A lower assist gas pressure of 2Bar is shown to produce larger particle diameters for the given parameters.
- Error bars are presented in Figure 7.1, however, they are very small and diffi-

cult to see as the error is so low for all results.

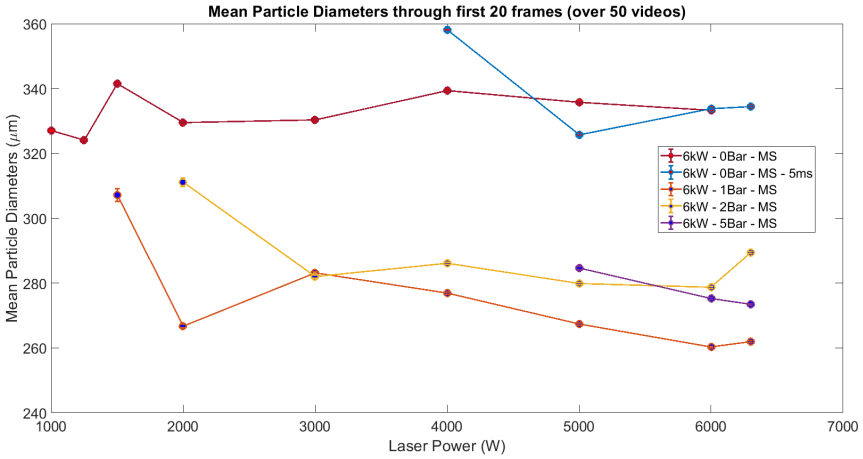


Figure 7.7: Mean Particle Diameters over 20 frames (for 50 videos each) - 6kW Laser, 10ms Pulse Width (5ms pulse width where specified), Mild Steel - 105mm Camera Lens

- Figure 7.7 shows a clear difference in mean particle diameter for no assist gas in comparison to a 1Bar, 2Bar or 5Bar assist gas, with a difference between 20 - 100 µm in mean particle size.

- Mean particle diameters appear to be noticeably higher for breakthrough powers, by up to 30 µm, for all results shown in Figure 7.7, except for no assist gas with a 10ms pulse width.

- Disregarding initial breakthrough powers, mean particle diameter varies by up to 20 µm with laser power for all 6kW laser results.

- No clear trends are shown for the 6kW laser mean particle diameter results in terms of power, other than for the breakthrough powers.

7.2.2 Particle Diameter Distribution Histogram - Particles combined for all parameters

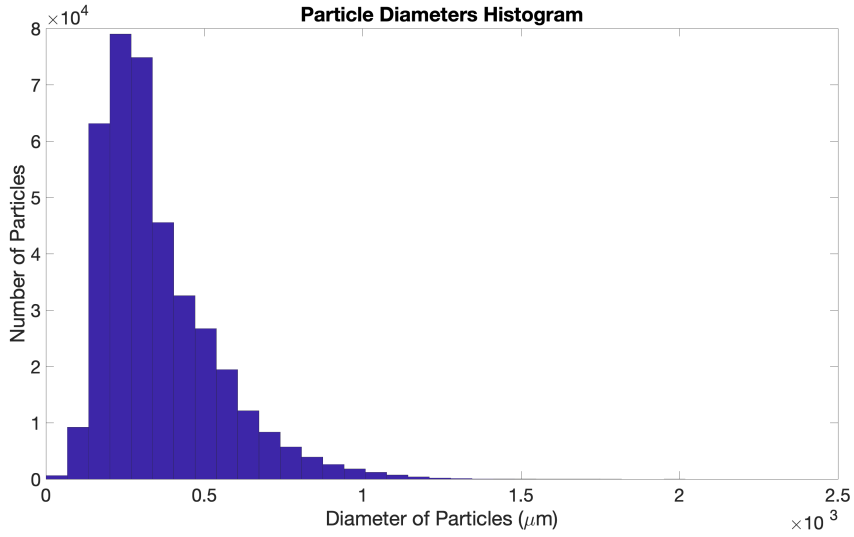


Figure 7.8: Particle Diameters over 50 videos - combined results for all parameters

- Figure 7.8 shows the particle diameter distribution combined for all parameters tested. On comparison, the same distribution is also shown across all parameters individually.
- Figure 7.8 shows rapid increase in particle diameter between 120 - 200 µm.
- An exponential decay is shown in particle diameter from 200 µm to 700 µm.
- The largest particle diameters are shown to be around 1000 µm
- Error bars are presented in Figure 7.1, however, they are very small and difficult to see as the error is so low for all results.

7.3 Momentum Results

Particle momentum in this section is derived from the particle diameter and velocity. The particles are assumed to be spherical to allow for calculation of the particle volume. The mass is calculated using the density of the materials and the calculated volume.

7.3.1 Mean Particle Momentum over 20 frames

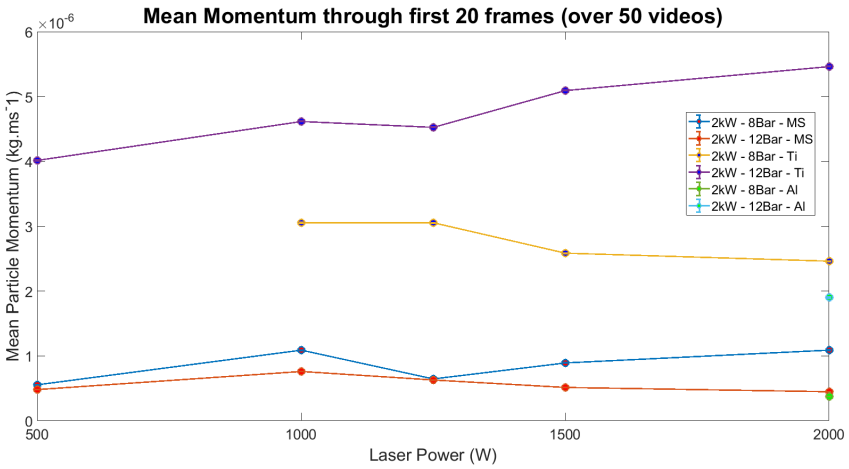


Figure 7.9: Particle Momentum Histograms over 50 videos - 2kW Laser - 105mm Camera Lens

- Figure 7.9 shows a relatively small variation in mean particle momentum between all laser powers - maximum variation is around $3x10^{-6}$ kg.ms^{-1}.

- A general increase in mean particle momentum is shown for 12Bar titanium with laser power of up to $1.5x10^{-6}$ kg.ms^{-1}. However, no clear trend with mean particle momentum is shown for laser power for any other parameter in Figure 7.9.

- Figure 7.9 clearly shows that mean particle momentum is higher for a 12Bar assist gas than an 8Bar assist gas for titanium and aluminium for all laser powers tested, with a difference of 1 - $3x10^{-6}$ kg.ms^{-1}. However, 8Bar is shown

to have a higher difference than 12Bar for mild steel, although only for a maximum of 0.5x10^{-6} kg.ms^{-1}.

- Titanium is shown to have a significantly larger mean particle momentum than mild steel for like assist gas pressures and laser powers, with a maximum difference of 4.5x10^{-6} kg.ms^{-1} for the results shown. For the few results shown, 8Bar aluminium is shown to have a very similar mean particle momentum to mild steel, whilst for 12Bar the mean particle momentum is around 1x10^{-6} kg.ms^{-1} higher than all 12Bar mild steel results.

- Error bars are presented in Figure 7.3, however, they are very small and difficult to see as the error is so low for all results.

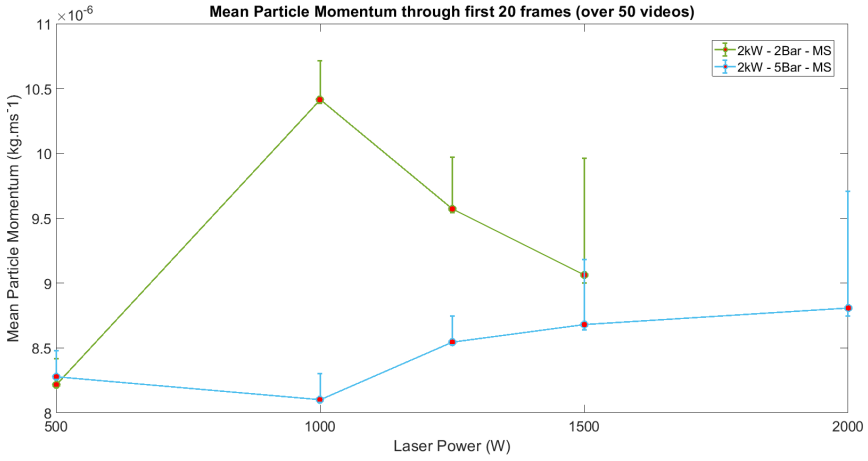


Figure 7.10: Particle Momentum Histograms over 50 videos - 2kW Laser - 60mm Camera Lens

- Figure 7.10 shows no clear pattern of mean particle momentum change with laser power. A maximum difference of mean particle momentum for different laser powers with with like assist gas for the parameters shown is 2x10^{-6} kg.ms^{-1}.

- For the results shown in Figure 7.10, in general, a 2Bar assist gas produces a higher mean particle momentum than a 5Bar assist gas for mild steel. A

maximum difference is shown of 2x10^{-6} kg.ms^{-1}.

Error bars are presented in Figure 7.3, however, they are very small and difficult to see as the error is so low for all results.

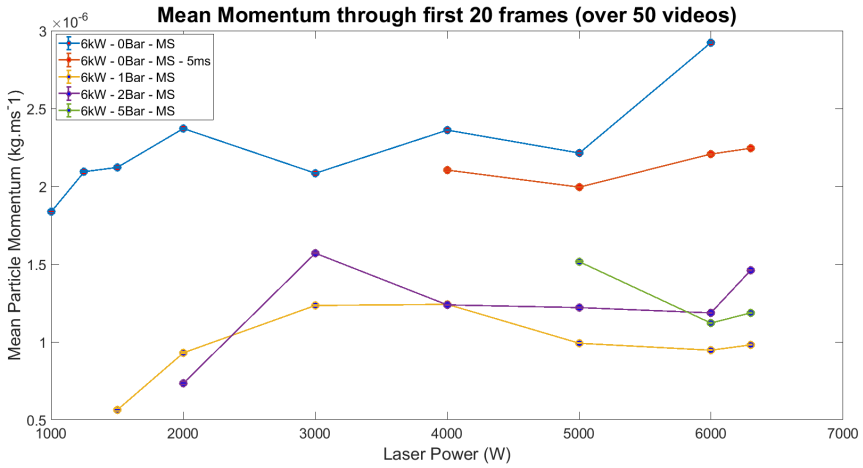


Figure 7.11: Particle Momentum Histograms over 50 videos - 6kW Laser - 105mm Camera Lens

- Figure 7.11 shows no clear pattern of mean particle momentum change with laser power. A maximum difference of mean particle momentum for different laser powers with like parameters is 1x10^{-6}kg.ms^{-1}.
- The results in Figure 7.11 show that mean particle momentum significantly higher for no assist gas tests than 1Bar, 2Bar and 5Bar assist gas pressures. A difference of 0.5 - 2x10^{-6}kg.ms^{-1} is shown for like powers.
- Mean particle momentum is shown to be lower for a 5ms pulse width than a 10ms pulse width for the parameters shown with like for like laser power. A difference of 0.25 - 1x10^{-6}kg.ms^{-1} is shown.
- Mean particle momentum is noticeably lower that for any other laser power for breakthrough powers for 1Bar, 2Bar and no assist gas tests. A difference is shown between 0.5 - 1x10^{-6}kg.ms^{-1} to all other laser powers with the same assist gas pressure.

- Error bars are presented in Figure 7.3, however, they are very small and difficult to see as the error is so low for all results.

7.3.2 Particle Momentum Distribution Histogram - Particles combined for all parameters

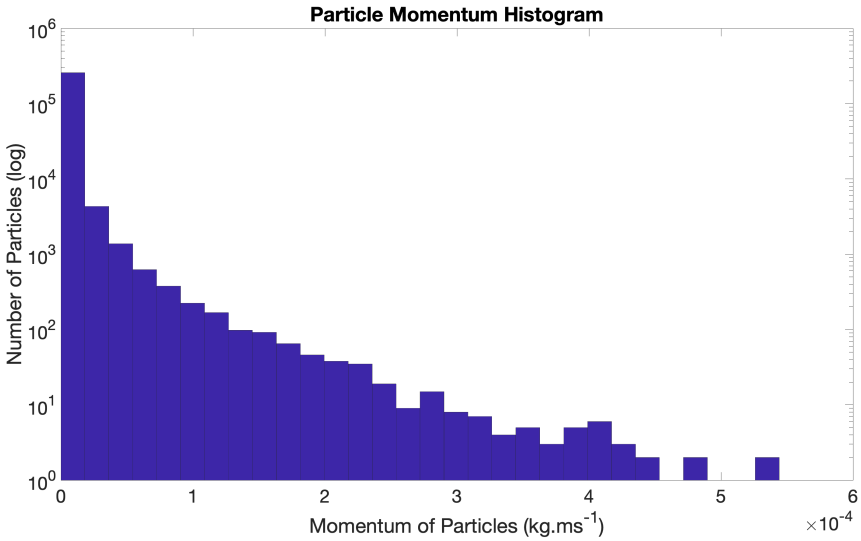


Figure 7.12: Particle Momentums over 50 videos - combined results for all parameters

- The histogram Figure 7.4 shows the particle momentum distribution combined for all parameters tested. When compared separately, a similar distribution is shown across all parameters.
- An exponential decay is shown in mean particle momentum.
- The largest particle momentums are shown to be just under $5.5x10^{-6}kg.ms^{-1}$

References

8

Rear Ejecta Particle Cloud Analysis

This section discusses the particle cloud contour plots results and analysis in order to further understand the trends discovered within the data.

* * *

8.1 Particle Cloud

For all of the videos taken, the particle positions, with respect to time, were overlaid on a single contour plot. The contour plots, as shown throughout this chapter, represent the density of particles in any particular location on screen at any particular time. These plots are especially useful graphics that are able to leverage the use of the automated software to analyse a large number of videos (50 per parameter) to visualise what is really happening in terms of particle cloud formation as an overall effect. If these videos were only analysed one by one it would not be possible to output this data and observe these trends.

As with many image analysis problems, the contour plots are very useful for visually observing trends, however scientifically analysing the plots and outputting quantitative data proves more difficult. To do this, the large number of contour plots have been assessed visually to assess any clear, recurring cloud shapes. Ten such shapes

were identified, these will be referred to as archetypes throughout this work. The ten archetypes are presented in section 8.1.1 and are labelled as oval, triangular, pointed, heart, square, mushroom, split, drop, keyhole and side point.

8.1.1 Archetype Plots

The following archetypes have been grouped into four types: triangular type, oval type and mushroom type. These groups have been assessed based on the shapes themselves and their relationships to specific parameters and other archetypes within the data. This has been done to simplify analysis in order to assess patterns within the data.

8.1.1.1 Triangular Types

The triangular, pointed and keyhole archetypes have been grouped together because they are similar in shape. All archetypes show a clear three point shape, albeit different in width and density.

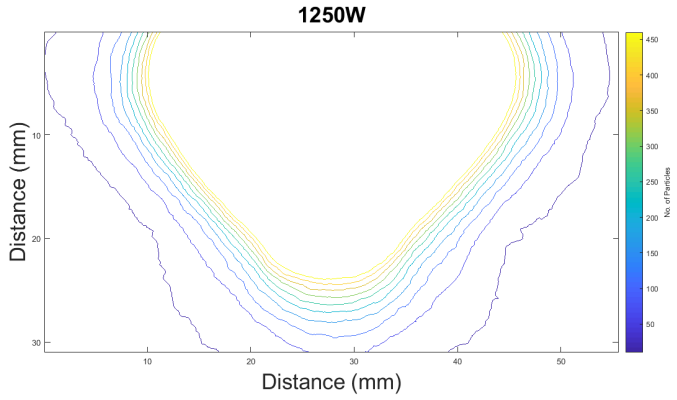


Figure 8.1: Triangular archetype, shown for 2kW laser, 5Bar nitrogen assist gas, mild steel, 1250W laser power

The triangular archetype shows a distinct three point shape, suggesting that the fastest particles are produced directly beneath the ejection point and very near to the test piece, near 180 degrees to the laser beam. The triangular archetype is shown

to be a secondary evolution of the oval shape, as shown in fig. 8.11, this is reflected by its large area in fig. 8.1.

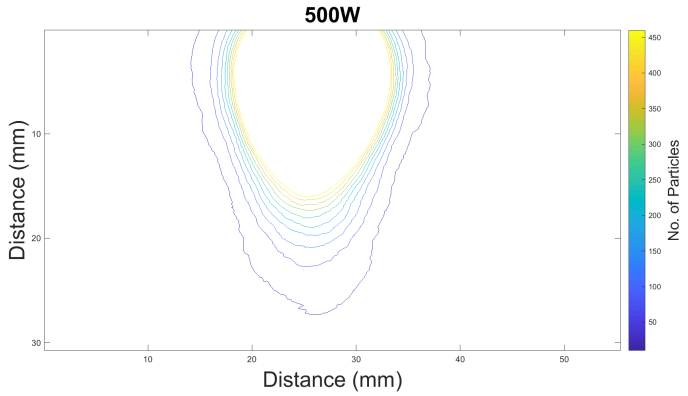


Figure 8.2: Pointed archetype, shown for 2kW laser, 12Bar nitrogen assist gas, titanium, 500W laser power

The pointed archetype also shows a three point shape. The shape appears much longer than it is wide but is actually only longer by a ratio of 4:5. The narrowing point, furthest from the initial breakthrough, accentuates the narrow appearance and suggests that the fastest particles occur directly below the breakthrough point. Figure 8.11 shows that the pointed archetype occurs both as a secondary evolution of the oval shape (similar to the triangular archetype), as well as an initial cloud shape in its own right.

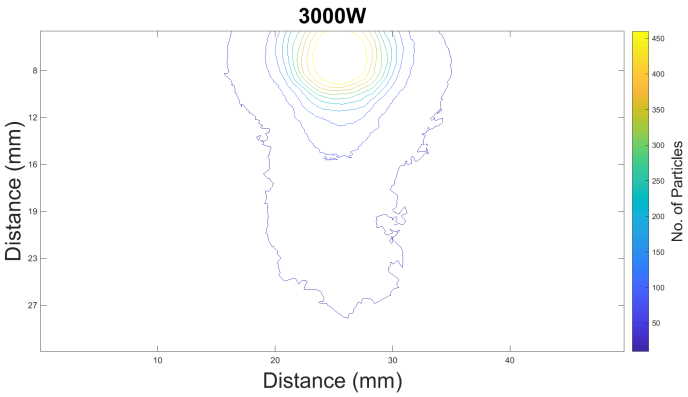


Figure 8.3: Keyhole archetype, shown for 6kW laser, 2Bar nitrogen assist gas, mild steel, 3000W laser power

The keyhole archetype is very similar to the pointed archetype in shape, however, its density nearest to the point is a lot smaller, as shown by the lack of contour lines in this region. This suggests that the fastest particles are again directly below the breakthrough point, however very few of these fast particles are present, relative to the total population. The keyhole archetype is a secondary cloud shape that usually follows the pointed archetype, as shown in fig. 8.11. Its shape is likely related to the initial fast jet, which could be explained by the fastest particles disappearing out of the image frame before the rest of the ejecta cloud has a chance to expand as much.

8.1.1.2 Oval Types

The oval and square type have been grouped together as the 'oval types' because they are very similar in shape. They are one of the most prevalent types across all parameters tested, as shown in fig. 8.13.

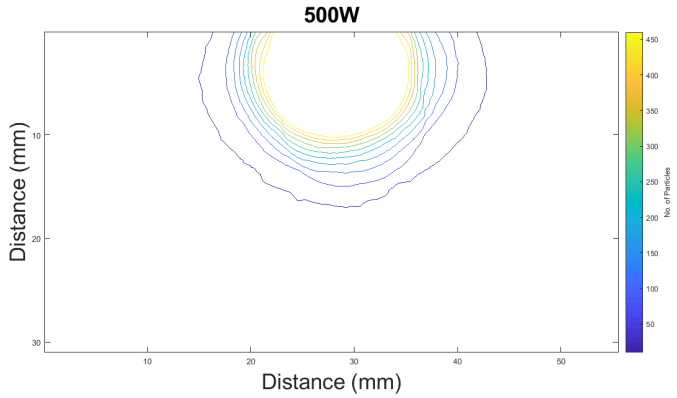


Figure 8.4: Oval archetype, shown for 2kW laser, 2Bar nitrogen assist gas, mild steel, 500W laser power

The oval archetype is the initial cloud shape for most of the 2kW laser tests, as shown in fig. 8.11 and is never shown as a secondary cloud shape. The archetype is wider than it is long at a ratio close to 2:1. This suggests that more particles are initially ejected radially at obtuse angles than downwards directly below the ejection

point.

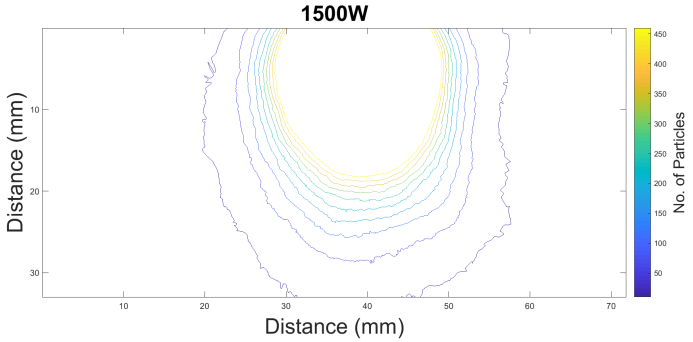


Figure 8.5: Square archetype, shown for 6kW laser, no assist gas, mild steel, 1500W laser power

The square archetype is very similar to the oval archetype, however, is only observed as a secondary ejection shape, as shown in fig. 8.11. It is slightly longer than it is wide and is always observed after the pointed archetype, as shown in fig. 8.11.

8.1.1.3 Heart Types

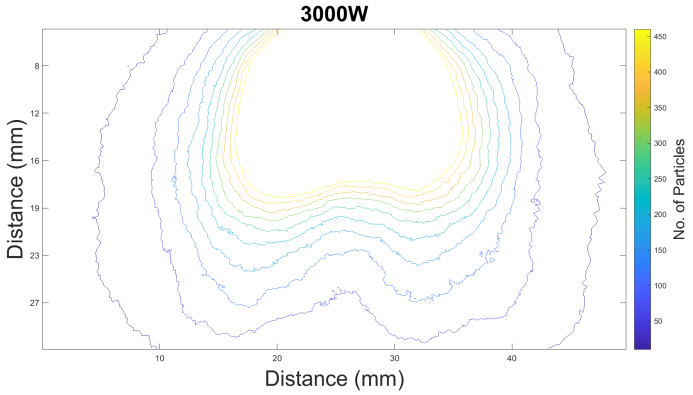


Figure 8.6: Heart archetype, shown for 6kW laser, 1Bar nitrogen assist gas, mild steel, 3000W laser power

The heart archetype is prevalent for the 6kW laser, as shown in fig. 8.11. It always presents as a secondary evolution of either the oval or the pointed archetype. The

shape shows a decrease in particle density directly below the ejection point. This decrease in density may be due to the high velocity of particles caught by the central fast jet being accelerated out of the frame at a much faster rate.

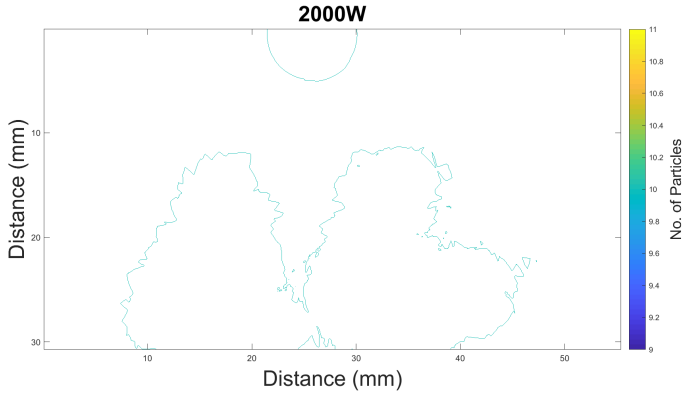


Figure 8.7: Split archetype, shown for 2kW laser, 12Bar nitrogen assist gas, aluminium, 2000W laser power

The split archetype is a secondary evolution of the mushroom archetype and is only seen for the 12Bar, aluminium, results. It is likely that the low density of the aluminium combined with the high gas pressure means that the central fast jet is more effective at accelerating a higher proportion of particles downwards. As with the heart archetype, the lack of density directly under the ejection point may be caused by the very high velocity of particles caught up in the middle of the central fast jet.

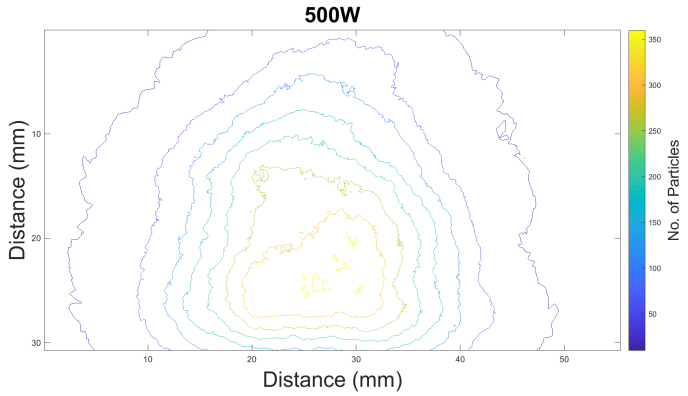


Figure 8.8: Drop archetype, shown for 2kW laser, 12Bar nitrogen assist gas, titanium, 500W laser power

The drop archetype is a secondary evolution of the pointed archetype and is only observed for titanium, as shown in fig. 8.11. The cloud shape shows a high density of particles expanding outwards as an inverted triangle from the ejection point. Less radial ejection near to the test piece is observed when compared to other archetypes.

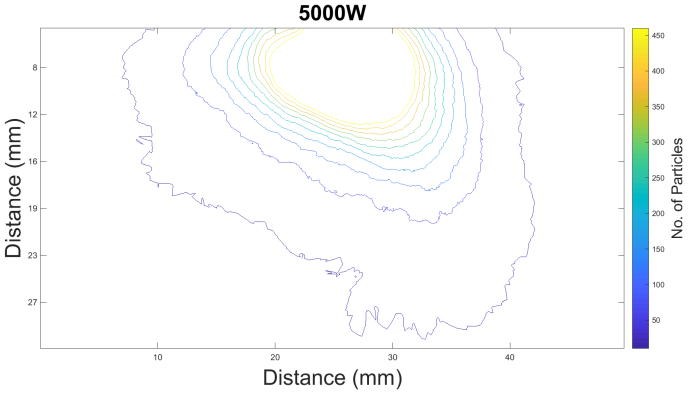


Figure 8.9: Side Point archetype, shown for 6kW laser, 5Bar nitrogen assist gas, mild steel, 5000W laser power

The side point appears similar to the pointed archetype with a lack of symmetry. As with the pointed archetype, it is presented both initially as the first cloud shape and as a secondary evolution of the oval archetype, as shown in fig. 8.11.

8.1.1.4 Mushroom Type

The mushroom type contains only the mushroom archetype, as it is geometrically unique when compared to the other archetypes.

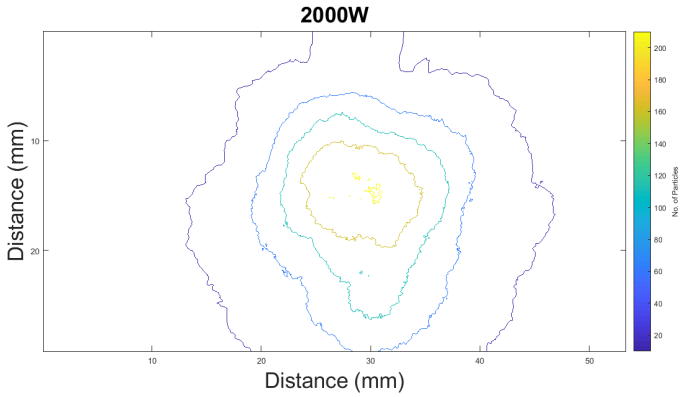


Figure 8.10: Mushroom archetype, shown for 2kW laser, 8Bar nitrogen assist gas, aluminium, 2000W laser power

The mushroom archetype is observed only for the aluminium results. It is seen as a secondary evolution of the pointed archetype, as shown in fig. 8.11. It shows a very narrow secondary stream of particles being ejected directly below the ejection point, following a relatively expansive particle cloud.

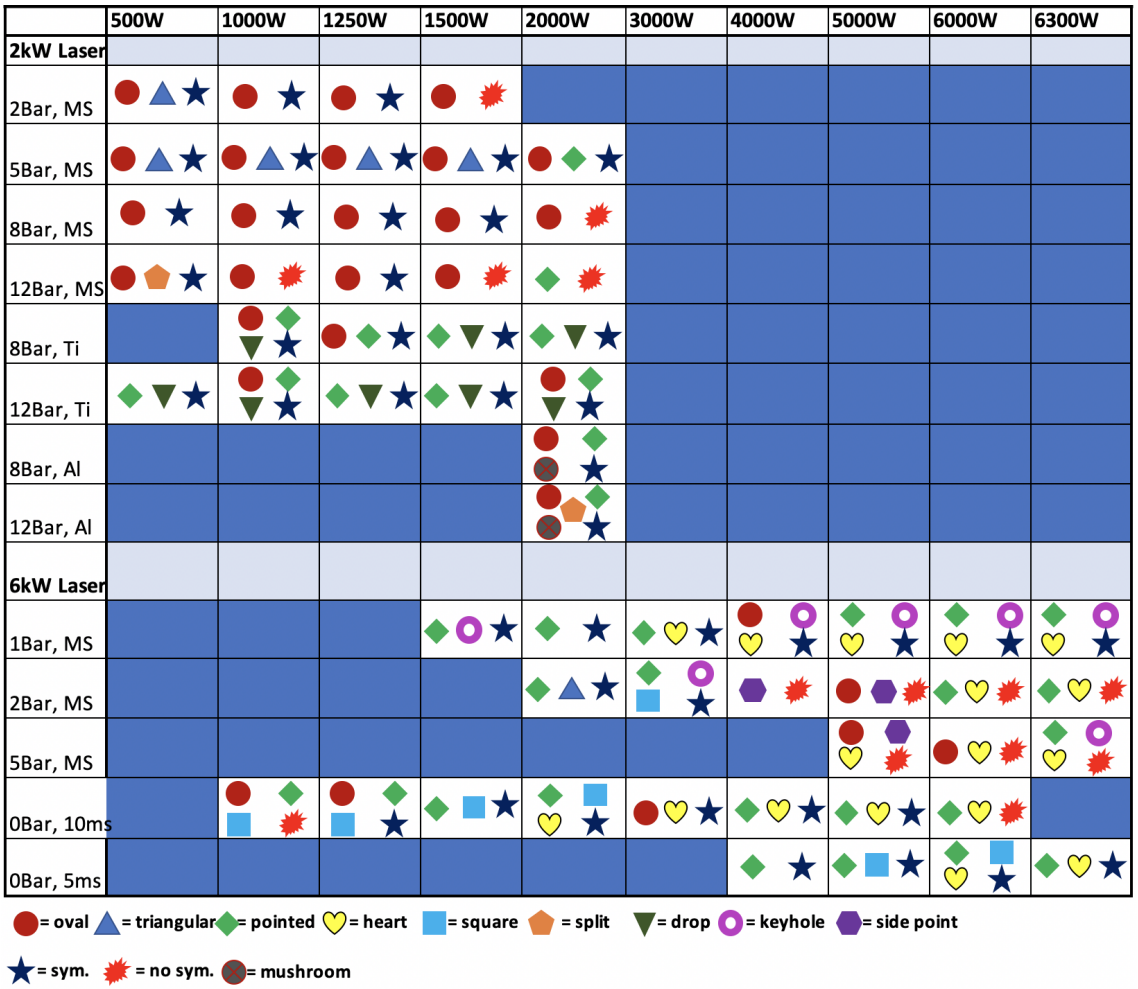


Figure 8.11: Archetype Table - all archetype shapes are shown in order of appearance, in relation to laser power, gas pressure and material type. Each cell represents data obtained across 50 videos

The archetype table, fig. 8.11, shows all of the occurring archetypes corresponding to each parameter tested, in the order in which they evolve. It is clear from the table that certain archetypes are prevalent for certain parameters. For example. the oval archetype is present in all but one of the 2kW, mild steel results. Whereas, the drop archetype is only observed for the titanium tests, whilst the mushroom archetype is only observed for the aluminium results. Many heart archetypes are shown for the 6kW laser results, whilst these are not observed at all for the 2kW laser results.

Other archetypes that are only observed for the 6kW laser results include keyhole, side point and square.

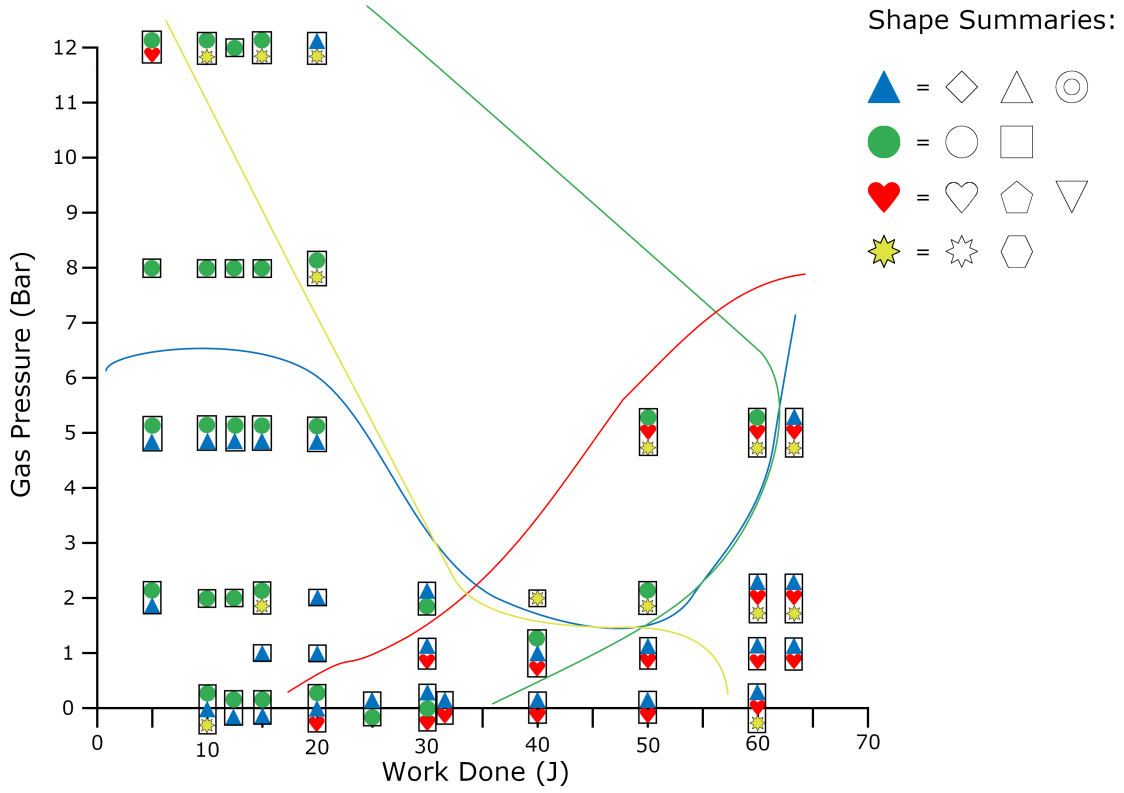


Figure 8.12: Archetypes Process Parameters Chart - shows a simplified version of the archetypes in terms of gas pressure and work done for mild steel only. The archetypes have been summarised in terms of similar shapes in order to clearly visualise patterns in the data. Coloured lines have been used to divide sections of the chart which mostly contain the archetype of the corresponding colour.

The archetype process parameters chart, fig. 8.12, shows the archetypes with respect to work done by the laser parameters and gas pressure for the mild steel results. Mild steel has been the focus for this analysis since this encompasses the majority of the results. The archetype summaries are used so that the data is easier to process visually, allowing for overarching patterns to be drawn in relation between archetype and process parameters. The patterns shown in fig. 8.12 by the coloured lines reflect

best estimations of the process parameters relationships to the archetypes based on the natural groupings that are observed in the data.

Figure 8.12 shows that the triangular type is observed for gas pressures below 8Bar and across all tested work done values. A dip in the triangular type is shown between 40 - 50 joules for gas pressures higher than two bar. In contrast, the oval type is shown across the full range of gas pressures tested and from 1 - 60 joules laser energy. However, it is clear that the oval type does not present for high laser energy (40 - 70 joules) when combined with low gas pressure (1 - 5Bar), but as gas pressure increases, the oval type is shown to present more frequently at higher laser energies. The heart type is shown to appear only at high laser energies (20J and higher). The trend in the data suggests that the heart type may be less likely to present as gas pressure increases if work done remains the same, however, this is mostly untested. The trends in fig. 8.12 clearly suggest that a lack of symmetry is more likely to occur as both work done by the laser and gas pressure increases.

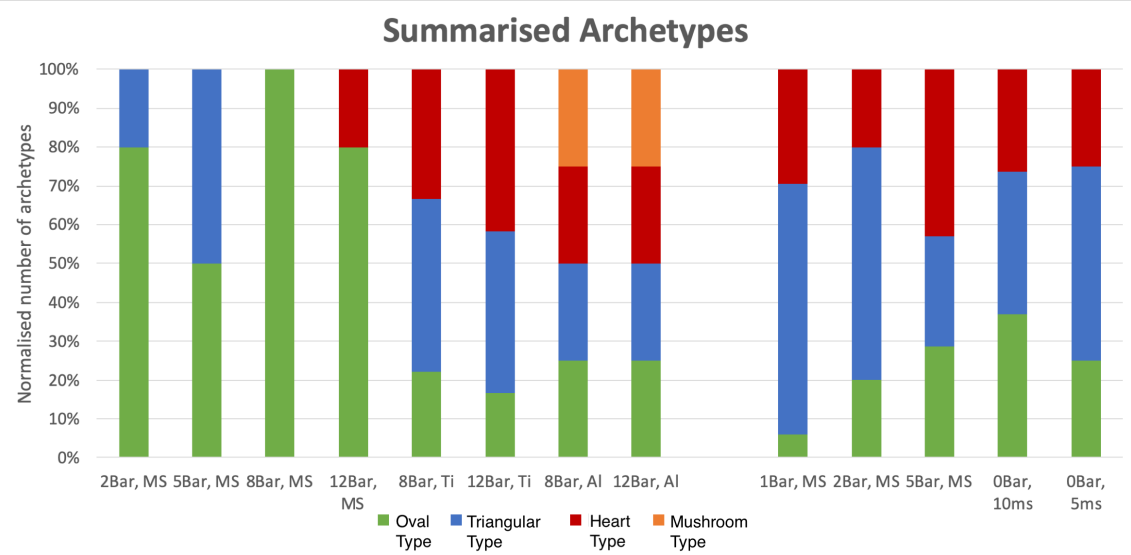


Figure 8.13: Summarised Archetypes Percentage Plot - plot shows the percentages of archetypes for each gas pressure and material type tested, split between the 2kW and 6kW lasers (left and right respectively)

Figure 8.13 shows the summarised archetypes in terms of percentage for each of the parameters tested. It is clear to see from the plot that the oval type is most common, appearing in all parameters tested, closely followed by the triangular type, the heart type and finally the mushroom type, which is only shown for the aluminium results. Figure 8.13 suggests that the triangular type does not present at high gas pressures (8 and 12Bar). Figure 8.13 also shows that the heart type is far more prevalent for mild steel for the 6kW laser results, as opposed to the 2kW laser. The heart type is also shown to be observed for all titanium and aluminium tests.

References

9

Rear Melt Ejecta Volume

This chapter presents data and analysis on rear melt ejecta volume, produced from the particle tracking results. Analysis of this data is directed at providing some useful metrics for readers who would like to optimise laser drilling parameters in order to minimise rear melt ejecta.

* * *

Many industries rely on laser drilling for its multitude of benefits. Micro-second pulse laser drilling in particular can be very useful due to its efficient method of material removal. However, an excess of rear melt ejecta can be a severe limitation in some areas.

Rear melt ejecta can be the cause of two problems in manufactured components. Firstly, rear melt ejection is the main process behind dross formation (see fig. 1.1 for an explanation of dross). Secondly, when drilling through closed components, rear melt ejecta can adhere to surfaces opposite to the drilling surface. The adherence of dross and ejecta onto these surfaces are often detrimental to high performance components that must perform well under high thermal, mechanical and or cyclic stress.

These problems often require additional steps and processes to overcome, such as the application of Anti-Spatter Composite Coatings by Lowe [9.1]. Another option is often to use entirely new drilling methods instead, such as Electro-Discharge Machining (EDM).

The following results and analyses in this chapter use statistical methods on the data obtained from particle tracking methods within this work. The data is used for parameter optimisation towards minimising rear melt ejecta volume. This will provide an insight for all laser drilling applications that could benefit from a minimisation of rear melt ejecta.

9.1 Relative Total Combined Rear Melt Ejecta Volume

To calculate rear melt ejecta volume, a summation of the volume of all rear melt ejecta particles was taken. Particle volume was calculated from the 95th percentile equivalent diameters, taken from the particle tracking results. The 95th percentile was used in order to ensure that no large particles skewed the data for comparison purposes.

This data was then divided by 50, in order to give a relative total combined rear melt ejecta volume per video (one single laser pulse). For plots where multiple sets of videos were used to give a single data point, the final value was divided by the number of sets of videos. This ensures that every data point given in this chapter represents the relative rear melt ejecta volume for one video.

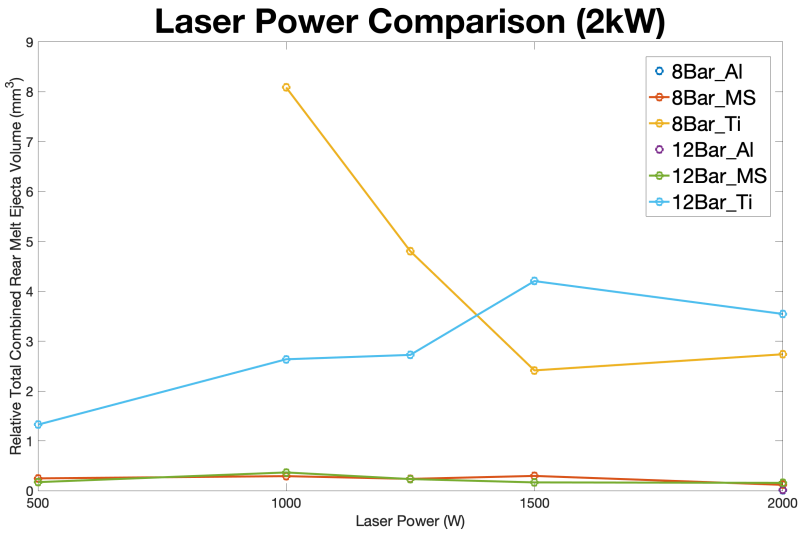


Figure 9.1: Laser power comparison with total combined rear melt ejecta volume for the 2kW laser experiments (different lens experiments have been excluded)

Figure 9.1 shows the relative total combined rear melt ejecta volume plotted against laser power in terms of gas pressure for the 2kW experiments only.

It is clear from fig. 9.1 that titanium produces a much larger combined ejecta volume than mild steel and aluminium for every power shown, with a minimum difference of $1\,\mathrm{mm}^3$. Aluminium is shown to produce a slightly smaller ejecta volume than mild steel for a 2000W laser power.

Figure 9.1 also shows that the variation in ejecta volume for the titanium results varies much more than that of mild steel between laser powers, with a maximum variation of around $7\,\mathrm{mm}^3$ for titanium compared to a maximum difference of around $0.1\,\mathrm{mm}^3$ for mild steel.

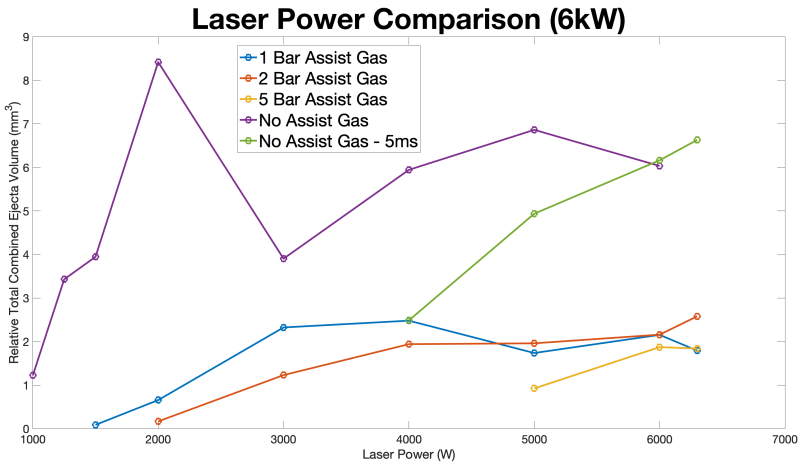


Figure 9.2: Laser power comparison with total combined rear melt ejecta volume for the 6kW laser experiments (different lens experiments have been excluded)

Figure 9.2 shows the relative total combined rear melt ejecta volume plotted against laser power in terms of gas pressure for the 6kW experiments only.

A distinct difference is shown in fig. 9.2 for ejecta volume in relation to whether or not an assist gas is used. The no assist gas tests with a 10ms pulse width generated considerably more ejecta at every power shown than the 1Bar, 2Bar and 5Bar assist gas results with a 10ms pulse width, with a minimum difference in volume of 1.5 mm^3 at 3000W laser power.

A general decrease in ejecta is shown in fig. 9.2 as power increases, suggesting that a higher gas pressure reduces ejecta volume. However, the decrease in the number of data points as gas pressure increases, also demonstrates that a higher gas pressure makes penetration at lower laser powers less likely.

The difference in pulse width for the otherwise like for like no assist gas results in fig. 9.2 suggests that a lower pulse width generates less ejecta.

9.2 Laser Power Relationship With Rear Melt Ejecta Volume

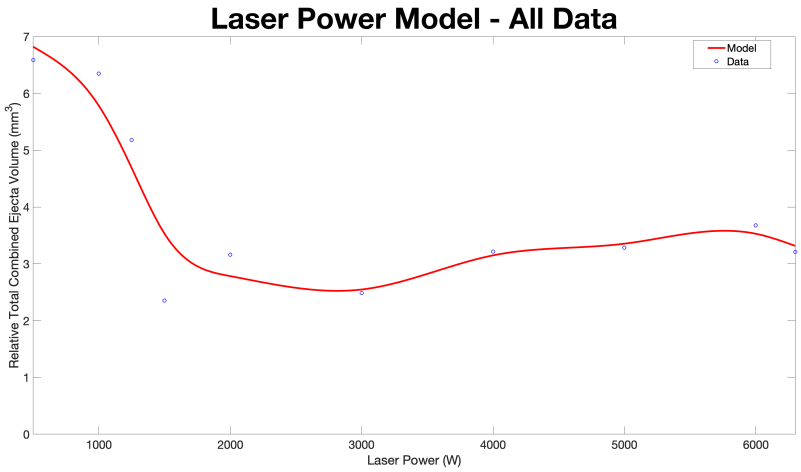


Figure 9.3: Plot of smoothing spline model fitted from the laser power and relative total combined ejecta volume results alongside the experimental data

Figure 9.3 shows a plot of the smoothing spline model fitted from the experimental data for laser power and ejecta volume alongside the experimental data. The model takes into account all of the data tested data in order to give an insight into the relationship of laser power with ejecta volume irrespective of other laser drilling parameters.

Several models were fitted to the data and assessed visually, as well as with the use of goodness of fit statistics. A smoothing spline was selected with the chosen smoothing parameter because it gave a good fit for the majority of the data, whilst identifying a clear trend. A general trend is more useful for this data, rather than passing through every data point. This is because the goal of this model is to identify a reasonable estimation of a laser power optimisation for minimal ejecta volume for any variation of given laser parameters, rather than a specific answer for this data set.

Smoothing spline model: f(x) = piecewise polynomial computed from p, where the

smoothing parameter p = 7.52 x 10^{-8}

Smoothing spline algorithm [9.2]:

$$p\sum_{i}(y_i - s(x_i))^2 + (1-p)\int\left(\frac{d^2s}{dx^2}\right)^2 dx \tag{9.1}$$

Where s = smoothing spline function, p = smoothing parameter, y = relative total combined ejecta volume (mm^3), x = laser power (W)

Goodness of fit statistics: SSE = 2.19, R^2 = 90%, RMSE = 0.869

Sum of Square Errors (SSE) measures the deviation of the fit to the actual values. A value of zero represents zero random error. This is useful for representing how useful the fit is for prediction.

The R^2 is the square of the correlation between the actual values and the predicted values. It shows that the smoothing spline fit explains 90% of the variation in the data from the average.

The Root Mean Squared Error (RMSE) is an estimate of the standard deviation of the random component in the data. Like SSE, a value of zero represents zero error, it is also useful in determining how useful the fit is for prediction.

A bounded optimiser function was run on the smoothing spline model to output the predicted laser power for which ejecta volume would be the lowest. The MATLAB function, fminbnd [9.3,9.4] was chosen as it is useful for nonlinear, bounded problems.

Bounds of 500W - 6300W were given, as the model is not expected to make predictions outside of the tested data range.

A laser power of 2814W was calculated as the laser power recommendation for minimising ejecta volume based on the results within this work.

Looking back at fig. 9.3, 2814W does agree with the lowest point on the plotted curve. However, the lowest data point shown, in terms of ejecta volume, is actually around 1500W. The advantage of using the model is that it takes into account the data point at 1500W as well as the much higher data points at 1250W and 2000W. Assuming that the data trend continues across all parameter variations in further testing, it is expected that these values may move around somewhat, therefore the likelihood of accurately identifying the trough at 1500W between two peaks is unlikely. Instead, by identifying a more stable minimum at 2814W, this laser power is more likely to produce a very low ejecta volume, even if not the absolute minimum possible.

Given this data, when attempting to minimise ejecta volume for varying laser parameters, it is suggested to use 2814W laser power. If the opportunity for testing is available, then it would be advised to test between 1000W - 2000W.

9.3 Gas Pressure With Rear Melt Ejecta Volume

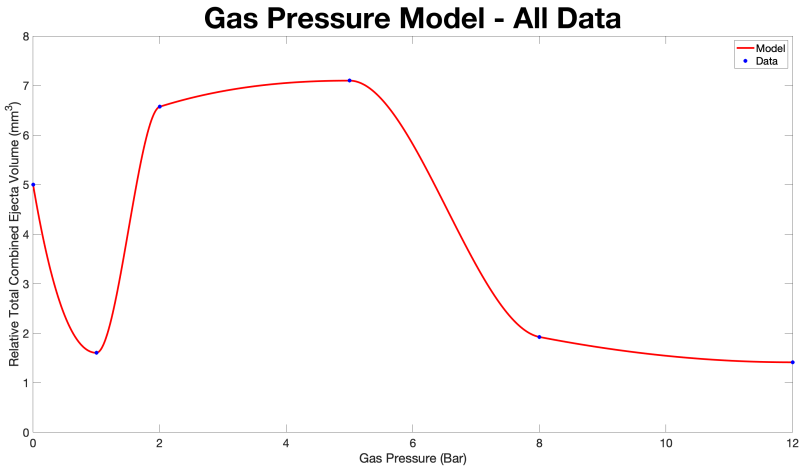


Figure 9.4: Plot of Piecewise Cubic Hermite Interpolating Polynomial (PCHIP) model fitted from the gas pressure and relative total combined ejecta volume results alongside the experimental data

Figure 9.4 shows a plot of the PCHIP model, which was fitted to the experimental data for gas pressure and ejecta volume, alongside the experimental data points. The gas pressure and ejecta volume used in this model was calculated from the full range of results that were obtained from the particle tracking method in this work. This means that this model provides a look at the direct relationship between gas pressure and ejecta volume, irrespective of other laser parameters, for this work.

Unlike the laser power smoothing spline model, it was very difficult to create a fit for the gas pressure data that identified a clear trend without systematically passing through every data point, based on visual analysis and goodness of fit values. Therefore, instead, a direct interpolation between the data points was conducted using a Piecewise Cubic Hermite Interpolating Polynomial (PCHIP). The PCHIP model is effective for creating a realistic smooth curve between the data points. This is useful for identifying the trend of the data and accurately predicting where missing data points may lie, making it useful for an optimisation function.

PCHIP model [9.5,9.6]: shape-preserving piecewise cubic interpolation

The PCHIP model repeatedly uses a cubic polynomial, of the order shown in eq. (9.2), to piece together a smooth interpolation between data points, whilst preserving shape based on the data point derivatives.

$$f(x) = a(x - x_1)^3 + b(x - x_1)^2 + c(x - x_1) + d \tag{9.2}$$

Where a, b, c, d = the calculated coefficients and x and x1 represent the limits of each interval.

Goodness of fit statistics: SSE = 0, R^2 = 100%

Since the model correctly identifies all data points, the SSE value is zero and the R^2 = 100%.

As with the laser power model, the bounded optimiser function, fminbnd [9.3,9.4]

was chosen for the gas pressure model, as it is effective for nonlinear, bounded problems.

Bounds of 0Bar -12Bar were given, as these were the limits of the experimental data.

Using the MATLAB fminbnd [9.3,9.4] function, an optimal gas pressure of 12Bar was calculated as optimal for minimising ejecta volume. Referring back to fig. 9.4, this agrees with the model plot, as the lowest point is seen at 12Bar. However, fig. 9.4 continues to trend downwards from 8Bar suggesting that a higher gas pressure may be optimal for minimising ejecta.

Taking into account the practicalities of using a high gas pressure, when applied to mass produced manufacturing products, for which laser drilling is a valued method. It is likely that too high of a gas flow may offset the benefits of the laser drilling process, due to the increase in expense that is required to increasingly often replenish the consumable gas flow. It is also taken into account that as gas pressure increases, penetration can become far less likely - as signified by the lack of data points with increasing gas pressure in fig. 9.2. For these purposes, the gas pressure model was also run between the bounds 0Bar and 8Bar gas pressure.

For the bounds 0Bar - 8Bar gas pressure, the fminbnd [9.3,9.4] function calculated a minimum of 1Bar, based on the data point at this value - shown on fig. 9.4. Therefore, it is suggested that if a balance between lower gas pressure and ejecta minimisation is sought, then 1Bar should be selected as the optimal gas pressure. However, if an absolute minimisation of ejecta is preferred, regardless of gas flow pressure, then a pressure of 12Bar should be used and higher pressures are worth testing.

9.4 Material Type With Rear Melt Ejecta Volume

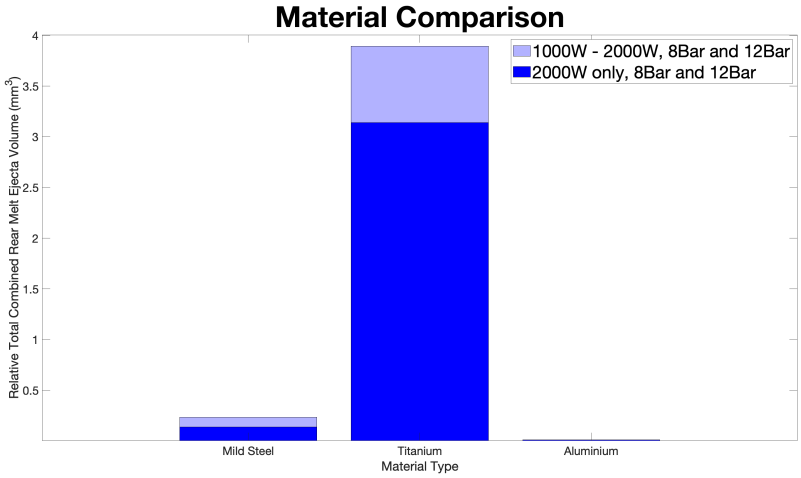


Figure 9.5: Bar chart comparing the three material types tested in this work with relative total combined rear melt ejecta

Figure 9.5 shows the relationship between rear melt ejecta and material type, where alike parameters have been used. 2000W only laser power results for 8 and 12Bar assist gas have been included in order to compare the aluminium results with mild steel and titanium, since experimental tests have been carried out for these parameters on all three materials.

1000W - 2000W laser power results for 8Bar and 12Bar results have been included for a mild steel to titanium comparison as these include all of the tests where the other experimental parameters are the same. As previously mentioned, these results are relative and have been averaged to provide the averagd results for a single video.

Since many more mild steel results are included in this work than for titanium or aluminium, a bar chart has been used rather than a model to give a clear, fair comparison of the materials. Although less data points are provided than for laser power and gas pressure, this comparison is still statistically useful due to the large

number of videos averaged for each data point.

Figure 9.5 clearly identifies that titanium produces significantly more rear melt ejecta than mild steel or aluminium for the parameters tested, with a difference of $3\,\text{mm}^3$ between titanium and aluminium results for 2000W laser power and $3.5\,\text{mm}^3$ between mild steel and titanium for 1000W - 2000W tests.

The comparison of mild steel to aluminium for 2000W results in fig. 9.5 shows that mild steel produces ten times more rear melt ejecta than aluminium.

This would suggest that given a choice of materials between mild steel, titanium and aluminium, in order to minimise rear melt ejecta volume, then aluminium should be used, followed by steel. What is perhaps most useful from this analysis is the identification of the significant impact that material choice can have on rear melt ejecta.

9.5 Pulse Width With Rear Melt Ejecta Volume

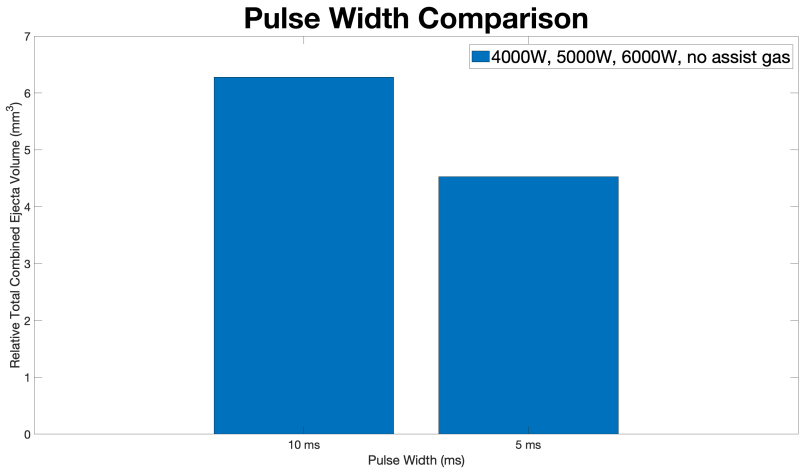


Figure 9.6: Bar chart two pulse widths tested with no assist gas for laser powers of 4000W, 5000W and 6000W

Figure 9.6 shows the relationship between relative rear melt ejecta and pulse width. The results from the 4000W, 5000W and 6000W laser power tests with no assist gas were selected because they were carried out with both 10ms and 5ms pulses.

As with material type, a model was not created for this data because there are much less 5ms pulse width tests than 10ms pulse width tests. Instead like for like parameters have been used to allow for a fair comparison.

Figure 9.6 clearly identifies that pulse width is 1.5 mm^3 lower in ejecta volume for a 5ms pulse than for 10ms pulses across the same parameters. This suggests that a 5ms pulse may be generally more effective for minimising ejecta volume than a 10ms pulse. However, it should be taken into account that fig. 9.2 suggests a trend where, when no assist gas is used, the volume of rear melt ejecta produced at a laser power above 6000W is more for a 5ms pulse than for a 10ms pulse.

9.6 Parameter Significance In Relation To Rear Melt Ejecta Volume

When optimising parameters with regards to minimising rear melt ejecta volume, it is important to rank the significance of the parameter in relation to the rear melt ejecta volume.

Since the rear melt ejecta volume models and bar charts have all been calculated in terms of relative total combined rear melt ejecta volume, they are comparable. In order to take advantage of this, a simple analysis was carried out to find the difference between the maximum and minimum rear ejecta volumes for each relationship. For the laser power and gas pressure models, the highest corresponding ejecta volume values were taken for the x data points 500W and 5Bar respectively. These x values were then fed into the models to output the maximum ejecta volumes as 6.82 mm^3 and 7.10 mm^3 respectively.

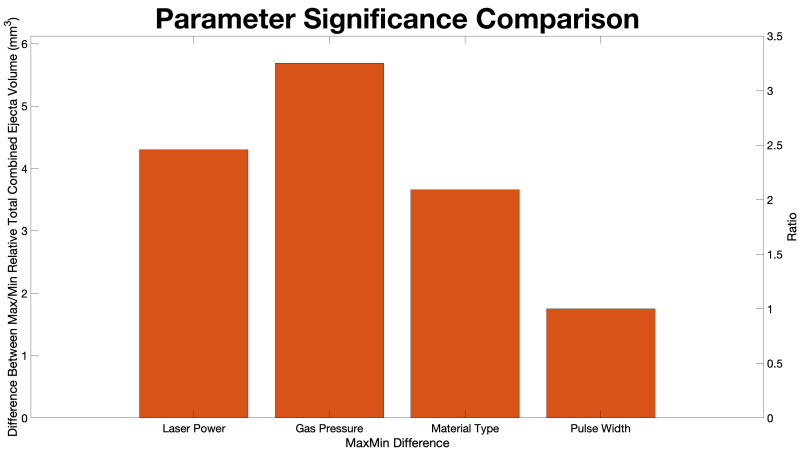


Figure 9.7: Bar chart of maximum / minimum difference in relative total combined ejecta volume, against relative total combined ejecta volume

Figure 9.7 represents which parameters have the highest effect on ejecta volume, based on the experimental data from the particle tracking results. Figure 9.7 depicts a ranking with gas pressure being the most influential parameter on ejecta volume, then laser power, closely followed by material type and finally followed by pulse width.

This would suggest that in order to minimise rear melt ejecta in the laser drilling process through parameter optimisation, it is best to first focus on gas pressure, laser power, material type and then finally pulse width. Based on the data assessed, this will provide the biggest reductions in rear melt ejecta with the least amount of parameter manipulation.

References

[9.1] D. K. Low, L. Li, and P. J. Byrd, "Spatter prevention during the laser drilling of selected aerospace materials," *Journal of Materials Processing Technology*, vol. 139, no. 1-3 SPEC, pp. 71–76, 2003.

[9.2] C. H. Reinsch, "Smoothing by spline functions," *Numerische Mathematik*, vol. 10, no. 3, pp. 177–183, Oct 1967.

[9.3] G. E. Forsythe, M. A. Malcolm, and C. B. Moler, "Computer methods for mathematical computations," *ZAMM - Journal of Applied Mathematics and Mechanics / Zeitschrift für Angewandte Mathematik und Mechanik*, vol. 59, no. 2, pp. 141–142, 1979.

[9.4] R. P. Brent, *Algorithms for Minimization without Derivatives*, 1st ed. Englewood Cliffs, New Jersey: Prentice-Hall, 1973.

[9.5] D. Kahaner, C. Moler, and S. Nash, "Numerical methods and software," *SIAM Review*, vol. 33, no. 1, pp. 144–147, 1991.

[9.6] F. N. Fritsch and R. E. Carlson, "Monotone piecewise cubic interpolation," *SIAM Journal on Numerical Analysis*, vol. 17, no. 2, pp. 238–246, 1980.

10

Discussion

This section discusses the results and analysis in order to further understand the trends discovered within the data.

* * *

10.1 Observations

10.1.1 Ejection Mechanisms

As opposed to short pulse width (i.e. ns to fs) laser drilling, for which the material removal is mostly achieved through vaporisation, long pulse width (millisecond) drilling removes material through a melt based mechanism [10.1]. The generally accepted premise for the removal of material in melt-based (millisecond pulse width) laser drilling, is that once irradiated, the upper layer of the test-piece heats up rapidly. This produces a small amount of vaporisation on the top most layer, with an expanding melt pool beneath, as shown in Figure 10.1.

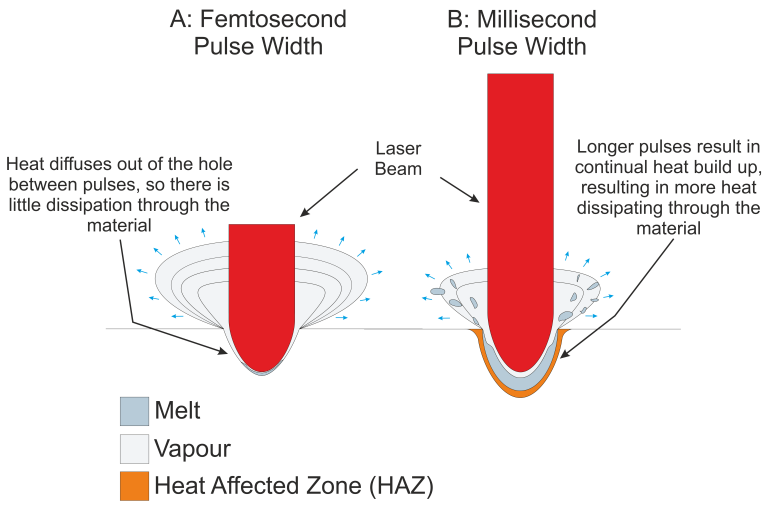


Figure 10.1: A) Laser ablation using femtosecond pulsewidth, B) Laser ablation using millisecond pulse width

A combination of the pressure created from the vaporised material above the melt pool and the thermal expansion of the material within the melt pool as well as the pressure created from an assist gas, if present, is thought to be the main contributor to material removal by ejection, both upwards, and rearwards after breakthrough [10.2] [10.3].

In 1995, when investigating upward ejection in millisecond pulse width laser drilling, on the laser side of the test-piece, Yilbas [10.4] identified the presence of two types of upward ejection mechanisms using streak photography. The first initial type of ejection produced a slower moving, more dispersed cloud of particles. This was followed by a second ejection, occurring 100 µs afterwards producing a continuous stream of smaller, faster moving particles, which tend to travel directly upward towards the laser source with minimal dispersion.

Yilbas [10.4] postulated that the first ejection type may be caused by a radial flow of liquid, forced along the hole walls by the pressure build up, the wall adherence caused by surface tension forces within the material. With the secondary ejection being caused by a large pressure build up due to explosive nucleate boiling mechanisms

within the melt pool.

Using up-to-date high-speed filming technology, the work in this study has identified a similar two mechanisms in the rear ejection of millisecond laser drilling. Although, the secondary type of ejection, a less dispersed stream of generally smaller, faster particles, which will be referred to as a central fast jet (Figure 10.2), has only been observed for the videos taken in this study with an assist gas.

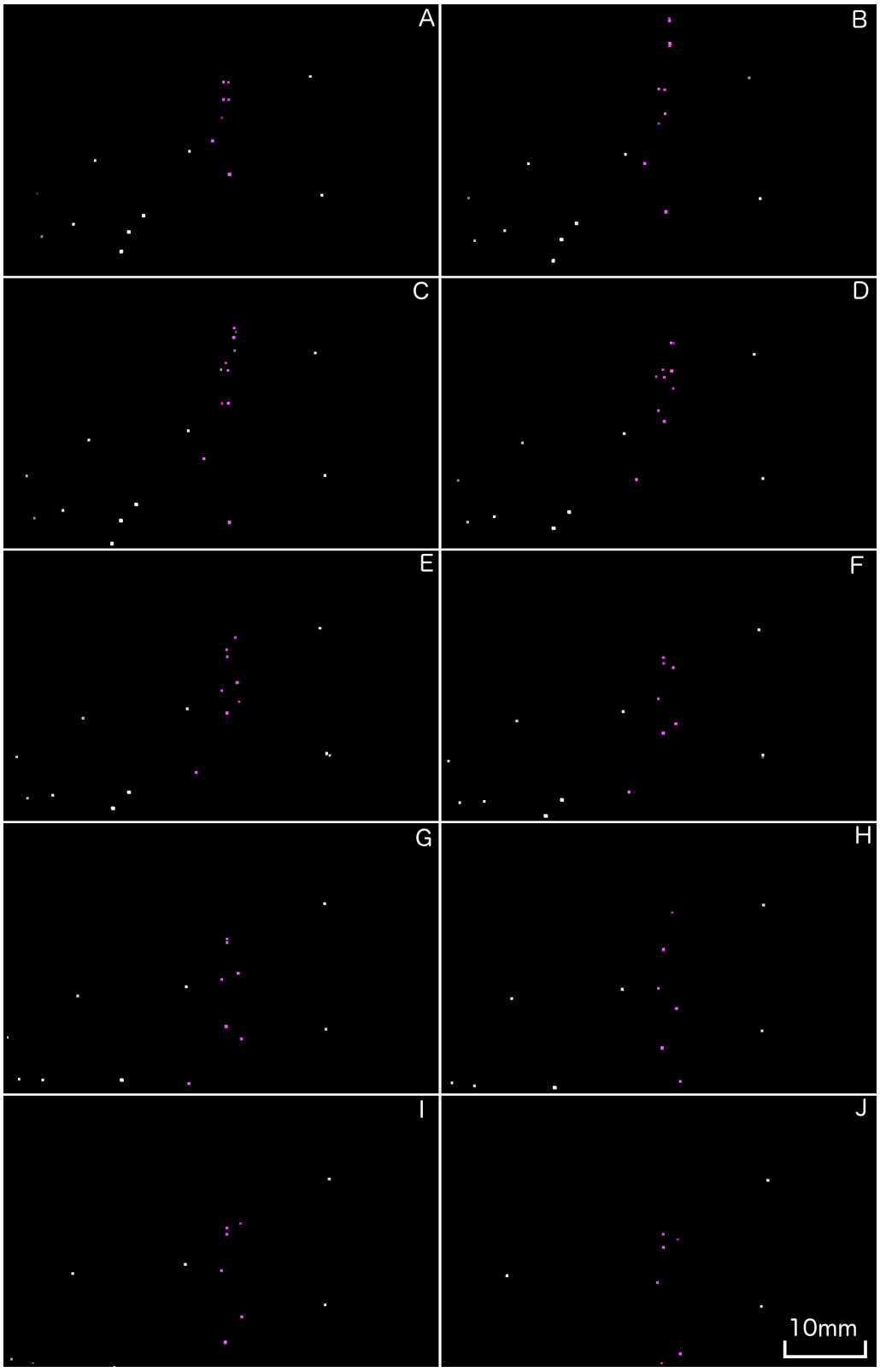


Figure 10.2: Presence of a Central Fast Jet, Highlighted in Red - 6kW Laser, 6300W, 5Bar Nitrogen Assist Gas, 10ms Pulse Width

It appears highly likely that the presence of the central fast jet within the rear ejection of laser drilling is likely to be a direct effect of the use of an assist gas adding to the pressure build up within the hole.

However, although the presence of a central fast jet has not been observed in any of the videos taken for laser drilling without an assist gas in this study, the presence of a stream of smaller, faster particles, ejected in a straight line directly below the breakthrough, *before* any other ejection has been observed. This initial jet is shown in Figure 10.3.

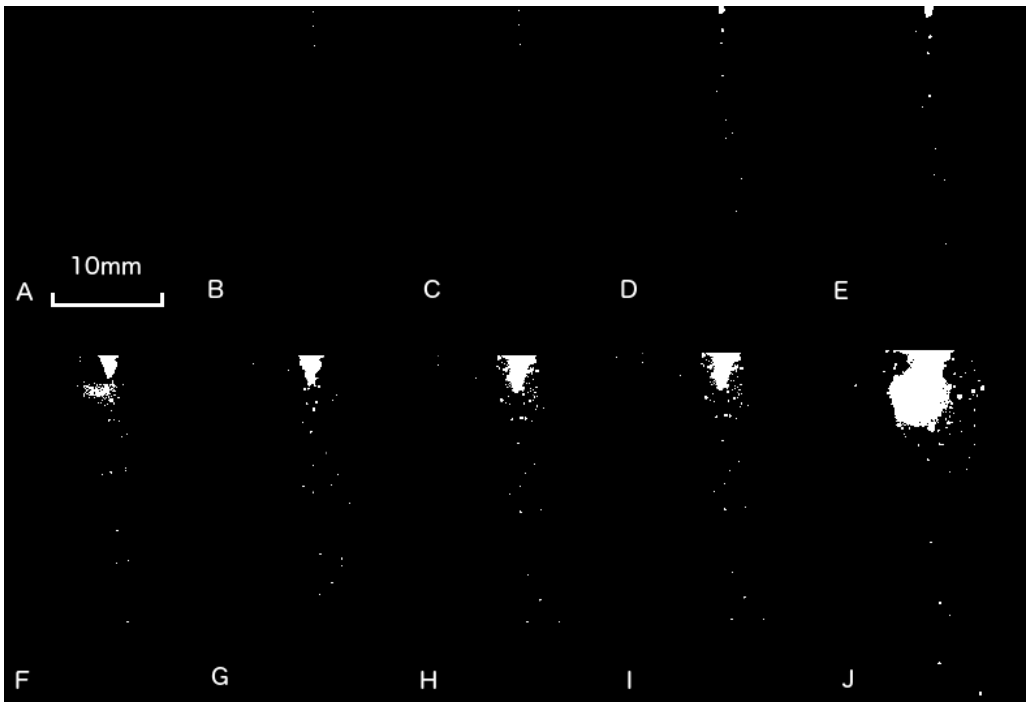


Figure 10.3: 6kW Laser, 1500W, no assist gas, 10ms pulse width - Initial fast jet is shown through ten consecutive frames (161 µs between frames) - radial ejection begins in frame 6 (figure F, 968 µs from breakthrough)

As well as occurring prior to any other ejection, the initial ejection observation has only been observed in a handful of videos for certain parameters, unlike the central fast jet, which is generally observed through all videos of the same parameters for which it is seen. Because this initial ejection appears to occur somewhat randomly

under certain conditions, and has been observed in experiments without an assist gas, it is possible that this process could be caused by nucleation mechanisms within the material, as hypothesised by Yilbas [10.4] for upward ejection.

However, this finding could also be related to the variance in size of the initial breakthrough hole and its evolution in time, as a smaller breakthrough hole early in the rear ejection process could lead to some particles being directionally ejected with a higher speed, with the momentarily smaller hole acting akin to a bullet in a gun barrel as shown in Figure 10.4. Whilst a larger hole would likely allow for a larger dispersion of particles with less velocity. Further evidence is required to confirm either of these two mechanisms.

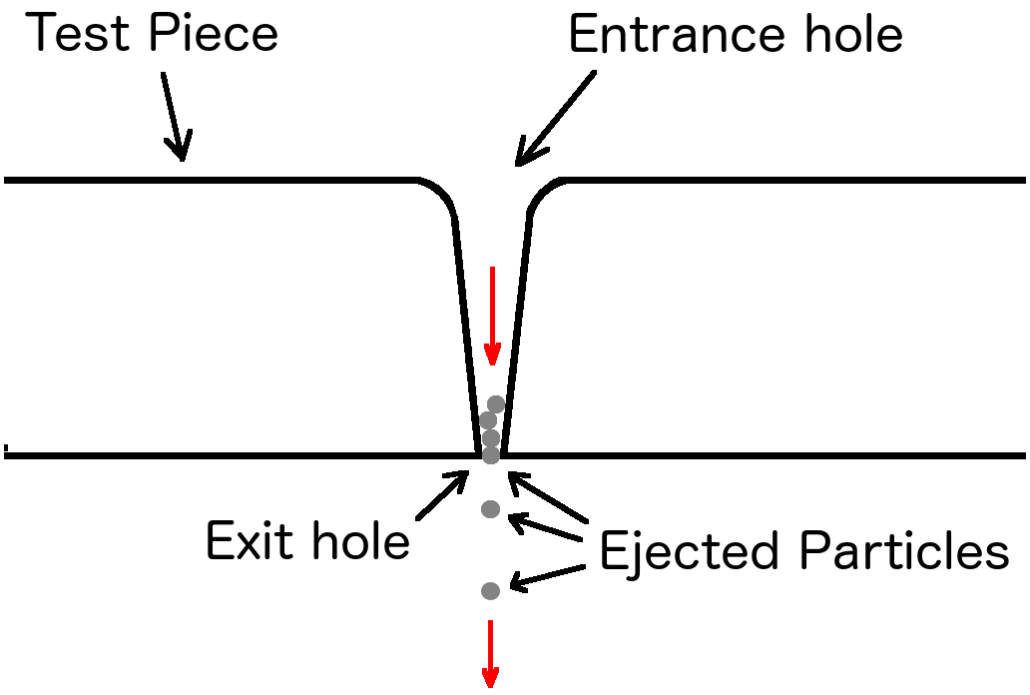


Figure 10.4: The schematic demonstrates how particles could be directed linearly in the early stages of ejection through a relatively small exit hole

Taking into account the infrequency of this initial stream, and the lack of presence of a central fast jet without an assist gas, it is likely that the scattered ejection of

slower particles make up the bulk of the rearwards material removal through ejection of the melt pool, when there is no assist gas present. It is also likely that adherence of the melt pool to the hole wall due to surface tension forces contributes to the wide angles of dispersion (up to 180 degrees) that have been observed in these videos. Figure 10.5 demonstrates how the surface tension forces may lead to wide angle ejection.

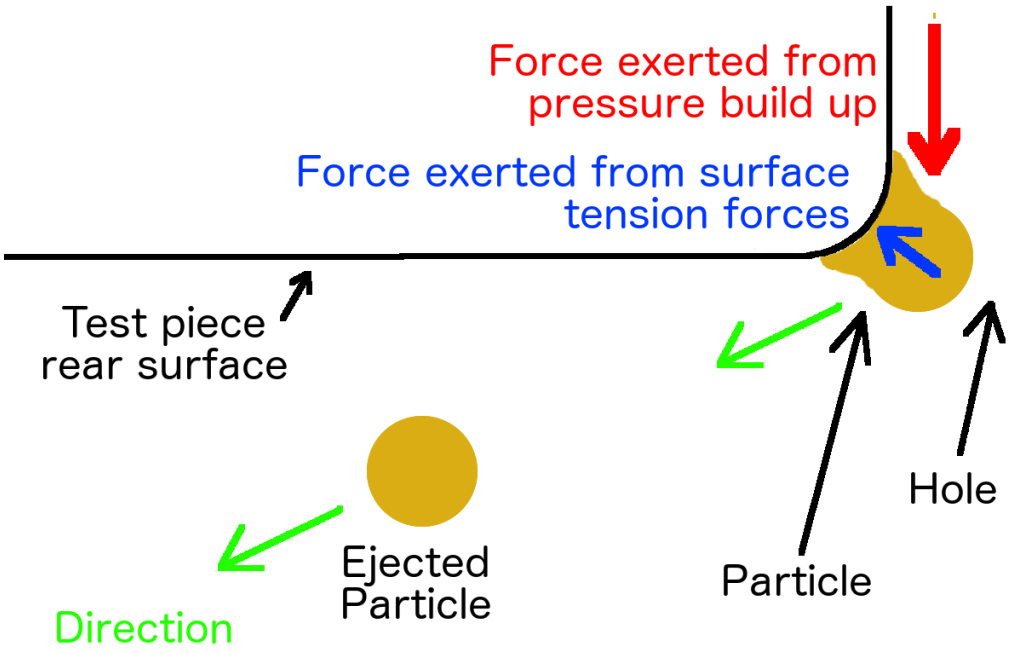


Figure 10.5: Schematic indicates how a combination of downward forces from pressure build up within the hole and the surfaces tension forces exerted on the melt pool can result in widely dispersed particles

The presence of these two mechanisms, which has been repeatedly cited within the literature, and the development of its further understanding could help those concerned with back wall strike applications to further understand the importance of assist gas in the milli-second laser drilling process.

This is because this work can provide a further understanding of the evolution of the rear debris cloud. Analysis of the number, size, velocity, direction and position of

individual particles relative to time within the cloud can allow for a prediction of the size and speed of the development of the cloud for specific parameters. Therefore, for specific parameters, predictions can be made as to whether or not ejecta will contact or adhere to a back wall surface.

10.1.2 Exploding Particles

The observation of the high-speed videos carried out within this work has unequivocally identified the presence of exploding particles (Figure 6.1) within the rear ejection cloud, produced during milli-second laser drilling.

The presence of exploding particles within rear melt ejection is most likely due to a quickly solidifying particle outer layer due to the cooling effects of air during ejection. Particles will, at least for a short time period, undergo a state in which they consist of a solid outer layer containing a liquid core. As the outer layer solidifies, it contracts, squeezing the inner liquid and leading to a build up of pressure. In turn, such a pressure build up within a confined volume will ultimately lead to an explosion in which either the particle is either divided up into exploding fragments, or a hole will form within the particle surface in which the remaining melt will explode out of, leaving a hollow shell and several newly solidifying particles.

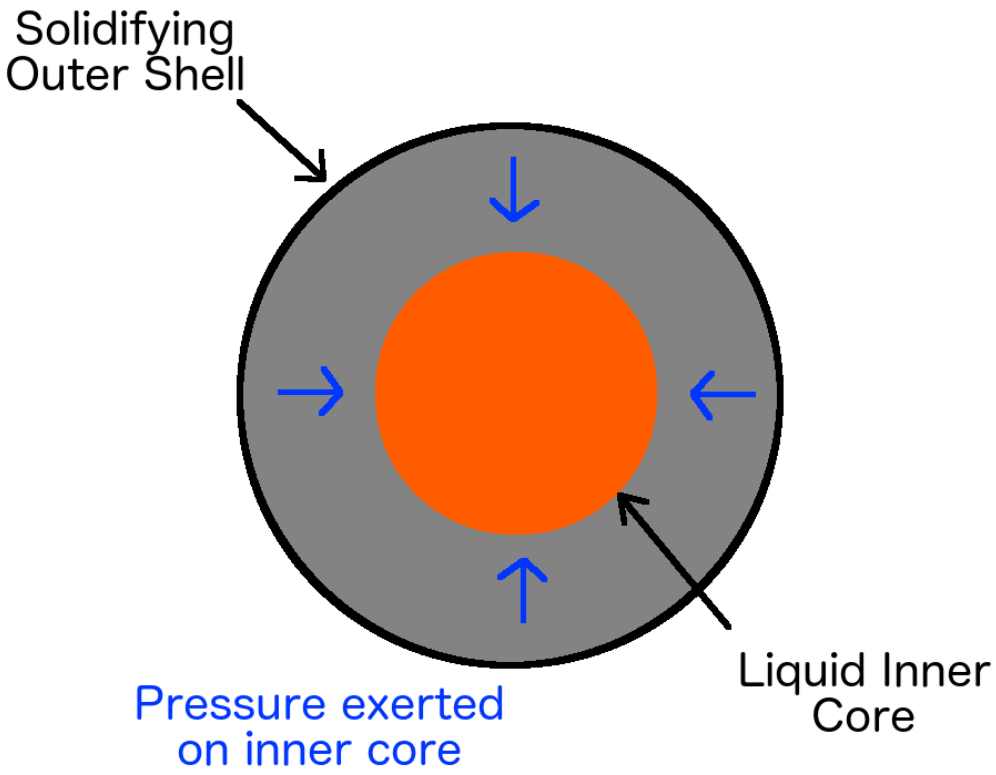


Figure 10.6: Visualisation of a cooling particle cross section with a solidifying outer shell exerting pressure upon a liquid core

The phenomenon of droplets exploding under rapid cooling is not exclusive to laser drilling, as shown by Wildeman [10.5], who demonstrates the same mechanism occurring within water droplets which have been supercooled on a hydrophobic surface.

SEM images of particles which were collected in this work provide further evidence of the theorised underlying particle explosion mechanism. Figure 10.7 identifies a solid particle outer shell which appears to have exploded, ejecting its liquid core due to the build up of high pressure.

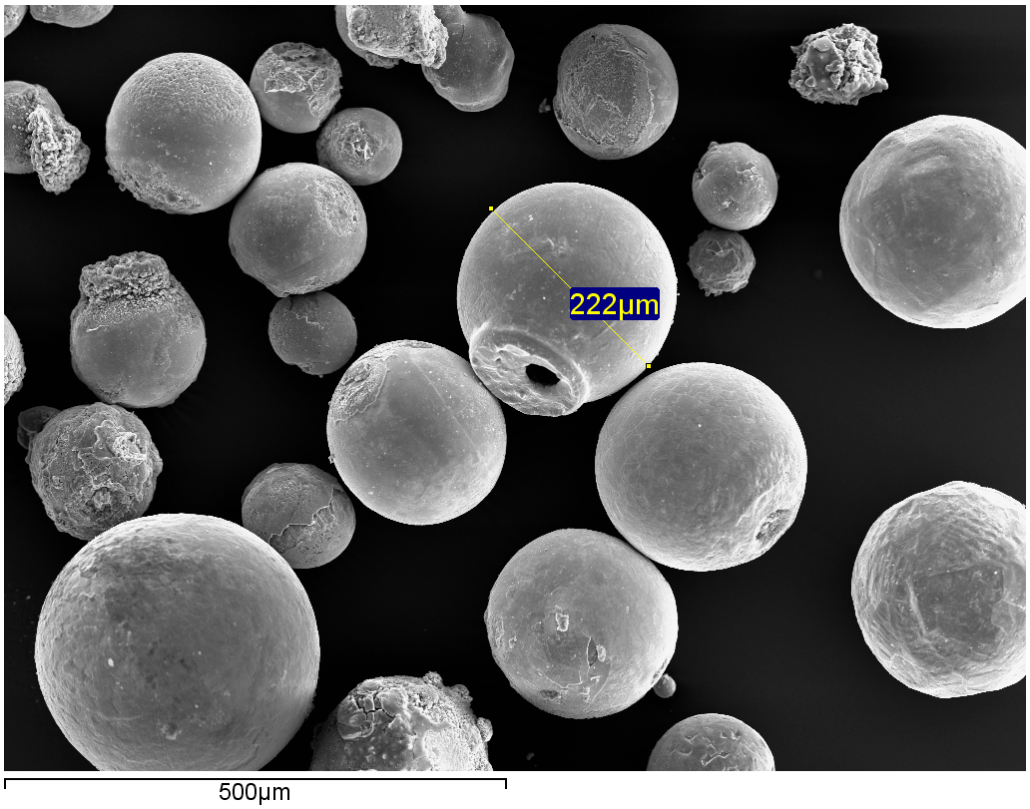


Figure 10.7: Scanning Electron Microscopy (SEM) image of mild steel particles captured from 2kW laser, 1000W laser power, 2Bar Nitrogen assist gas experiments

Explosions of particles ejecting their liquid core under rapid cooling are also apparent within the recorded high-speed videos (Figure 10.8), where a single particle suddenly appears as several, whilst maintaining its general direction and without losing size.

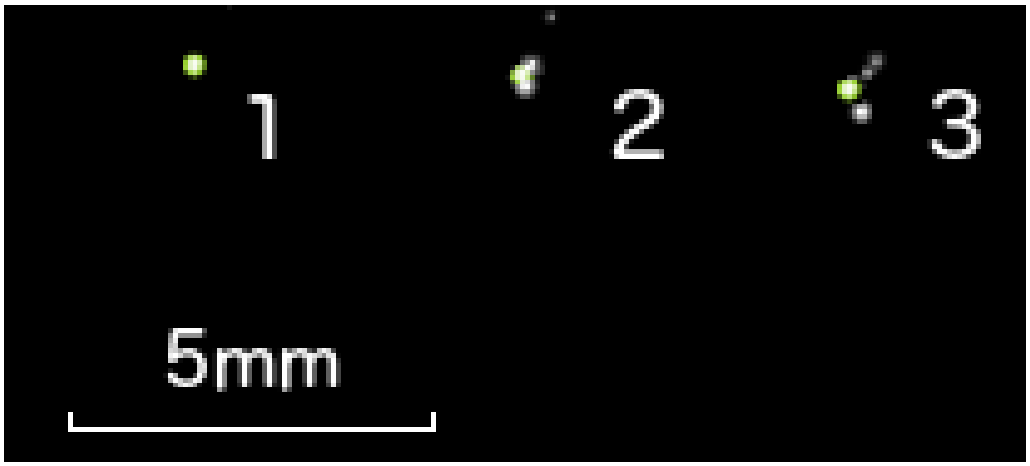


Figure 10.8: Exploding particle (in green) retaining its size and direction through explosion, shown as 3 frames (484 µs) - 2kW Laser, 1000W Laser Power, 2Bar Nitrogen Assist Gas

Exploding particles have been observed frequently throughout the different parameters used within this work, however, they have not been found in the aluminium test videos. Although, this is not conclusive, as less videos were recorded for the aluminium tests than mild steel and titanium (as many of the conditions tested were not adequate for the breakthrough of aluminium). However, whether exploding particles do not occur in the millisecond laser drilling of aluminium or they are just less frequent, it is likely that this is to do with the high specific heat capacity of aluminium - around 895 - 933J/kg.K, compared with 498J/kg.K and 513 - 599J/kg.K for steel and titanium respectively [10.6]. Aluminium's ability to dissipate heat quickly may allow the molten core of particles to cool much more quickly than those of mild steel and titanium, preventing a pressure build up large enough to cause particle explosion.

The presence of exploding particles in the rear ejecta cloud results in changes in particle number, velocity, size and direction of the ejecta cloud. These changes also mean that the exploding particles will add in some uncertainty into the predictions of the particle debris cloud. However, the relatively low number of exploding parti-

cles compared to total number of particles means that the overall uncertainty will likely be negligible when observing the evolution of the debris cloud over 50 total videos.

10.2 Particle Number

It is important to acknowledge that the particle numbers listed account only for those rear ejected particles which are visible within the focus of a thin plane, 1.87mm in width, due to the minimal focal length of the camera, rather than an all around view. Although the particle directions vary through individual videos, the frequent symmetry seen through the contour plots suggests that 50 videos are sufficient to enough to cancel out any individual video directional bias and produce a fairly, randomly distributed set of results.

A lot of unexpected variation is observed between the different parameters shown in the particle number graphs shown in Section 6.3, which identifies the common industry problem that it is very difficult to predict how a particular material may react to laser drilling under a range of parameters without testing. However many trends can be observed.

Many clear differences can be observed between the particle number graphs produced using the 2kW laser, as shown in Section 6.3.1 and the 6kW laser, as shown in Section 6.3.2. When comparing these two sets of results, it is important to know that both lasers have a similar spot size of around 200 µm, meaning that the laser powers are directly comparable. However, as well as the higher potential power of the 6kW laser, the 6kW laser differs from the 2kW laser in beam shape.

The 6kW laser beam produces a more gaussian profile than the 2kW laser, which produces a beam profile that is more top-hat. This is reflected in the beam profile measurements which give the M^2 values as 6.05 and 23.3 for the 6kW laser and the

2kW laser respectively - whilst a perfect gaussian beam has an M^2 value of 1.

As well as the beam profile, the 2kW and 6kW lasers differ in nozzle size, 1mm in diameter vs. 3mm in diameter respectively. This is important as the assist gas is passed through the nozzle. Therefore, even though the recorded pressure may be the same between certain parameters, the mass flow rate will be much higher for the 6kW laser.

The same parameters have been used for 2Bar and 5Bar results from each of the different lasers, suggesting that they are ideal for comparison. However, a 60mm lens, rather than the 105mm lens which was used for all of the other results. In order to try to make the results comparable the larger frame sized 60mm lens images have been cropped to match those of the 105mm frame. As the 60mm lens was also used for recording from further away, the particles did not appear as bright on the screen, meaning that the dimmest particles were not being identified. In an attempt to balance this out, the exposure time was set to 4 µs rather than 1 µs which was used with the 105mm lens.

The first difference between the two lasers are the laser powers at which breakthrough occurs. Breakthrough occurred at the lowest power tested, 500W with the 2kW laser with a 10ms pulse width, for both a 2Bar and 5Bar assist gas. For the 6kW laser with a 10ms pulse width, the lowest power that breakthrough occurred at was 1500W for the 2Bar assist gas and 4000W for the 5Bar assist gas.

This lack of penetration by the 6kW laser at the lower powers is most likely caused by the difference in nozzle diameter. The area of the nozzle orifice for the 6kW laser is 9 times larger than the 2kW laser and therefore is very likely to produce a higher mass flow rate at the same pressure - the velocity of the gas flow is required to calculate the exact values. A higher mass flow rate exiting the nozzle could eject the melt pool upwards too quickly, preventing the transfer of thermal energy within the material, ultimately limiting the depth of the melt pool.

However, the more gaussian shaped beam profile of the 6kW laser produces a less evenly dispersed power distribution across the area of the 200 µm spot size than the more top-hat 2kW laser beam profile. At the same laser power a more top-hat beam profile will create a wider, shallower and more cylindrical hole whilst a more gaussian beam profile will create a narrower, deeper and more tapered hole as demonstrated by Sharma using COMSOL modelling techniques [10.7]. Therefore, the effect of the larger nozzle on limiting the depth of penetration must be sufficient enough to cancel out the differences in drilling depth caused by the beam profile differences between the two lasers to explain the differences in breakthrough powers.

Because penetration was not possible for the lower powers, there are no like for like matches of particle tracking results between the two lasers used within this work. The closest match is 1500W, 2Bar assist gas and 2000W, 5Bar assist gas for the 2kW laser with 2000W laser power, 2Bar assist gas for the 6kW laser.

Three materials were tested using the 2kW laser, 1mm thick mild steel, 1mm thick titanium and 2mm thick aluminium. Each of these were tested using assist gas pressures of 8Bar and 12Bar with a 10ms pulse width through powers 500W to 2000W. In comparison, breakthrough occurred for all powers for the mild steel results and the 12Bar titanium tests, however breakthrough did not occur for 500W laser power with the 8Bar titanium tests and only occurred at 2000W for aluminium with both assist gas pressures.

The thickness of the aluminium, which is double that of the mild steel and titanium, will definitely contribute to whether or not breakthrough occurs at certain powers. However, preliminary testing using the 2kW laser, a 10ms pulse width and 2Bar nitrogen assist gas has proven capable or penetrating 2mm thick mild steel for 1000W laser power (500W was not tested). Therefore, as well as the increased thickness compared to the other materials tested, it is likely that the relatively high specific heat capacity of aluminium plays a large part in why 2mm thick aluminium

was not penetrated by laser powers below 2000W.

The specific heat capacity at 100 °C for aluminium is 895 - 933J/kg.K, compared with 498J/kg.K for steel and 513 - 599J/kg.K for titanium [10.6]. Specific heat capacity is a measure of the amount of heat needed to raise the temperature of 1kg of a material to 1 kelvin and in this case, represents the ability of the material to dissipate heat energy across the material and away from the hole. Therefore, aluminium's increased ability to dissipate heat energy away from the hole means that a smaller melt pool will be formed with the same laser pulse compared to that of mild steel or titanium, and will cool quicker, meaning that more laser energy will be required to achieve breakthrough. Additionally, the high reflectivity of aluminium, compared with mild steel and titanium, likely reduces the amount of energy absorbed from the laser radiation and therefore there will be less heat energy available within the material for material removal under the same conditions. The large difference in melting temperatures must also be considered, with mild steel, 1540 - 1595 °C [10.6], being similar to titanium at 1671 °C [10.6] compared with aluminium at a much lower 660 °C [10.6].

The lack of penetration for 500W laser power with a 2Bar assist gas for titanium is also likely due to the slightly lower specific heat capacity of titanium than steel. However, penetration does occur at 500W laser power when the assist gas pressure is increased to 5Bar due to the increased pressure occurring within the hole. This is because an increased build up in pressure from the assist gas means that melted material will be removed more quickly, creating space for material deeper within the hole to be melted by the laser pulse.

In terms of particle number, the cumulative number of particles through 20 frames increases from 8Bar to 12Bar for all three materials. However, at 2000W laser power, titanium has around 10 times the number of cumulative particles, with mild steel having around 10,000 more particles over 50 videos than aluminium at 12Bar whilst

being similar at 8Bar, as shown in Figure 6.4.

Figure 6.4 also shows that titanium consistently has a higher number of cumulative particles than mild steel for matching parameters. Whilst mild steel steadily decreases in particle number as power increases for both 8Bar and 12Bar, titanium is more varied through 8Bar and 12Bar, with little overall change except for a large jump in particle number of almost 100% between 500W and 1000W for 8Bar.

It is reasonable to assume that the decrease in particle number with increase in laser power for mild steel, as shown in fig. 6.4 , is due to a more efficient material removal process due to the higher input of energy. If a hole is drilled quicker, due to a higher input energy, ejection will take place sooner, removing the melt pool faster. Consequently, there is less time for heat to dissipate through the material from the current melt pool and therefore, expand the melt pool. Ultimately, this means that overall, a smaller melt pool is formed, resulting in decreased rear ejection with increased laser power.

This effect may not be noticeable at these powers for titanium or aluminium due to the higher specific heat capacity of the material. A higher specific heat capacity means that heat will dissipate across the material faster and a 2000W laser power may not be high enough to interrupt this process. It is therefore reasonable to assume that for both titanium and aluminium, the number of particles ejected rearwards would decrease at some point due to an increased laser power input above 2000W for identical conditions. Further work would be required to investigate this.

The majority of testing was carried out at a single pulse width of 10ms. However, 2ms, 5ms and 10ms pulse width tests were carried out using the 6kW laser with no assist gas on mild steel. Laser powers 500W - 6300W were tested for 2ms and 5ms pulse widths and 500W - 6000W for a 10ms pulse width. For a single pulse, penetration did not occur for any of the 2ms pulse width tests, penetration occurred at 4000W and higher for single 5ms pulses and for 1000W and over for single 10ms

pulses.

For like powers, 5ms pulses consistently produced a smaller number of particles than 10ms pulses, the difference between which, decreased as power and overall particle number increased as shown in Figure 6.5.

Energy per pulse is equal to the laser power multiplied by the pulse width, for example for 1000W laser power, a 10ms pulse emits 10J of energy, a 5ms pulse emits only 5J of energy and a 2ms pulse emits only 2J of energy. Of course, the overall energy provided by a laser pulse influences its potential for breakthrough, a high energy provided means that there is more chance of breakthrough when compared to a small one. However, the results provided for the parameters tested suggest that pulse width, as well as energy provided, plays a large part in whether or not breakthrough is achieved.

For the 6kW laser with no assist gas, a single 2ms pulse at 6300W laser power (12.6J) repeatedly failed to penetrate 1mm of mild steel, as did a 5ms pulse at 3000W laser power (15J), as shown in fig. 6.3. However, breakthrough was consistently achieved with a single 10ms pulse at 1000W (10J). This shows that, for the given set up, 2ms and 5ms pulses are less effective at drilling than 10ms pulses. The most likely reason for this is to do with the absorbance of the mild steel test piece. Absorbance is a dynamic process in laser drilling, because absorptivity of a material changes as oxide layers are removed, material starts to melt or vaporise and a hole begins to form. The complex effect of these variables have been investigated by Bergstrom, [10.8], who demonstrates the difficultly in predicting the dynamic absorption of materials in laser processing for 1 µs pulses. Although the exact mechanism is unclear, it is likely that a larger proportion of the shorter pulses (2ms and 5ms) interacts with the initial solid state outer surface of the test-piece, than the longer pulse which can be absorbed later, therefore, bypassing any oxide layer and potentially being absorbed by molten material, which may mean that a larger percentage of the longer pulse is

absorbed.

Work by Markcoons et al. [10.9] using the same 2kW laser and similar set-up as used in this work, with a 1Bar argon assist gas experimentally demonstrated the minimum laser power required for breakthrough for 0.8mm, 1mm and 2mm thick mild steel for 4ms, 6ms and 25ms pulse widths. Calculating the energy of each pulse from these results shows that for the 2kW laser under these parameters, increasing pulse width leads to a decrease in efficiency, with shorter pulse widths being more effective for achieving breakthrough with the same energy, as shown in Figure 10.9. The contradictory trends seen here between the 6kW laser and the 2kW laser regarding pulse width and its effect on drilling efficiency further back up the likelihood that the complex mechanisms behind material absorption are the cause, because the difference in beam shape between the two lasers, with the 6kW laser being more gaussian, is likely to impact the differences in absorption.

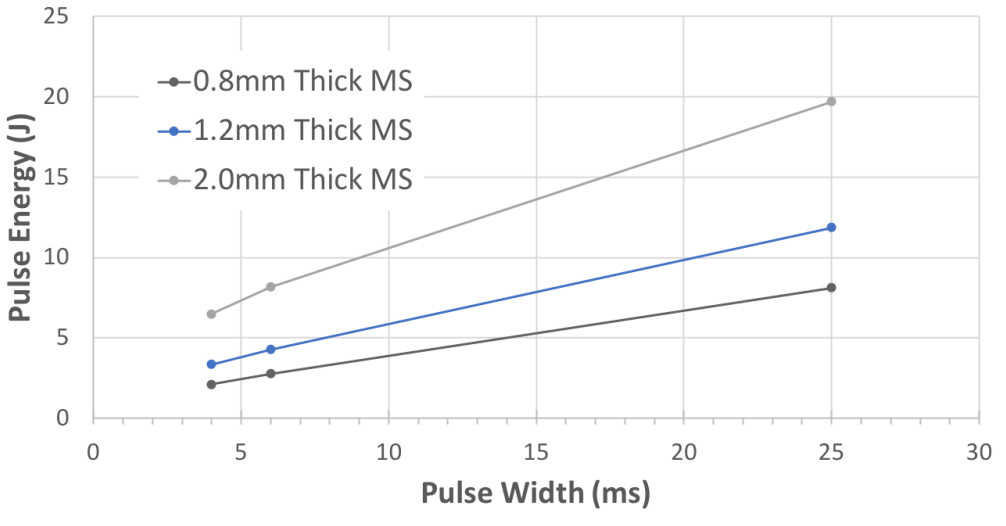


Figure 10.9: Markcoons et al. [10.9] results for minimal breakthrough power displayed as laser pulse energy vs. pulse width - 2kW laser, 1Bar Argon assist gas, Mild Steel

For the 2kW laser, 2Bar, 5Bar, 8Bar and 12Bar assist gas pressures have been tested under various parameters, whilst 0Bar, 1Bar, 2Bar and 5Bar have been tested for the 6kW laser. As previously discussed, the gas pressures of the 2kW laser and

the 6kW laser are not directly comparable because of the difference in nozzle size - with a 1mm nozzle orifice for the 2kW laser and a 3mm nozzle orifice for the 6kW laser.

For the 2kW laser results, it is important to note that a 60mm lens was used with a 4 µs exposure time for the 2Bar and 5Bar results, whilst a 105mm lens was used with a 1 µs exposure time for the rest of the work conducted in this study. Although the larger 60mm lens images have been cropped to the same size as the 105mm images, it must be assumed that they are not directly comparable. Taking this into account, when looking at Figure 6.4, a general trend can be observed for the 2kW laser in that an increase in assist gas pressure produces an increase in particle number.

The opposite effect can be observed in Figure 6.5, with an increase in assist gas pressure being inversely related to particle number, with no assist gas producing the highest number of particles. These results demonstrate that the presence of an assist gas has a clear influence on the number of particles ejected. This is expected because as well as participating to clear the melt pool, the force provided by the assist gas adds kinetic energy into the drilling process which may assist in the overcoming of surface tension forces in the initial melt pool, creating the potential for increased number of droplets. This reasoning can help to explain why the number of particles increase with assist gas pressure for the 2kW laser. However, the decrease of particle number with an increase in assist gas for the 6kW laser can be explained by the effect of the assist gas on the melt ejection fraction and the time taken for the evacuation of the melt pool.

It may be that the larger mass flow rate produced by the larger nozzle of the 6kW laser produces a larger pressure build up in the hole early on in the ejection process, before breakthrough is achieved. If so, this could result in a larger proportion of the melt pool being upwardly ejected, leaving less material to be ejected rearwards, resulting in a smaller number of particles to be observed. Also, a quicker evacuation

of the melt pool could remove energy from the process, as the removal of hot molten material also takes away the thermal energy stored within it. This means that there is less time for the heat to dissipate across the material, overall resulting in a smaller melt pool and therefore less material removal and a smaller number of particles.

When looking at the effect of laser power with particle number, Figure 6.4 shows an inverse relationship, with particle number decreasing as laser power increases. The peaked distribution of particles with respect to time also appears to flatten as laser power increases. This trend is not apparent with titanium, as particle number remains similar between different powers, although a large increase is seen from 500W to 1000W for the 12Bar results.

Again, the opposite trend is seen for the mild steel results with the 6kW laser to that of the 2kW laser, with particle number generally increasing with laser power, as shown in Figure 6.5. However, for all 10ms pulses, a decrease in laser number is seen between 6000W and 6300W with an assist gas and 5000W - 6000W for no assist gas. An unexpectedly high number of particles are also seen for 2000W laser power with no assist gas, when compared to the apparent trend.

For the same pulse width, assuming particle size is constant, it is logical to expect that an increased laser power will lead to an increased number of particles as a larger energy input into the hole should create a larger melt pool and therefore more ejection as is seen with the 6kW results. However, as previously discussed, a quicker breakthrough time, or material being ejected more quickly, could result in a smaller melt pool, as there is less time for thermal energy to dissipate across the material. This is likely the reason why, for the 2kW laser, particle number decreases as power increases for the parameters investigated. A faster breakthrough time could occur due to the higher laser power introduced. At a higher laser power, an increased amount of vaporisation of the top layer of material would occur. Although, this effect

is still small for a millisecond pulse width, it could cause a higher pressure build up, leading to a quicker evacuation of the melt pool, resulting in quicker breakthrough. Therefore, a higher laser power will lead to a quicker time to breakthrough, which may lead to less dissipation of heat through the material by conduction/convection as thermal energy is lost more quickly from the system in the form of the melt pool. The higher pressure caused by increased vaporisation early on the melt ejection process could also lead to an increased amount of upward ejection in relation to rear melt ejection, further explaining the results seen with the 2kW laser.

10.3 Particle Velocity

Figure 7.1 shows the overall mean particle velocities for each set of 2kW laser results across the first 20 frames of ejection. A clear trend is seen across all materials and powers, with mean velocity increasing between 0.5 - 1 ms^{-1} between 8Bar and 12Bar assist gas pressures. This is expected as a higher assist gas pressure produces a higher velocity gas flow, which can accelerate the speeds of ejected particles. Generally, little change in mean velocity is seen between different powers.

Higher mean velocities are seen for the 2Bar and 5Bar particle velocities, approximately 5 ms^{-1} higher than that of those seen for the 8Bar and 12Bar mild steel results. Analysis of the particle numbers has already shown a clear difference between the 2Bar and 5Bar results, with a significantly higher number of particles being observed. It is possible that the use of the 60mm lens with the 4 µs exposure time is more sensitive to smaller particles, which are not visible with the 105mm lens with a 1 µs exposure time. Due to their size, it is likely that these smaller particles, which are only seen with the 60mm lens are moving more quickly. This could explain why a significantly higher mean velocity is seen for the 2Bar and 5Bar results. For this reason, it is not possible to draw a clear comparison of these pressures with the other results.

It is also clear that particles from the titanium and aluminium test pieces are ejected with a velocity of around 2 - 4 ms^{-1} faster than the mild steel test pieces - except for 500W laser power with a 12Bar assist gas for which the mean titanium velocity is similar to that of mild steel. A higher velocity for titanium and aluminium compared to steel is to be expected due to the lower density of titanium at 4510kg/m^3 [10.10] and aluminium at 2700kg/m^3 [10.10] compared with 7850kg/m^3 [10.11] for steel. A higher velocity is also seen for aluminium when compared to titanium, as expected with regards to density, although this is only comparable for 2000W as penetration was not achieved with the aluminium test piece for lower powers.

Figure 7.3 shows the overall mean particle velocities for each set of 6kW laser results across the first 20 frames of ejection. A higher mean velocity is seen with no assist gas compared to 1Bar and 2Bar through all powers except for 3000W, where there is little difference and the same is seen with 5Bar velocities, except for at 5000W where the no assist gas mean velocity is around 1 ms^{-1} lower. This suggest that, if any, the presence of an assist gas has a negative effect on mean particle velocity, the opposite of what is seen with the 2kW laser. However, it may be that for the 6kW laser the assist gas pressure is causing the smallest, fastest particles to accelerate to velocities which cannot be tracked due to the limitations of the particle tracking program used. The generally lower tracking efficiency produced by higher assist gas pressure further supports this theory, as shown in fig. 6.7 for the 6kW laser. Mean velocity is 4 - 5 ms^{-1} lower for the 1Bar and 2Bar results than those tested with no assist gas.

Figure 7.3 also shows that for the 1Bar and 2Bar assist gas, 6kW laser results, for the initial breakthrough powers, 1500W and 2000W respectively, the mean particle velocities are particularly low, around 4 ms^{-1}. This may be due to a a smaller pressure build up because of a more efficient drilling process with less melt, as the minimal melting is carried out to achieve breakthrough. A smaller pressure build up could also occur near breakthrough due to a larger amount of upward ejection as time

until breakthrough will likely take longer near the breakthrough threshold.

Figure 7.4 shows the particle velocity distribution for all results combined. The same distribution is also shown across all parameters individually. A similar distribution pattern across all parameters demonstrates the usefulness of using the mean particle velocity across multiple frames.

Figure 7.4 shows that particle number doubles between 2 - 4ms^{-1}. When compared to the individual distributions, as well as those given for particle size in **??**, it is clear that this is most likely due to the difficulty in observing very small particles with the given camera set-ups. This is apparent because there is a clear correlation between the fastest particles also being the slowest particles - this is confirmed in the momentum results, shown in fig. 7.12. Therefore, a lack of magnification in the filming set-up means that the smallest and fastest particles are not recorded, this is a prior known limitation of the set-up. This explains why a rapid mean particle velocity increase is shown in fig. 7.4.

An exponential decay occurs with velocity increase, as shown in fig. 7.4. This is due to the distribution of particle sizes, as many more small particles are observed than large. The smallest particles are faster than larger particles, as expected. This is because less energy is required to accelerate a smaller particle to the same speed as a larger particle.

Figure 7.4 shows that the largest particles are around 80ms^{-1}, whilst the majority of particles appear to be around 5ms^{-1} for all parameters, as indicated by the peak on fig. 7.4.

10.4 Particle Size

The 2kW laser results, given in fig. 7.6 and fig. 7.5, show a variation of up to 60 µm in mean particle diameter when assist gas pressure and material type are the same.

However, no consistent trends can be drawn from this data that suggest that particle size is directly linked to laser power for the 2kW laser.

This is not true for the 6kW laser results shown in fig. 7.7, as a clear trend is shown for breakthrough powers for all parameters tested except for the no assist gas tests with a 10ms pulse width. A noticeable decrease in mean particle diameter is shown from the breakthrough power to all other laser powers for the same parameters by up to 45 µm when compared to the general trend of mean particle size with laser power.

As previously discussed in section 10.3, a difference in the results for the initial breakthrough powers have also been observed in the velocity results for the 6kW laser. This suggests a clear difference in the laser drilling mechanism for breakthrough powers with the 6kW laser and, as theorised, for the velocity differences. This can be explained by the likelihood that drilling with a laser power nearest to the breakthrough threshold will be a more efficient process than one further from the threshold. This is because there is likely to be a smaller pressure build up with a smaller melt production and possibly increased removal of material by upward ejection. The lower the pressure in the hole, the less force that will be exerted upon the melt pool within the hole, this, combined with less heat due to a smaller melt pool could mean that less energy is available to overcome the surface tension forces necessary to separate a viscous melt pool into multiple particles. Taking this into account, it appears logical that larger particles would be expected at laser powers nearest to the breakthrough threshold. However, this effect is likely limited at a certain laser power as breakthrough speed increases in such a way that extra energy is not necessarily added to the system in the terms of increased melt pool or pressure build up. This explains why mean particle diameter does not continue to decrease as laser power increases for these results.

For the 2kW laser the variation in mean particle diameter between 8Bar and 12Bar

titanium is similar to that for 8Bar and 12Bar mild steel, around 50 µm, as well as that between 2Bar and 5Bar mild steel, as shown in fig. 7.5. This suggests that there is no outstanding difference between titanium and mild steel in terms of their change in particle diameter with laser power. However, there is a clear difference between titanium and mild steel with regards to mean particle diameter. Figure 7.5 shows titanium to have a mean particle diameter to around 100 - 150 µm higher than that of mild steel throughout the parameters tested for an 8Bar and 12Bar assist gas. It must be acknowledged that the 2Bar and 5Bar mild steel results are not comparable in this aspect due to the differences in lens and exposure time used.

Figure 7.7 shows that mean particle diameters are approximately 20 - 100 µm larger without an assist gas for the 6kW laser. The introduction of an assist gas to the system likely increases the pressure within the hole. A higher pressure in the hole means that more energy is available for the melt pool to overcome the surface tension forces within the material to separate into particles upon ejection. Therefore, it is likely that the smaller mean particle diameter seen with the assist gas tests is a direct cause of the assist gas and an increased pressure build up within the hole.

Although little data is available for comparison, fig. 7.7 suggests that the difference of mean particle diameter with pulse width is minimal, as there is little variation between the no assist gas, 10ms pulse width and 5ms pulse width. However, more data is required to confirm this.

Figure 7.8 shows the particle diameter distribution for all results combined. The same distribution is also shown across all parameters individually. A similar distribution pattern across all parameters demonstrates the usefulness of using the mean particle diameter across multiple frames, as done in the previous results.

Figure 7.8 shows that particle number increases rapidly from 0 to 0.3 µm. When compared to the individual distributions, it is clear that the camera set-up limitations make it difficult to observe the smallest particles. This is due to the calibration

factor used for these tests, which limits the smallest particle size to 69 µm. As well as this, the smallest particles will likely cool quickest due to their small size, this will make them invisible on the videos due to their lack of brightness, explaining why many of the smallest particles appear to be missing from fig. 7.8.

An exponential decay occurs with diameter increase, as shown in fig. 7.8. This is due to the distribution of particle sizes, as many more small particles are produced than large.

Figure 7.8 also shows that the largest particles produced are around 1000 µm. The majority of particles are around 200 µm - as indicated by the peak in fig. 7.8.

10.5 Particle Momentum

To make the most of the particle diameter and particle velocity results it is important to look at their relationship to each other as well as individually in order to get a better understanding of the rear melt ejection process. This has been done by comparing momentum against particle number. As well as shedding some light on the relationship between particle size and velocity, momentum helps in understanding the effects of different materials in laser drilling and how they can affect the rear melt ejecta process.

Firstly, looking at the mean momentum plots shown over the 20 initial frames, as shown in section 7.3.1, it is clear to see from fig. 7.9 that, for the 2kW laser results, there is relatively little change in momentum between different laser powers. This suggests that laser power does not have a large influence on momentum for the 2kW laser parameters. A clear difference is seen between the 2Bar and 5Bar mild steel results and the 8Bar and 12Bar mild steel results, however, as with the other results, this is not a fair comparison due to the different lenses and exposure times used to record these videos. However, there is a clear difference shown between

mild steel and titanium for the results shown, with titanium having around 0.2 - 4 x 10^{-5} kg.ms^{-1} higher mean momentum than mild steel through all laser powers. Aluminium is more difficult to compare as only one power was tested, but the mean momentum is around 0.1 x 10^{-5} kg.ms^{-1} higher than mild steel for the 12Bar tests, whereas for 8Bar the difference is negligible.

For the mean particle momentum results shown in Figure 7.9, it can be seen that the difference between 8Bar and 12Bar mild steel results, up to 0.5 x 10^{-5} kg.ms^{-1}, is much smaller than the difference between the 8Bar and 12Bar titanium results, up to 0.3 x 10^{-5} kg.ms^{-1} and the 8Bar and 12Bar aluminium results, up to 0.1 x 10^{-5} kg.ms^{-1}.

Figure 7.11 shows the mean particle momentum through the first 20 frames for the 6kW laser results. In comparison with the 2kW laser results, the 1Bar and 2Bar results from the 6kW laser are very close to that of the 2kW laser, 8Bar and 12Bar mild steel results, between 0.5 - 1 x 10^{-6} kg.ms^{-1} for similar laser powers.

The 6kW results in fig. 7.11 also suggest that the rear ejected particles from the no assist gas tests have a higher mean momentum, between 0.5 - 2 x 10^{-6} kg.ms^{-1} higher, than the tests with assist gas. As discussed previously, this may be due to the potential of the assist gas to increase upward ejection, thereby reducing rear ejection and to clear the melt pool faster, which could result in an overall lower absorption of the laser pulse energy by radiation.

As is shown with the 2kW laser mean momentum results, the 6kW laser mean momentum results show no clear trend between laser power and momentum, with a maximum variation of around 1 x 10^{-6} kg.ms^{-1} between different laser powers for the same parameters. Generally, little difference is seen in variation when comparing mild steel results between the two lasers with like for like filming conditions.

No clear trend is shown between the 1Bar, 2Bar and 5Bar results in fig. 7.11, despite

the clear importance of assist gas to momentum, as shown by the difference between tests with and without assist gas. However, the no assist gas, 5ms pulse width results are 0.25 - 0.75 x 10^{-6} kg.ms^{-1} lower in mean momentum than the no assist gas 10ms pulse width results. This is likely due to the less energy supplied by the shorter 5ms pulse than the 10ms pulse.

Figure 7.12 shows the particle momentum distribution for all of the results combined. As with the particle size and velocity distributions, a similar distribution is shown across all parameters individually. Because the distribution is similar across all parameters, this shows that the mean particle momentum is a useful statistic for comparing different parameters.

Figure 7.12 shows a similar distribution for both the overall particle velocity and particle size distributions, however the decay is shown to be much more rapid in momentum with particle number than is observed for velocity and diameter individually, this is why a logarithmic axis has been used for particle number in fig. 7.12.

Figure 7.12 shows that the highest momentum particles are around 600 x 10^{-6}kg.ms^{-1}, whilst the majority of particles are less than 10 x 10^{-6}kg.ms^{-1}.

10.6 Particle Cloud Distribution

Figure 8.13 demonstrates how the oval archetype is the most prevalent throughout all of the parameters. The oval archetype, shown in fig. 8.4, reflects an evenly dispersed particle cloud, and is often seen at the initial stage of the particle cloud evolution. The high frequency of this archetype through many parameters suggest that it is common for the majority of the initial particles to leave the exit hole at similar times and similar speeds.

The pointed archetype, shown in fig. 8.2, represents an early stage in the particle cloud evolution where the particles directly below the exit hole are shown to be

ahead of all of the other particles in the cloud. It is possible that this is a direct cause of the initial jet, which has been identified in the videos, as shown in fig. 10.3. Figure 8.13 suggests that the initial jet may be less common in the 2kW laser, mild steel experiments, as the pointed archetype is observed much less frequently here than for other parameters.

The triangular archetype, shown in fig. 8.1 is mostly observed for the 2kW, 5Bar, mild steel tests and is always secondary to the oval archetype. It is possible that a plug effect is taking place due to the assist gas, as shown in fig. 10.10. It is possible that the melt within the hole, which is continually ejected over the first 3226 µs, is acting as a dynamic plug to the faster moving nitrogen assist gas. It may be that a proportion of the assist gas is being forced out to the sides of the exit hole, propelling some of the melt with it. Of course, such a pressure from the assist gas on a large mass of melt would also inevitably lead to a point of increased particle velocity and density directly below the exit hole, which is reflected in fig. 8.1.

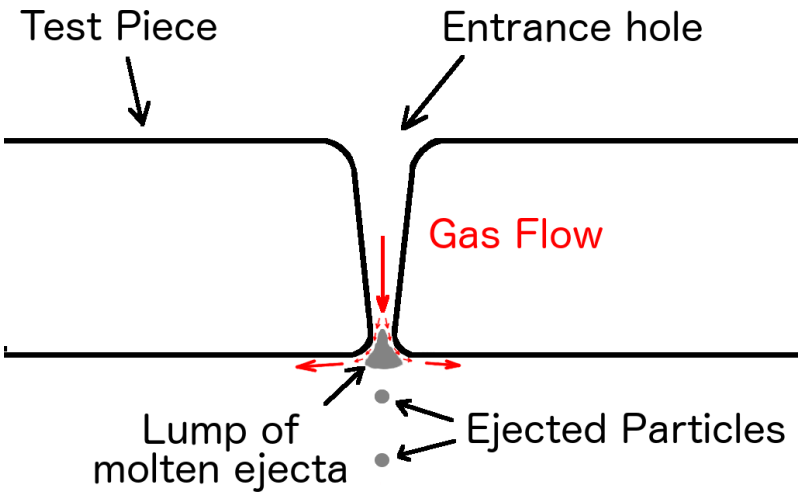


Figure 10.10: Schematic demonstrating how melt within the hole can act as plug, forcing assist gas out to the side

The heart archetype, shown in fig. 8.6, shows a gap in the outermost particle cloud directly below the exit hole. Although this would suggest there are less particles, or slower particles present at this point, it is likely the opposite scenario. Upon reviewing the videos, it is clear that the fastest particles tend to emerge directly below the exit hole. It is possible that for the 6kW laser, many of these particles are moving so fast that they disappear off of the screen early in the ejection process, therefore, the heart archetype, which tends to occur later in the particle cloud evolution reflects the particle density after many of these faster particles have left the screen.

The square archetype, shown in fig. 8.5, is generally only observed during the no assist gas tests, where it is quite common. The flatter shape on the bottom, furthest from the exit hole, demonstrates the lack of a point which may otherwise be caused by an assist gas. However, since the cloud is not evenly spread as a semi-circle, it is apparent that a higher proportion of particles are accelerated downwards, directly below the exit hole. This suggests that a higher proportion of the build up of pressure within the hole is transmitted downwards, rather than sideways. The surface tension forces in radial ejection may also magnify this effect, since the mechanism described in fig. 10.5 may essentially act as a brake on the radially ejected particles, when there is no assist gas to force them along.

The mushroom archetype, shown in fig. 8.10, has only been shown to occur for the tests using aluminium. This mushroom archetype depicts a particle cloud evolution in which particles expand out fairly evenly, before shrinking back in to a bottleneck close to the exit hole. This could be a direct effect of the lower density of aluminium when compared with mild steel and titanium. Whilst the faster moving particles continue to expand outwards, the slower moving particles may not have the inertia to overcome the pull of the assist gas, which is primarily channelled directly below the exit hole. As well as this, the high-speed assist gas (8Bar and 12Bar) likely strips particles from the inside of the hole, which are still hot enough to overcome

surface tension forces.

The split archetype, shown in fig. 8.7, depicts a particle cloud with two separate sections, separated by a lack of particle density directly below the exit hole. This is most likely a direct effect of the mushroom archetype, also affecting mainly the aluminium tests, it is possible that the central fast jet has accelerated the lower density particles quickly off of the screen, leaving two separate clouds on either side which are not affected by the gas flow. With regards to the 2kW laser, 12Bar assist gas, 500W laser power result, the split archetype also likely occurs due to the high-speed central fast jet, caused by the 12Bar assist gas, accelerating the particles directly below the exit hole off of the screen.

The drop archetype, shown in fig. 8.8, is shown to occur only for the tests using titanium. The drop archetype occurs late in the particle cloud evolution process when pressure is much less within the hole. As with the mushroom archetype, it is possible that the inertia of the ejected particles is not enough to overcome the high gas pressures (8Bar and 12Bar) at this point. Therefore, the particles are directed straight downwards, resulting in the observed narrowing effect. As well as this, the high gas pressure is likely stripping particles from the hole which are still hot enough to overcome surface tension forces. The lower density of titanium, compared to mild steel, explains why this archetype is not observed for mild steel.

The keyhole archetype, shown in fig. 8.3, is only observed for the 6kW laser parameters with an assist gas, mostly for the 1Bar assist gas pressure, mild steel results. As this archetype does not occur without assist gas, it is likely that it is a direct effect of the central fast jet. It is possible that this is observed for the 6kW laser and not the 2kW laser because the larger nozzle may create an increased central fast jet effect, even when measured pressure is lower. Further testing of the gas flow outlet pressure may provide more information to explain this. The keyhole archetype is similar to the pointed archetype, however, it is only observed as a secondary

archetype and shows a much lower particle density around the point furthest from the exit hole. The low density around this point is likely caused by few high-speed particles, greatly accelerated by the central fast jet.

The side point archetype, shown in fig. 8.9 demonstrates that the particle debris cloud is not always symmetrical. In fact, when viewing individual videos, it is common for the ejecta to be preferential to either side within the video. It is likely that this random selection occurs simply due to short moments in time where melt may preferentially adhere to either side of the hole, altering the assist gas flow and directing the melt in a random direction. It was hoped that 50 videos of each parameter would be enough to balance out these random changes in direction, and for many parameters it has been, demonstrated by the largely symmetrical contour plots (approximately 70%).

However, for all of the non-symmetrical plots, it was found that they all preferentially adhere to the right hand side. Due to the unlikelihood of this occurring by chance, it is reasonable to assume that there is some systematic error playing a part in the laser set-up - which was used for both the 2kW and 6kW lasers. As this same lack of symmetry is observed for some of the no assist gas results, it is unlikely to be related to the assist gas. Therefore, the most likely reason is that some systematic error has favourably influenced a right hand side ejection pattern either from the set up of the test piece itself or the laser beam set up. Since the test piece was frequently altered throughout the experiment and several different test pieces were used, it is possible that the laser beam set-up is slightly out of line. It is recommended that further experiments undergo a laser calibration process to ensure that the beam is as straight as possible to negate this effect in future work. However, as this error has not carried through to the majority of videos it may in fact simply be down to chance, in which case a larger number of videos would be recommended in future testing in order to make sure that this is not the root of the problem.

Figure 8.11 shows how different archetypes correspond to different drilling parameters, and the order that which archetypes present for each set of videos. Figure 8.11 clearly shows that some archetypes are more likely to appear for certain parameters, and patterns can be observed in the sequential appearance of particular archetypes. For example, fig. 8.11 shows that either the oval or the pointed archetype present in the initial stages of ejection for every parameter tested, with the exception of 4000W, 2Bar, mild steel, for which the side point archetype is initially observed. This shows that the earliest stages of the particle cloud evolution are predictable for all parameters. It is also clear from fig. 8.11 that the pointed archetype occurs much more frequently as the initial stage of the rear ejecta cloud for the 6kW laser tests for mild steel, compared with the 2kW laser tests. Figure 8.11 also shows that the mushroom cloud is unique to the aluminium tests, whilst the drop archetype is unique to the titanium tests. Figure 8.11 shows that the heart archetype is frequently observed during the 6kW laser tests, whilst not at all for the 2kW laser tests. This is also true for the square archetype, however this is observed almost exclusively for the no assist gas tests.

In order to simplify the analysis of the patterns shown in fig. 8.11, each archetype has been summarised into a group. These groups are made up of the triangle type, oval type, heart type and mushroom type. The complete summary list is shown in fig. 8.12. The shape summaries have been plotted in fig. 8.12 and fig. 8.13 for further analysis. Figure 8.12 clearly shows that that general trends apply to the archetype observations relative to assist gas pressure and laser energy for the mild steel results.

Figure 8.12 shows that the triangular type is observed across all laser energies tested, mostly for assist gas pressures below 8Bar. The triangular types: pointed, triangular and keyhole archetypes, are characterised by an initial point of high velocity particles directly below the exit hole. Figure 8.12 suggests that a higher gas pressure is not directly tied to this particle cloud type as it is only observed at lower gas pressures

for mild steel. In fact, the triangular type is shown to be commonly observed within the no assist gas tests, as shown in fig. 8.13. However, the triangular type is shown to be common in the higher pressure, 8Bar and 12Bar, assist gas pressures for the titanium and aluminium tests, as shown in fig. 8.13.

Figure 8.12 shows that the oval type is observed across the full range of gas pressures tested and from 1 - 60 joules laser energy. However, fig. 8.12 also shows that for 40 - 70 joules laser energy, the oval type is only observed proportionally as gas pressure increases. This may be because a higher laser energy is more likely to promote a higher pressure in the drilled hole, increasing the chances of a pointed archetype, rather than an oval archetype in the earliest stages of ejection. Although a higher gas pressure can act to increase hole pressure, it may also act to decrease hole pressure due to an increase in upward melt ejection. This is especially true for the larger nozzle that is used for the 6kW laser, for which the highest laser powers are tested. This may explain why oval types are proportionally correlated with higher gas pressures at higher laser energies.

The heart type is definitively shown to be much more likely as laser energy and assist gas pressure increases in fig. 8.12. It is expected that the heart type would increase with laser energy as these archetypes are directly related by the effects of the central fast jet, caused by an assist gas. However, it is unclear why the heart types are more prevalent at higher laser energies. It is possible that an increased number of particles make this type more likely, as an increased number of particles means that more particles are more likely to be influenced by the assist gas. In this case, it is possible that this trend is drawn because particle number increases as laser power increases for the 6kW laser results - with which all of the higher laser powers are carried out.

Figure 8.12 also shows that asymmetry within the rear ejecta cloud is more likely at higher gas pressures and higher laser energies. It is unclear why this trend is shown,

as the cause of the lack of symmetry is also unknown, but assumed to be systematic error. However, a higher assist gas pressure and higher laser energy reflects a higher total energy being imparted into the system. Therefore, adding a higher overall energy to the system may exaggerate the systematic error which is imparted into the system.

It is clear that a lot can be learned by analysing the particle density in respect to time using the contour plot method. The identification of trends within this data can provide a powerful new insight into the complexities of the mechanisms of the micro-second laser drilling process.

References

[10.1] J. Hartnett, T. Irvine, Y. Cho, and G. Greene, *Advances in Heat Transfer*, ser. Advances in Heat Transfer. Elsevier Science, 1999, vol. 33, no. p192.

[10.2] D. Abidou, N. Yusoff, N. Nazri, M. A. Omar Awang, M. A. Hassan, and A. A. Sarhan, "Numerical simulation of metal removal in laser drilling using radial point interpolation method," *Engineering Analysis with Boundary Elements*, vol. 77, no. September 2016, pp. 89–96, 2017.

[10.3] S. Basu and T. DebRoy, "Liquid metal expulsion during laser irradiation," *Journal of Applied Physics*, vol. 72, no. 8, pp. 3317–3322, 1992.

[10.4] B. S. Yilbas, "Study of liquid and vapor ejection processes during laser drilling of metals ," *Journal of Laser Applications*, vol. 7, no. 147, 1995.

[10.5] S. Wildeman, S. Sterl, C. Sun, and D. Lohse, "Fast Dynamics of Water Droplets Freezing from the Outside in," *Physical Review Letters*, vol. 118, no. 8, pp. 1–5, 2017.

[10.6] F. Cverna and A. Committee, *ASM Ready Reference: Thermal properties of metals*, ser. ASM Ready Reference Series. ASM International, 2002.

[10.7] S. Sharma, Y. Pachaury, S. N. Akhtar, and J. Ramkumar, "A study on hydrodynamics of melt expulsion in pulsed Nd: YAG laser drilling of titanium," in *COMSOL Conference Pune*, 2015.

[10.8] D. Bergström, "The absorption of laser light by rough metal surfaces," *Thesis*, p. 226, 2008.

[10.9] D. Markcoons and K. Voisey, "An Investigation to Determine if the Laser Drilling Capabilities of a 2 kW Fibre Laser can be Enhanced Using Pulse Train Shaping," vol. 39, no. 1/2, pp. 17–33, 2017.

[10.10] C. Smithells, *Metals Reference Book*. Elsevier Science, 2013. [Online]. Available: https://books.google.co.uk/books?id=hUIvBQAAQBAJ

[10.11] M. Blair and T. Stevens, *Steel Castings Handbook, 6th Edition*. Steel Founders' Society of America, 1995. [Online]. Available: https://books.google.co.uk/books?id=QG3_QqmPZ_AC

11

Conclusions and Future Work

This section presents the overall conclusions drawn from this project and future work which could make use of these findings to further the understanding of the laser melt ejection mechanism and other areas of academic interest.

* * *

11.1 Conclusions

Three key rear ejection mechanisms were discovered, the initial fast jet, the central fast jet and radial ejection. The central fast jet was found to be a direct effect of an assist gas, whilst both the initial jet and radial ejection mechanisms were observed during tests with no assist gas.

Within the rear ejecta particle cloud, spontaneous exploding particles were observed across a range of parameters. Based on the observational analysis of the results in this thesis, these explosions are caused by a pressure build up within the particle. This pressure build up is likely caused by the rapid cooling and contraction of the particle surface. Evidence has been provided to suggest that during the explosion process, the liquid core of the particle can be squirted out to form multiple individual

droplets.

The particles within the rear ejecta cloud of laser drilling were measured using image analysis and particle tracking methods to provide data on the velocity, size and momentum of the particles. A similar distribution was observed for particle velocity, size and momentum individually across all parameters. The majority of particles were found to be relatively small and slow, with very few relatively fast, large particles. An exponentially decreasing relationship was shown for number of particles when compared with particle velocity, particle size and particle momentum separately.

Across all parameters, mean velocity was observed to be 4 - 13ms^{-1}, with a maximum velocity above 80ms^{-1}. Mean particle diameter was observed to be 180 - 500 µm with a maximum of 2500 µm. Mean particle momentum was observed to be 0.5 - 10 x 10^{-6} kg.ms^{-1} and maximum particle momentum was observed to be 550 x 10^{-5} kg.ms^{-1}.

The presence of an assist gas and its corresponding parameters were found to be significantly influential on the rear melt ejecta cloud. Assist gas and its effects were shown to be related to specific rear ejecta cloud shapes. Increase in assist gas pressure was found to directly affect particle number within the ejecta cloud depending on the mass flow rate due to nozzle size. Using no assist gas during tests was found to have significant effects on the rear melt ejecta cloud. Lack of an assist gas was shown to increase the number of particles ejected by 17 - 80%, as well as their mean diameter, which increased by 20 - 100 µm.

Change in laser irradiance was shown to generally have little effect on the mean particle velocities, particle size or overall particle momentum of the rear melt ejecta cloud. However, laser irradiance did have a direct effect on number of particles. Both positive and negative correlations were observed for the different laser set-ups tested.

It was also observed that, for the testing of mild steel, when laser power was increased to just above what was required for through hole penetration, differences occurred in the rear ejecta particle cloud. Particle velocity was shown to be 40 - 50% lower than what it was for higher laser powers, whilst particle diameter were between 7 - 16% larger.

Material type was shown to be an important contributor to the properties of the rear melt ejecta cloud. It was observed that material properties affected the overall evolution of the rear ejecta cloud shape, the number of particles velocity and particle size. For the materials tested in this work, it was found that the mean velocity of particles within the rear melt ejecta cloud was highest for aluminium, followed by titanium and finally mild steel for like parameters. Titanium was also shown to produce significantly more particles, up to 88% more for the same parameters, than the other two materials, with much larger particle diameters, 100 - 150 µm larger.

The results in this work demonstrate that a smaller pulse width is less effective at penetrating a through hole in a material when total work done by the laser is equal. This disagrees with a previous study which has shown an opposite effect [11.1].

Recurring shapes of the rear melt ejecta cloud were grouped into ten different archetypes. These archetypes were grouped into different types and related to drilling parameters. It is clear from this analysis that certain archetypes and archetype sequences are related to certain drilling parameters. Trends were also observed in the relation of specific archetypes to gas pressure and work done by the laser. The cloud shapes also provide some insight into the various mechanisms that have been identified in this work and how they tie in with specific laser parameters.

Statistical methods applied to the results from the image analysis and particle tracking methods within this thesis have been used to identify the most important process

parameters in laser drilling that can be adjusted to minimise the total volume of rear melt ejection. In the following order of importance, these are: gas pressure, laser power, material type and pulse width. Applied to results within this work, non-linear relationships between laser power and the total rear melt ejection volume and gas pressure and the total rear melt ejection volume have been observed. It has also been shown that a lower pulse width, for equivalent laser power, reduces the total amount of rear melt ejecta. It has also been shown that titanium produces a significantly higher melt volume that mild steel and aluminium under the same laser drilling parameters.

Overall, the use of high-speed filming, image analysis and particle tracking methods have proved useful within this thesis for providing an insight into the rear melt ejection process within laser drilling. It is also clear that the behaviour of the rear melt ejecta cloud is directly related to various laser drilling parameters and that this relationship is complex and generally non-linear.

Some key questions have been raised in the findings of this work, including: why are clear trends, such as those found between laser power and particle number, for the 2kW laser directly opposed to those found for the 6kW laser? Why is the rear melt ejecta particle cloud so different at near optimal breakthrough laser powers compared to higher powers? And, why do the findings of a seemingly linear positive correlation between pulse width and work done to achieve breakthrough in this work directly disagree with a linear negative correlation for the same results of another study with similar parameters? Theories have been provided within the discussion of this thesis, however, further investigation must be carried out to test their validity.

11.2 Future Work

In many respects, this project appears to be the first real in-depth analysis with a focus on the rear melt ejection of long pulse laser drilling rather than its impact

on resulting holes. Because of this, there is a large scope for the progression of future work. Firstly, an investigation of further parameters would be beneficial to increasing the overall insight of the process. Using the results found in this work as a base, particular parameters of interest would include the investigation of titanium and aluminium with the 6kW laser, as well as a more complete look at the influence of a range of pulse widths for all of the parameters tested. No assist gas experiments for the 2kW laser would also prove very beneficial, as this would allow a clear comparison of beam diameters, which was unfortunately not possible in this project due to equipment care concerns.

To further round out the investigation of these results, it would prove useful to carry out all of the tests with both the 60mm and 105mm lenses for both 1 µm and 4 µm exposure lengths. This would allow for a direct comparison of the differences in both lens and exposure time, which appear to have influenced the results carried out in this work. This, alongside the potential comparison of other lenses and exposure times, would show how much they can really influence the particle tracking process and would help to determine the most optimal set-up possible which would help to increase the efficiency of the particle tracking program and further validate the acquired results.

As well as varying lenses and exposure times, it would be useful to compare different cameras and their results. Ideally, a much faster frame rate could dramatically improve the effectiveness of the particle tracking program, as this would allow for the successful tracking of the particles with maximal velocity. Similarly, better cameras could help in the tracking of the smallest particles, although similar results could be obtained with the addition of higher quality lenses.

As demonstrated in this project, multiple particle tracking algorithms were implemented and changed in multiple revisions of the particle tracking program which was ultimately used. Although this has dramatically improved the results within

this work, there is always the potential for improvement. Therefore, application of new and further developed particle tracking algorithms to the high-speed videos recorded would be useful for providing a direct comparison of different techniques in an attempt to improve tracking efficiency. Similarly, complimentary techniques, such as streak tracking methods, which were also investigated for the same videos during this project [11.2], applied to all of the parameters investigated could provide a new look at the videos with a more accurate assessment of the highest velocities and an improved tracking efficiency.

The introduction of two or more cameras to the high-speed filming set-up could prove useful in improving the depth perception of the videos. Theoretically, this could allow for a full 3D view of the ejection process, which would improve particle tracking efficiency and allow for a better idea of the particle dispersion pattern which is seen in single videos, as although analysis of a large number of videos with the current method can balance out direction bias, it is not able to provide a clear view of the variation in 360 particle dispersion for individual videos.

Another technique which could be used with high-speed videos is colour mapping. This could be used to determine the particle temperature in relation to time and the rate of cooling of these particles. A similar method has been demonstrated by Sun [11.3], who has used the Stefan-Boltzman (Equation (11.1)) law to calculate the temperature of different regions within an open flame using images.

$$I = \sigma \times T^4 \tag{11.1}$$

Where intensity I equals the Stefan Boltzmann constant σ multiplied by the temperature T to the power of four.

This technique is also common within astronomy for identifying different types of stars by temperature, blue stars being hotter than our yellow sun, which we know because of the shorter wavelength of blue light, and red stars being cooler, due to its longer wavelength. The relationship between wavelength and temperature is

demonstrated by Wein's displacement law - Equation (11.2) .

$$\lambda_{MAX} = b \times T \tag{11.2}$$

Wein's displacement law, shown in Equation (11.2), shows that wavelength λ_{MAX} equals the constant of proportionality b multiplied by the temperature T.

These temperature measurements are only relative to other objects within an image without calibration. An object of known temperature, with respect to size, material and shape must be visible in an image in order to calculate a calibration factor. This can be achieved using a pre-calibrated black body furnace, which can be used to define the brightness of very high temperatures which are difficult to create accurately within a normal working environments. Sun [11.3] used a similar calibration technique for the temperature measurements of different regions within an open flame. However, this requires the use of a high cost, pre-calibrated black body radiator.

Further work could also make further use of the current results obtained in this project. For example, the use of a flux counter program would allow for the counting of particles as they passed through a particular region on the screen. This would allow for an assessment for the number or particles that pass through this line and off of the screen at any point in time, as opposed to only being able to count the number of particles within each frame. Figure 11.1 demonstrates the an appropriate flux counter line, of which particles would be counted when passing through.

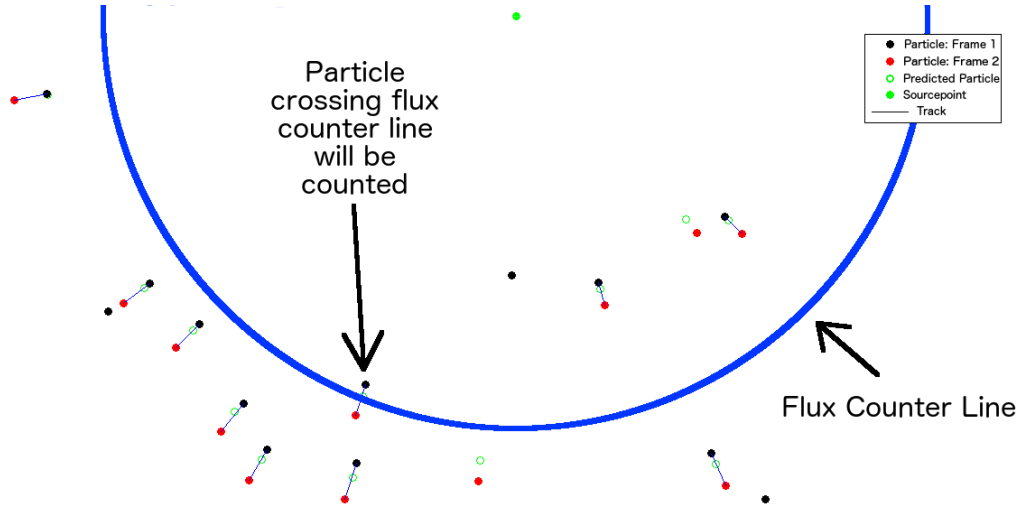


Figure 11.1: Flux counter line

References

[11.1] D. Markcoons and K. Voisey, "An Investigation to Determine if the Laser Drilling Capabilities of a 2 kW Fibre Laser can be Enhanced Using Pulse Train Shaping," vol. 39, no. 1/2, pp. 17–33, 2017.

[11.2] C. Jones, D. B. Hann, K. T. Voisey, and S. Aitken, "Application of high speed filming techniques to the study of rearwards melt ejection in laser drilling," *Journal of Laser Applications*, vol. 29, no. 2, p. 022204, 2017. [Online]. Available: http://lia.scitation.org/doi/10.2351/1.4983269

[11.3] J. Sun, C. Xu, B. Zhang, M. M. Hossain, S. Wang, H. Qi, and H. Tan, "Three-dimensional temperature field measurement of flame using a single light field camera," *Optics Express*, vol. 24, no. 2, pp. 1118–1132, January 2016, © 2016 Optical Society of America. One print or electronic copy may be made for personal use only. Systematic reproduction and distribution, duplication of any material in this paper for a fee or for commercial purposes, or modifications of the content of this paper are prohibited. [Online]. Available: http://strathprints.strath.ac.uk/60684/

12

Appendix

* * *

12.1 Simple Tracker Copyright

Copyright (c) 2016, Jean-Yves Tinevez Copyright (c) 2009, Yi Cao Copyright (c) 2011, Jean-Yves Tinevez All rights reserved.

12.2 Uncertainty Calculations

This section denotes the mathematical process taken in calculating the uncertainty for the particle velocities, diameters and momentum and other necessary calculations in order to quantify the total uncertainty that is included in the results section. Ultimately, these calculations show that the uncertainty for these results are very low, relative to the actual values, due to the large number of overall particles analysed over numerous videos.

12.2.1 Particle Velocity

$$\sigma_V = \pm\sigma_{CF} \pm \sigma_L \pm \sigma_t + \sigma_{DoF}$$

$$ConfidenceLevel(95\%) = \frac{2 \times \sigma_V}{\sqrt{n_{tP} - 1}}$$

Where:

σ_V = Velocity uncertainty, σ_{CF} = Calibration factor uncertainty, σ_L = Track measurement uncertainty, σ_t = Time uncertainty, σ_{DoF} = Depth of field uncertainty, n_{tP} = Total number of particles tracked

Depth of Field Uncertainty (σ_{DoF})

Depth of field uncertainty is calculated using the maximum possible limit of track length due to depth of field. This is expressed as a velocity using the time between frames.

$$a = \sqrt{c^2 - (\frac{DoF}{2})^2}$$

$$D = c - a$$

$$\sigma_{DoF} = \frac{D}{t}$$

Where:

c = Maximum allowable track length, DoF = Depth of field D = Maximum length uncertainty t = Time between frames

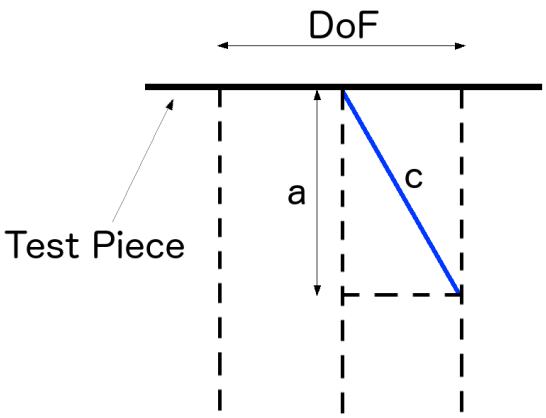


Figure 12.1: Depth of field uncertainty is calculated geometrically from the largest allowable track length

Calibration Factor Uncertainty (σ_{CF}) Calibration factor uncertainty is calculated using the uncertainty in measured values when calculating the calibration factor.

$$\sigma_{CF} = \sigma_{L_{CF}} + \sigma_{P_{CF}}$$

$$\sigma_{L_{CF}}(\%) = \frac{\delta_{L_{CF}}}{L_{CF}} \times 100$$

$$\sigma_{P_{CF}}(\%) = \frac{\delta_{P_{CF}}}{P_{CF}} \times 100$$

Where:

L_{CF} = Length measured on calibration plate in metres, $\sigma_{L_{CF}}$ = Error in length measured on calibration plate due to ruler measurements, P_{CF} = Length measured on calibration plate measured on screen in pixels, $\sigma_{P_{CF}}$ = Error of length measured on calibration plate in pixels, due to on-screen measurement

Track Measurement Uncertainty σ_L

$$\sigma_L(\%) = \frac{\delta_L}{L} \times 100$$

Time Measurement Uncertainty σ_t

$$\sigma_t(\%) = \frac{\delta_t}{t} \times 100$$

12.2.2 Particle Diameters

$$\sigma_D = \pm\sigma_{CF} \pm \sigma_M \pm \sigma_{DoF}$$

$$Confidence Level(95\%) = \frac{2 \times \sigma_D}{\sqrt{n_P - 1}}$$

Where:
σ_D = Diameter uncertainty, σ_{CF} = Calibration factor uncertainty, σ_M = Diameter measurement uncertainty, σ_{DoF} = Depth of field uncertainty, n_P = Total number of particles

Calibration Factor Uncertainty (σ_{CF}) Calibration factor uncertainty is calculated using the uncertainty in measured values when calculating the calibration factor.

$$\sigma_{CF} = \sigma_{L_{CF}} + \sigma_{P_{CF}}$$

$$\sigma_{L_{CF}}(\%) = \frac{\delta_{L_{CF}}}{L_{CF}} \times 100$$

$$\sigma_{P_{CF}}(\%) = \frac{\delta_{P_{CF}}}{P_{CF}} \times 100$$

Where:

L_{CF} = Length measured on calibration plate in metres, $\sigma_{L_{CF}}$ = Error in length measured on calibration plate due to ruler measurements, P_{CF} = Length measured on calibration plate measured on screen in pixels, $\sigma_{P_{CF}}$ = Error of length measured on calibration plate in pixels, due to on-screen measurement

Particle Diameter Measurement Uncertainty (σ_M)

Diameter is calculated from the 'Equiv. Diameter' function used within MATLAB, which reverse calculates diameter from each particle's area. Therefore, the error in diameter must take into account the calculated area.

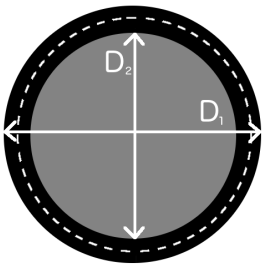


Figure 12.2: The dotted line represents the true particle size, whilst D_1 and D_2 demonstrate the size of a diameter of the particle +1 pixel and -1 pixel respectively

$$D_1 = D + (2 \times 0.5)$$

$$D_2 = D - (2 \times 0.5)$$

$$\delta_A = \pi(\frac{D_1}{2})^2 - \pi(\frac{D_2}{2})^2$$

$$\sigma_A(\%) = \frac{\delta_A}{A}$$

$$\sigma_M = \frac{\sigma_A}{2}$$

Where:
D = Particle diameter, D_1 = Mean particle diameter +1 pixel, D_2 = Mean particle diameter +1 pixel, δ_A = Absolute error in area calculation, σ_A = Percentage error in area, A = Mean particle area, σ_M = Measurement error due to diameter measurement

Depth of Field Uncertainty (σ_{DoF})

$$\sigma_{DoF}(\%) = (\frac{DoF}{d}) \times 100$$

linebreak

Where:
d = Distance between camera and object, DoF = Depth of field

12.2.3 Particle Momentum

$$\sigma_{Mom} = \pm\sigma_V \pm \sigma_D$$

$$ConfidenceLevel(95\%) = \frac{2 \times \sigma_{Mom}}{\sqrt{n_P - 1}}$$

Where:

σ_D = Diameter uncertainty, σ_V = Velocity uncertainty, σ_{Mom} = Momentum uncertainty, n_P = Total number of particles